

**MODELING OF ENVIRONMENTAL EFFECTS ON THERMAL DETECTION
OF SUBSURFACE DAMAGE FOR CONCRETE BRIDGES**

A Dissertation

presented to

the Faculty of the Graduate School

at the University of Missouri-Columbia

In Partial Fulfillment

of the Requirements for the Degree

Doctor of Philosophy

by

RILYA RUMBAYAN

Dr. Glenn Washer, Dissertation Supervisor

MAY 2013

© Copyright by Rilya Rumbayan 2013

All Rights Reserved

The undersigned, appointed by the dean of the Graduate School, have examined the dissertation entitled

**MODELING OF ENVIRONMENTAL EFFECTS ON THERMAL DETECTION
OF SUBSURFACE DAMAGE FOR CONCRETE BRIDGES**

presented by **Rilya Rumbayan**

a candidate for the degree of **Doctor of Philosophy**

and hereby certify that, in their opinion, it is worthy of acceptance.

Dr. Glenn Washer

Dr. Hani Salim

Dr. Brent Rosenblad

Dr. Steven Neal

ACKNOWLEDGEMENTS

I thank God for giving me strength throughout my study in University of Missouri. He gave me grace to complete the work even though it took me longer than expected. The completion of this work would also not be possible without the support of professors, colleagues, friends, and family. I would like to express my deepest appreciation to my supervisor, Dr. Glenn Washer, for his valuable advises, support and encouragement throughout my study. I would also like to thank my committee members: Dr. Hani Salim, Dr. Brent Rosenblad, and Dr. Steven Neal for their feedback, guidance and support. Thanks are due to all my professors for the excellent education they offered me during my study.

I am grateful to Fulbright scholarship for awarding the scholarship and to University of Missouri for the research assistantship, which made this study possible. I express my thanks to Ms. Becky Showmaker for her support as supervisor in sponsored student program. I also thank my colleagues: Seth Nelson, Naveen Kumar, Richard Fenwick, Justin Schmidt, and Mr. Michael Trial, that supported me in many ways during my study. I must thank to staff members in Department of Civil Engineering: Ms. Mary McCush, Ms. April Klug, and Ms. Connie Taylor for their support throughout my study. Finally, the greatest thanks go to my beloved family for their prayers, unconditional love and understanding from my initial preparation to the present stage of this study.

TABLE OF CONTENTS

ACKNOWLEDGEMENTS	ii
LIST OF FIGURES.....	ix
LIST OF TABLES	xiii
ABSTRACT.....	xiv
1. INTRODUCTION	1
1.1 Background.....	1
1.2 Problem Statement.....	3
1.3 Goal and Objectives	5
1.4 Research Approach.....	6
1.5 Outline of Dissertation	10
2. LITERATURE REVIEW	12
2.1 Introduction.....	12
2.2 Mechanisms of Concrete Bridge Deterioration	12
2.2.1 Corrosion of rebar in concrete	13
2.2.2 Cracking, delaminations, and spalling of concrete.....	14
2.3 Technologies for Subsurface Defect Detection in Concrete	15
2.3.1 Conventional methods.....	15
2.3.2 Nondestructive evaluation (NDE) technologies.....	16
2.3.2.1 Impact echo (IE)	17
2.3.2.2 Ground penetrating radar (GPR)	18
2.3.2.3 Infrared (IR) thermography	19

2.4	Theoretical Foundation of IR Thermographic	20
2.4.1	Basic principles of IR thermography	20
2.4.2	IR thermography instruments.....	22
2.4.3	Overview of heat transfer.....	25
2.4.3.1	Heat transfer mechanisms.....	25
2.4.3.2	Thermal inertia.....	28
2.4.3.3	Theory of heat diffusion	29
2.4.3.4	Transient heat transfer.....	30
2.5	Application of IR Thermographic	31
2.5.1	Active and passive IR thermography measurement	31
2.5.2	Advantages and limitations of IR thermography measurement	32
2.5.3	Previous investigations on the use of IR thermography for concrete bridge inspection.....	33
2.5.3.1	Environmental conditions.....	34
2.5.3.2	Void depths and void thicknesses.....	35
2.5.3.3	Material contained in the delamination.....	36
2.5.3.4	Material properties of concrete	37
2.5.3.5	Asphalt overlays	38
2.5.3.6	Discussion	39
3.	NUMERICAL MODEL DEVELOPMENT AND MODEL EVALUATION	40
3.1	Introduction.....	40
3.2	Numerical Model Descriptions.....	41
3.2.1	Geometry and material properties	41
3.2.2	Boundary conditions	43

3.2.3	Mesh density.....	45
3.3	Simulation Results.....	48
3.3.1	Thermal images.....	49
3.3.2	Surface temperatures and thermal contrasts.....	51
3.4	Evaluation of Model Performance	56
3.4.1	Trend curve of thermal contrasts	56
3.4.2	Correlation analysis	60
3.4.3	Error analysis.....	62
3.4.4	Comparison of the model results with the experimental results.....	68
3.5	Conclusion.....	71
4.	PARAMETRIC STUDIES	73
4.1	Introduction.....	73
4.2	Parametric Study Case 1: Effect of varying void depths and void thicknesses.....	74
4.2.1	Description.....	74
4.2.2	Results and discussions	78
4.2.2.1	Estimation depth of void.....	84
4.2.2.2	Minimum void thickness.....	85
4.2.2.3	Determining effect of reinforcing steel	86
4.2.2.4	Numerical and field experimental comparison	87
4.3	Parametric Study Case 2: Effect of the materials in delamination	89
4.3.1	Description.....	89
4.3.2	Results and discussions	89
4.4	Parametric Study Case 3: Effect of material properties of concrete ...	91

4.4.1	Description.....	91
4.4.2	Results and discussions	92
4.5	Parametric Study Case 4: Effect of asphalt overlays.....	94
4.5.1	Description.....	94
4.5.2	Results and discussions	94
4.6	Example of the Post-test Model Analysis	96
4.6.1	Description of the field testing.....	97
4.6.1.1	Field testing [43]	97
4.6.1.2	The coring test [43]	99
4.6.1.3	The weather patterns surrounding the field test.....	101
4.6.2	The predictive model analyses	103
4.6.3	The post-test model verification.....	105
4.7	Conclusion.....	106
5.	EQUATION DEVELOPMENT FOR MAXIMUM THERMAL CONTRAST OF SUBSURFACE DAMAGE IN CONCRETE	110
5.1	Introduction.....	110
5.2	Multi-parameter Regression Analysis	110
5.3	Equation Development for the Surface Exposed to Direct Solar Loading (the South Side).....	112
5.3.1	Dataset for the equation development.....	112
5.3.2	Correlation analysis of all variables	115
5.3.3	Variable selection for the equation development	116
5.3.4	The final equation for the South side	118
5.3.5	Residual analysis for the South side.....	120
5.3.6	Equation verification	121

5.3.6.1	Comparison of the equation results with the numerical model results	121
5.3.6.2	Comparison of the equation results with the experimental results.....	123
5.3.6.3	Case examples (the South side).....	124
5.4	Equation Development for the Shaded Surface (the North Side)	126
5.4.1	Dataset for the equation development.....	126
5.4.2	Correlation analysis of all variables	128
5.4.3	Variable selection for the equation development	129
5.4.1	The final equation for the North side.....	130
5.4.2	Residual analysis for the North side	132
5.4.3	Equation verification	133
5.4.3.1	Comparison of the equation results with the numerical model results	133
5.4.3.2	Comparison of the equation results with the experimental results.....	134
5.4.3.3	Case examples	135
5.5	Conclusion.....	137
6.	SUMMARY	139
6.1	Major Results	139
6.1.1	Numerical Model Development and Model Evaluation	139
6.1.2	Parametric Studies	141
6.1.3	Equation Development for Maximum Thermal Contrast of Subsurface Damage in Concrete.....	143
6.2	Recommendations.....	146
	BIBLIOGRAPHY	147

APPENDIX A.....	152
APPENDIX B.....	172
APPENDIX C.....	179
APPENDIX D.....	192
APPENDIX E.....	200
VITA	208

LIST OF FIGURES

Figure 1.1	Summary of research approach.....	9
Figure 2.1	Thermal response of delaminations in concrete: (A) day time condition [12]; (B) night time condition; (C) surface temperature and thermal contrast as a function of time	22
Figure 2.2	Infrared region in the electromagnetic spectrum [34]	23
Figure 2.3	Typical components of an IR thermography.....	25
Figure 2.4	The heat transfer mechanisms for concrete with environmental interaction	26
Figure 3.1	Concrete block containing subsurface voids: (A) model; and (B) photograph of experimental test.....	42
Figure 3.2	Environmental parameters as boundary conditions in simulation on November 5, 2007: (A) solar radiation; (B) ambient temperature; and (C) wind speed.....	44
Figure 3.3	Meshing in COMSOL	46
Figure 3.4	Thermal contrast of the model using different type of element density.....	47
Figure 3.5	Estimated maximum thermal contrast and computation time using different mesh density	48
Figure 3.6	Typical thermal images of the thermal behavior for the South side of the concrete block: (A) the model result at noon; (B) the experimental test result at noon; (C) the model result at 8:00 p.m.; and (D) the experimental test result at 8:00 p.m.	50
Figure 3.7	Modeled surface temperature for the South face of the block (November 5, 2007)	52
Figure 3.8	Modeled surface temperatures for the North face of the block (May 5, 2008).....	53

Figure 3.9	The time varying thermal contrast for the South face of the block; Solid line is for the moving average an hour. Dash line is for the raw data.	55
Figure 3.10	The time varying thermal contrast the North face of the block; Solid line is for the moving average an hour. Dash line is for the raw data.	55
Figure 3.11	Comparison of model predicted and field-measured of thermal contrast for the South (sunny) side: (A) 51 mm deep target, and (B) 76 mm deep target	57
Figure 3.12	Comparison of model predicted and field-measured of thermal contrast for the North (shaded) side: (A) 51 mm deep target, and (B) 76 mm deep target	59
Figure 3.13	Percentage distribution for thermal contrast differences between model-predicted and field-observed of the sunny side: (A) 25 mm deep target; (B) 51 mm deep target; (C) 76 mm deep target; and (D) 127 mm deep target.	66
Figure 3.14	Percentage distribution for thermal contrast differences between model-predicted and field-observed of the shaded side: (A) 25 mm deep target; (B) 51 mm deep target; (C) 76 mm deep target; and (D) 127 mm deep target.	67
Figure 3.15	Predicted maximum thermal contrasts obtained from FEM model versus actual maximum thermal contrasts obtained from the experimental testing (for the South side).....	69
Figure 3.16	Predicted maximum thermal contrasts obtained from FEM model versus actual maximum thermal contrasts obtained from the experimental testing (for the North side)	70
Figure 4.1	The basic geometry of the concrete model	74
Figure 4.2	Three consecutive days of environmental parameters as a boundary condition in simulation: (A) solar radiation; (B) ambient temperature; and (C) wind speed	77
Figure 4.3	The time varying thermal contrast: (A) as a function of void depth, and (B) as a function of void thickness.....	79
Figure 4.4	(A) Effect of void depth on the maximum thermal contrast and (B) Effect of void thickness on the maximum thermal contrast.....	80

Figure 4.5	Values obtained for constant A and constant K for exponential expressions fitted to the maximum thermal contrast-void depth data in variation of void thickness	83
Figure 4.6	The surface temperatures at a reference point of the model with rebar and without rebar	87
Figure 4.7	The comparison between the maximum thermal contrasts of model-predicted and the experimental data: (A) the sunny side, and (B) the shaded side	88
Figure 4.8	The time varying thermal contrast as a function of the materials present in the void.....	90
Figure 4.9	Effect of void material on the maximum thermal contrast.....	91
Figure 4.10	Effect of material properties of concrete on the maximum thermal contrast: (A) thermal conductivity; (B) volumetric heat; and (C) emissivity.....	93
Figure 4.11	The time varying thermal contrast as a function of asphalt thickness: (A) 51 mm deep void (B) 76 mm deep void.....	95
Figure 4.12	Effect of asphalt thickness on the maximum thermal contrast	96
Figure 4.13	The measured thermal contrast detected during the field test [43].....	98
Figure 4.14	Photograph of the coring operation [43].....	99
Figure 4.15	Photographs of core locations : (A) Red delamination; and (B) Green delamination [43].....	100
Figure 4.16	Three consecutive days of environmental parameters as a boundary condition in simulation: (A) solar radiation; (B) ambient temperature; and (C) wind speed.....	102
Figure 4.17	Thermal contrast as a function of void thickness for 51 mm deep void	104
Figure 4.18	Values obtained for constant A and constant K from the model under a particular weather condition shown in Fig.14.	105
Figure 5.1	Data check for outliers: (A) Daily maximum solar loading and (B) Daily average wind speed over 6 a.m. to 6 p.m. period.....	113

Figure 5.2	Minitab output for multiple regression analysis of ΔT_{\max} versus $e^{-0.02 \times \text{depth}}$, $SL_{\text{(Total)}}^{1/4}$, $T_{\text{air (Max)}}$, $T_{\text{air (Avg)-1}}$, $W_{\text{(Avg 23)}}$	119
Figure 5.3	Residual of the maximum thermal contrast vs. environmental variables: (A) Solar loading; (B) Ambient temperature change; (C) Wind speed; and (D) Residual histogram for the maximum thermal contrast	121
Figure 5.4	Predicted versus actual maximum thermal contrast obtained from the FEM results (based on the South side dataset)	122
Figure 5.5	Predicted versus actual maximum thermal contrast obtained from the experimental results (based on the South side dataset)	124
Figure 5.6	The comparison among the maximum thermal contrast of the equation, the FEM model, and the experimental testing	125
Figure 5.7	Data check for outliers: (A) Daily maximum air temperature, and (B) Daily average wind speed over 6 a.m. to 12 p.m.....	127
Figure 5.8	Minitab output for multiple regression analysis of ΔT_{\max} versus $e^{-0.02 \times \text{depth}}$, $T_{\text{air(Change*)}}$	131
Figure 5.9	(A) Residual of the maximum thermal contrast vs. Ambient temperature change; and (B) Residual histogram for the maximum thermal contrast	132
Figure 5.10	Predicted versus actual maximum thermal contrast obtained from the FEM results (based on the North side dataset).....	134
Figure 5.11	Predicted versus actual maximum thermal contrast obtained from the Experimental results (based on the North side dataset)	135
Figure 5.12	The comparison among the maximum thermal contrast of the model equation, the FEM model, and the experimental testing ..	136

LIST OF TABLES

Table 3.1	Material properties of the concrete block model.....	42
Table 3.2	Mesh Statistics	46
Table 3.3	Thermal contrast correlations (r) between the model and the experimental results. N is number of cases.	62
Table 3.4	Time-series error analysis of thermal contrast differences between the model and the experimental results. <i>MBE</i> is mean bias error, <i>MAE</i> is mean absolute error, and <i>RMSE</i> is root mean squared error.....	64
Table 4.1	An example input parameters for a simulation in Case 1	75
Table 4.2	Result for simulations involving void depths (d) and void thicknesses (z) on maximum thermal contrast (ΔT_{max}).....	81
Table 4.3	Example of estimation of maximum thermal contrast ($d=51$ mm deep void)	84
Table 4.4	Material properties for Case 2 involving different materials contained in the void and the sound concrete.....	89
Table 4.5	The field test results including the coring results and the maximum thermal contrast (ΔT_{max}) from thermography images..	100
Table 5.1	Descriptive statistics of data in the South side datasets.....	114
Table 5.2	Pearson correlation coefficient (R) matrix for the South side datasets	115
Table 5.3	Best subsets regression method on the maximum thermal contrast for the South side datasets.....	118
Table 5.4	Descriptive statistics of data in the North side datasets	128
Table 5.5	Pearson correlation coefficient (R) matrix for the North side datasets	129
Table 5.6	Best subsets regression method on the maximum thermal contrast for the North side datasets	130

MODELING OF ENVIRONMENTAL EFFECTS ON THERMAL DETECTION OF SUBSURFACE DAMAGE FOR CONCRETE BRIDGES

Rilya Rumbayan

Dr. Glenn Washer, Dissertation Supervisor

ABSTRACT

This study developed a numerical model to predict thermal contrasts for subsurface delaminations based on a given set of environmental conditions. The finite element method (FEM) was used to perform 3-D, transient heat transfer analysis of a concrete block with voids intended to provide an idealized model of delaminations. The effectiveness of the modeling was evaluated by comparing the thermal contrasts predicted by the model to those obtained from experimental testing of an actual concrete block of the same dimensions. The correlation and error analysis between the model and the experimental testing results indicated that the model could be an effective tool for the prediction of anticipated thermal contrasts.

Key parameters were studied using the verified model, such as the depth and thickness of a delamination, materials present in the delamination, asphalt overlays, and the material properties of the concrete. The effect of these parameters on the thermal contrast developed on the surface above a delamination was assessed. An example model analysis was presented to illustrate the model application for the thermal measurements during a field test.

The model results provided valuable information on the expected responses when using thermography to detect delaminations in a concrete bridge deck.

A practical equation was also proposed using a statistical approach for predicting the maximum thermal contrast at various void depths under various environmental conditions. The results compared well to the FEM model and to the experimental testing.

1. INTRODUCTION

1.1 Background

Reinforced concrete is commonly used as a construction material for highway bridge structures. One of the most significant deterioration mechanisms in reinforced concrete is corrosion of the embedded reinforcement steel, which results in subsurface damage to the concrete. As the steel corrodes, it expands, causing tension stresses in the surrounding concrete [1]. These tensile stresses result in cracks or subsurface fracture planes in the concrete at, or near, the level of the reinforcement. These subsurface fracture planes are commonly referred to as *delaminations*. As the deterioration process continues, a rupture between the delaminated region and the main structural component can occur, which results in spalling of the concrete [2].

This kind of damage affects concrete bridge safety and serviceability. Spalling of the concrete deck surfaces can affect the ability of the deck to carry traffic at normal speeds, may accelerate the overall deterioration of the deck, and can require maintenance or renovation activities that disrupt traffic [3, 4]. Concrete spalling on the underside of an overpass bridge can be a safety hazard to traffic passing below if concrete falls from the bridge onto moving traffic [5].

For these and other bridge components, delaminations and spalling are indicative of deterioration and active corrosion, such that locating and defining the extent of this damage provides important information regarding the current condition and future repair needs.

Various conventional techniques are used to detect subsurface delaminations, including sounding with hammers or rods and chain dragging. These methods require hands-on access to the surfaces being inspected, are subjective, and can be inaccurate [6, 7]. For highway bridges, achieving the access necessary to reach key bridge components for sounding can require special access equipment such as man lifts, and often requires lane closures that disrupt traffic. In the case of chain dragging, only bridge decks and other horizontal surface can be inspected.

Due to the access requirements of conventional techniques and their inherent subjectivity, nondestructive evaluation (NDE) techniques have been explored as a means of reducing the access requirements and improving the quality of inspection in various bridge components (deck, soffit, abutment, and parapet). Some of the NDE techniques are sonic testing, impact echo (IE), ground penetrating radar (GPR) technology, and infrared (IR) thermography [2, 4, 8-11]. Sonic testing, sometimes implemented using an IE approach, requires impact at the surface of the material under test, such that hands-on access to that surface is always required. In the case of GPR, air-coupled antennae can be used to reduce required traffic control for some bridge decks, but generally

need a period of lane closure to the surface to be implemented. Of these technologies, IR thermography is the only method that does not require direct access to the surface under inspection because images can be captured from distances of 30 m using appropriate optical lenses [12]. IR thermography utilizes the heat energy radiated by an object to characterize its subsurface conditions. Subsurface defects in concrete, such as delaminations, affect the rate of heat transfer through the thickness of the concrete and hence result in surface temperature differentials with respect to sound (defect-free) areas. The surface temperatures are recorded by a thermography camera in the form of real time images (thermograms) that are interpreted to detect and characterize subsurface delaminations in the concrete.

1.2 Problem Statement

Thermographic imaging technique provides a practical tool for the detection of delaminations from a distance without direct access to the surface; however, the effectiveness of the technique is highly dependent on environmental conditions at the time, and prior to when a thermal image is captured. The thermal gradient in the concrete that results from certain environmental conditions, such as solar loading, drives heat transfer in the concrete that is disrupted by subsurface delaminations, resulting in variations in surface temperature (i.e. thermal contrast) that are used to identify the location of subsurface damage in the thermal image.

Currently, limited research and development are available on thermal detection of subsurface damage in concrete under varying environmental effects. Most research studies focused on the detectability of the subsurface delamination under a single set of environmental variables, that is at a certain point in time. Also, these research efforts focused on the detection of subsurface delaminations in concrete bridge decks exposed to solar radiation [2, 6, 13, 14]. Research efforts by Washer, et al. [12, 15-17] have studied the effect of environmental conditions not only in the bridge deck, but also in the bridge deck soffit, and other bridge components. These efforts have included constructing a large concrete block with simulated voids, and analyzing the effects of environmental parameters over a 6 month period. The concrete block was aligned such that the South face of the block was exposed to direct solar loading, while the North face of the block was not exposed to direct solar loading. In these configurations, the South face provided a model of sunny side and the North face provided a model of shaded side.

For practical inspection scenarios, the environmental conditions obviously cannot be controlled and vary on a day-to-day basis. Therefore, a full understanding of various environmental conditions affecting concrete bridge components at the time of imaging is necessary to make subsurface damage detection most effective. An accurate model that can estimate the anticipated level of thermal contrast based on the anticipated depth of a delamination and for a given set of actual environmental conditions could provide an essential tool for

the inspection of concrete bridge components. Such a model could be used to assess the combination of solar loading, ambient temperature change and wind speed during, or leading up to, a field inspection to predict the anticipated thermal contrast for a delamination at a given depth. This data could then be used to evaluate if sufficient conditions exist to make it likely that a delamination would be detected, to estimate the depth of a detected delamination based on the thermal contrast, and to determine if detected thermal differences correspond with actual subsurface defects. The research reported herein describes the development of such a model, and illustrates its application to practical inspection scenarios.

1.3 Goal and Objectives

The goal of this study is to improve the reliability of bridge condition assessments. The objectives of this study are to:

1. Develop a numerical model to predict the thermal response for subsurface voids (i.e. delaminations) in concrete under various environmental conditions, for the purpose of providing an analytical tool to support the thermographic inspection of concrete bridge components,
2. Evaluate the model performance by comparing to the experimental data,

3. Study the effect of different field test parameters expected to influence the detectability of the subsurface voids,
4. Apply the model for revealing thermal contrast from thermography measurements (post-test model), and
5. Develop and verify equations to predict thermal contrasts based on environmental conditions.

1.4 Research Approach

The research had four distinct phases as summarized in Figure 1.1. The first phase of the research was comprised of a literature search that includes mechanisms of concrete bridge deterioration, typical techniques for subsurface damage detection in concrete, theoretical foundations of IR thermography, applications of IR thermographic in concrete, and mechanisms of heat transfer. The previous experimental testing that studied the effect of environmental conditions on the surface temperature of a concrete block containing subsurface voids at different depths [18, 19] was outlined

The second phase of the research focused on numerical simulation model development. The model was developed using the finite element method (FEM) in COMSOL-Multiphysics and verified using actual experimental test data [18, 19] from the concrete block containing simulated voids. Actual weather patterns, i.e. the actual weather conditions (solar loading, ambient temperature variations and

wind speeds) recorded during experimental testing were used as model inputs such that the resulting thermal contrasts from the model and actual experimental data could be compared. Analysis of the correlation and error were used to determine if the model was likely to be an effective tool for predicting thermal contrasts based on a given set of weather conditions.

The third phase of the research project involved a series of parametric studies based on the numerical modeling. The following four cases of key parameters expected to influence the detectability of the subsurface voids were performed:

- Case 1: The effect of varying void depths and void thickness on thermal contrast.
 - A simplified estimation of void depth from the measured thermal contrast was developed.
 - Minimum thickness of detectable void was evaluated.
- Case 2: The effect of different materials contained in the delamination void.
 - Modeling was completed for a void filled with air, water, ice and epoxy.
 - In addition, a Styrofoam-filled void was analyzed to compare with the experimental test data.
- Case 3: The effect of the material properties of the concrete.

- The properties included thermal conductivity, volumetric heat, and emissivity
- Case 4: The effect of asphalt overlay.

An example of the post-test model analysis was also presented to analyze the thermal contrast of subsurface voids in concrete, given the known weather patterns surrounding the test, and the depth and thickness of a delamination in a real bridge deck. The post-test model results were then compared to the measured thermal contrast detected by an IR thermography.

The next phase of the research focused on development of a practical equation to predict the maximum thermal contrast for both the surface exposed to direct solar loading (the South side) and the shaded surface (the North side). The equation model was developed statistically using multi-parameter regression analysis to establish a functional relationship among the maximum thermal contrast at various depths of voids in the concrete, obtained through the numerical simulation, and the daily environmental variables datasets over a 6 month period recorded through the experimental testing. Finally, the prediction equation model was verified by comparing the maximum thermal contrast results with those obtained from both the numerical simulation model and the experimental data.

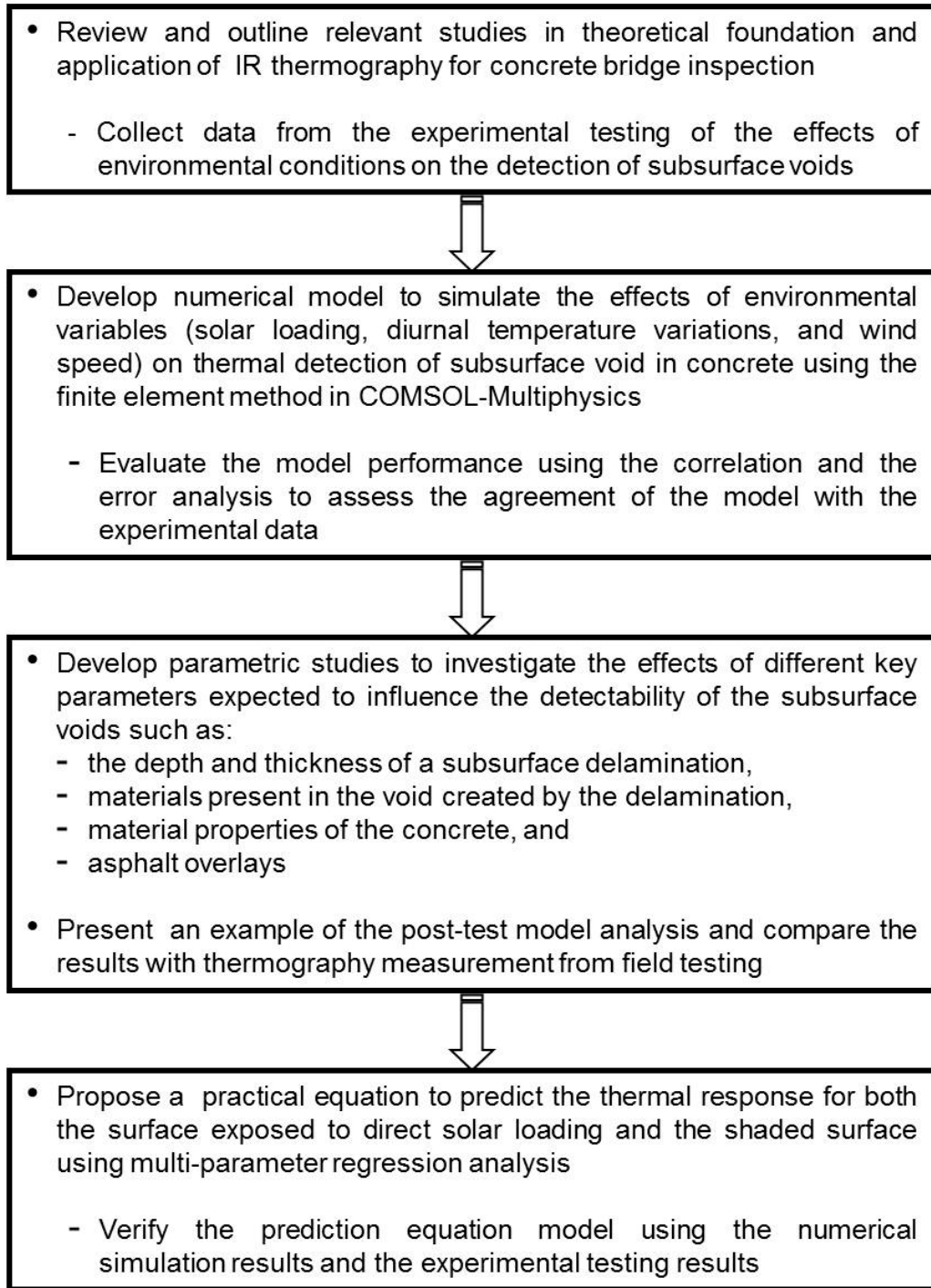


Figure 1.1 Summary of research approach

1.5 Outline of Dissertation

This dissertation is composed of six chapters. Chapter 1 introduces the background, problem statement, goal and objectives, research approach, and outline of the dissertation.

Chapter 2 summarizes the literature review related to this study. It includes mechanisms of concrete bridge deterioration, and technologies for subsurface defect detection in concrete. The chapter also contains the theoretical foundations and the application of IR thermography for concrete bridges. A short review of heat transfer is introduced in this chapter. Relevant studies that were done on the use of IR thermography for concrete bridge inspection are reviewed.

The numerical model development and verification are discussed in Chapter 3. This chapter introduces the FEM in COMSOL-Multiphysics that was used to simulate the effects of environmental conditions on the detection of subsurface voids in concrete. Model descriptions including geometry, material properties, boundary conditions and mesh density are presented. Thermal images, surface temperatures and thermal contrast obtained from the numerical simulation are reported. The evaluation of the model performance using correlation and error analysis is also discussed.

Chapter 4 presents parametric studies of the key parameters affecting the detectability of the subsurface voids. The effect of void depth, void thickness, different materials present in the delamination void, material properties of the

concrete, and asphalt overlay are carried out and the results are discussed. Also, a simple procedure for void depth estimation and minimum thickness of detectable void estimation are demonstrated in this chapter. An example of the post-test model based numerical simulation is also presented.

Chapter 5 describes a range of statistical procedures to develop an equation to predict the maximum thermal contrast from the daily environmental variables. The procedures are discussed separately for the sunny side and the shaded side. This chapter introduces the multi-parameters analysis that was used to obtain regression equations of the maximum thermal contrast at various depths of void in concrete. The verification of the proposed equations with finite element simulations and the experimental data is also presented.

Finally, Chapter 6 summarizes all major results of this research and recommendation for future research.

2. LITERATURE REVIEW

2.1 Introduction

This chapter describes the literature review relevant to infrared thermography technique for detecting subsurface delamination in concrete bridges. First, mechanisms of concrete bridge deterioration and overview of technologies for detecting a subsurface delamination are presented. Second, relevant studies in theoretical foundation and application of IR thermography for concrete bridges are outlined.

2.2 Mechanisms of Concrete Bridge Deterioration

Deterioration of concrete bridge components is one of the major bridge maintenance problems affecting bridges in the United States. The primary mechanism of the deterioration is corrosion of embedded reinforcement (rebar), which leads to cracking, delamination, and spalling of concrete [13]. Details about this issue are discussed in this section.

2.2.1 Corrosion of rebar in concrete

Concrete normally provides reinforcing steel with excellent corrosion protection. The high-alkaline environment in concrete creates a passive film that protects the steel from corrosion. However, corrosion of steel can occur when oxygen and moisture are present and the passivity of the steel is destroyed or dissolved either by decrease in pH value due to carbonation of the concrete or by chloride ions intrusion (or a combination of these two factors) [5].

Carbonation of concrete is the result of the reaction of carbon dioxide (CO_2) and other acidic gases in the air and the alkaline constituents of cement paste. As a result, the alkalinity of the concrete is reduced and the steel is no longer protected against corrosion. Fortunately, carbonation rates are generally low, typically no more than about 1 mm a year for good quality concrete. Therefore, carbonation-induced corrosion has not been considered as serious a problem in concrete structures as corrosion induced by chloride ions.

Disruption of the passive film by chlorides is the most prevalent and damaging cause of corrosion of steel in concrete. The steel is susceptible to corrosion initiation when penetration of chloride ions at the steel surface exceeds a chloride threshold concentration level, which is dependent on many factors including: quality of concrete, relative humidity and temperature of the concrete, and pH value of the pore solution. There are two sources by which chloride ions may be introduced into the concrete: internal sources, such as the cement,

aggregate, and water used to make the concrete, and external sources such as deicing chemicals or seawater.

Corrosion of steel in concrete is an electrochemical process. In this process, steel is converted to iron-oxides, also known as rust. The volume of rust products is about four to six times larger than that of steel [20]. This volume increase induces internal tensile stresses in the concrete.

2.2.2 Cracking, delaminations, and spalling of concrete

Cracking is initiated in the concrete when internal tensile stresses induced by corrosion exceed the tensile strength of the concrete. Cracking affects concrete deterioration by providing access of chlorides, oxygen, and moisture to the reinforcing steel. In this case, the presence of cracking can increase the rate of corrosion. As the corrosion process continues, it causes a delamination (i.e. a subsurface fracture plane parallel to the surface of the concrete), which occurs frequently at the depth of the reinforcing steel. Delaminations may extend over a substantial area beneath the concrete surface. These delaminations may become separated from the concrete, resulting in a spall.

The corrosion-induced spalling of concrete has been a concern to transportation agencies due to the potential serviceability and safety issues for concrete bridge structures. For concrete bridge decks, spalling can affect the condition of the riding surface and may accelerate the overall deterioration of the structural components beneath the deck. Concrete spalling on the undersurface

of an overpass bridge can be more critical, as it raises safety issues to traffic below the bridge [21, 22].

2.3 Technologies for Subsurface Defect Detection in Concrete

As described before, the subsurface fracture plane, or delamination, can affect the structural integrity of concrete and lead to further deterioration and damage. Detection of this type of damage in its initial stages is critical to identifying repair and maintenance needs. This section discusses the most commonly applied methods for identifying subsurface delaminations in concrete, including conventional methods and NDE methods. The basic principles, advantages and limitations of these evaluation methods/technologies are briefly described in this section.

2.3.1 Conventional methods

Two common types of conventional methods that are based on sounding to detect delaminations on concrete are hammer sounding and chain dragging. The hammer sounding method involves tapping the surface of a concrete member with a hammer at multiple locations and listening for a distinctive sound produced. A dull or hollow sound is created when delaminated concrete is encountered, and a clear ringing sound is heard on non-delaminated concrete.

For large horizontal surface areas, such as bridge decks, chain drag is used to detect delaminations with reasonable accuracy. This method involves

dragging a chain over the bridge deck surface. Similar to the hammer sounding method, areas of non-delaminated concrete will produce a clear ringing sound, and areas of delaminated will produce a hollow sound. The typical chain used for inspection consists of about five segments of 1-inch link chain of $\frac{1}{4}$ inch diameter steel approximately 18 inches long attached to an aluminum or copper tube about 3 feet in length [23]. The procedure of the method can be found in ASTM D4580-03 (procedure B) [24].

The main advantages of both chain dragging and hammer sounding methods are simplicity, portability and low operating cost [8]. However, these methods require direct access to the surfaces being inspected. For highway bridges, achieving the access necessary to reach key bridge components for sounding can require special access equipment such as man lifts, and often requires lane closures that disrupt traffic. In the case of chain dragging, it cannot be performed on vertical members of a bridge and thus is limited to the topside of bridge decks. In addition, these methods cannot quantitatively analyze the amount of deterioration in concrete and use the subjective interpretations of the operator regarding the sound produced by tapping the bridge with a hammer or by dragging the bridge deck with a chain [25].

2.3.2 Nondestructive evaluation (NDE) technologies

Nondestructive evaluation (NDE) is defined as testing that causes no structurally significant damage to concrete [26]. This term is also called as nondestructive testing (NDT) or nondestructive inspection (NDI). NDE

techniques are increasingly being considered for defect detection in various bridge components due to the access requirements of conventional sounding methods and their inherent subjectivity. The common NDE techniques have been narrowed to impact echo (IE), ground penetrating radar (GPR) technology, and infrared (IR) thermography. Details about the principles, the instrumentations used, data analysis techniques, and some inherent limitations of these technologies are provided in the American Concrete Institute Report ACI 228.2R-98 [26].

2.3.2.1 Impact echo (IE)

The IE testing technique is a stress-wave method which uses mechanical energy to transmit a sound wave into the concrete. The basic principle of the IE method involves impacting the surface of the concrete with a small diameter impactor and detecting and recording the response. Details about the procedures of the method are described in ASTM C1383-04 (procedure B) [27]. A stress pulse is initiated into a concrete by mechanical impact on the surface. The P-waves (i.e. primary waves or compression waves) and the S-waves (i.e. secondary waves or shear waves) produced by the stress pulse propagate into the concrete along hemispherical wave fronts. The waves are reflected by changes in acoustic impedance of the material under investigation (i.e. at internal interface between the concrete and subsurface delaminations). The arrival of these reflected waves, or echoes, at the surface where the impact was generated produces displacements that are measured by a receiving transducer and

recorded using a data-acquisition system. Frequency analysis of displacement wave forms is used to interpret the IE data. In such analysis, the time domain signal is converted into a frequency domain using the fast Fourier transform (FFT) technique [26].

The main advantages of IE testing are the versatile equipment and the relatively brief duration of the testing procedure [23]. The IE responses of internal subsurface defects in concrete can also be classified according to the type, depth, and size of a defect [28]. However, the implementation using this method requires impact at one surface of the tested concrete, such that hands-on access to that surface is always required. In addition, interpretation of the results of this method is not as simple as hammer sounding and chain drag method.

2.3.2.2 Ground penetrating radar (GPR)

The GPR testing technique uses electromagnetic waves to investigate the condition of the concrete and defect corrosion damage. A high frequency electromagnetic wave, typically from 1 GHz to 2.5 GHz, is emitted via an antenna into the concrete under investigation. The reflected energy caused by changes in dielectric properties of the material (i.e. at internal interface between concrete and steel reinforcing) is detected by a receiver antenna and recorded for analysis [29]. This technique can be implemented using air-coupled or ground-coupled antennas. Details of the procedure for GPR testing are described in ASTM D 6087-08 [30].

The advantage of the GPR testing is its ability to detect corrosion damage on concrete decks with overlays. The application of the technique also permits high-speed scanning on bridge decks with minimum traffic control requirements. When conducting inspections, either using air-coupled antennas or ground-coupled antennas, the distance between antennas and the bridge deck surface is properly determined in accordance with recommended standard. For example, ASTM standard notes that air-launched antenna requires a transverse distance of less than 1 m (3 ft) and a longitudinal distance of less than 150 mm (6 in.) to the surface to be implemented [30]. This means that a period of lane closure or partial lane closure may be required for conducting the testing. For ground-coupled antennas, the antenna is dragged along the surface, obviously requiring lane closure to be implemented. In addition, an experienced inspector is required to operate equipment and interpret results.

2.3.2.3 Infrared (IR) thermography

Infrared (IR) thermography has been developed for detecting subsurface delaminations in concrete without direct access to the concrete surface, as required by other methods (as described above). The IR data can be collected without direct access to the surface under investigation, because images can be captured from distances of 30 m using appropriate optical lenses [12]. This means that lane closures and traffic control are not required for conducting the testing.

IR thermography is based on two principles: (1) a surface emits energy in the form of electromagnetic radiation, and (2) subsurface delamination in the concrete affects heat flow through the concrete [26]. A description in the next section provides details on this method.

2.4 Theoretical Foundation of IR Thermographic

The objective of this section is to understand the theoretical aspects of IR thermography. A brief review of the basic principles of the IR thermography and a review of IR instruments are presented. An overview of heat transfer is also included in this section.

2.4.1 Basic principles of IR thermography

Thermography employs infrared sensors to detect thermal radiation emitted from materials, and creates an image of surface temperatures based on the emitted radiation [26]. The energy of emitted radiation is described by the Stefan Boltzmann Law, which states that the power radiated by a material is directly proportional to the fourth power of its absolute temperature as

$$q_{rad} = \epsilon\sigma T^4 \quad \text{Eq. 2.1}$$

in which ϵ is infrared emissivity of the material, σ is the Stefan-Boltzmann constant ($5.67 \times 10^{-8} \text{ W m}^{-2} \text{ K}^{-4}$), and T is the surface temperature of the material. Emissivity, ϵ , describes how efficiently a material transfers energy by radiation

heat transfer. It is a unitless value defined as the fraction of energy emitted relative to the radiation of a perfect emitter or blackbody [31].

In concrete, subsurface anomalies such as delaminations interrupt heat flow producing localized differences in the surface temperature [2]. These localized variations in surface temperature affect the amount of infrared radiation emitted from the surface, as shown schematically in Figure 2.1. As concrete warms during the daytime, the surface temperature of a delamination is higher than the temperature of the sound concrete (Fig. 2.1A). Conversely, as concrete cools during the nighttime, the surface temperature of the concrete above a delamination may be lower than the temperature of the sound concrete (Fig. 2.1B) [32]. The location of subsurface delaminations can be identified by analyzing the surface temperature variations. These surface temperature variations are examined in terms of thermal contrast to perform quantitative analysis of data in this study (Fig. 2.1C). Thermal contrast, ΔT , was defined as

$$\Delta T = T_{void} - T_{sound\ concrete} \quad \text{Eq. 2.2}$$

where T_{void} is the surface temperature above a void area (i.e. delamination) and $T_{sound\ concrete}$ is the surface temperature in the intact area of the concrete. It can be seen from Figure 2.1.C that a thermal contrast curve may have maximum thermal contrast (ΔT_{max}) at a distinct time (t_{max}) over the course of a typical day. In this study, the maximum thermal contrast was considered in evaluating some of the capabilities and limitations of a FEM model (described later in Chapter 3)

for detecting the subsurface voids under a variety of field test parameters, including varying environmental conditions.

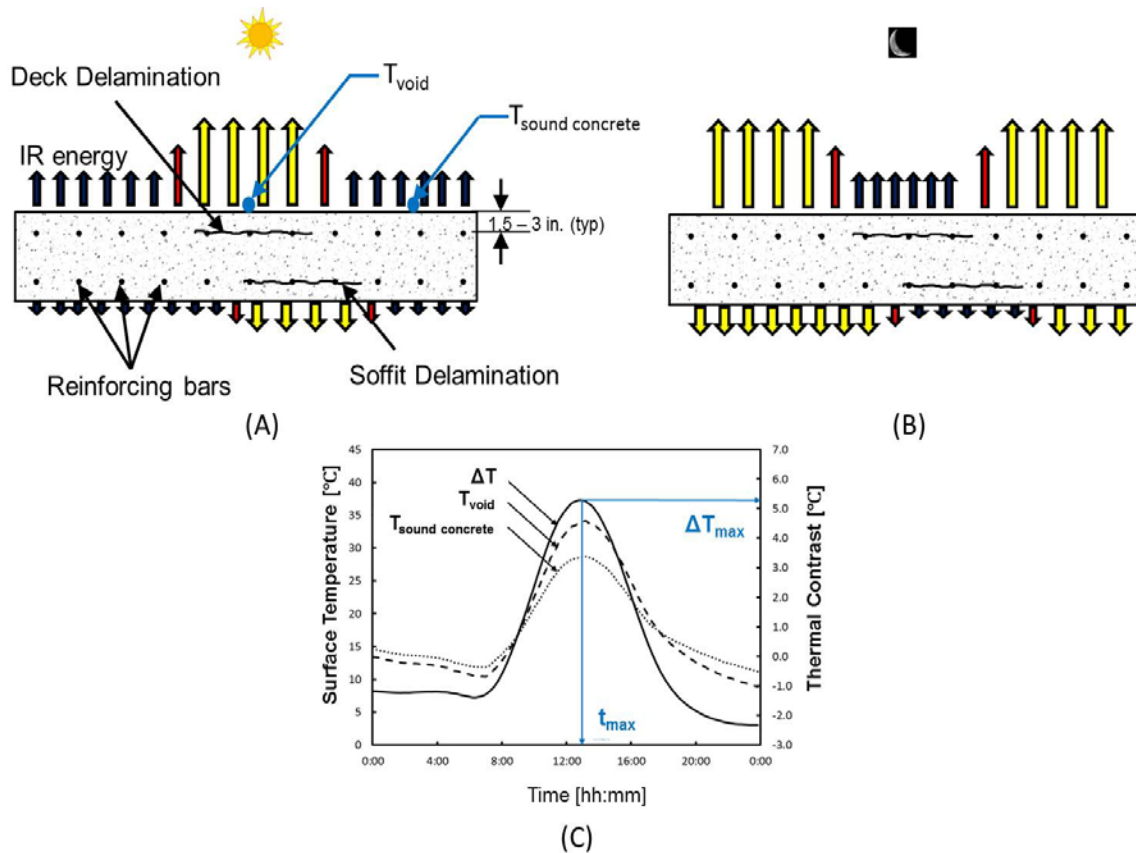


Figure 2.1 Thermal response of delaminations in concrete: (A) day time condition [12]; (B) night time condition; (C) surface temperature and thermal contrast as a function of time

2.4.2 IR thermography instruments

An IR camera measures and images the emitted infrared radiation from an object. The fact that radiation is a function of object surface temperature makes it possible for the camera to calculate and display this temperature. IR covers a

portion of the electromagnetic spectrum (EM) as shown in Figure 2.2. The infrared spectral region starts at $0.75\ \mu\text{m}$ where the region of visible perception ends and it ends at about $100\ \mu\text{m}$. It is further divided into four sub-regions as the near infrared ($0.75\text{-}3\ \mu\text{m}$), the middle infrared ($3\text{-}6\ \mu\text{m}$), the far infrared ($6\text{-}15\ \mu\text{m}$) and the extreme infrared ($15\text{-}100\ \mu\text{m}$). The near infrared and far infrared regions are used in most commercial IR cameras to capture a thermal image [33].

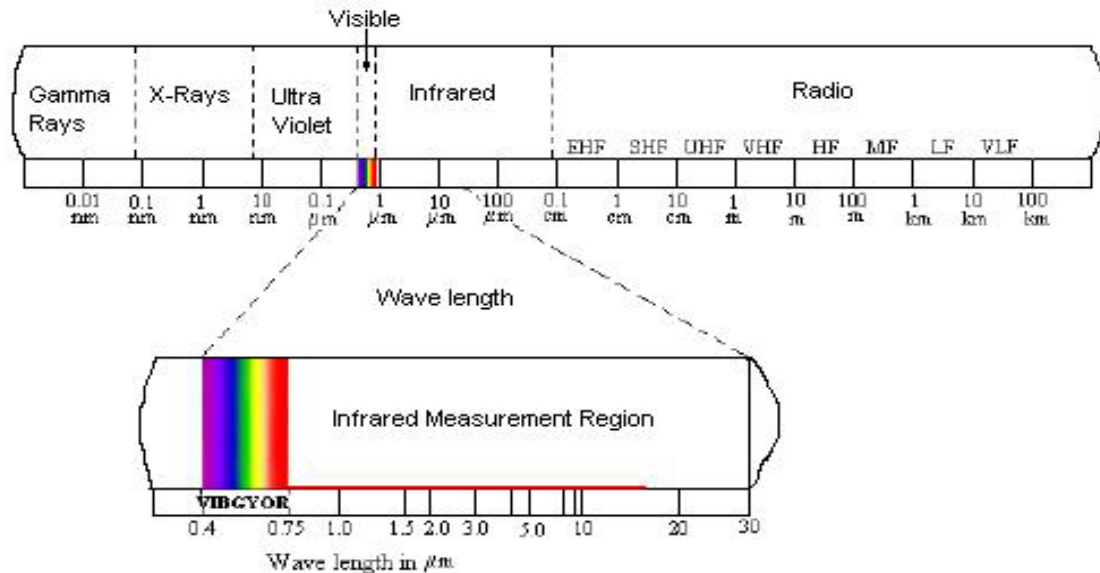


Figure 2.2 Infrared region in the electromagnetic spectrum [34]

The configuration of a typical instrument for IR thermography is shown in Figure 2.3. The main components of IR camera are a lens, spectral filter, a detector, and electronics and software for processing and displaying IR images and temperatures on a monitor [34]. The optical lenses for IR cameras are

typically made of germanium, which is a convenient material due to the high index of refraction for infrared wavelengths between 2 and 12 μm and opaqueness to wavelengths outside of the 2 to 20 μm region. The germanium lens collects the energy from a target surface and focuses it on the detector. This allows the lens to serve as a filter for visible and UV radiation that would otherwise be incident on the detector. The remaining infrared wavelengths outside of the 2 to 20 μm band are removed using in-line spectral filters that are placed in front of the detector. The infrared detector is a device that converts the radiant infrared energy into a measurable electrical signal. The IR camera used in this research use microbolometer focal plane array (FPA) technology, which is a type of thermal detector made of a material whose electrical conductivity varies with temperature change due to incident radiation. The electrical signal is then converted to single pixel containing temperature data by applying an appropriate calibration factor. Data obtained by the detector unit are digitized and displayed as shades of gray or color, depending on the data analysis software. For example, cooler or hotter regions are identified by different colors compared to the surrounding concrete bridge deck as shown in Figure 2.3 (right image). These different colors represent different temperatures.

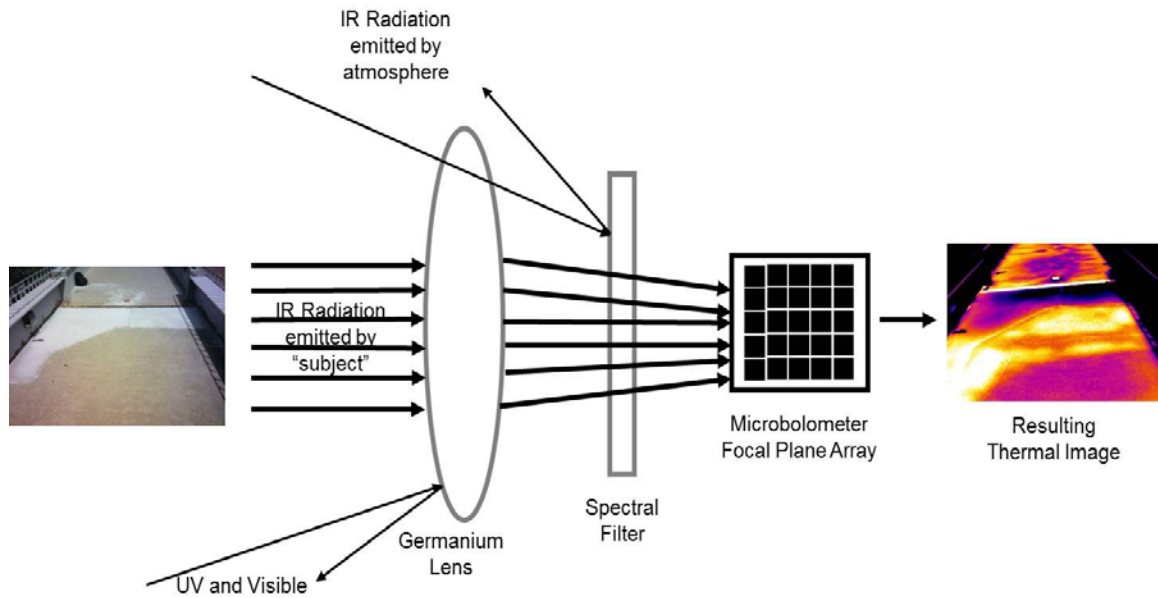


Figure 2.3 Typical components of an IR thermography

2.4.3 Overview of heat transfer

The overview of heat transfer, thermal properties, theory of heat diffusion and transient heat transfer are presented below.

2.4.3.1 Heat transfer mechanisms

Heat transfer takes place in three modes known as conduction, convection, and radiation. Figure 2.4 shows the heat transfer mechanisms that occur for a concrete block in the ambient environment schematically, including radiant heating from the sun, forced and natural convection, and emitted infrared radiation from the concrete surface that takes place at the concrete surface-atmospheric boundary, and conduction that occurs in the concrete itself [35].

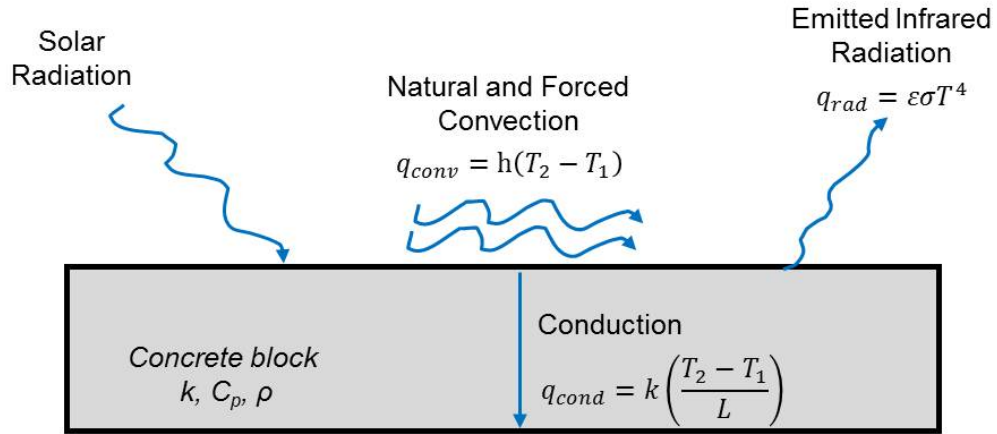


Figure 2.4 The heat transfer mechanisms for concrete with environmental interaction

The thermal energy due to the sun's rays received by the concrete surface, q_s , can be generalized as

$$q_s = \alpha_s I_s \quad \text{Eq. 2.3}$$

in which α_s is the absorptivity of concrete and I_s is the total solar radiation on concrete surface. Absorptivity, α_s , is a measure of the efficiency of receiving radiated heat. It depends on the color and the texture of the surface. An absorptivity of 1 indicates that a material absorbs all incident radiated heat and reflects none. The solar radiation, I_s , depends on geographical location and the position of the sun relative to the surface of the concrete, which varies over the course of a day and throughout the year.

The thermal energy transfer by convection, q_{conv} , as a result of temperature differences between the concrete surface and the surrounding air is given generally by Newton's law of cooling as

$$q_{conv} = h(T_2 - T_1) \quad \text{Eq. 2.4}$$

in which h is a convection coefficient, T_2 is the surface temperature of the concrete, and T_1 is the ambient temperature. The convection coefficient is a function of several parameters such as wind velocity, surface roughness, thermal properties of the air, and surface area. The convective heat transfer is positive when the ambient temperature is less than the temperature of the concrete, such as may occur when radiant heating from the sun warms the concrete above the ambient temperature. In this case, increased wind speed will result in increased energy transfer from the concrete to the surrounding environment, reducing the surface temperature of the concrete and thereby diminishing the thermal gradients in the concrete. If the ambient temperature is warmer than the concrete, such as would be typical when ambient temperatures are increasing but there is no heating from the sun, i.e. shady conditions, then the convective heating transfer is negative. Under this scenario, increased wind speed will accelerate the heat transfer to the concrete, and increase the thermal gradients in the concrete.

The thermal energy of emitted radiation, q_{rad} , is given by Eq.2.1. As described before, IR thermography uses this emitted radiant energy to measure the surface temperature of the concrete.

Within the concrete solid, heat transfer via conduction occurs and is affected by the thermal properties of the concrete. For the one dimensional plane, the thermal energy transfer by conduction, q_{cond} , can be expressed as

$$q_{cond} = k \left(\frac{T_2 - T_1}{L} \right) \quad \text{Eq. 2.5}$$

in which k is the thermal conductivity and L is the concrete thickness in the direction of heat flow. Thermal conductivity, k , indicates how quickly heat flows through the material. It is a measure of the rate at which heat passes perpendicularly through a unit area of homogeneous material of unit thickness for a temperature difference of one degree. k is expressed as $W/(m^2K)$. The thermal conductivity of concrete is dependent on the aggregate types used in the concrete mixture [31].

2.4.3.2 Thermal inertia

Thermal inertia or thermal mass, I , is a measure of the ability of the material to conduct and store heat. It is computed as the square root of the product of thermal conductivity (k), density (ρ), and heat capacity (C_p) as

$$I = \sqrt{k\rho C_p} \quad \text{Eq. 2.6}$$

Heat capacity (i.e. specific heat) is defined as the amount of heat needed to raise the temperature of a unit mass of a material by one degree. This property describes the ability of material to store heat. The volumetric heat of a material can be calculated as the product of the density and the specific heat of the material. It is a measure of the quantity of heat required to produce a unit temperature change in a unit volume [36].

2.4.3.3 Theory of heat diffusion

The theory of diffusion in isotropic homogeneous material is governed by the Fourier equation [36]:

$$\frac{\partial T}{\partial t} = \alpha \cdot \nabla_{x,y,z}^2 T \quad \text{Eq. 2.7}$$

in which T is the temperature, t is time and ∇^2 is the Laplacian operator. In the Cartesian coordinate system, the Laplacian of temperature is defined as

$$\nabla^2 = \frac{\partial^2}{\partial x^2} + \frac{\partial^2}{\partial y^2} + \frac{\partial^2}{\partial z^2} \quad \text{Eq. 2.8}$$

Eq. 2.7 shows that the temperature at any point in the material changes with time during transient heat flow.

Thermal diffusivity, α , in Eq.2.7 indicates how quickly a material changes temperature and is defined as

$$\alpha = \frac{k}{c_p \cdot \rho} \quad \text{Eq. 2.9}$$

where k is thermal conductivity, c_p is heat capacity, and ρ is density of the material. A high thermal diffusivity means that heat transfer through a material will be fast and the amount of storage will be small. Materials with a high thermal diffusivity respond quickly to changes in temperature. On the other hand, low thermal diffusivity indicates a slower rate of heat transfer and a large amount of heat storage. Materials with low thermal diffusivity respond slowly to an imposed temperature difference [31].

2.4.3.4 Transient heat transfer

The effective use of quantitative IR thermography for subsurface void detection and void characterization in concrete requires the study of the transient heat transfer phenomenon. Theoretically, this phenomenon could be solved using direct computation of the theory of diffusion (described in section 2.4.3.3) or using numerical analysis.

For a simple case, such as one-dimensional transient heat flow, Eq. 2.7 can be solved as follows [36]:

$$T_d = T_\infty + (T_i - T_\infty)\text{erf}\left(\frac{y}{2\sqrt{\alpha t}}\right) \quad \text{Eq. 2.10}$$

where T_d is temperature at any depth in the material, T_∞ is the applied constant temperature at the surface of the material, T_i is the initial temperature of the material, and **erf** is Gaussian error function. This equation shows that the temperature within the material changes in a nonlinear manner upon a step change in surface temperature.

For more complex cases, where the material has subsurface voids (heterogeneous thermal properties at various depths and thickness), and is subjected to complex boundary conditions, the transient heat transfer cannot be solved using direct computation. Numerical modeling is the only analytical method capable of simulating the transient heat transfer. The finite element method (FEM), finite volume method (FVM), or finite difference method (FDM) can be considered to solve the differential equation in Eq. 2.7. Using these

methods, the temperature at discrete points in the concrete can be obtained. Moreover, the accessibility of the numerical method via computer simulation (software) makes it more effective, and the capability of the method allows simulation of different heat transfer scenarios such as varying of boundary conditions, a variety of void characterization conditions, and varying of material properties.

2.5 Application of IR Thermographic

The objective of this section is to understand the applications of IR thermography for nondestructive evaluation of concrete bridges. The description of IR testing procedures and advantages and limitations of IR thermography testing are presented below. This section also includes brief summaries of previous investigations on the use of IR thermography for concrete bridge inspection.

2.5.1 Active and passive IR thermography measurement

There are two testing approaches for IR thermography depending on the presence of an external heat source known as: (1) the active approach, and (2) the passive approach. The active approach uses an external thermal stimulus to induce the required heat flow condition on the concrete under testing. An external heat source such as an electric heater is generally used over the surface concrete and the surface temperature is monitored and analyzed. Based on the external stimulus, different methods of active thermography have been

developed such as pulse thermography, step heating, lock-in thermography, and vibro-thermography.

The passive approach uses natural heat sources such as solar heating and night time cooling on the concrete under testing. For example, enough solar radiation can cause a substantial temperature difference between the defect and the sound area of a bridge deck. This approach is used for the research reported here.

2.5.2 Advantages and limitations of IR thermography measurement

The most common advantages of IR measurement are that it is non-contact, much faster than conventional methods, and easy to analyze in comparison to other NDE techniques such as GPR. As described before, no direct hands-on access is required between the IR camera and the concrete under inspection since the testing can be conducted from a distance by using the appropriate lens. Therefore, lane closure and traffic control surrounding the testing area are not required. The time required for testing is considerably reduced since a single infrared image can cover a large area not only for a bridge deck but also for a soffit (underside) surface of the concrete and other concrete components. In addition, the IR testing can be conducted during both day and night time and the IR image can also be interpreted easily in the field.

However, the effectiveness of IR measurement is highly dependent on environmental conditions at the time, and prior to, when a thermal image is captured. Variations in test response occur with varying environmental

conditions, such as solar radiation, ambient air temperature, wind speed, cloud cover, and precipitation [26]. The solar loading drives radiant heat transfer in the concrete. Ambient temperature and wind drive convective heat transfer in the system. Clouds reduce intensity of incident solar radiation during the day and reflect infrared radiation at night, slowing heat transfer at the concrete surface. Rain may lead to concrete surface cooling, thus masking thermal effects from the surface. Water below 0 °C forms ice in voids. For that reason, the appropriate environmental conditions are required to achieve the heat flow conditions needed to detect the presence of subsurface delaminations. In addition, characteristics of the subsurface defect (i.e. delamination depth, delamination thickness, and material in delamination) also affect the test response. For example, as the depth of the delamination increases, it becomes more difficult to detect. Based on these considerations, the variation in environmental conditions and characteristics of the subsurface defect were the subject of the research reported herein.

2.5.3 Previous investigations on the use of IR thermography for concrete bridge inspection

This section focuses on previous investigations of key parameters expected to affect the detectability of the subsurface delaminations in concrete. The parameters include environmental conditions, delamination depths, delamination thicknesses, materials present in the delamination, material properties of concrete, and asphalt overlays.

2.5.3.1 *Environmental conditions*

Early studies by Manning found that delaminations in concrete decks could be detected using thermography in field tests [37] [38]. The ability of thermography to detect subsurface delamination was sensitive to environmental variables such as solar radiation, wind, ambient temperature, humidity, and cloud cover. His studies found that the delaminations could be detected over a wide range of ambient temperatures since the delaminated areas heat up faster due to solar loading, and could develop surface temperature from 1^oC to 3^oC higher than the surrounding areas.

ASTM D4788-03 [39] describes the required conditions for detecting delaminations in bridge decks using thermography. This standard indicates that thermographic imaging is dependent on the amount of direct sunlight, the ambient temperature change, and wind speed, and provides generalized guidance on appropriate conditions for detecting delaminations in bridge decks. Thermography has been found to be unreliable when wind speeds are above 7 m/s [37] to 9 m/s [40] since the wind increases convection cooling and reduces surface temperature differences.

Recent studies by Washer [16, 17] have investigated the application of thermography for subsurface delamination detection in concrete. This research studied the effect of environmental conditions such as direct solar loading, ambient temperature variation, wind speed, and humidity on the surface temperature of a concrete block containing subsurface voids at different depths.

Subsurface delaminations were simulated using Styrofoam targets at various depths. It was found that direct, uninterrupted solar loading and low wind speeds provided optimum conditions for detection of targets for the south side of the block, while high rates of change in ambient temperatures were needed to create thermal contrast for the north side of the block, where no solar loading was present. Quantitative values for the amount of solar loading, average wind speeds and ambient temperature variations were determined statistically from the experimental results and used to develop guidelines for the use of thermography in the field [15]. Parts of the experimental results of this study provide the input and verification data for the present work in described herein.

2.5.3.2 Void depths and void thicknesses

Holt, Maser, and others presented several studies addressing the effect of delamination depth on the thermal contrast [13, 37]. Holt found that the magnitude of thermal contrast correlates with the depth of a delamination. Shallower delaminations are associated with larger thermal contrasts than deeper delaminations. The field data from Manning supported Holt's interpretation. The results of their studies confirmed that delaminations located near the surface heated more rapidly and to a higher thermal contrast than deeper delamination.

A study by Allport [41] showed that the thermal contrast decreases rapidly with the depth of a void, the loss in thermal contrast (**c**) being approximately proportional to the cube of the depth (**d**) as

$$c \approx \frac{1}{d^3} \quad \text{Eq. 2.11}$$

where c is defined by Allport as

$$c = \frac{T_d - T_b}{T_b} \quad \text{Eq. 2.12}$$

where T_d is the surface temperature above the defect and T_b is the surface temperature in the sound material. This result was based on the quantitative evaluation of single-sided transient video thermography (TVT). In this study, a pulsed or stepped surface heating (active thermography) was used as external heating over the composite plate with internal voids at depth from 0.5 mm to 4 mm.

Maser also investigated the effects of variable delamination thickness under a certain set of environmental variables using thermal model [2]. The results revealed that the thickness of the delamination affected the magnitude of the temperature difference (i.e. thermal contrast). Increasing the delamination thickness by a factor of five increased the maximum thermal contrast by a factor of four. These studies indicate that both the depth of a void (i.e. delamination) and its thickness affect the magnitude of the thermal contrast observed.

2.5.3.3 Material contained in the delamination

Air-filled void is the most commonly postulated model to represent a subsurface delamination. However, in the field application, the material which fills a delamination is not necessarily air. Other possible void-filling materials are

water, ice, and epoxy used to repair concrete. Water filled voids would be expected under saturated concrete surfaces. The water turns to ice in the delamination when temperatures drop below freezing [6]. In the case of deteriorated concrete, epoxy is sometimes used to fill a delamination and/or cracks in the concrete, with the goal of extending the useful life of the components.

These materials that may be contained within a void have different thermal conductivity, heat capacity, and density in comparison to the sound concrete. Among these properties, thermal conductivity is a main property affecting temperature contrast between the void area and the sound area [6]. Since the thermal conductivity of air is considerably lower than that of concrete, the significant temperature differences between a thin delaminated area and the thicker sound concrete can be expected when the material contained in the void is air. On the other hand, since the thermal conductivity of water is not significantly lower than that of concrete, clear thermal differences at water filled voids would not be expected for steady state. However, for transient case, the thermal contrast can be produced because of the differing heat capacity of water and sound concrete [6].

2.5.3.4 Material properties of concrete

As shown in Eq.2.7, the thermal diffusivity (α) of the material affects the transient heat transfer. Both thermal conductivity and volumetric heat are the primary material properties linked to thermal diffusivity. The thermal diffusivity of

concrete varies with the water content of the material. However, this property would not be expected to vary much within the concrete, so the effect of varying material properties of concrete might be too small to generate detectable indications [6].

As shown in Eq.2.1, the emissivity of the concrete is another important surface property to consider when using IR thermography to measure thermal contrast associated with delaminations. The property measures the ability of a material to radiate energy compared to a perfect blackbody radiator ($\epsilon=1$). In practical terms, this means that when using thermographic technique to scan large areas of concrete, the inspector must be aware of differing surface emissivity caused by such things as oil spots, rubber tire tracks and dirt on the surface. These surface conditions can change the emissivity of the concrete surface, resulting variation in emitted radiation appear as temperature differences in the thermal image [13].

2.5.3.5 Asphalt overlays

Asphalt overlays are often used to provide suitable riding surfaces on concrete bridge decks. These overlays affect thermal response apparent in images collected in the field. The overlay makes the identification of subsurface voids (i.e. delaminations) more complex than the conditions without overlays, because overlay reduces the thermal contrast associated with the voids. Additionally, debonding between the overlay and the concrete introduce another thermal contrast interpretation, separate from the detection of delaminations [6].

Some field test data that illustrated the effect of an overlay, were presented by Manning and Maser. Manning found that the maximum surface temperature difference (i.e. the maximum thermal contrast) of a delamination in a concrete deck with 3.1 inch (79 mm) bituminous overlay was 2⁰C under ideal summer conditions with no clouds or wind. For bare deck, this maximum thermal contrast was 4.5⁰C under similar conditions [38]. Maser investigated the response of infrared detection systems using a one dimensional transient heat transfer model. This analytic study revealed that the thermal contrast produced by a delamination under an overlay ranged from 0.5⁰C to 2.5⁰C [2]. This thermal contrast is much smaller than that for bare concrete, which exhibits a temperature range from 3⁰C to 8⁰C.

2.5.3.6 Discussion

Based on these previous research efforts, the parameters affecting the thermal contrast produced by a subsurface void in concrete include:

- Depth of void and thickness of void
- Material contained within the void
- Material properties of the concrete
- Presence of an asphalt overlay

In the research reported herein, these parameters were examined analytically using the validated numerical model described in Chapter 3. Results of these studies are discussed in Chapter 4, section 4.2, 4.3, 4.4, and 4.5.

3. NUMERICAL MODEL DEVELOPMENT AND MODEL EVALUATION

3.1 Introduction

This chapter discusses the development of numerical model to model environmental effects on the thermal contrast produced by subsurface voids in concrete. First, the FEM in COMSOL computer software is introduced as a tool to simulate the effects of environmental conditions on the detection of subsurface voids. Next, model descriptions including geometry, material properties, boundary conditions and mesh density are described. The model used the same geometry as the block constructed in the experimental study by Washer, Bolleni, and Fenwick [15, 18, 19]. The material properties were obtained from typical values available in the published literature. The boundary conditions in the model were the weather parameters recorded in the experimental study. The mesh density for the model was determined to provide a balance between mesh size and processing time and achieve an accurate model. Therefore, the numerical model results could be compared to the experimental testing results. Finally, the evaluation of model performance by conducting correlation and error analysis is presented.

3.2 Numerical Model Descriptions

As described in section 2.4.3.4, the transient thermal behavior of the concrete block can be analyzed using numerical tools such as the finite element method (FEM), the finite volume method (FVM), and the finite difference method (FDM). In this study, FEM was used for analyzing the effect of subsurface voids on heat transfer through a large concrete block under the actual weather conditions of solar radiation, ambient temperature variation, and wind speed. All the analytical simulations were performed using COMSOL-Multiphysics. **Appendix A** shows simulation details for one month (November 2007).

3.2.1 Geometry and material properties

Figure 3.1A shows the three dimensional geometry of the concrete block that was simulated using the FEM. The concrete block model had the same geometry as the block constructed for use in the experimental study [18, 19], which is shown in Figure 3.1B. The constructed block is a 2.4m x 2.4m by 0.9m in thickness, and included Styrofoam targets (305 x 305 x 13 mm in dimension) at depths of 25, 51, 76, and 127 mm on each side. These Styrofoam targets have thermal conductivity close to that of air, such as would be present at a subsurface delamination in concrete. Thermocouples were embedded in the concrete block to monitor internal thermal responses, and wiring from these thermocouples can be seen in the photograph (Figure 3.1B).

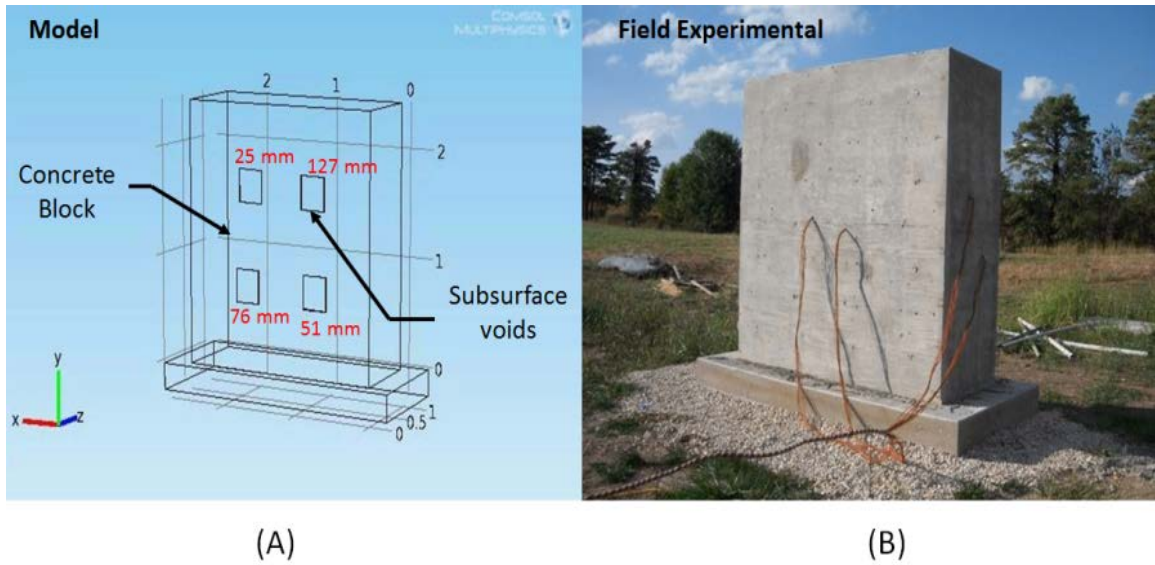


Figure 3.1 Concrete block containing subsurface voids: (A) model; and (B) photograph of experimental test.

The thermal conductivity, the specific heat, the emissivity, and the density for the materials used in this model which were obtained from available published data [42] are summarized in Table 3.1.

Table 3.1 Material properties of the concrete block model

Material Properties	Concrete	Void (Air)
Thermal Conductivity, k	1.8 W/m.K	0.024 W/m.K
Specific heat, C_p	1000 J/kg.K	700 J/kg.K
Emissivity, ϵ	0.95	-
Density, ρ	2300 kg/m ³	1.2 kg/m ³

3.2.2 Boundary conditions

The boundary conditions in the model consisted of the weather parameters recorded in the experimental study [15]. A commercial weather station located adjacent to the concrete block monitored the parameters of solar radiation, air temperature and wind speed over a 6 month period. Details regarding the experimental measurement protocol, analysis, and results were given in previous works by Washer [15-17].

Figure 3.2 shows a single day of data as an example of the input data used to model the boundary conditions of the block. The data shown in the Figure shows the solar radiation (Fig. 3.2A), variation of ambient temperature (Fig. 3.2B) and wind speed (Fig. 3.2C). The time period shown in the figures is midnight (0:00 hrs) to midnight (0:00 hrs). In the experimental study, data on weather conditions and thermal images of the block were recorded at 10 minute time intervals, and this interval was used as the time-step in the FEM. Consequently, data from the FEM and the experimental data could be compared directly for each 10 minute time interval.

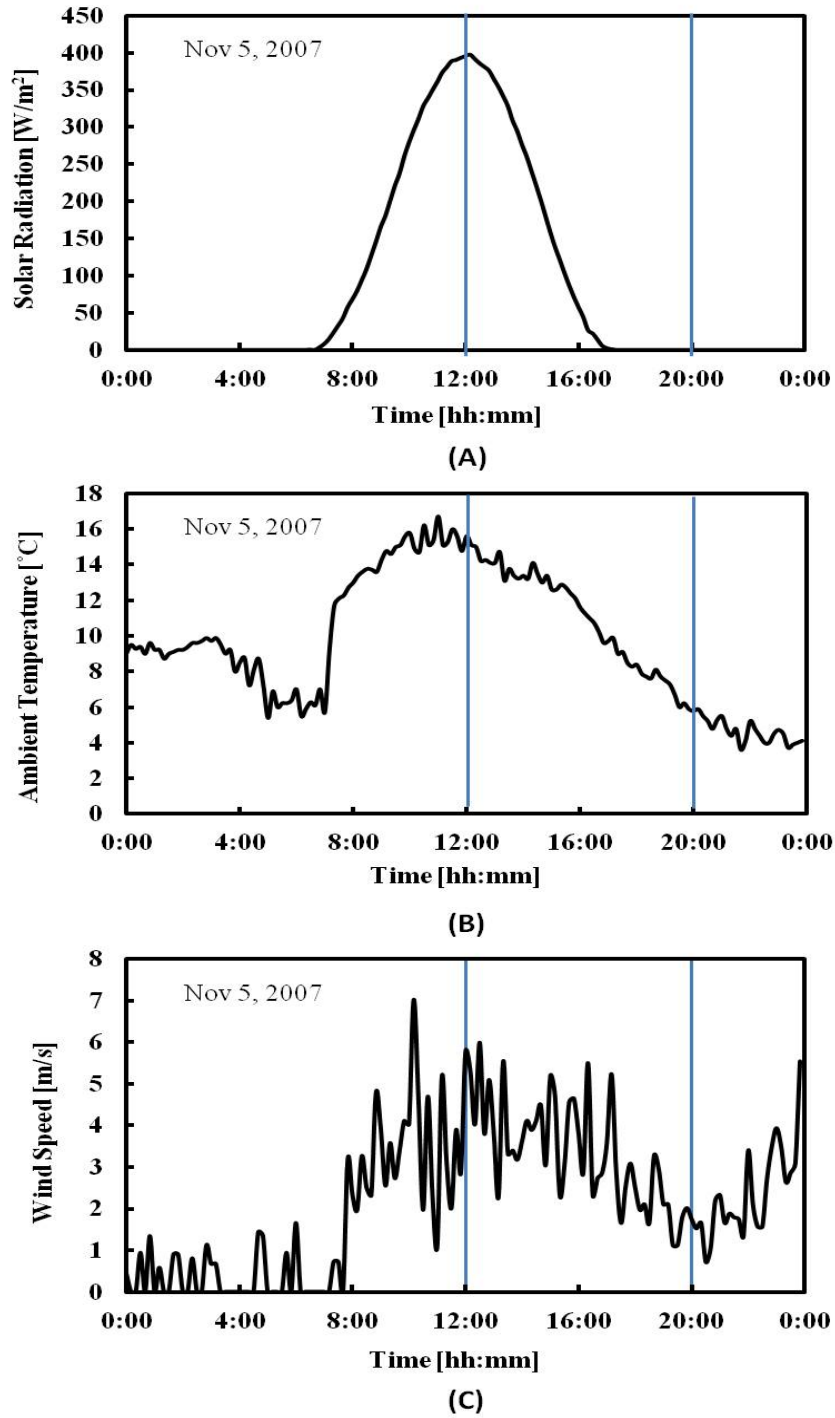


Figure 3.2 Environmental parameters as boundary conditions in simulation on November 5, 2007: (A) solar radiation; (B) ambient temperature; and (C) wind speed

The inclination of the concrete surface with respect to the direction of the sun's rays was considered in the model, to adjust field-measured isotropic solar radiation measurements. The intensity and incident angle of solar radiation were applied as an inward heat flux onto the vertical plane boundary of the concrete block, adjusted appropriately to represent the actual field conditions. The ambient temperature variation and wind speed were simulated as convective heat transfer on the surface boundaries of the concrete block model.

A three month period (89 days) on the South side and a three month period (92 days) on the North side of the concrete block were modeled. The model was simulated separately for each month for both the South face (i.e. the surface exposed to direct solar loading) and the North face (i.e. the shaded surface) of the block. The initial temperature for each monthly simulation was the surface temperature of concrete block at midnight (0:00 hrs) in the first day of each month, which was obtained from thermocouple measurements in the experimental test.

3.2.3 Mesh density

The mesh density for the model was determined to provide a balance between mesh size and processing time and achieve an accurate model. In the model developed, the concrete block was meshed using the free meshing feature in COMSOL. In this feature, a 3D physical domain was discretized by tetrahedral and triangular elements (Figure 3.3).

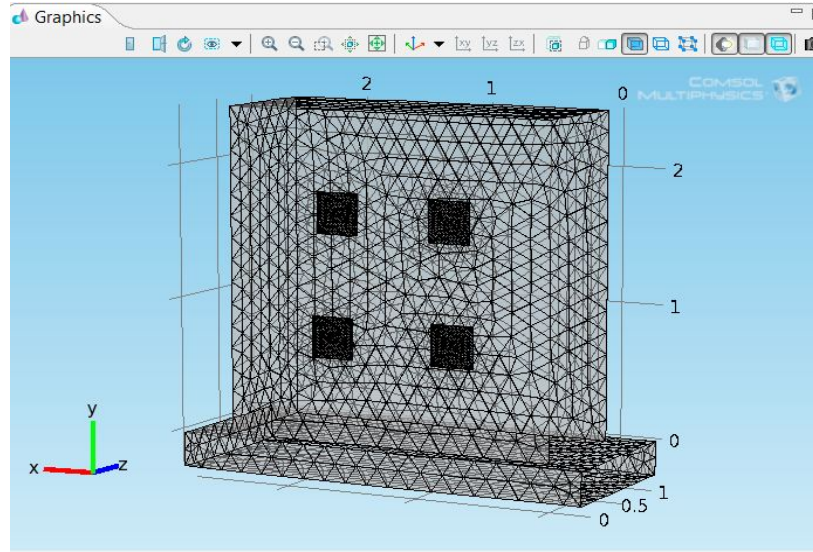


Figure 3.3 Meshing in COMSOL

Different types of element density in COMSOL (course, normal, finer, extra fine, and extremely fine), as shown in Table 3.2, were utilized in a convergence study to determine the optimal mesh density.

Table 3.2 Mesh Statistics

Element type	Coarse	Normal	Finer	Extra fine	Extremely fine
Tetrahedral elements	9642	19465	100045	205668	657496
Triangular elements	1369	2495	9996	16616	31972
Edge elements	281	381	824	1060	1460
Vertex elements	48	48	48	48	48
<u>Domain element statistics</u>					
Number of elements	9642	19465	100045	205668	657496
Minimum element quality	0.002958	0.00824	0.09848	0.08452	0.1333
Average element quality	0.5535	0.6385	0.7125	0.7335	0.7608
Element volume ratio	5.20E-05	8.395E-0.5	1.64E-04	2.65E-04	8.85E-04
Mesh volume [m ³]	6.362	6.362	6.362	6.362	6.362

Figure 3.4 shows a week of the thermal contrast data for 51 mm deep void as an example of using different types of element density in the model. It was found that the thermal contrasts differed slightly for the finer, extra fine, and extremely fine mesh density over the course of a week.

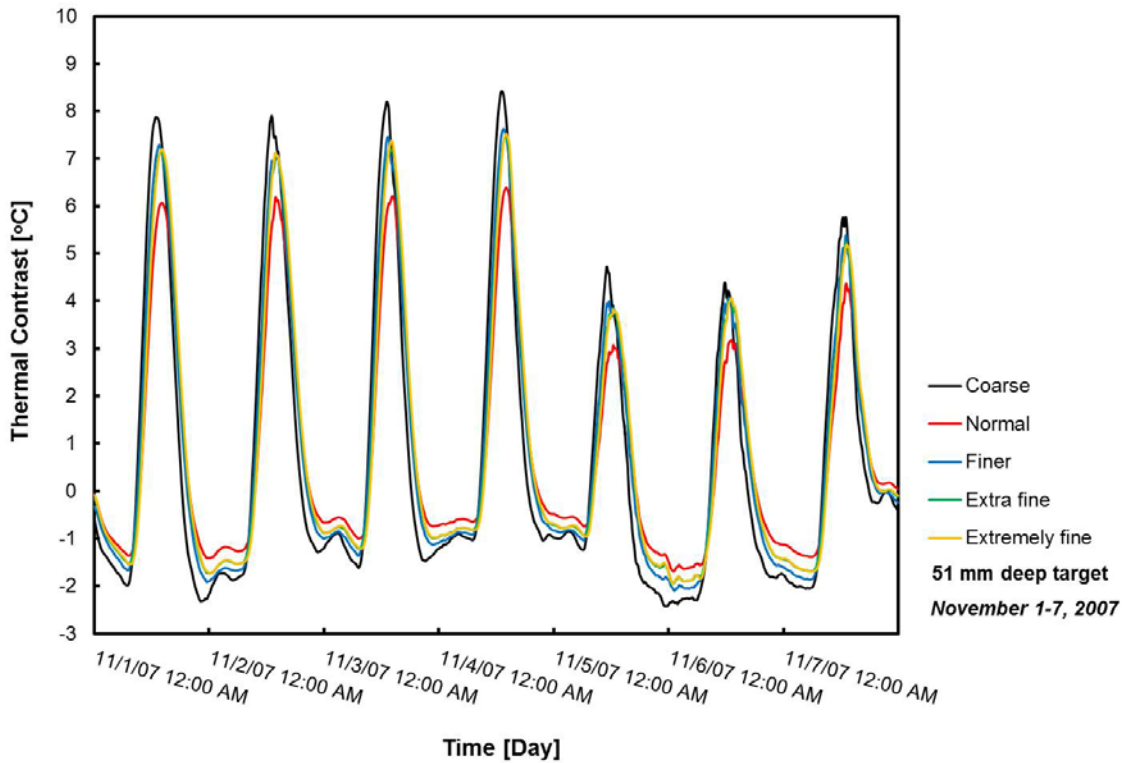


Figure 3.4 Thermal contrast of the model using different type of element density

Figure 3.5 shows an example of the maximum thermal contrast and the computation time in a particular day (November 5, 2007) for 51 mm deep void using different types of mesh density. It can be observed that the maximum thermal contrasts for the finer, extra fine and extremely fine mesh density had a

small difference value. However, the extra fine and extremely fine mesh density were more computationally intensive than the finer mesh density. Therefore, the “finer” element size (highlighted column in Table 3.2) was selected as a balance between computational economy and accuracy in solution, resulting in 100045 total elements in the model.

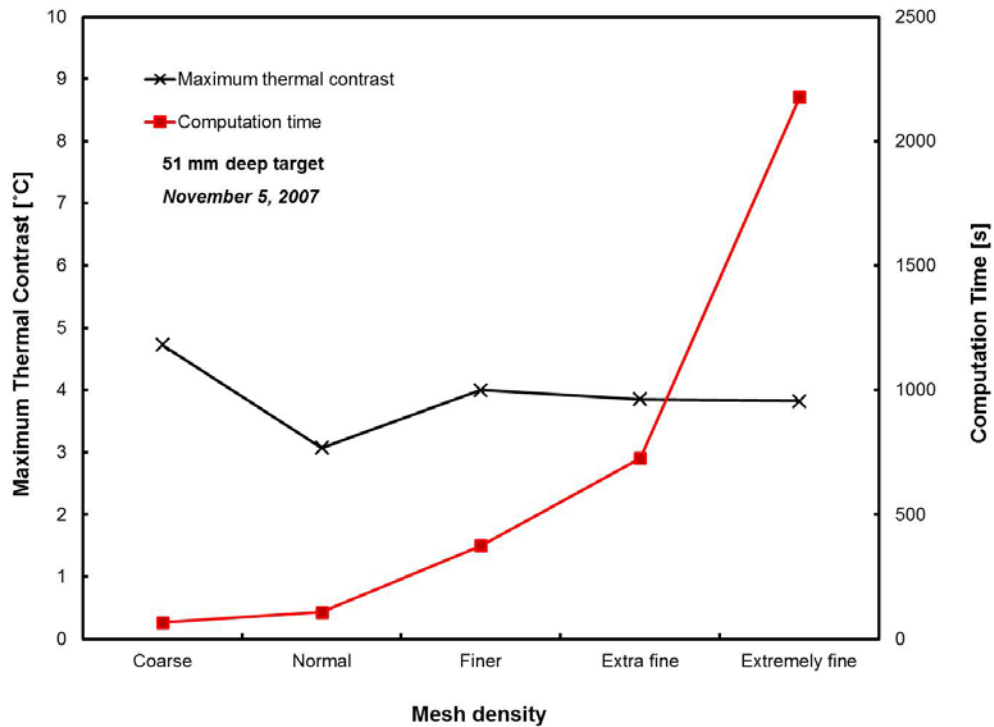


Figure 3.5 Estimated maximum thermal contrast and computation time using different mesh density

3.3 Simulation Results

Simulation results of the numerical modeling, including thermal image, surface temperature and thermal contrast, are presented below.

3.3.1 Thermal images

Figure 3.6 displays an example of typical thermal images obtained from the model for the South face of the block and the actual image data collected in the experimental test. The data inputs for solar radiation, ambient temperature change and wind speed are shown in Figure 3.2 for this particular day. Figure 3.6A shows the surface temperature distribution obtained from the model at 12:00 p.m. (12:00 hours), and Figure 3.6B shows the actual thermal image collected at that time during experimental testing. In the figure, variations in surface temperature are represented on a color scale applied over a temperature span of 7°C. Figure 3.6C shows the surface temperature distribution obtained from the model at 8:00 p.m. (20:00 hours) of the same day. Figure 3.6D shows the actual thermal image at that time from the experimental test. As shown in the figures, the surface temperature distributions obtained from the model closely represented the data collected in the thermal image obtained during the experimental test.

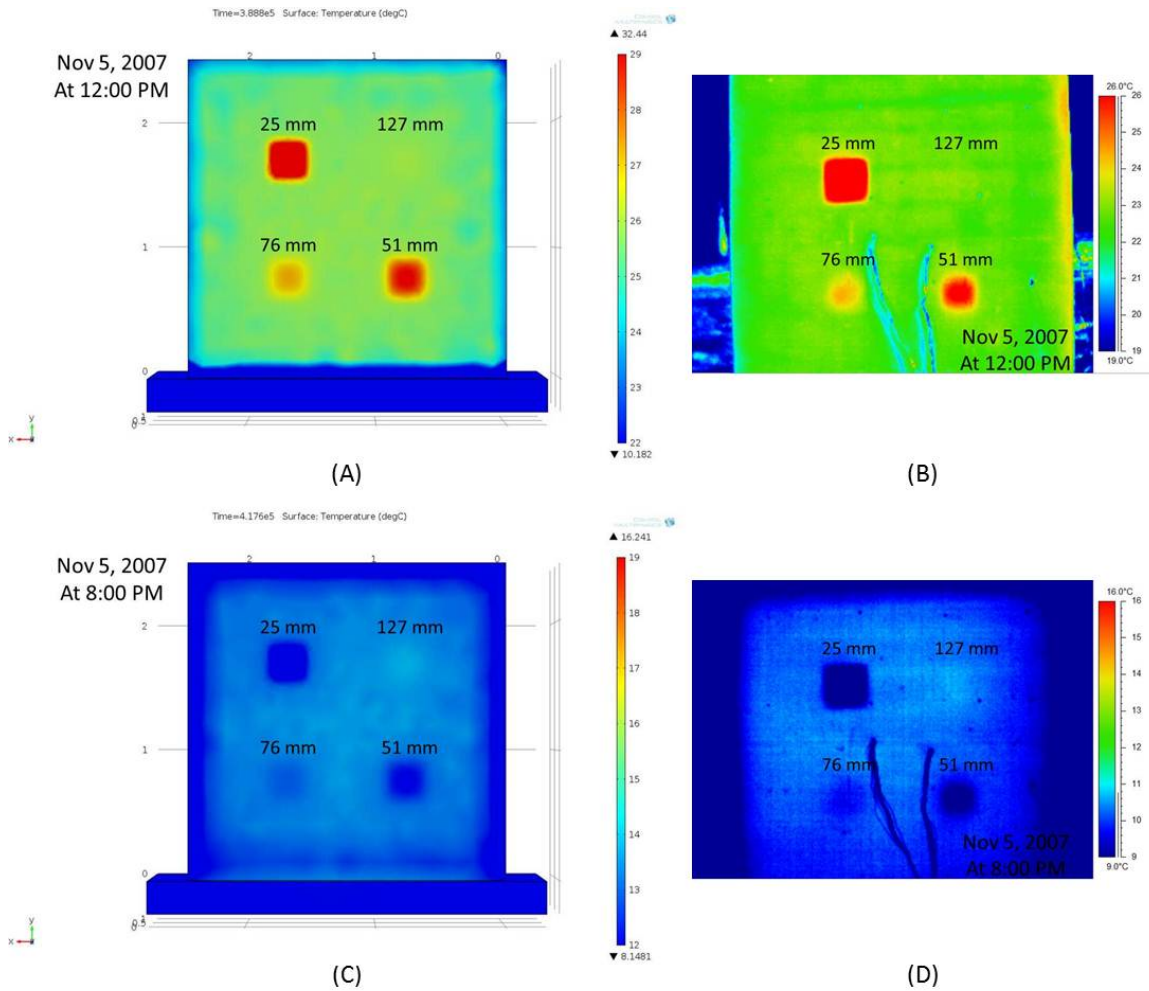


Figure 3.6 Typical thermal images of the thermal behavior for the South side of the concrete block: (A) the model result at noon; (B) the experimental test result at noon; (C) the model result at 8:00 p.m.; and (D) the experimental test result at 8:00 p.m.

The variation of temperature contrast with the depth of the target can also be observed in Fig. 3.6, as well as the transient changes in the thermal contrast at each target location. A positive thermal contrast is obtained when solar loading from the sun is present (12:00 p.m.), and the negative thermal contrast is observed when solar loading is removed and ambient temperatures are cooling

(8:00 p.m., see Fig. 3.2). This figure illustrates the utility of the model for analytically predicting the thermal images that would be obtained in the field with an IR camera, using actual weather conditions (solar loading, ambient temperature variations and wind speed) as inputs for the model. It should be noted that the images shown here are a subset of the data resulting from the simulation; in the modeling, the entire month was modeled for producing such images for each 10 minute time interval throughout the month.

3.3.2 Surface temperatures and thermal contrasts

An example of the modeled surface temperatures and resulting thermal contrasts for the South and the North face of the block are described in this section. All the results are presented in **Appendix B**.

Figure 3.7 shows an example of the modeled surface temperature for the South face of the block. The data shown is for the same day as that shown in Figures 3.2 and Figure 3.6. It can be observed from Figure 3.7 that between the hours of 0:00 and ~8:00, the surface temperature of the deepest target (127 mm) was greatest and the shallowest target (25 mm) was lowest. In the following time period, ~8:00 to ~16:00, the situation was reversed, with the 25 mm deep target having a greater surface temperature.

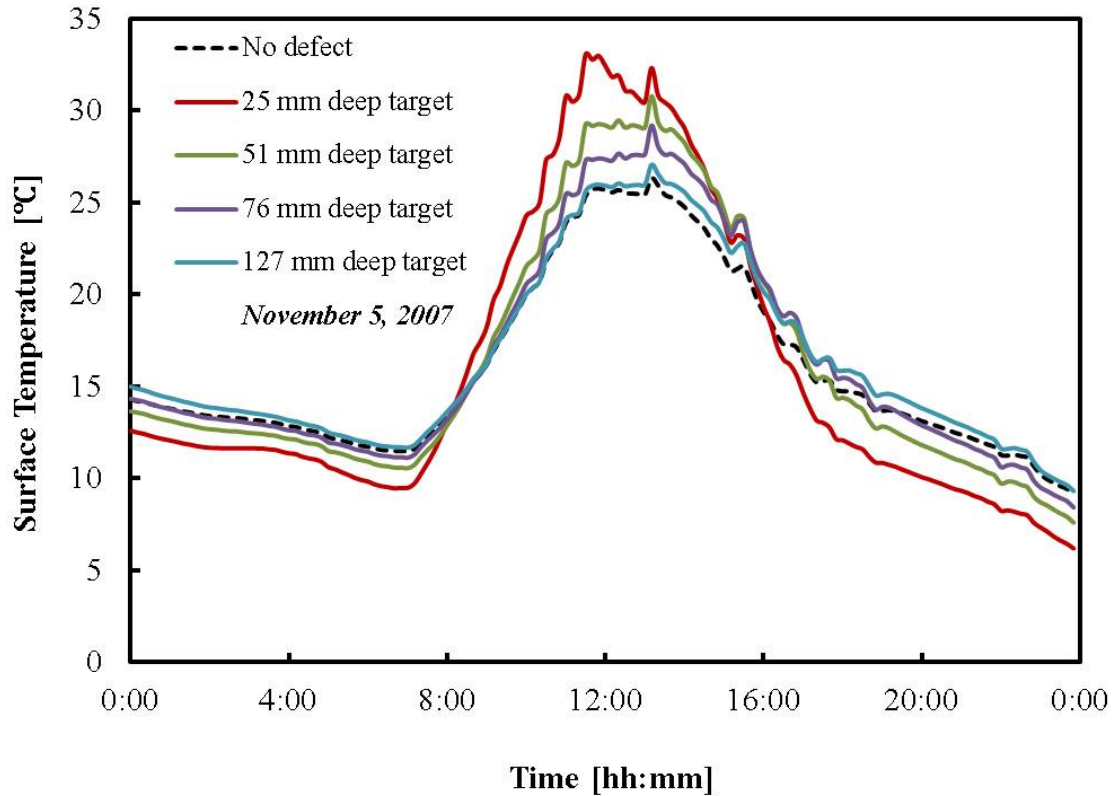


Figure 3.7 Modeled surface temperature for the South face of the block (November 5, 2007)

The typical modeled surface temperatures for the North side are shown in Fig. 3.8. The significant difference between the surface temperatures from the North side and the South side was the increased change in magnitude observed for the South side that results from the radiant heating of the sun; for the North side, only convective heat transfer from the environment was occurring, and as a result, the change in surface temperature over the course of the day was less pronounced.

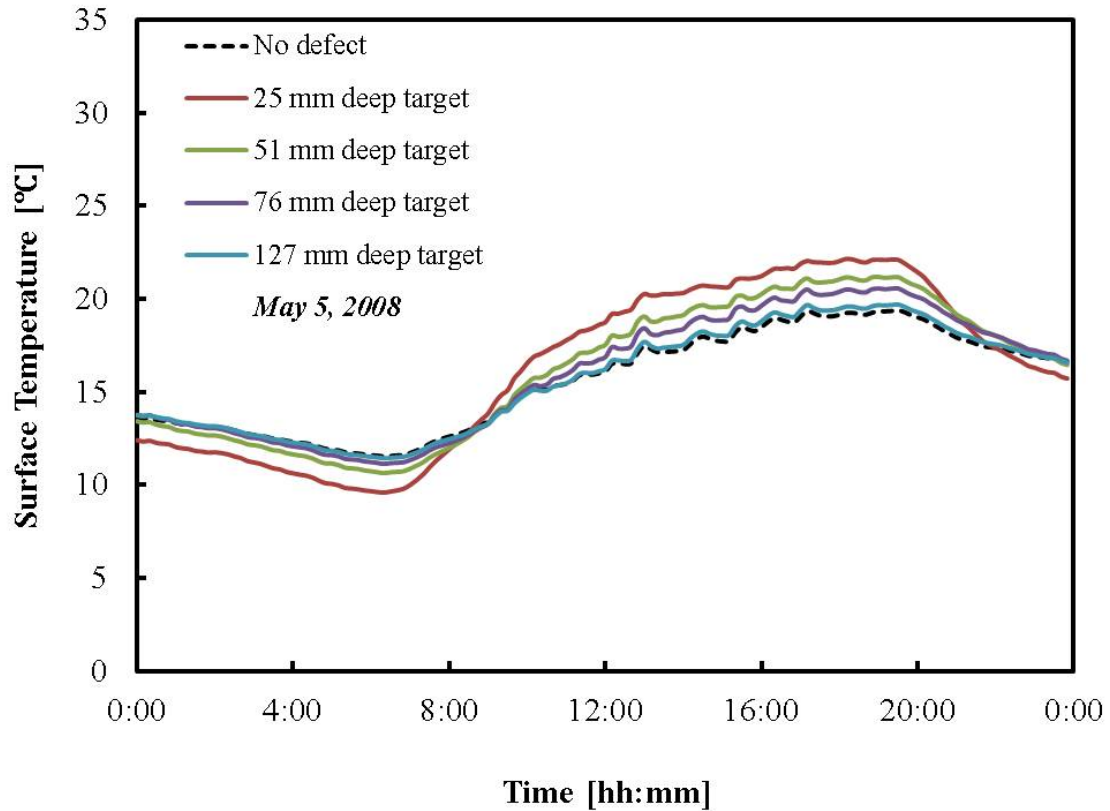


Figure 3.8 Modeled surface temperatures for the North face of the block (May 5, 2008)

The surface temperatures shown in Fig. 3.7 and 3.8 were used to calculate the time-varying thermal contrast for each of the subsurface voids, and these data are shown in Fig. 3.9 and 3.10, respectively. These thermal contrasts were calculated using Eq. 2.2. The thermal contrast data were processed using a 1-hour moving average to filter short-term transient spikes in the thermal contrast data. The moving average of thermal contrast data is shown as solid lines, and the raw data of the thermal contrast is shown as dash lines. As can be seen in thermal contrast results, these transient spikes are primarily in the South

side data, and result from short-term effects such as a cloud moving in front of the sun, or a short period of sunshine on an otherwise cloudy day. For the South face (Fig. 3.9), the thermal contrast for each of the targets starts increasing at different times of the day, with deeper targets developing thermal contrast later in the day. Also, the maximum thermal contrast is decreased as the target depth increases, as would be expected. The maximum thermal contrast for 25, 51, 76 and 127 mm deep targets at the day was approximately 7°C, 4°C, 2°C and 1°C, respectively. The North face (Fig. 3.10) has a lower thermal contrast value for each target, and these contrasts are more consistent over the course of the day, as shown in the Figure. The maximum thermal contrast for target depth of 25, 51, and 76 mm was approximately 3 °C, 2 °C, and 1 °C, respectively. For the 127 mm deep target, the maximum thermal contrast was minimal due to the depth of the target.

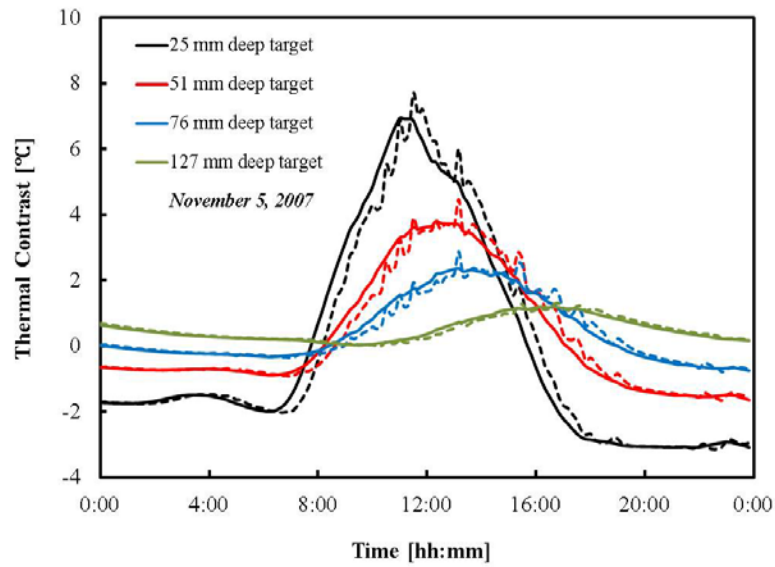


Figure 3.9 The time varying thermal contrast for the South face of the block; Solid line is for the moving average an hour. Dash line is for the raw data.

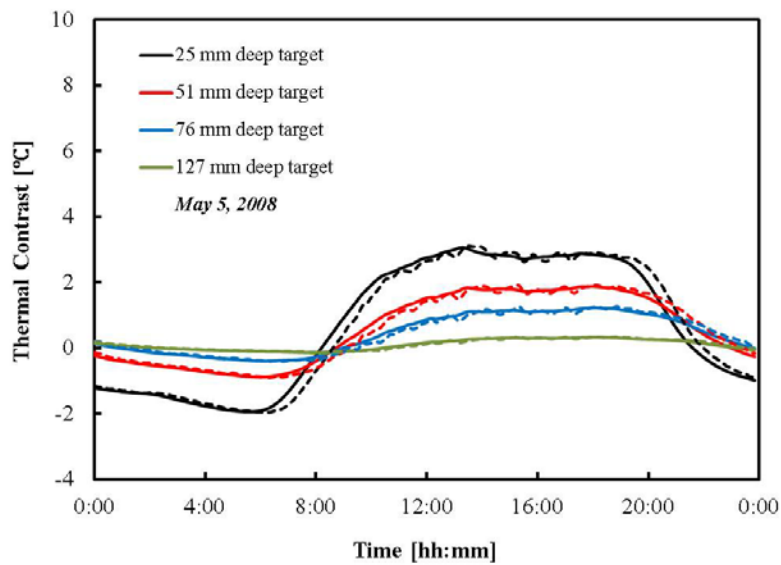


Figure 3.10 The time varying thermal contrast the North face of the block; Solid line is for the moving average an hour. Dash line is for the raw data.

3.4 Evaluation of Model Performance

The objective of the model evaluation in this section is to quantify the level of agreement between thermal contrast results from the model and actual field test. Analysis was performed by comparing trend curves and correlations of thermal contrast data between the model and the experimental test results over the entire month. Analysis of the error and bias was also conducted to assess the agreement of the model with the actual field test results.

3.4.1 Trend curve of thermal contrasts

The trend curve of time series thermal contrast data obtained from the developed model was compared to those obtained from the experimental testing in 10 minutes intervals over the six months. The comparison reported herein is focused on the 51-mm and 76-mm deep targets, which most closely represent typical depths where delaminations may occur in a concrete structure.

Figure 3.11 shows a month of the thermal contrast data for 51-mm and 76-mm deep targets as an example of the comparison between model-predicted and field-measured results for the South side of the block. It can be observed that the curve patterns of the thermal contrast results from the model are in reasonably good agreement with the field experiment, that is, the overall trend of the model-predicted data is consistent with the field-measured data, generally, over the course of a month.

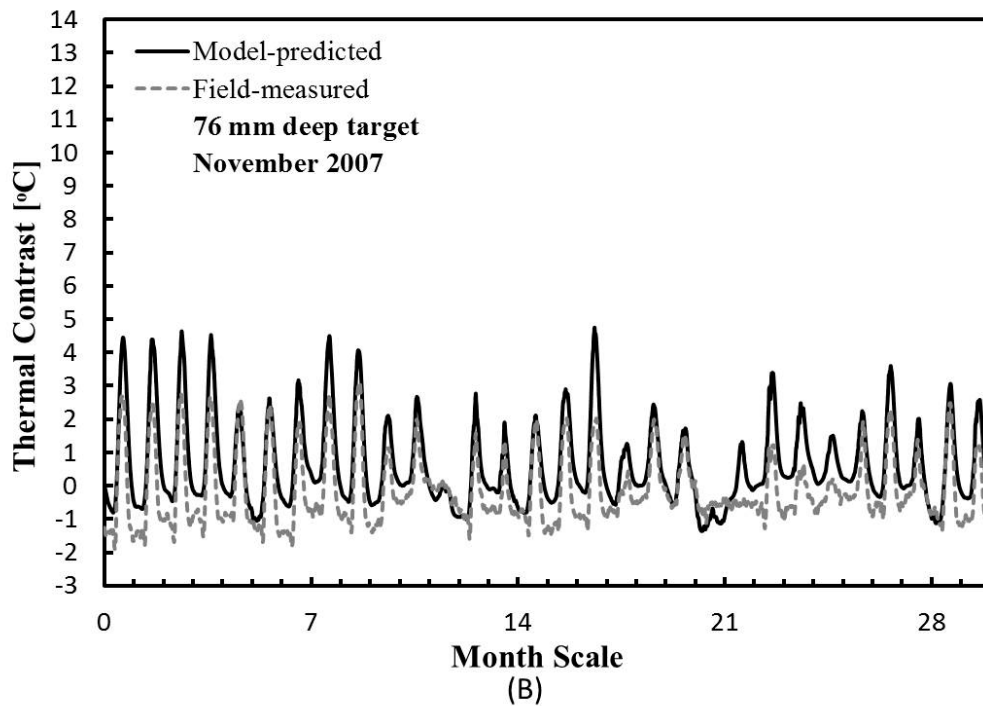
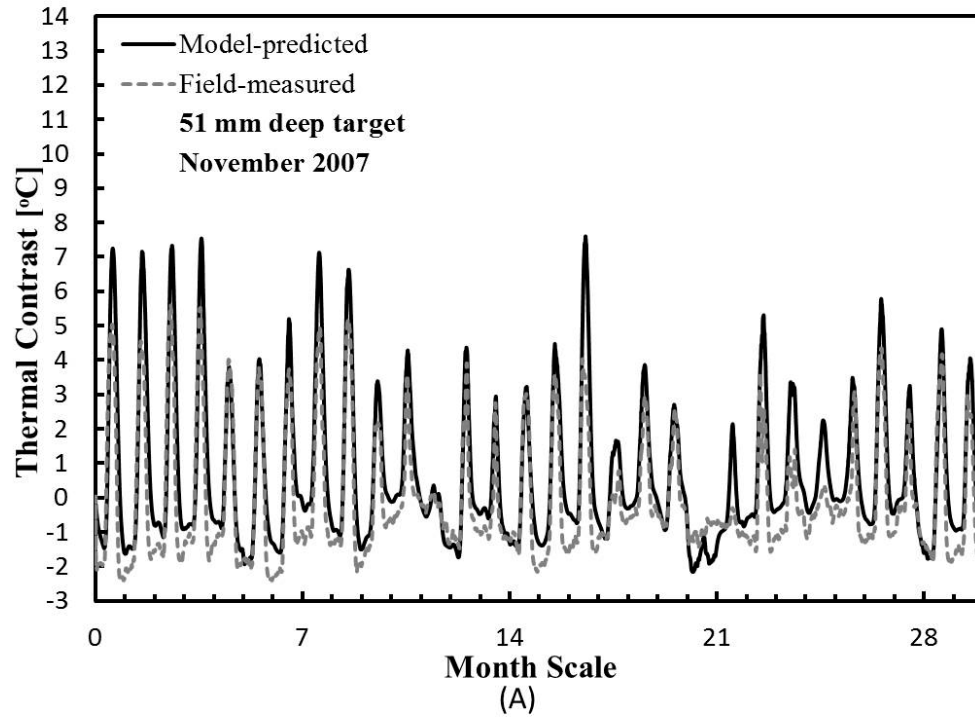


Figure 3.11 Comparison of model predicted and field-measured of thermal contrast for the South (sunny) side: (A) 51 mm deep target, and (B) 76 mm deep target

Figure 3.12 shows an example of the trend curve comparison between model-predicted and field-measured thermal contrast for 51 mm and 76 mm deep target for the North side of the block. In this case, there appears to be less agreement between the model and the experimental test results. It should be noted that 11 days of the month (May 2008) shown is a rainy day. The effects of over a half inch of rain throughout those days may be a source of this agreement. This preliminary analysis, nonetheless, showed that the curve patterns of the time varying thermal contrasts from the model reflected some patterns in the experimental results, indicating good potential for further research. The entire results for the trend curves comparison could find in **Appendix C**.

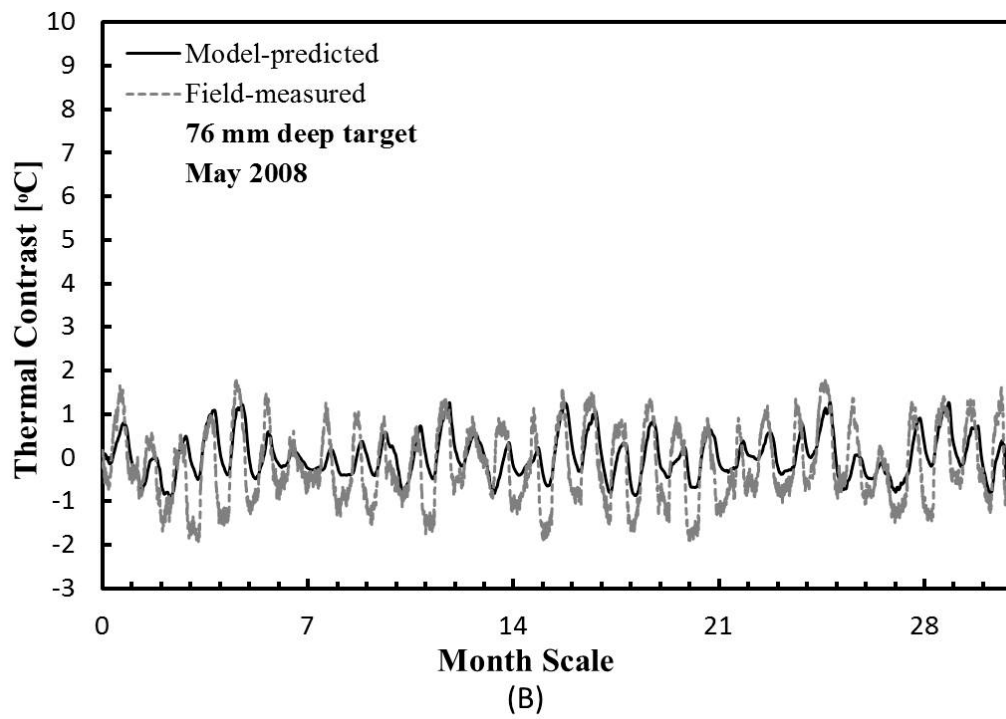
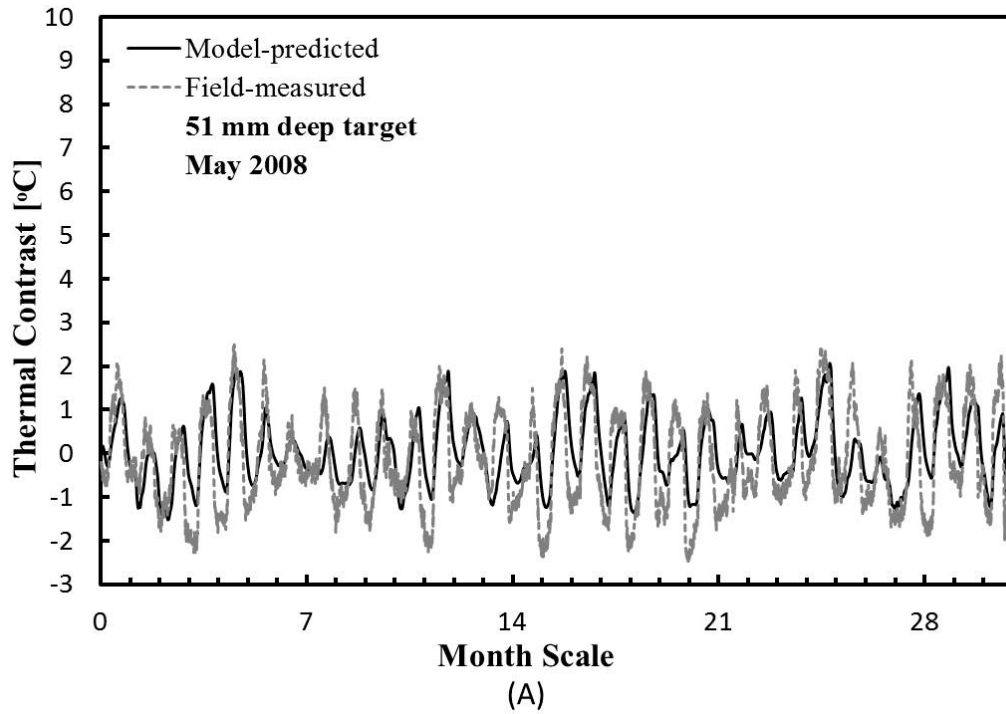


Figure 3.12 Comparison of model predicted and field-measured of thermal contrast for the North (shaded) side: (A) 51 mm deep target, and (B) 76 mm deep target

3.4.2 Correlation analysis

The Pearson correlation (r) analysis was completed to measure how estimated values and observed values of thermal contrast are linearly associated in data results (based on 10 minute time intervals) over the 6 month period. This analysis was calculated mathematically from Eq.3.1

$$r = \frac{\sum_{i=1}^N (P_i - \bar{P}) (O_i - \bar{O})}{[\sum_{i=1}^N (P_i - \bar{P})^2 \sum_{i=1}^N (O_i - \bar{O})^2]^{0.5}} \quad \text{Eq.3.1}$$

in which N is number of cases; P_i is the thermal contrasts obtained from the model; \bar{P} is the average value of the thermal contrasts obtained from the model; O_i is the thermal contrasts obtained from the experimental data, and \bar{O} is the average value of the thermal contrasts obtained from the experimental data. The ideal value for r is 1 or -1. If r is close to 0, there is little linear association between estimated values and observed values of thermal contrast.

In these analyses, days in which rain occurred were excluded because water on the surface of the concrete would affect the emissivity of the concrete and evaporation could affect the thermal behavior of the block. Consequently, practical thermal inspections of bridges are not conducted on rainy days.

Examining all the datasets of the South (sunny) side together, the thermal contrast correlations between model results and field observed for 25 mm, 51 mm, 76 mm and 127 mm targets were 0.93, 0.92, 0.89 and 0.68, respectively, as shown in Table 3.3 (highlighted row). Those values indicate high correlations

between model and experimental results. When the North (shaded) side is examined, the correlation coefficients were 0.78, 0.70, 0.70, and 0.49 for the 25 mm, 51 mm, 76 mm and 127 mm targets, respectively. It can be noted that the model correlates better in the sunny side compared to the shaded side. The absence of solar radiation in the shaded side is likely responsible for the lower correlation, since this provides a strong driving force for thermal contrast on the South side of the block. On the North (shaded) side, convective heat transfer results in much lower magnitude contrasts, and the correlation between the model and the experimental results is decreased.

Further analysis using cross-correlation method could optimize the correlation coefficient for the time shifted thermal contrasts. It should be noted that the cyclic nature of the model data was shifted slightly in time relative to the experimental data. These data were not adjusted to accommodate this shift; doing so would reduce the error measurements.

Table 3.3 Thermal contrast correlations (*r*) between the model and the experimental results. N is number of cases.

Pearson correlations (<i>r</i>) of thermal contrast between model and field results				
South (Sunny) Side				
Month	25 mm target	51 mm target	76 mm target	127 mm target
November, 2007 (N=3888)	0.932	0.925	0.903	0.702
December, 2007 (N=3888)	0.936	0.915	0.895	0.784
January, 2008 (N=3600)	0.923	0.927	0.877	0.546
Total Average (N=11376)	0.930	0.922	0.892	0.677
North (Shade) Side				
May, 2008 (N=2880)	0.769	0.691	0.677	0.433
June, 2008 (N=3024)	0.770	0.673	0.687	0.516
July, 2008 (N=3024)	0.805	0.721	0.734	0.514
Total Average (N=8928)	0.781	0.695	0.699	0.488

3.4.3 Error analysis

The error analysis was also completed to evaluate the magnitude of variations between the model and experimental test results and to evaluate the accuracy of the model predictions. In this study, the mean bias error (MBE), the mean absolute error (MAE), and the root mean squared error (RMSE) were used in time-series error analyses. These analyses were calculated mathematically from the following equations:

$$MBE = N^{-1} \sum_{i=1}^N P_i - O_i \quad \text{Eq.3.2}$$

$$MAE = N^{-1} \sum_{i=1}^N |P_i - O_i| \quad \text{Eq.3.3}$$

$$RMSE = \left[N^{-1} \sum_{i=1}^N (P_i - O_i)^2 \right]^{0.5} \quad \text{Eq.3.4}$$

in which N is number of cases; P_i is the thermal contrasts obtained from the model; O_i is the thermal contrasts obtained from the experimental data. MBE , MAE , and $RMSE$ are in °C. The ideal value for MBE , MAE , and $RMSE$ is 0.

The results of MBE , MAE , and $RMSE$ are given in Table 3.4. On average, the mean bias of the sunny side dataset was $\sim 0.70^\circ\text{C}$ for both 51 mm and 76 mm deep target, and the mean bias of the shaded side dataset was $\sim 0.2^\circ\text{C}$ for both 51 mm and 76 mm deep target. It can be seen that almost all of the MBE results produce positive values, indicating that the model tends to overestimate the thermal contrast. The unaltered magnitudes (absolute values) of each thermal contrast difference between the model and the test results of the sunny side dataset were about 0.78°C and 0.70°C for 51 mm and 76 mm deep target, respectively. The absolute values of thermal contrast difference of the shaded side dataset were 0.7°C and 0.6°C for 51 mm and 76 mm deep target, respectively.

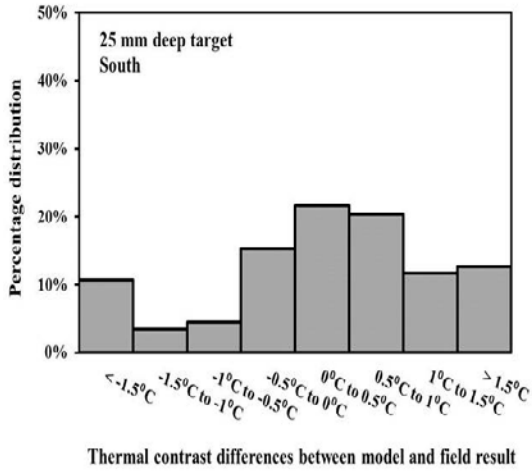
The root mean square error (RMSE) values of each thermal contrast difference between the model and the experimental results of the sunny side dataset were 0.98°C and 0.84°C for 51 mm and 76 mm deep target, respectively. For the shaded side, the RMSE values were 0.88°C and 0.67°C for 51 mm and 76 mm deep target.

It can be seen, from examining the MBE, MAE, and RMSE values for both the sunny and the shaded side, the model seemed to be robust exhibiting lower errors (below 1°C), except for the 25-mm deep target. These results indicate that the model simulates the magnitude of thermal contrast well.

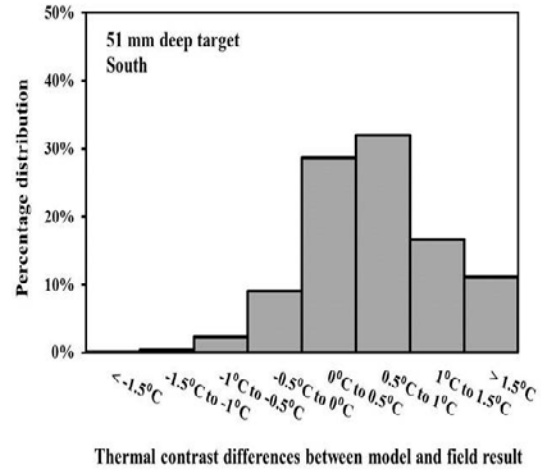
Table 3.4 Time-series error analysis of thermal contrast differences between the model and the experimental results. *MBE* is mean bias error, *MAE* is mean absolute error, and *RMSE* is root mean squared error.

Side	Depth [mm]	MBE [°C]	MAE [°C]	RMSE [°C]
The South (Sunny) N=11376	25	0.21	1.04	1.44
	51	0.70	0.78	0.98
	76	0.67	0.70	0.84
	127	0.53	0.56	0.66
The North (Shaded) N=8928	25	0.17	0.86	1.12
	51	0.22	0.70	0.88
	76	0.22	0.56	0.67
	127	-0.02	0.22	0.27

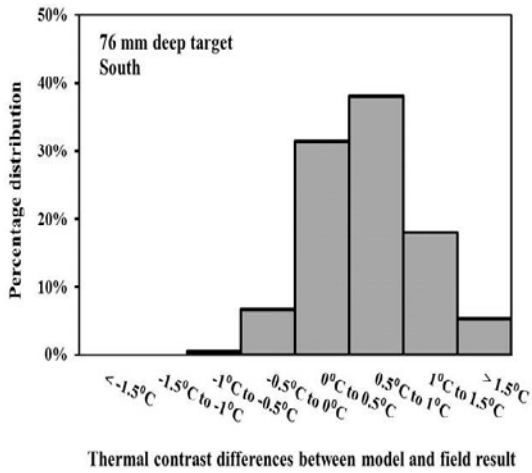
Figure 3.13 and 3.14 show the results of the percentage distribution for the thermal contrast differences between model and experimental for all datasets of the sunny side and the shaded side, respectively. They are grouped into ranges from lower than -1.5°C to higher than 1.5°C with increment 0.5°C . For all datasets of the sunny side with 51 mm deep target (Fig. 3.13.B), 72% are within 1°C difference, and 38% are within 0.5°C difference. For that side with 76 mm deep target (Fig. 3.13.C), 77% are within 1°C difference, and 38% are within 0.5°C difference. For all datasets of the shaded side with 51 mm deep target (Fig. 3.14.B), 76% are within 1°C difference, and 42% are within 0.5°C difference. For the side with 76 mm deep target (Fig. 3.14.C), 86% are within 1°C difference, and 50% are within 0.5°C difference. The distribution of thermal contrast differences is more concentrated in the range 0.5°C to 1°C for the sunny side, and in the range 0°C to 0.5°C for the shaded side. It can be deduced that the model predicts the thermal contrast with reasonable accuracy, but was least accurate for the shallowest void (25 mm).



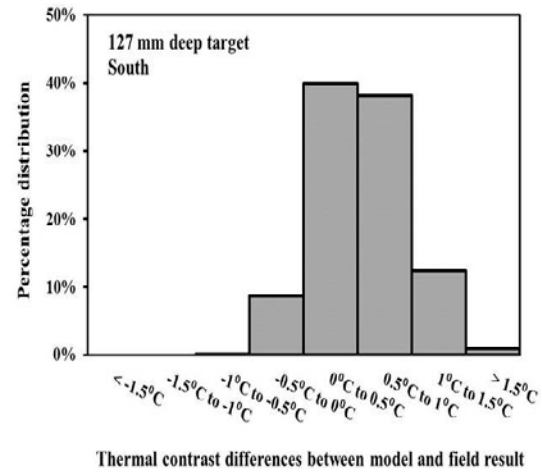
(A)



(B)

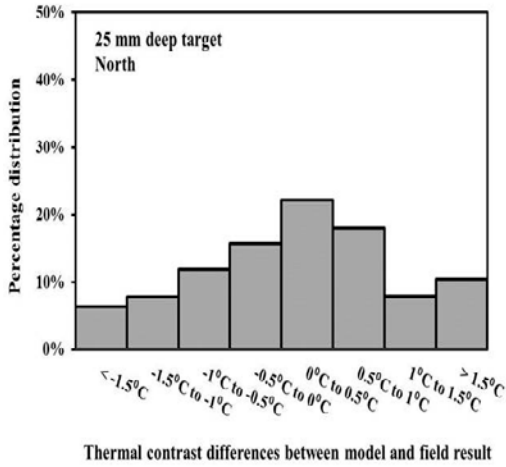


(C)

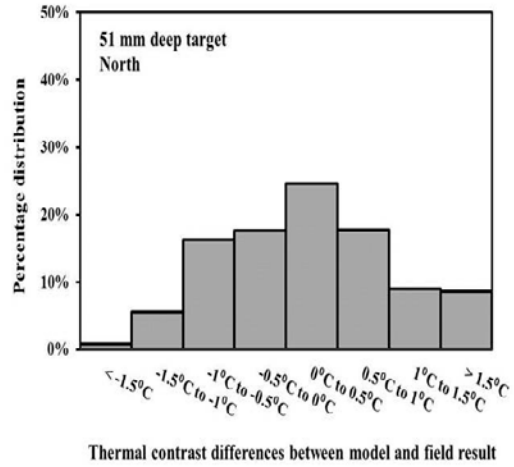


(D)

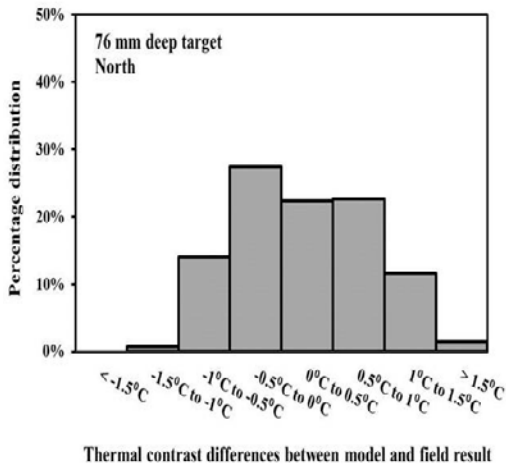
Figure 3.13 Percentage distribution for thermal contrast differences between model-predicted and field-observed of the sunny side: (A) 25 mm deep target; (B) 51 mm deep target; (C) 76 mm deep target; and (D) 127 mm deep target.



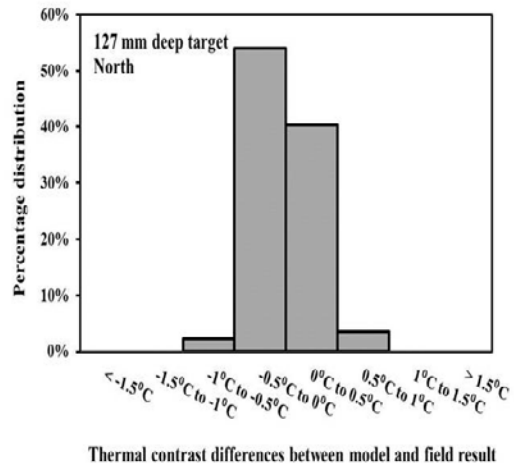
(A)



(B)



(C)



(D)

Figure 3.14 Percentage distribution for thermal contrast differences between model-predicted and field-observed of the shaded side: (A) 25 mm deep target; (B) 51 mm deep target; (C) 76 mm deep target; and (D) 127 mm deep target.

3.4.4 Comparison of the model results with the experimental results

The maximum thermal contrast obtained by the model developed under the study was compared to the previous experimental testing to assess the reliability of the model. Figure 3.15 shows the predicted maximum thermal contrast obtained from the FEM model versus actual maximum thermal contrast obtained from the experimental testing for the South side. As Fig.3.15 shows, the maximum thermal contrast determined by the model (dash line) has reasonable agreement ($R^2 = 0.792$) with the experimental data. The estimated maximum contrasts by the model may be slightly better when ΔT_{max} measured from the experimental in the range 1°C to 7.0°C. For this range, the differences of maximum contrast from both the developed model and the experimental result were within 1°C. These results indicate that the developed model was reasonable accuracy for the data in the study.

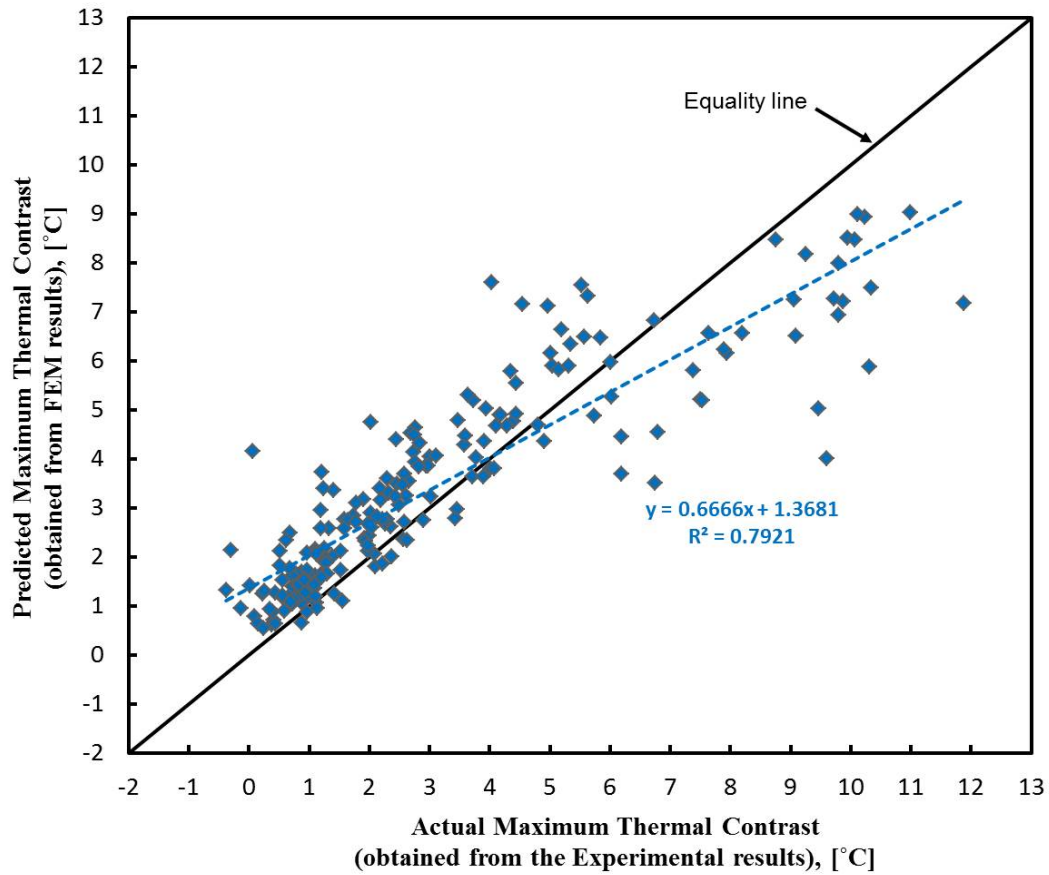


Figure 3.15 Predicted maximum thermal contrasts obtained from FEM model versus actual maximum thermal contrasts obtained from the experimental testing (for the South side)

For the North side, the predicted maximum thermal contrast obtained from the FEM model versus actual maximum thermal contrast obtained from the experimental testing was shown in Figure 3.16. It can be seen that the maximum thermal contrast determined by the developed model (dash line) has reasonable agreement ($R^2=0.72$) with the experimental data. The estimated maximum

contrasts by the model were different within 1°C with those obtained in the experimental data. These results indicate that the developed model was reasonable accuracy for the data in the study.

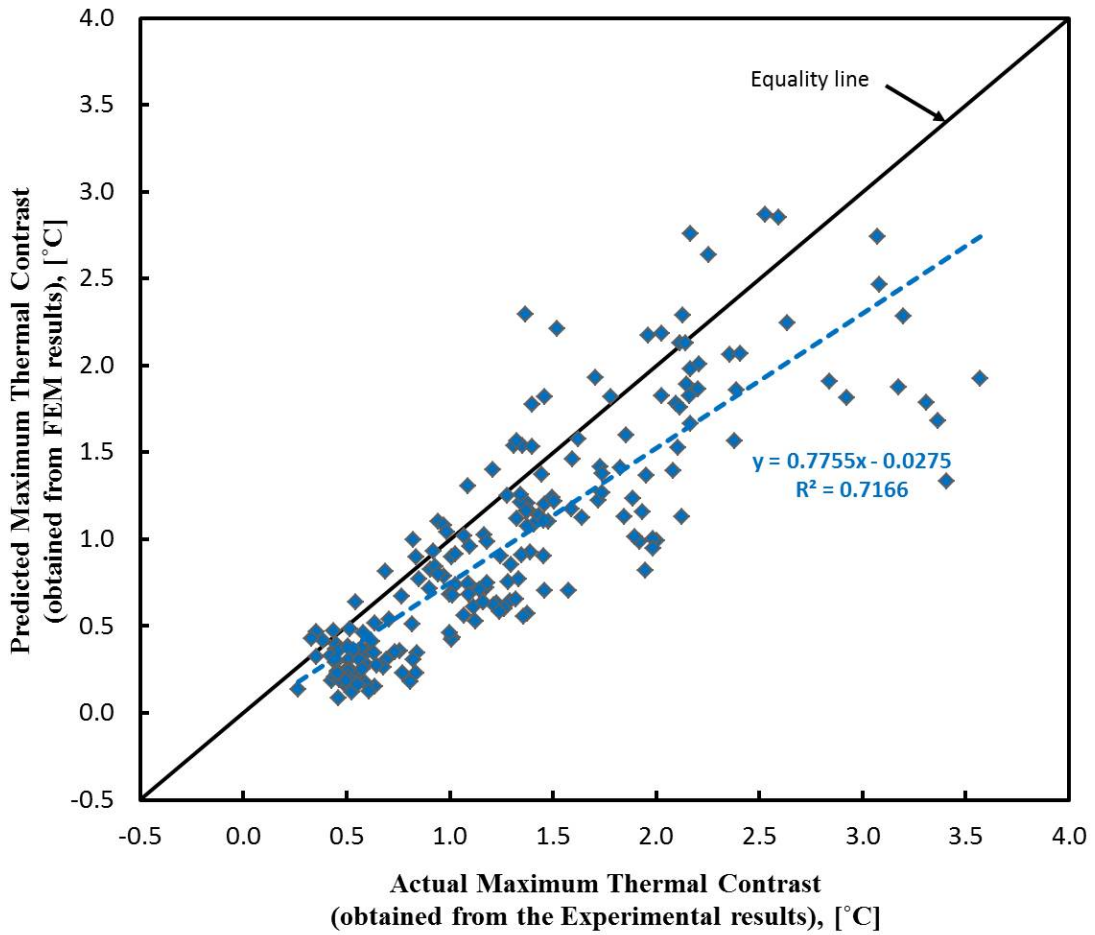


Figure 3.16 Predicted maximum thermal contrasts obtained from FEM model versus actual maximum thermal contrasts obtained from the experimental testing (for the North side)

3.5 Conclusion

This chapter has presented results from modeling of environmental effects on thermal detection of subsurface damage in concrete. A 3D, nonlinear loading, numerical model of transient heat transfer was developed using finite element analysis to study the environmental effects on thermal response of simulated subsurface voids in a large concrete block. The effects of solar radiation, ambient temperature variation, and wind speed on the thermal images that appear on the South and North side of the concrete block model with subsurface voids were presented.

The model performance was evaluated by comparing the thermal contrast of the model results with those reported from a previous experiment. It was found that the model provided an overall pattern of temperature contrasts that were similar to the pattern of experimental results, showing the model was successful in capturing the basic physical behavior of concrete block. Thermal contrast correlations between model and experimental results on the South side were 0.92 and 0.89 for 51 mm and 76 mm deep target, respectively. These results were better than the correlation on the North side (0.70).

An evaluation of the model performance was also made from the quantitative difference measured with the experimental results. For the South (sunny) side, the distribution of thermal contrast differences is concentrated in the range 0.5 °C to 1 °C for both 51 mm and 76 mm deep target. For the North (shaded) side, the distribution of thermal contrast differences is within 0.5 °C for

both the 51 mm and 76 mm deep targets. With respect to *MBE*, *MAE* and *RMSE*, overall the model seemed to generate good results with errors below 1°C. These results indicate that the model predicted the thermal contrasts with reasonable accuracy when compared to experimental data.

Based on these data, it was concluded that the model developed in this study was sufficiently accurate to provide a useful tool for estimating the thermal contrasts resulting from subsurface voids in the concrete, and provide a tool to support practical thermal inspections. For example, the model could be used to predict if a particular day's weather would produce the thermal contrasts required to be imaged using a common thermal camera given the anticipated depth of a delamination and predicted weather conditions. Alternatively, such a model could be used in a post-test analysis of data to estimate the depth of a delamination, given the known weather patterns surrounding the test and the measured thermal contrast detected during the test.

In the next chapter, the model proposed would be used for analyzing the effect of different field test parameters such as: a variety of void geometries (depth and thickness), a variety of different materials contained in the delamination, asphalt over the void, and material properties of the concrete.

4. PARAMETRIC STUDIES

4.1 Introduction

In the previous chapter, a numerical model to predict the thermal contrasts resulting from subsurface voids (i.e. delaminations) in concrete under environmental conditions was developed using the FEM. The model was verified using the experimental test data, and the results indicated that the model could be an effective tool to support the thermography inspection of the concrete. In this chapter, the use of the same model to evaluate the effects of different key parameters expected to influence the detectability of the subsurface voids in concrete is presented. These key parameters include: void depth and thickness, material contained in the void, material properties of concrete, and asphalt overlay. For simplification in these parametric studies, the geometry of the block and boundary conditions were changed on the previous model described in Chapter 3. The 3-dimensional model (Figure 4.1) with three consecutive days of environmental data as boundary conditions (Figure 4.2) was used. The results of these parametric studies are discussed. An example of the post-test model analysis is also provided that illustrates the capability of the model to estimate the maximum thermal contrast.

4.2 Parametric Study Case 1: Effect of varying void depths and void thicknesses

The first parametric study involved a concrete block with an embedded air void to simulate the effect of a subsurface delamination at different depths and of different thicknesses.

4.2.1 Description

Figure 4.1 shows the basic geometry for the case which consists of a concrete block 2.4 m wide by 2.4 m long and 0.9 m deep with a square void inserted. The void was to simulate a delamination. The thermal properties of air were used to describe the voided area. The depths of the voids were 25, 51, 76, and 127 mm from the front surface of the block, the lateral size of the void was taken as 305 mm square and the void thickness ranged from 0.5 mm to 15 mm.

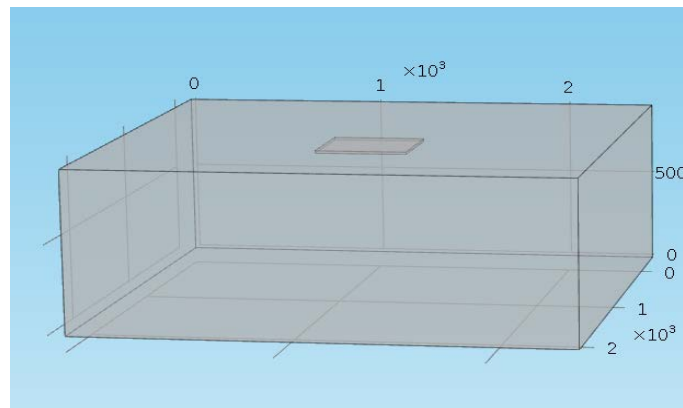


Figure 4.1 The basic geometry of the concrete model

Three days of weather data, which were obtained from the experimental study (the sunny side), were simulated as boundary conditions. The solar radiation (Fig 4.2A), the ambient temperature (Fig. 4.2B), and the wind speed (Fig. 4.2C) were applied in the model. Solar radiation was simulated only at the top surface of the concrete block. Convective cooling was simulated at the top surface and the bottom surface of the concrete. Table 4.1 shows an example input parameters for a simulation in Case 1.

Table 4.1 An example input parameters for a simulation in Case 1

Input parameter	Value	Description
rho_concrete	2300 [kg/m ³]	Density of concrete
Cp_concrete	1000 [J/(kg.°C)]	Heat capacity of concrete
k_concrete	1.8 [W/(m.°C)]	Thermal conductivity of concrete
e_concrete	0.95	Emissivity of concrete
Size of the void	305 x 305 x 13 [mm ³]	
Depth_from_surface	51 [mm]	Depth of void from the surface of concrete
Material of void	Air	
rho_void	1.2 [kg/m ³]	Density of void
Cp_void	700 [J/(kg.°C)]	Heat capacity of void
k_void	0.024 [W/(m.°C)]	Thermal conductivity of void
Solar radiation	Solar radiation data on the sunny side	3 consecutive days of the solar radiation data
Air temperature variations	Ambient temperature data on the sunny side	3 consecutive days of air temperature data
Wind speed	Wind speed data on the sunny side	3 consecutive days of wind speed data
T_initial	12 [°C]	Initial surface temperature
Time step	10 minutes	

All simulations were run using 10 minutes time step over a period of three consecutive days. The purpose of modeling three days of data was to allow the concrete block to achieve its thermal inertia for transient heat flow. Only data results of the final 24 hours of the third day were used in the analysis. The initial temperature of the concrete block was taken to be the same as the initial surface temperature obtained from thermocouple measurement in the experimental test. The model was meshed using the tetrahedral meshing feature from the COMSOL program. The “extra fine” element size was selected as a balance between computational economy and accuracy in the solution, since only three days of environmental data were used as boundary conditions.

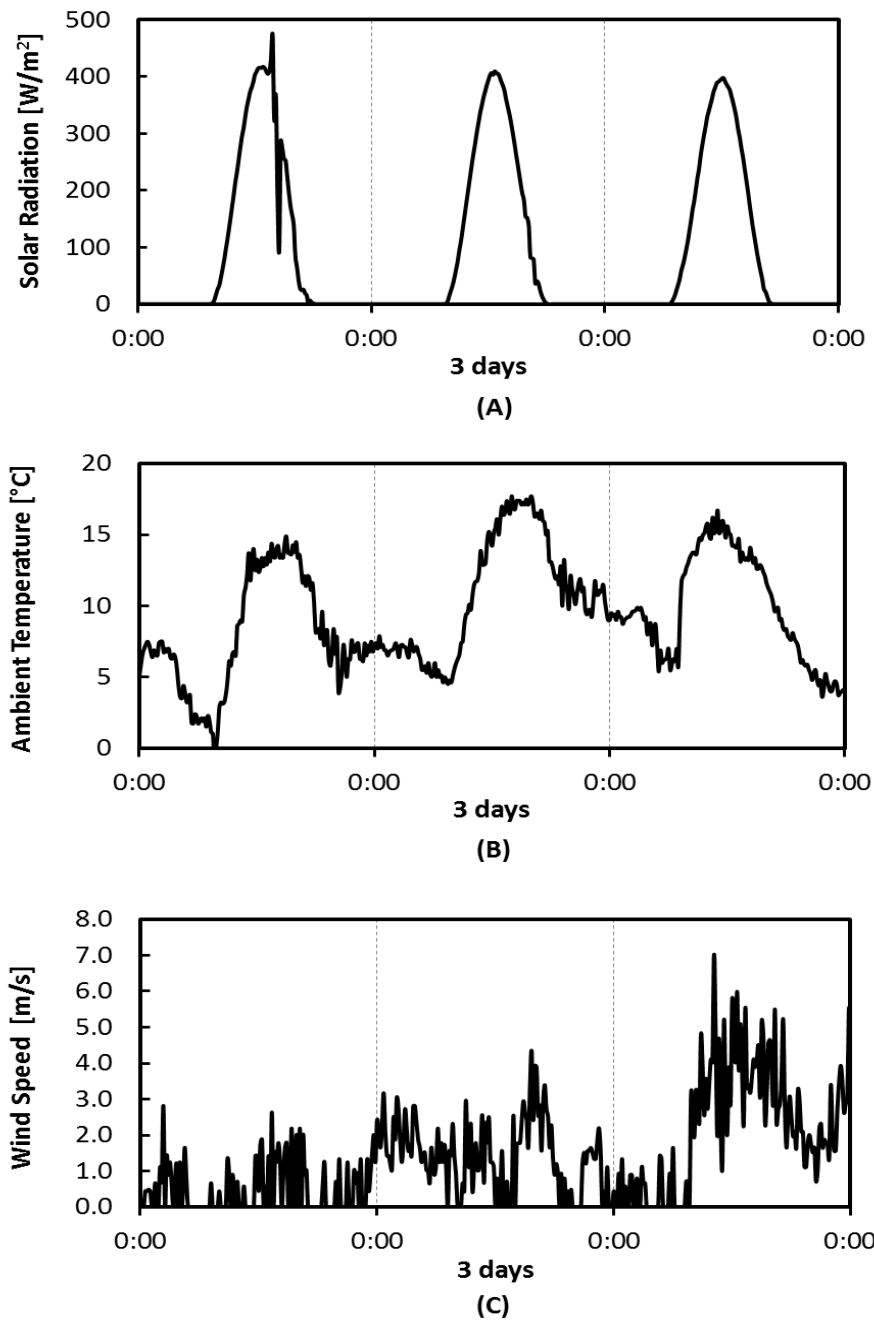


Figure 4.2 Three consecutive days of environmental parameters as a boundary condition in simulation: (A) solar radiation; (B) ambient temperature; and (C) wind speed

4.2.2 Results and discussions

The results of the simulation provided transient thermal images of the concrete surface. These thermal images presented data on the surface temperature in response to the weather conditions for different depths and different thicknesses of voids. For quantitative analysis, surface temperatures as a function of time from a point above the void (T_{void}) and a reference point where there is no void ($T_{sound\ concrete}$) were compared and these surface temperature differences (i.e. thermal contrast) were calculated using Eq.2.2.

Figure 4.3A illustrates an example of the effect of varying void depths on the thermal contrast produced by an air-filled void (for 13 mm void thickness). The results indicated that increasing depth of the void reduced the thermal contrast. The void located near the concrete surface resulted in maximum thermal contrast and the shortest time to achieve maximum thermal contrast, while deep voids resulted in low maximum thermal contrast and a longer time period to achieve that contrast. The thickness of the air-filled void was also found to affect the thermal contrast as shown in Figure 4.3B (for 51 mm deep void). It should be noted that these results were appropriate for the simulations under the particular weather condition as shown in Fig.4.2.

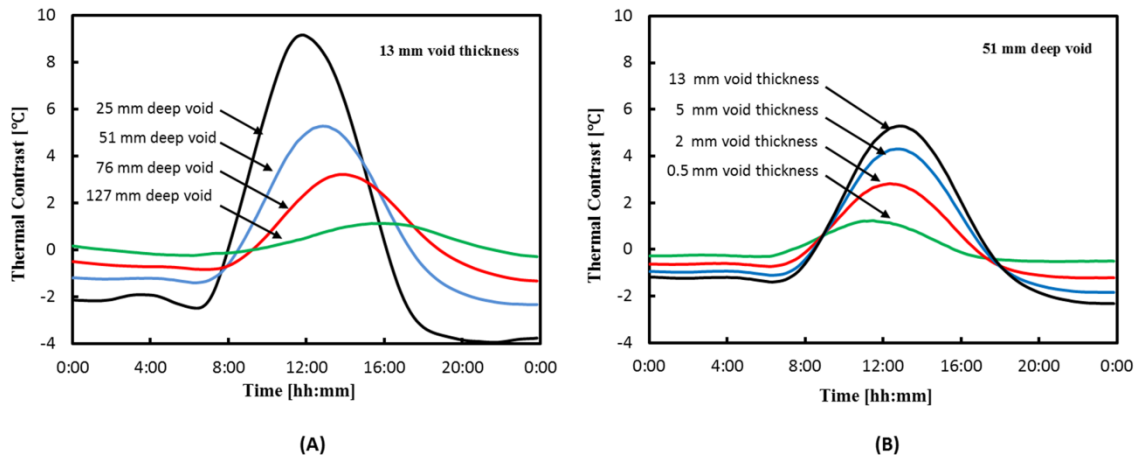
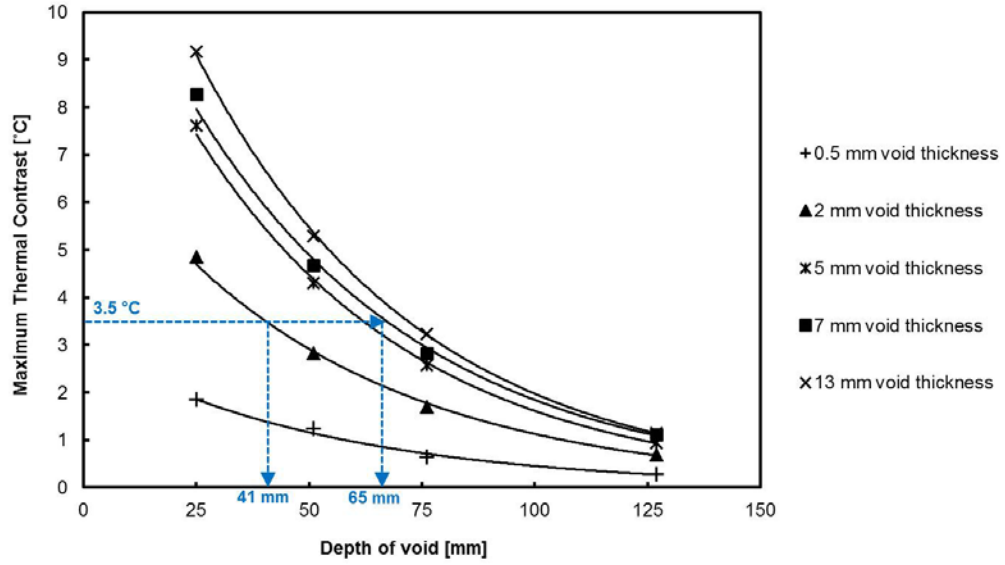


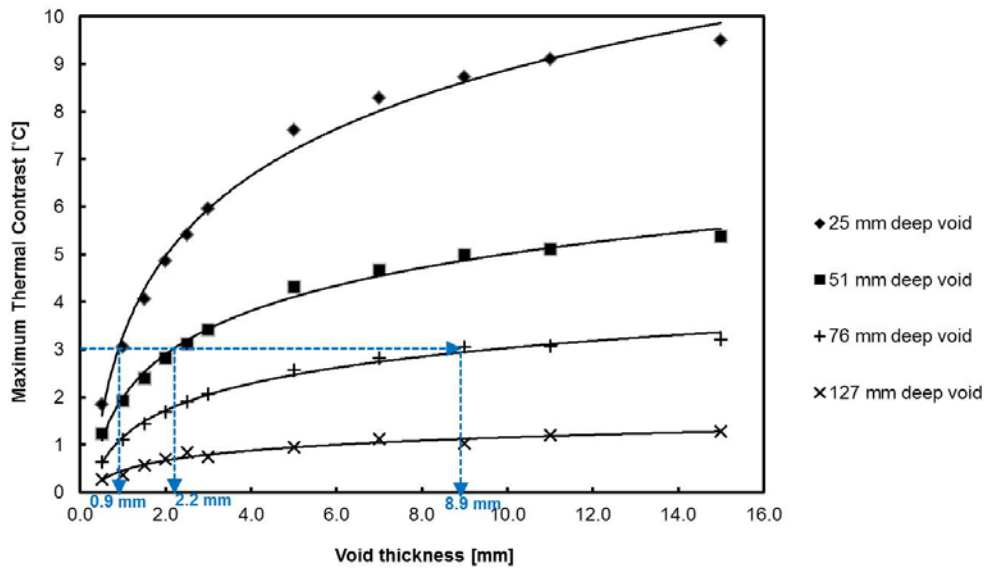
Figure 4.3 The time varying thermal contrast: (A) as a function of void depth, and (B) as a function of void thickness

Figure 4.4 and Table 4.2 summarize the results of the maximum thermal contrast from voids at various depths and thickness for this case. The results show some interesting details regarding the effect of void depth and void thickness on the thermal contrast. The maximum thermal contrast decreased nonlinearly for increasing void depths (Fig.4.4A), such as for a void thickness of 2 mm, the maximum thermal contrast for 25 mm, 51 mm, 76 mm, and 127 mm deep void was 4.86°C, 2.82°C, 1.69°C, and 0.69°C, respectively. In addition, Fig.4.4B shows that the bigger the void thickness, the greater the thermal contrast. For example, in case of 51 mm deep void, the maximum thermal contrast increased from 1.24°C to 5.29°C with increasing thickness from 0.5 mm to 13 mm. The variation of the maximum thermal contrast with void depths could be fit by the exponential function, and the variation of the maximum thermal

contrast with void thickness could be fit by the logarithm functions (inversion of the exponential functions).



(A)



(B)

Figure 4.4 (A) Effect of void depth on the maximum thermal contrast and (B) Effect of void thickness on the maximum thermal contrast

Examining all the coefficient of determination results in Table 4.2, the values of R^2 varied from 0.989 to 0.999. Those values indicate the maximum thermal contrast strongly depends on the void depth that followed the trends of exponential functions as

$$\Delta T_{max} = Ae^{K \cdot d} \quad \text{Eq. 4.1}$$

where ΔT_{max} is the maximum thermal contrast in °C, d is the depth of void in mm, e is the natural exponential base ($e \sim 2.71828$), A and K are constants. Equation 4.1 was fitted to the maximum thermal contrast-void depth data in variation of void thickness (z) from 0.5 mm to 13 mm. The best-fit exponential function was obtained by an iterative least-square (maximum likelihood) method using the Excel program.

Table 4.2 Result for simulations involving void depths (d) and void thicknesses (z) on maximum thermal contrast (ΔT_{max})

Void thickness, z [mm]	The maximum thermal contrast, ΔT_{max} [°C]				The best fitting exponential functions for ΔT_{max} [°C]	
	25 mm deep void	51 mm deep void	76 mm deep void	127 mm deep void	$\Delta T_{max} = A \cdot e^{K \cdot d}$	R^2
0.5	1.85	1.24	0.64	0.28	$2.96e^{-0.019 \cdot d}$	0.989
1	3.06	1.92	1.11	0.37	$5.39e^{-0.021 \cdot d}$	0.998
2	4.86	2.82	1.69	0.69	$7.54e^{-0.019 \cdot d}$	0.998
3	5.96	3.42	2.06	0.74	$9.78e^{-0.020 \cdot d}$	0.999
5	7.62	4.31	2.57	0.95	$12.37e^{-0.020 \cdot d}$	0.999
7	8.28	4.68	2.83	1.12	$12.97e^{-0.020 \cdot d}$	0.998
9	8.73	4.98	3.06	1.03	$14.69e^{-0.021 \cdot d}$	0.999
11	9.11	5.12	3.08	1.20	$14.38e^{-0.020 \cdot d}$	0.998
13	9.18	5.29	3.23	1.14	$15.16e^{-0.020 \cdot d}$	0.999

In this method, the constant, **A**, determines the maximum thermal contrast when the depth of the void was 0 for each void thickness. The results of **A**, as shown in Figure 4.5A, indicate that **A** varies due to changes in the void thickness. In general, the values of **A** increased with increasing void thickness and their relationship could be expressed by the natural logarithm (**ln**) of **z** as

$$\mathbf{A} = 3.852 \ln(\mathbf{z}) + 5.294 \quad \mathbf{Eq. 4.2}$$

The strong dependence between **A** and the void thickness was indicated by the coefficient of determination of 0.982.

The constant **K** reflects the rate at which the maximum thermal contrast-void depth curve changes slope and indicates the shape of the curve. Larger values of **K** lead to faster rates of growth, and vice versa. The results of **K**, as shown in Figure 4.5B, indicate that **K** did not change significantly with increasing void thickness. The average value of **K** was about -0.02 for the void thickness in this study. When the term of e^K in Eq.4.1 was replaced by a constant **B**, as the base of the exponential equation, the value of **B** could be obtained as 0.980 ($B = e^K = 2.71878^{-0.02} = 0.980$). This means that the maximum thermal contrast decreased by a constant multiple of 0.980 as the void depth increased over the depth of void range used in the model (25 mm to 127 mm).

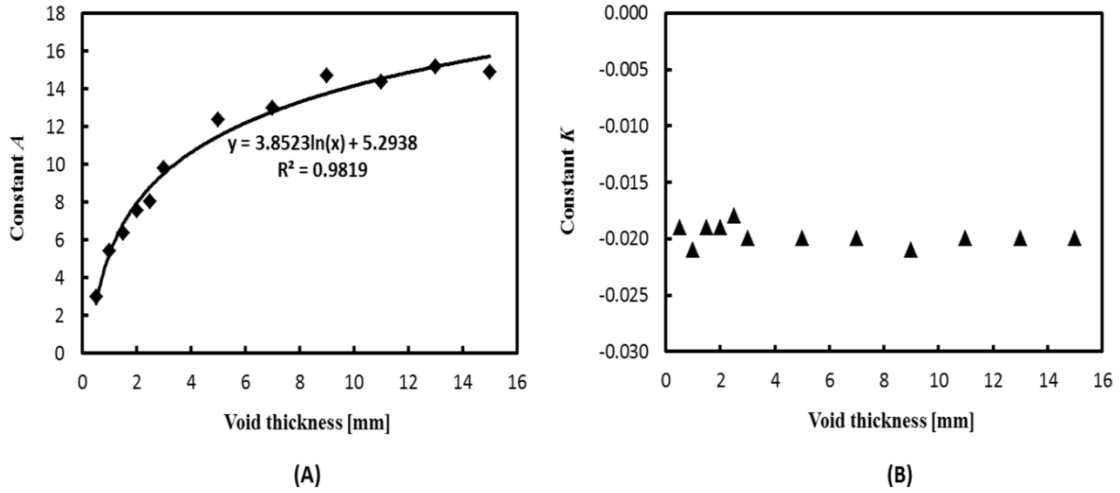


Figure 4.5 Values obtained for constant A and constant K for exponential expressions fitted to the maximum thermal contrast-void depth data in variation of void thickness

Based on the exponential expressions obtained in this case, the relationship between the maximum thermal contrast (ΔT_{max}), void depth (d) and void thickness (z) could be expressed by substituting the value of A in Eq.4.2 and the value of B into Eq.4.1, therefore

$$\Delta T_{max} = (3.852 \cdot \ln(z) + 5.294) \cdot 0.98^d \quad \text{Eq. 4.3}$$

where ΔT_{max} in $^{\circ}\text{C}$ and both d and z are in mm. For example, the maximum thermal contrast was computed using Eq.4.3 for three different thicknesses: 0.5 mm, 2 mm, and 7 mm, which represent as a thin void thickness, a typical void thickness, and a thick void thickness, respectively, and for 51 mm deep void. The results from the calculations were presented in Table 4.3. It can be seen that the maximum thermal contrasts obtained from Eq.4.3 matched with those obtained in Table 4.2. Again, it should be noted that the use of Eq.4.3 for

predicting the maximum thermal contrast was proper for the model under a particular set of weather conditions in Fig.4.2.

Table 4.3 Example of estimation of maximum thermal contrast ($d=51$ mm deep void)

Void thickness, z [mm]	$A = 3.852 \ln(z)+5.294$	Maximum thermal contrast [°C]
0.5	2.62	$\Delta T_{\max} = 2.62 \times 0.98^d = 0.9$
2	7.96	$\Delta T_{\max} = 7.96 \times 0.98^d = 2.8$
7	12.79	$\Delta T_{\max} = 12.79 \times 0.98^d = 4.6$

4.2.2.1 Estimation depth of void

Inversion of Eq.4.3 as expressed in Eq.4.4 allows for the estimation of the depth of the void, given the known weather patterns surrounding the test, the measured thermal contrast detected during the test, and the anticipated thickness of a delamination. The depth of void could be obtained mathematically from the following equation

$$d = \left[\frac{\ln(\Delta T_{\max}) - \ln(A)}{K} \right] \quad \text{Eq. 4.4}$$

where ΔT_{\max} is the maximum thermal contrast in °C, A is the constant determined in the Eq.4.2, and K is -0.020.

The use of Fig.4.4A (highlighted as the blue dash lines) was a simple procedure to estimate the depth of void graphically. For example, for a 3.5°C

maximum thermal contrast, the estimated void depth was approximately 41 mm when the void thickness was 2 mm. It was predicted as 65 mm when the void thickness was 7 mm.

4.2.2.2 Minimum void thickness

The model could also be used to evaluate the capability and limitation of the detectable void. For example, it could estimate the minimum thickness of the detectable void, either mathematically or graphically, when the expected maximum thermal contrast and the anticipated depth of a void were given. It could be determined mathematically from the following steps:

- Establish the expected maximum thermal contrast (ΔT_{max}) and the anticipated void depth (d).
- Obtain the constant A by using inversion of Eq.4.1.

$$A = e^{\ln(\Delta T_{max}) - Kd} \quad \text{Eq. 4.5}$$

- Substitute the value of A in Eq.4.5 to Eq.4.2, therefore

$$z = e^{0.260 \cdot A - 1.374} \quad \text{Eq. 4.6}$$

The use of Fig.4.4B (highlighted as the blue dash lines) was a simple procedure to estimate the minimum thickness of the detectable void graphically. For example, in the case of a 3°C maximum thermal contrast, the minimum thickness of detectable void was approximately 0.9 mm, 2.2 mm, and 8.9 mm when void depth was 25 mm, 51 mm, and 76 mm deep, respectively. It could not be detected when the void depth was 127 mm. Figure 4.4B also showed that the

influence of the void thickness on the maximum thermal contrast was significant in the case of voids near the surface (25 mm, 51 mm and 76 mm deep voids), but the influence was small on the deepest void (127 mm deep).

4.2.2.3 Determining effect of reinforcing steel

A concern at the beginning of this study was whether the rebar in the concrete would affect prediction of the surface temperature. Two models were simulated to determine the effect of rebar. One model was plain, unreinforced concrete, and the other was the concrete with reinforcing. The concrete models were similar in dimension and specification. For the model which included rebar, 12.7 mm diameter steel bars were used. The corresponding value of thermal conductivity, specific heat, and density from the steel reinforcement was then specified as 44.5 W/m°C, 475 J/kg°C, and 7850 kg/m³, respectively. The ratio of the rebar to the concrete area was 0.2%.

For this study, the surface temperatures at a reference point of the concrete block with and without rebar (in the same location) were compared as shown in Figure 4.6. The results indicated that the rebar did not affect significantly the thermal behavior of the concrete block. The small difference in the surface temperature results did not justify the high increment in computation time for the model with rebars. Therefore, the internal rebar was not considered for the simulations in this study.

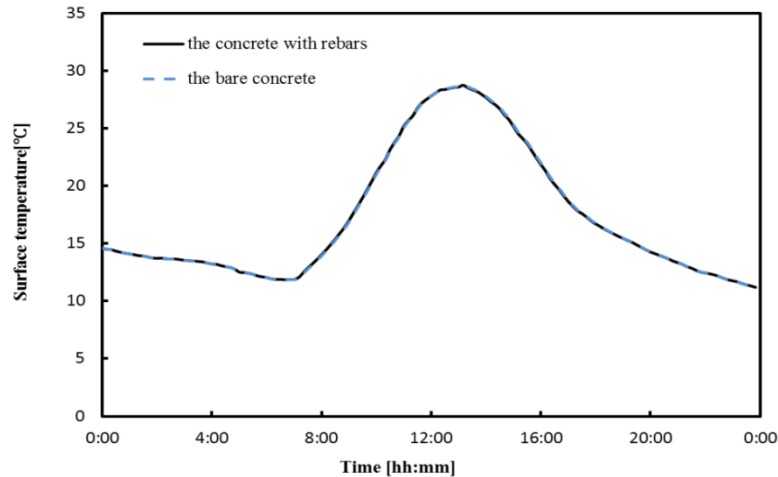


Figure 4.6 The surface temperatures at a reference point of the model with rebar and without rebar

4.2.2.4 Numerical and field experimental comparison

For model verification, the predicted maximum thermal contrasts for the South side were compared to those obtained from the experimental testing (Figure 4.7A). In these comparisons, the thickness of the void was 13 mm, and the material present in the void was Styrofoam.

The results show that the maximum thermal contrasts of the model-predicted were slightly higher than those contrasts of the experimental data, except for 25 mm deep void. The maximum thermal contrasts for the simulations were 8.59°C, 4.94°C, 2.96°C and 1.10°C for 25 mm, 51 mm, 76 mm and 127 mm deep voids, respectively, while the experimental results indicated the maximum thermal contrasts were 9.80°C, 4.02°C, 2.56°C and 0.98°C for 25 mm, 51 mm, 76 mm and 127 mm deep voids, respectively. Figure 4.7A also presents the exponent curve fit for both the model prediction and the experimental data.

In addition, by using the same procedure as described in previous sections, a model for the North side was also proposed. The comparison between the model results and the experimental data of the maximum thermal contrast were summarized in Figure 4.7B. The results show that the maximum thermal contrasts of the predicted model were slightly underestimated than those contrasts of the experimental data. The maximum thermal contrasts for the model predicted were 3.11°C, 1.96°C, 1.30°C and 0.56 °C for 25 mm, 51 mm, 76 mm and 127 mm deep voids, respectively, while the experimental data indicated the maximum thermal contrasts were 4.05°C, 2.39°C, 1.72°C and 0.84 °C for 25 mm, 51 mm, 76 mm and 127 mm deep voids, respectively. It can be seen that the variation of the maximum thermal contrast with void depths could be fit well by the exponential function where the values of R^2 were almost 1.

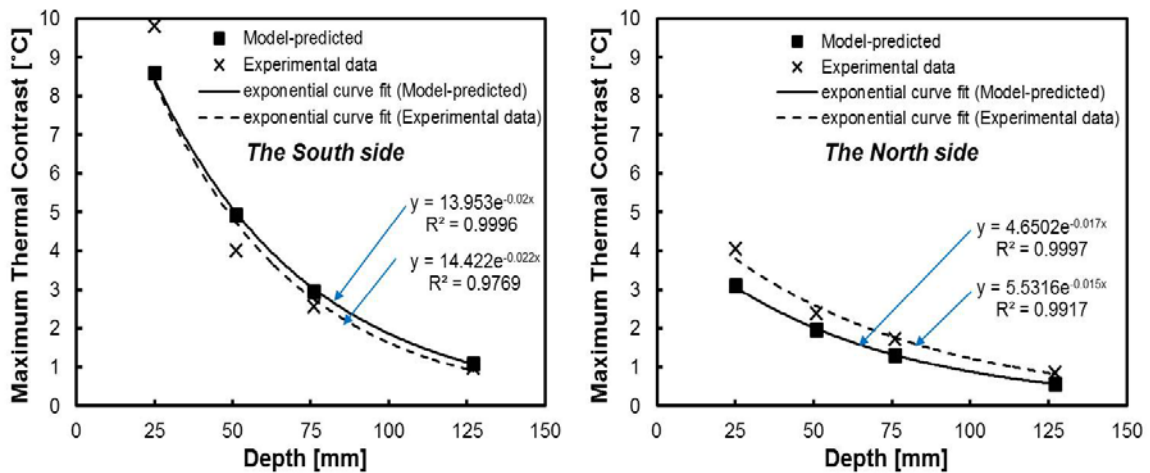


Figure 4.7 The comparison between the maximum thermal contrasts of model-predicted and the experimental data: (A) the sunny side, and (B) the shaded side

4.3 Parametric Study Case 2: Effect of the materials in delamination

4.3.1 Description

Similar to the first case, a simple model of a concrete block with a variety of materials contained in the delamination void was proposed and used to predict thermal response under weather conditions for the particular days shown in Fig. 4.2. Table 4.4 shows a group of analysis which included five different materials in the void. The material in void was represented with the properties of air, water, ice, epoxy and Styrofoam in each model and was located at the center of the block. The thickness of the void was 13 mm in these simulations.

Table 4.4 Material properties for Case 2 involving different materials contained in the void and the sound concrete

Material	k [W/(m °C)]	C _p [J/(kg °C)]	ρ [kg/m ³]
Void (air)	0.024	700	1.2
Void (Styrofoam)	0.027	1300	35
Void (water)	0.6	4200	1000
Void (ice)	2.2	2050	915
Void (epoxy)	1.24	1200	1530
The sound concrete	1.8	1000	2300

4.3.2 Results and discussions

Figure 4.8 shows the time varying thermal contrast as a function of materials present in the void for the 51 mm deep void. The results showed that

when the void was filled with air, the substantial difference in thermal conductivity (k) between air and concrete (Table 4.4) supported expectations of significant thermal contrasts between a void area and the sound concrete. Since the thermal conductivity of water, ice, and epoxy adhesive was not substantially different than that of concrete, the thermal contrasts of these materials in the void were not more pronounced. In addition, the results showed that the differing specific heat (C_p) of air and Styrofoam would be expected to produce a small difference in the thermal contrast. There was also a small difference in thermal contrast among water, ice, and epoxy. However, it can be noted that the thermal conductivity of the material in void dominated the thermal contrast behavior.

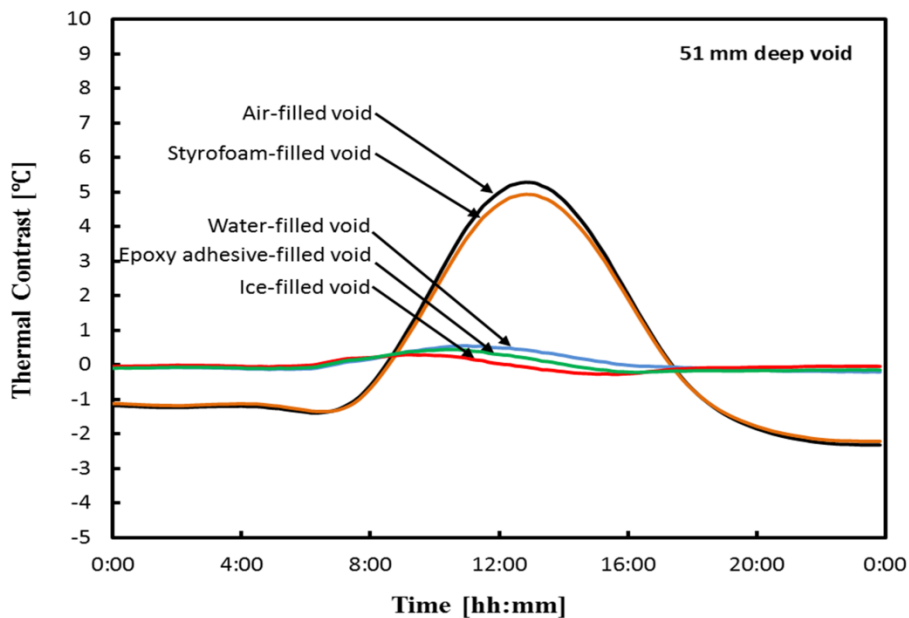


Figure 4.8 The time varying thermal contrast as a function of the materials present in the void

The characteristic maximum of thermal contrast for different materials contained in the void can be summarized in Figure 4.9. It can be clearly seen that the maximum thermal contrasts for air-filled void and Styrofoam-filled void were detected more easily than the others filled materials.

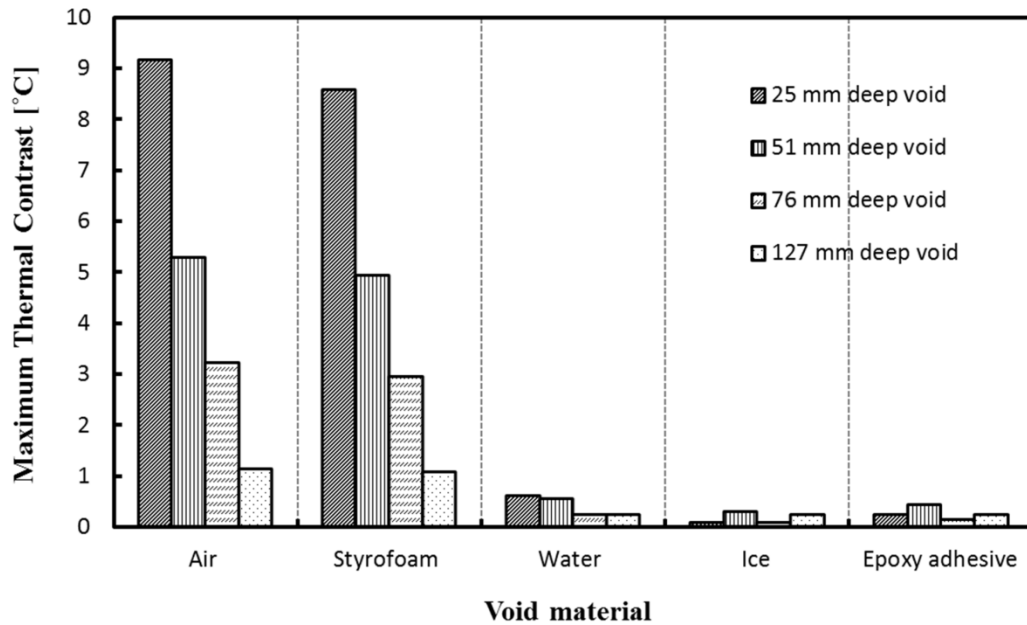


Figure 4.9 Effect of void material on the maximum thermal contrast

4.4 Parametric Study Case 3: Effect of material properties of concrete

4.4.1 Description

A simple model of a concrete block was used to predict thermal response under the same weather conditions as in the first case and the second case. In

this case, the thermal properties of interest are thermal conductivity, volumetric heat (i.e. the product of a material's specific heat and the density), and emissivity of the concrete itself. The thermal conductivity of the bulk concrete material varied from 1.6 to 2.3 W/(m·°C) and the volumetric heat was in the range 1.8×10^6 to 2.5×10^6 J/(m³·°C). The emissivity of the concrete varied from 0.75 to 0.95. A total of 16 finite element models were simulated to evaluate the effect of these properties on the thermal contrast. The thermal properties of air were used to describe the voided area. The depth of the void was 51 mm from the front surface of the block, and the thickness of the void was 13 mm in these simulations.

4.4.2 Results and discussions

Figure 4.10A, Figure 4.10B and Figure 4.10C present the maximum thermal contrast for the different thermal conductivities, the various volumetric heats and the emissivity of the concrete, respectively. The results show that the maximum thermal contrast appears better for higher thermal conductivity than those obtained for lower conductivity. In contrast, the influence of the volumetric heat of the concrete shows that the lower the volumetric heat, the better the thermal contrast is, as same as the influence of the emissivity of the concrete.

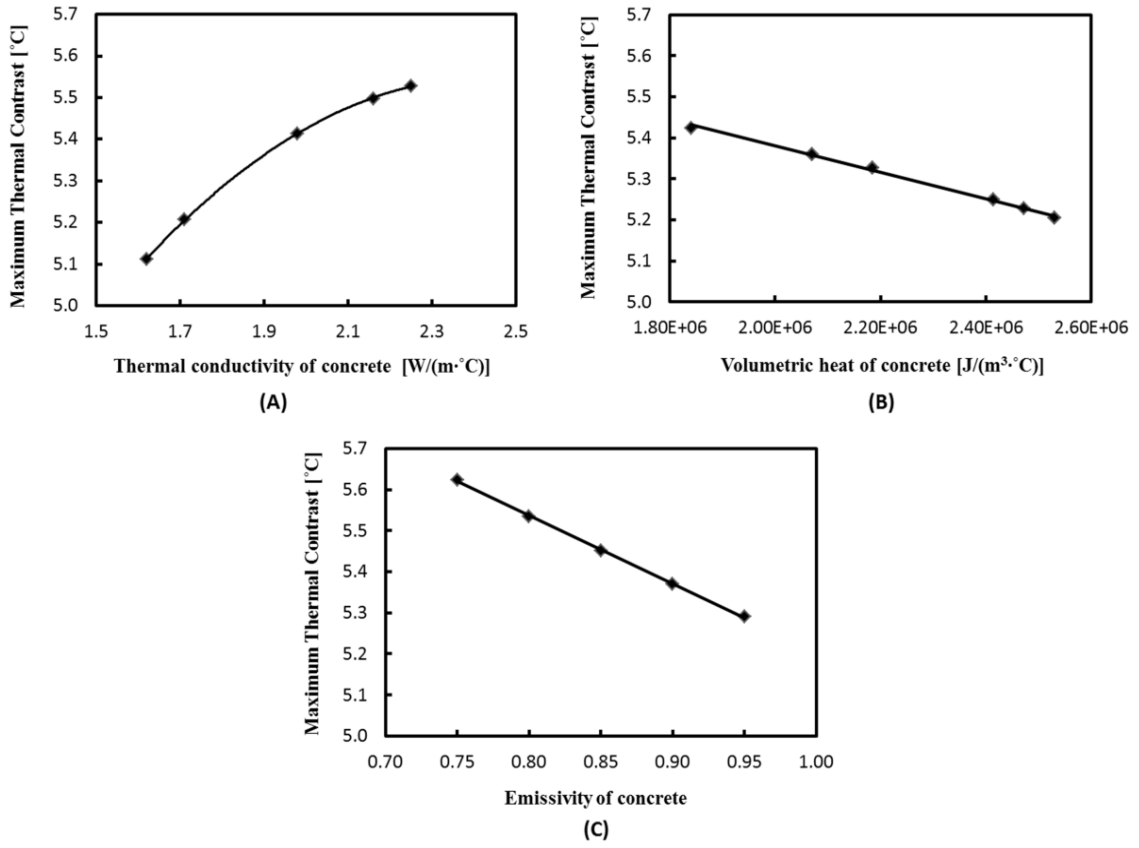


Figure 4.10 Effect of material properties of concrete on the maximum thermal contrast: (A) thermal conductivity; (B) volumetric heat; and (C) emissivity

Overall, the results of Case 3 show that the thermal properties of the concrete had a small effect on the thermal contrast in the model. An increase on the thermal conductivity of the concrete by 40% tends to enhance the thermal contrast only by 8%. Increases of the volumetric heat by 38% may diminish the contrast only 4%. An increase of the emissivity from 0.75 to 0.95 tends to decrease the thermal contrast as 0.3°C.

4.5 Parametric Study Case 4: Effect of asphalt overlays

4.5.1 Description

The thermal model was applied to concrete with an asphalt overlay to investigate the effect of varying asphalt thickness on the thermal contrast produced by an air filled void. Similarly to the previous cases, a model of the concrete with a variety of asphalt thickness from 40 mm to 120 mm was used to predict thermal contrast under the weather conditions as shown in Fig.4.2. In addition, a model without asphalt overlay was also simulated. The thermal properties of air were used to describe the voided area. The depth of the void was 51 mm and 76 mm from the front surface of the block, and the thickness of the void was 13 mm in the simulations.

4.5.2 Results and discussions

Figure 4.11 shows the time varying thermal contrast as a function of the asphalt thickness. The results showed that the present of asphalt overlay in the model reduced the thermal contrast. The thicker the overlay, the smaller the maximum thermal contrast became.

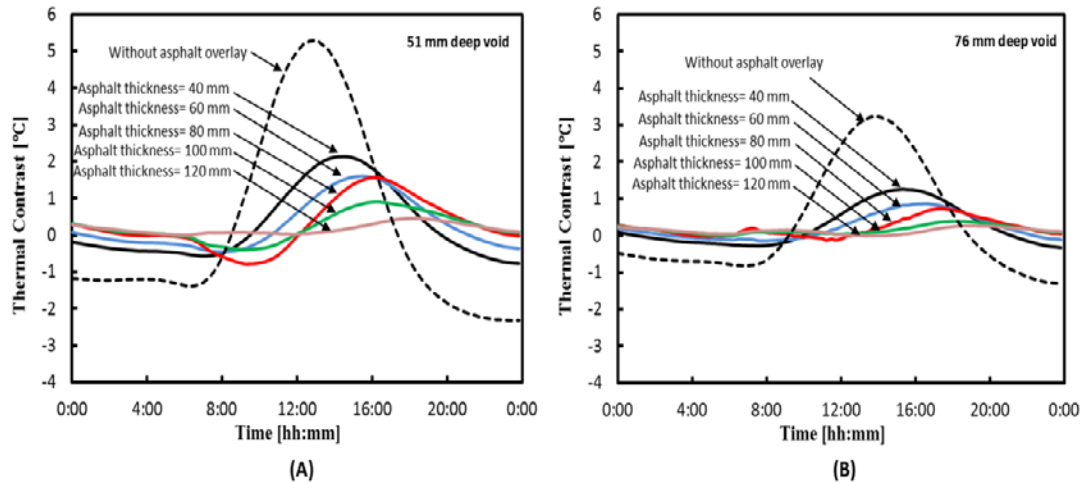


Figure 4.11 The time varying thermal contrast as a function of asphalt thickness: (A) 51 mm deep void (B) 76 mm deep void

The relationship between the maximum thermal contrast and asphalt thickness for 51 mm deep void and 76 mm deep void with 13 mm void thickness is shown in Figure 4.12. The trends of the predictions were same as the first case (i.e. effect of varying void depths) since the overlay was a thermal mass above the void. Thus, the mass reduced the thermal contrast associated with the void. It can also be seen that there was a certain condition of asphalt thickness for which the thermal contrast would be too small (less than 0.5 °C) to be measured. This result shows the limits of applicability of IR thermography to asphalt-overlaid concrete bridge delamination detection.

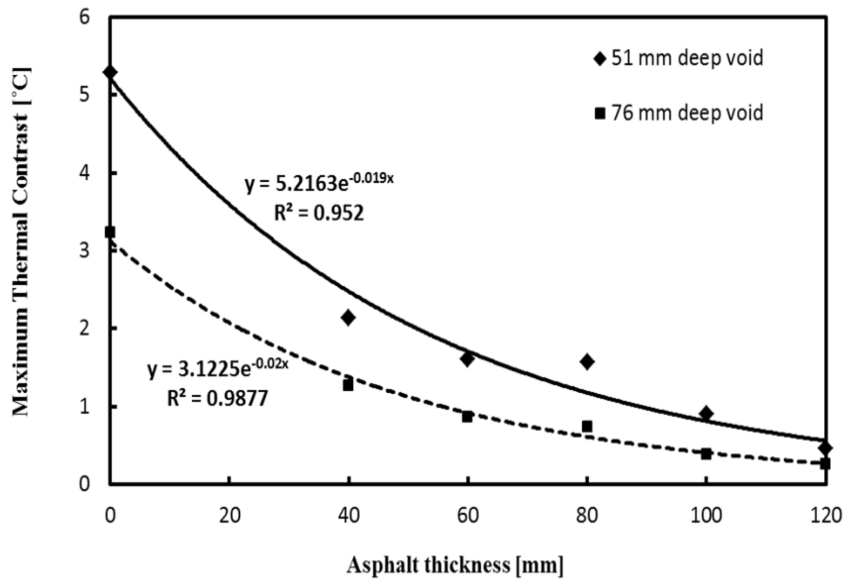


Figure 4.12 Effect of asphalt thickness on the maximum thermal contrast

4.6 Example of the Post-test Model Analysis

An example of the post-test model analysis is shown to evaluate the capability of the model to estimate the maximum thermal contrast, given the known weather patterns surrounding the field test and the anticipated characteristics of void (depth and thickness). The hourly weather data including solar radiation, ambient temperature, and wind speed were obtained from nearby weather station, where the field thermography testing was located. The characteristics of void were obtained from the field coring test. The capability of the model was evaluated by comparing the thermal contrasts predicted by the model and those detected by thermography inspection during the field test.

4.6.1 Description of the field testing

The object test was the College Bridge, which is a pedestrian bridge over College Avenue, Columbia, Missouri. The bridge is roughly 40 years old, constructed in the early 1970s by the Missouri Department of Transportation and Stephens College. An upgraded project to replace the main walkway of the bridge was conducted in the summer 2012. The deck was constructed with ~51 mm (2 in.) concrete overlay, as determined by coring after the field testing.

4.6.1.1 Field testing [43]

The first field test involved collecting thermal images of the surface of the bridge at one-hour intervals, during 6:30 a.m. and 10:30 p.m. on June 8, 2012. These thermal images captured using FLIR T620, which is a hand-held infrared camera. Thermal sensitivity of 0.04°C coupled with a 307,200 pixel display provided extremely accurate thermal images in real time.

Figure 4.13A shows the digital image of the bridge section that was investigated. Figure 4.13B to Figure 4.13F display a subset of time-series thermal images were captured by the infrared camera on the section. These images vary throughout the day during the thermography testing.

Each thermal image shows three spot temperatures (T_1 , T_2 , and $T_{sound\ concrete}$) which were the subject locations of the study. T_1 and T_2 were the surface temperatures at the locations where the cores (color coded “red” and “green”, respectively) were taken. It was assumed a subsurface void existed at these

areas, based on the thermal images. $T_{\text{sound concrete}}$ was the surface temperature of the sound concrete.

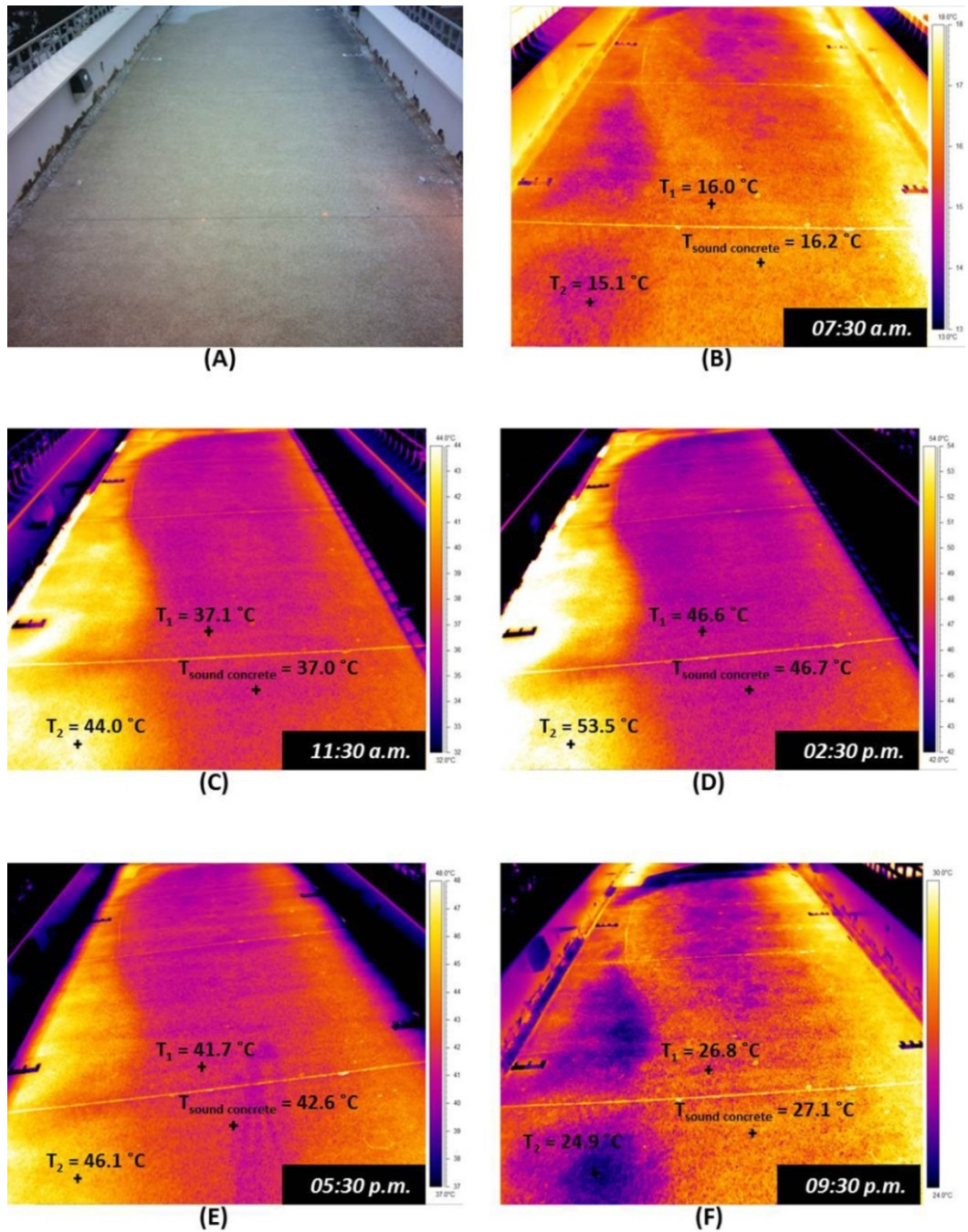


Figure 4.13 The measured thermal contrast detected during the field test [43]

For quantitative analysis, the apparent temperature differences (i.e. thermal contrast) between the voids and the sound concrete were calculated using Eq. 2.2. The results of the time varying thermal contrasts of the case in Fig.4.13 are shown in Figure 4.17 as “field data 1” and “field data 2”. The field data 1 was obtained from $T_1 - T_{\text{sound concrete}}$ and the field data 2 was obtained from $T_2 - T_{\text{sound concrete}}$. The maximum thermal contrasts (ΔT_{max}) for each field data were listed in Table 4.5.

4.6.1.2 The coring test [43]

After evaluation of the thermal contrast, cores were taken at selected locations to confirm the existence of voids and to determine their depth and thickness. Figure 4.14 shows the photography when the coring test was operated.



Figure 4.14 Photograph of the coring operation [43]

Data of the coring test were collected for two locations (color coded as red and green delamination) as shown in Figure 4.15, and the results were given in Table 4.5.

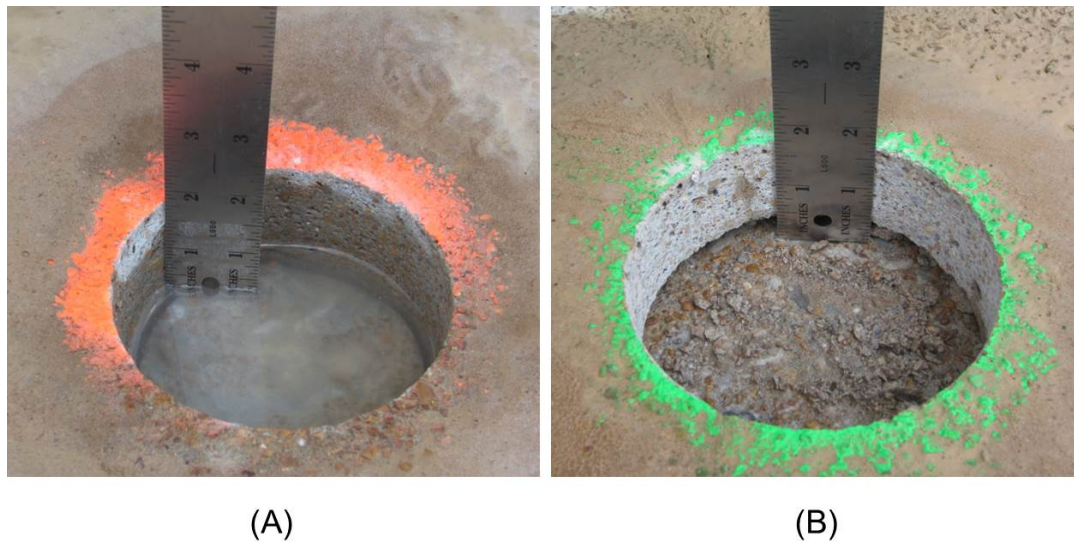


Figure 4.15 Photographs of core locations : (A) Red delamination; and (B) Green delamination [43]

Table 4.5 The field test results including the coring results and the maximum thermal contrast (ΔT_{max}) from thermography images.

Field test (The coring color coded)	Depth of void*	Thickness of void*	Condition*	ΔT_{max} **
Field data#1 (Red)	~51 mm	0	no interface gap	0.5°C
Field data#2 (Green)	~43 mm	~4 mm	air-filled void	7.3°C

* Obtained from coring data

** Obtained from thermography images

4.6.1.3 The weather patterns surrounding the field test

In this example, environmental data for the concrete model were gathered over 3 days from June 6 and June 8, 2012. The hourly data of solar radiation (Figure 4.16A), air temperature of the environment (Figure 4.16B), and wind speed (Figure 4.16C) were obtained from nearby weather station in Sanborn field, Columbia, MO.

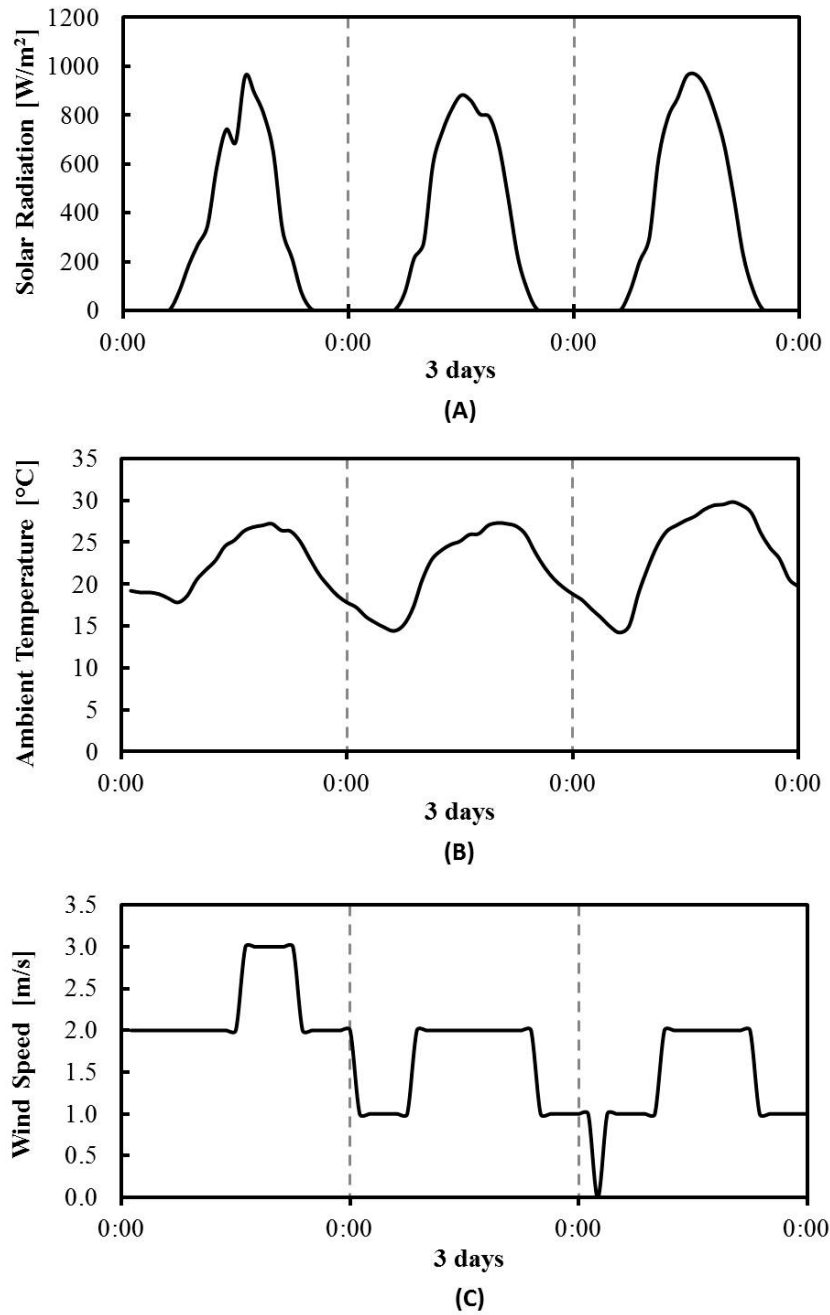


Figure 4.16 Three consecutive days of environmental parameters as a boundary condition in simulation: (A) solar radiation; (B) ambient temperature; and (C) wind speed

4.6.2 The predictive model analyses

An analytic study was carried out to predict the way in which infrared imaging technique responds to the bridge conditions. These predictions provided a basic understanding of the usefulness of the technique.

The thermal response was predicted using a 3-dimensional transient heat transfer model (a similar process as described in section 4.2). The model was simulated using a concrete block as shown in Fig.4.1. The hourly weather data were simulated as boundary conditions in the model. These actual weather data were gathered over 3 consecutive days prior to the field thermography testing (in the analysis, the model results of the final 24 hours were used to verify with the thermography data). The effect of varying void thicknesses on the thermal contrast produced by an air-filled void at a depth of 51 mm was simulated, and the result was shown in Figure 4.17. It can be seen that the model incorporated potential variations of the thermal contrast with the measured thermal contrast detected by the thermography camera during the field test.

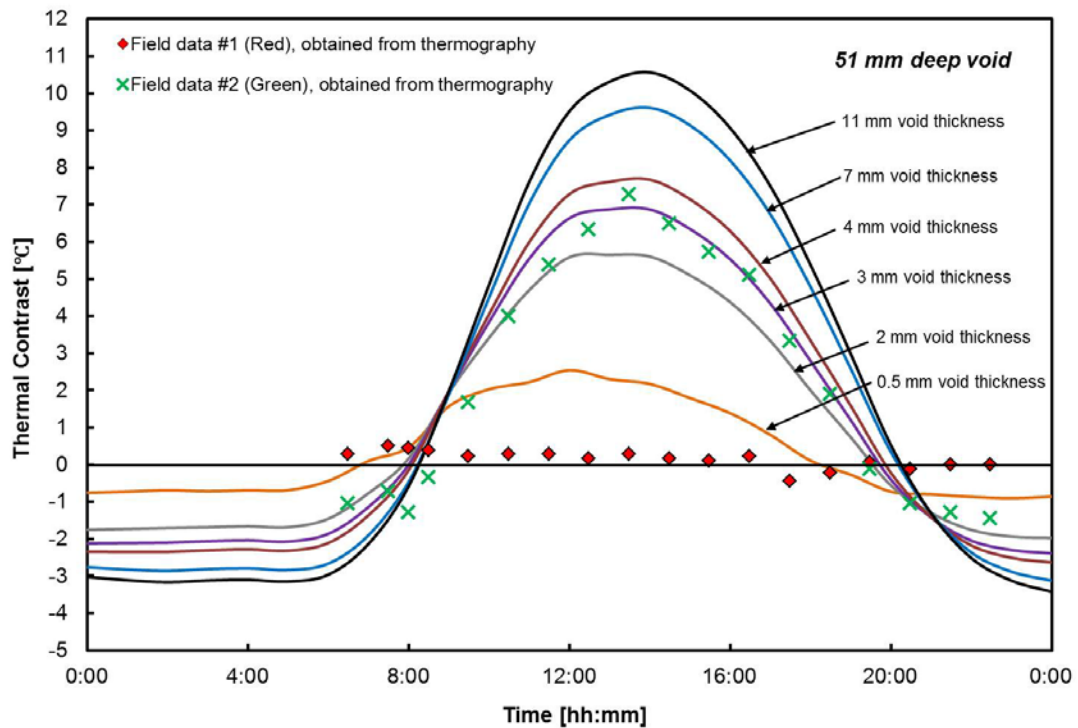


Figure 4.17 Thermal contrast as a function of void thickness for 51 mm deep void

Similar analysis procedures as described in section 4.2 were applied for predicting the maximum thermal contrast in response to the weather conditions in Fig.4.16 for different depths of void and different thicknesses of void.

Figure 4.18 shows the values obtained for constant A and constant K for exponential expressions fitted to the maximum thermal contrast-void depth data in variation of void thickness. The value of constant A and the constant K were obtained as: $A = (6.814 \cdot \ln(z) + 9.285)$ and $K = -0.017$, respectively.

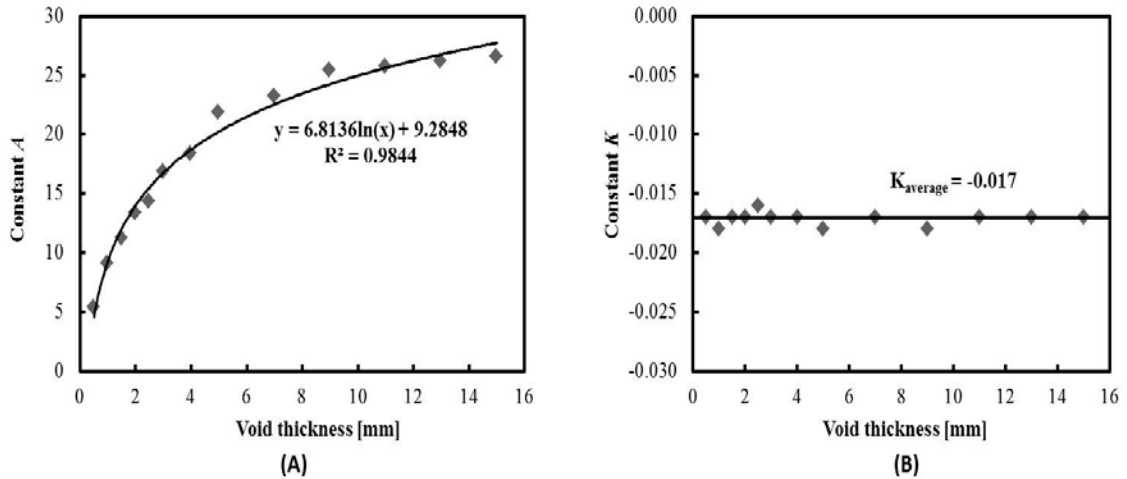


Figure 4.18 Values obtained for constant A and constant K from the model under a particular weather condition shown in Fig.14.

The results indicate the relationship between the maximum thermal contrast (ΔT_{max}), void depth (d) and void thickness (z) could be fit by the function as

$$\Delta T_{max} = (6.814 \cdot \ln(z) + 9.285) \cdot 0.98^d \quad \text{Eq. 4.7}$$

where ΔT_{max} in $^{\circ}\text{C}$ and both d and z are in mm. The term of 0.98 in Eq.4.7 was obtained from $e^K = 2.71878^{-0.017} = 0.98$. This means that the maximum thermal contrast decreased by a constant multiple of 0.98 as the void depth increased over the depth of void range used in the model (25 mm to 127 mm).

4.6.3 The post-test model verification

For the model verification, the maximum thermal contrasts predicted by the Eq.4.7 and those obtained from the field test using infrared themography were compared. The predicted maximum thermal contrasts were computed

using the void thickness and the void depth obtained from the coring test. For a 43 mm void depth and a 4 mm void thickness (the coring with “green” coded), the predicted maximum thermal contrast by Eq. 4.7 was approximately 7.9°C, while the measured maximum thermal contrast detected by the field thermography testing was 7.3°C (Table 4.5). The Eq.4.7 could not estimate the maximum thermal contrast for the coring with “red” coded because it was found no interface gap at the location after the field coring test. The maximum thermal contrast obtained from thermography image (0.5°C) confirmed there was debonding between the overlay and the concrete.

The results of the post-test model analysis shows that the model could predict the maximum thermal contrast of subsurface voids in concrete under a given set of environmental conditions surrounding the test and the anticipated depth and thickness of a delamination.

4.7 Conclusion

This chapter focused on the evaluation of the effect of key parameters expected to influence the detectability of the subsurface voids. These parameters included void depth, void thickness, material contained within the void, material properties of the concrete, and presence of an asphalt overlay. These parameters were examined analytically using the validated numerical model.

The findings from the study of the effect of varying void depths and void thicknesses demonstrated that the maximum thermal contrasts were a function of both the depth of the void and the thickness of the void. The maximum thermal contrast decreased exponentially by a constant multiple of 0.98 as the void depth increased. The maximum thermal contrast increased nonlinearly (as a logarithm function) with increasing thickness of the void. The results also showed that changes in maximum thermal contrast were more pronounced for voids located closer to the surface. The study had led to a simple procedure for estimating the depth of a void as a function of the thickness of the void and the thermal contrast as demonstrated by using Eq.4.4. The investigation of the minimum detectable void demonstrated that the minimum thickness was determined by the depth of the void and the expected maximum thermal contrast as shown in Eq.4.6. In addition, the effect of reinforcing steel (rebar) in the concrete was also evaluated. The result indicated that the presence of the rebar was not significant on thermal behavior of the concrete in this study.

The results from the study of the effect of different materials contained in subsurface void (i.e. delamination) demonstrated that air-filled void produced a significant thermal contrast compared to water-filled void, ice-filled void, and epoxy adhesive-filled void. The differences of the thermal contrast for each material in the void arose from different thermal behavior due to different properties of heat conduction and/or specific heat compared to the thermal properties of the sound concrete.

The findings from the study of the effect of varying material properties of the concrete indicated that variations in the thermal conductivities, volumetric heats, and emissivity of the concrete produced systematic variations in thermal contrast. The maximum thermal contrast increased as the thermal conductivity of the concrete increased. The maximum thermal contrast decreased as the volumetric heat of the concrete increased, as same as the effect of the emissivity of the concrete. However, variations in these properties had a small effect on the thermal contrast. Thus, the success of the thermographic testing will not depend strongly on the specific values of the thermal properties of the concrete.

The results from the study of the effect of asphalt overlays on the concrete indicated that the presence of an asphalt overlay reduced the maximum thermal contrast. The thicker the overlay, the more limited the thermal contrast from a void. The prediction of the relationship between the maximum thermal contrast and asphalt thickness followed the trends described in the first case (i.e. effect of varying void depths) since the overlay was a thermal mass above the void.

Evaluation of the analytical results with the experimental data was done by comparing the maximum thermal contrast (ΔT_{max}). The differences between the maximum thermal contrast of model-predicted and the experimental data for the sunny side were 1.21°C, 0.92°C, 0.40°C and 0.12°C for 25 mm, 51 mm, 76 mm and 127 mm deep voids, respectively. The differences between the maximum thermal contrast of model-predicted and the experimental data for the shaded side were 0.94°C, 0.43°C, 0.42°C and 0.28°C for 25 mm, 51 mm, 76 mm and 127

mm deep voids, respectively. These results indicate that the model predicted the maximum thermal contrasts with reasonable accuracy when compared to the experimental data.

An example of model validation was also presented that compares the predicted model of void characteristics (depth and thickness) with actual void presented by the core testing. The model was developed under a given set of actual weather conditions surrounding the test, and the measured thermal contrast detected using an infrared camera on the same locations as the coring tests were taken. It was found that the model result was sufficiently accurate to predict the void depth and thickness when compared to the coring data.

Based on the results of these studies, it was concluded that the model developed provided valuable information on the expected responses and possible limitations of using thermographic technique to detect subsurface voids in concrete bridge.

In the next chapter, the model proposed will be used to develop a simple multiple linear regression equation to establish a functional relationship between the thermal contrast at various void depths and daily environmental parameters. Such the equation could be used to asses if a particular day's weather would produce the thermal contrast required to be imaged using a common thermal camera given the anticipated depth of a delamination and predicted weather conditions.

5. EQUATION DEVELOPMENT FOR MAXIMUM THERMAL CONTRAST OF SUBSURFACE DAMAGE IN CONCRETE

5.1 Introduction

This chapter describes the development of a practical equation to predict the maximum thermal contrast at various depths of void in concrete based on a dataset composed of various environmental variables. A range of statistical procedures were used to obtain the equation including: statistical outlier removal, descriptive statistics, correlation analysis, variable selection, multi-parameter regression analysis, statistical test, and residual analysis. The procedures are discussed separately for the South (sunny) side and the North (shaded) side. The verification of the proposed equations with finite element simulations and the experimental data was also evaluated.

5.2 Multi-parameter Regression Analysis

In this study, multi-parameter regression analysis was used to develop a functional relationship between the maximum thermal contrast at various depths of void in the concrete and environmental variables based on daily data analysis. The daily maximum thermal contrast, as a “*response variable*”, was extracted

from the maximum hourly running average of thermal contrast at each depth of void obtained in the FEM model. Selected characteristics of the daily environmental conditions data, as a set of “*predictor variables*”, were extracted from the solar loading, ambient temperature, and wind speed dataset obtained in the experimental testing. Specifically, the following characteristics of the daily weather variables were extracted: maximum daily solar loading, total daily solar loading, maximum daily temperature, minimum daily temperature, average daily temperature, average daily wind speed, average quarterly wind speed, and daily precipitation. The best (i.e. the most influential or most valid) subset of the predictor variables and the corresponding best-fitting regression model on the response variable was determined.

Furthermore, the maximum daily thermal contrasts estimated by statistical analyses were compared to those measured from the experimental field. If the chosen model equation provides sufficiently accurate prediction for estimating the maximum thermal contrast in the experimental results, such that the model equation could be used to assess specific daily environmental variables during, or leading up to, a field inspection, to predict the anticipated thermal contrast for a delamination at a given depth. This equation could then be used to predict if a particular day’s weather would produce the thermal contrasts required to be imaged using a common thermography camera given the anticipated depth of a delamination and predicted weather conditions. Alternatively, such that the equation could be used in a post-test analysis of data to estimate the depth of a

delamination, given the known daily weather conditions surrounding the test and the measured thermal contrast detected during the test.

5.3 Equation Development for the Surface Exposed to Direct Solar Loading (the South Side)

A range of statistical analyses were performed on the daily data of environmental variables to develop a model equation for predicting the maximum thermal contrast at various depths of void in the concrete.

5.3.1 Dataset for the equation development

The equation was developed based on the South side dataset over a period of 3 months. During this period, days in which rain occurred were excluded from the dataset because water on the surface of the concrete would affect the emissivity of the concrete and evaporation could affect the thermal behavior of the concrete.

A series of boxplot graphs was used to assess the data distributions for each variable (response variable and predictor variables) and to detect data points that appeared to be irregular (i.e. outlier). A boxplot (also known as a box-whisker graph) is a tool of graphically depicting groups of a dataset [44]. The bottom and the top of the box are the 25th and 75th percentile (the lower and upper quartiles, respectively), and the middle of the box is the 50th percentile (i.e. median). The ends of the whiskers represent the highest data value within the

upper limit and the lower limit. Data values beyond the whiskers consider as outliers. For example, the boxplots as shown in Figure 5.1A and 5.1B represent the distribution of the daily maximum solar loading and the daily average wind speed over 6 a.m. to 6 p.m. period, respectively. The outliers (symbolized by asterisks) beyond the whiskers indicate the data that were excluded for the regression analysis. This way was taken to minimize data errors in analysis.

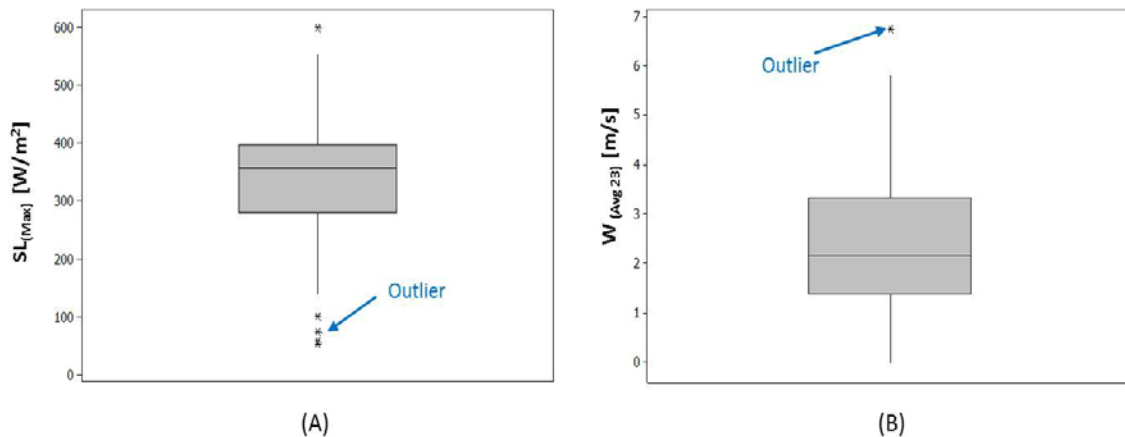


Figure 5.1 Data check for outliers: (A) Daily maximum solar loading and (B) Daily average wind speed over 6 a.m. to 6 p.m. period.

The filtering of the daily weather variables and the daily maximum thermal contrast of the South side dataset from the outlier's data resulted in a total of 205 data points for model equation development. These data were listed in **Appendix D** by date (November 2007 to January 2008), environmental variables (including solar loading, ambient temperature, and wind speed), depth of voids (25 mm, 51 mm, 76 mm, and 127 mm), and the maximum thermal contrasts.

Descriptive statistics of the dataset in Appendix D were listed in Table 5.1. The maximum thermal contrast ranged from 0.55°C to 9.03°C, while the daily total solar loading ranged from approximately 703 W·hr/m² to 2309 W·hr/m². The ranges for daily ambient temperature change and daily average wind speed were 2.3°C to 19.4°C, and 0.51 m/s to 5 m/s, respectively.

Table 5.1 Descriptive statistics of data in the South side datasets

Variable*	N	Mean	Std.Dev.	Minimum	Maximum	Range
SL_(Max)	205	356.81	68.03	176.97	554.94	377.97
SL_(Total)	205	1577.50	411.80	703.90	2309.00	1605.20
SL_(Total)^{1/4}	205	6.26	0.45	5.15	6.93	1.78
SL_(Total)-1	205	1486.40	524.10	252.00	2309.00	2057.00
T_{air (Max)}	205	281.49	7.75	263.87	298.15	34.28
T_{air (Min)}	205	269.63	6.71	255.04	284.87	29.83
T_{air (Change)}	205	11.85	3.70	2.33	19.39	17.06
T_{air (Avg)}	205	275.58	7.03	259.57	291.09	31.52
T_{air (Avg)}-1	205	275.64	6.87	259.57	291.09	31.52
W_(Avg 1)	205	1.56	1.39	0.00	5.43	5.43
W_(Avg 2)	205	2.27	1.38	0.00	5.66	5.66
W_(Avg 3)	205	2.97	1.29	0.56	5.92	5.36
W_(Avg 4)	205	1.88	1.52	0.00	4.86	4.86
W_(Avg 23)	205	2.62	1.23	0.54	5.79	5.25
W_(Avg)	205	2.17	1.09	0.51	5.06	4.56
W_(Max)	205	5.86	1.81	2.55	10.82	8.27
d	205	73.02	37.03	25.00	127.00	102.00
e^{-0.02*depth}	205	0.29	0.19	0.08	0.61	0.53
ΔT_(Max) obtained from FEM	205	3.45	2.11	0.55	9.03	8.48

*Description of each variable is shown in **Appendix D**.

5.3.2 Correlation analysis of all variables

Correlation analysis was performed to find the potential variables to be considered in the model equation. All predictor variables listed in Table 5.1 were considered in the correlation analysis, including depth of the void, solar loading, ambient temperature, and wind speed. Non-linear transformations of some predictor variables were also considered. The results of the correlation analysis were listed in Table 5.2.

Table 5.2 Pearson correlation coefficient (R) matrix for the South side datasets

	$\Delta T_{(Max)}$	d	$e^{-0.02 \cdot depth}$	$SL_{(Max)}$	$SL_{(Total)}$	$SL_{(Total)}^{1/4}$	$T_{air (Change)}$	$T_{air (Avg)}$	$W_{(Avg 1)}$	$W_{(Avg 2)}$	$W_{(Avg 3)}$	$W_{(Avg 4)}$	$W_{(Avg 23)}$	$W_{(Max)}$
$\Delta T_{(Max)}$	1.000	-0.793	0.817	0.159	0.278	0.280	0.250	0.022	-0.106	-0.136	-0.191	-0.129	-0.176	-0.179
d	-0.793	1.000	-0.951	0.047	0.055	0.055	0.056	0.014	-0.051	-0.068	-0.103	-0.051	-0.092	-0.093
$e^{-0.02 \cdot depth}$	0.817	-0.951	1.000	-0.061	-0.071	-0.071	-0.073	-0.018	0.066	0.088	0.134	0.066	0.119	0.121
$SL_{(Max)}$	0.159	0.047	-0.061	1.000	0.595	0.614	0.402	0.101	0.034	0.058	-0.127	-0.162	-0.034	-0.134
$SL_{(Total)}$	0.278	0.055	-0.071	0.595	1.000	0.992	0.580	-0.040	-0.101	-0.010	-0.248	-0.353	-0.135	-0.231
$SL_{(Total)}^{1/4}$	0.280	0.055	-0.071	0.614	0.992	1.000	0.590	-0.050	-0.069	0.028	-0.223	-0.332	-0.101	-0.213
$T_{air (Change)}$	0.250	0.056	-0.073	0.402	0.580	0.590	1.000	0.311	-0.153	0.096	0.040	0.130	0.075	0.012
$T_{air (Avg)}$	0.022	0.014	-0.018	0.101	-0.040	-0.050	0.311	1.000	0.061	0.158	0.189	0.076	0.187	0.303
$W_{(Avg 1)}$	-0.106	-0.051	0.066	0.034	-0.101	-0.069	-0.153	0.061	1.000	0.778	0.415	0.038	0.653	0.627
$W_{(Avg 2)}$	-0.136	-0.068	0.088	0.058	-0.010	0.028	0.096	0.158	0.778	1.000	0.705	0.331	0.929	0.798
$W_{(Avg 3)}$	-0.191	-0.103	0.134	-0.127	-0.248	-0.223	0.040	0.189	0.415	0.705	1.000	0.667	0.917	0.885
$W_{(Avg 4)}$	-0.129	-0.051	0.066	-0.162	-0.353	-0.332	0.130	0.076	0.038	0.331	0.667	1.000	0.534	0.472
$W_{(Avg 23)}$	-0.176	-0.092	0.119	-0.034	-0.135	-0.101	0.075	0.187	0.653	0.929	0.917	0.534	1.000	0.910
$W_{(Max)}$	-0.179	-0.093	0.121	-0.134	-0.231	-0.213	0.012	0.303	0.627	0.798	0.885	0.472	0.910	1.000

Table 5.2 shows that $e^{-0.02 \cdot d}$ had a significant correlation with ΔT_{max} (R=0.817). The correlation between ΔT_{max} and $SL_{(Total)}^{1/4}$ was 0.280, that was slightly better correlated than $SL_{(Max)}$ (R=0.159). $T_{air (Change)}$ was not strong

correlated with ΔT_{max} ($R=0.250$). The correlation between ΔT_{max} and $T_{air(Avg)}$ was almost nonexistent ($R=0.022$). $W_{(Avg\ 2)}$ and $W_{(Avg\ 3)}$ were slightly better correlated ($R=-0.136$ and $R=-0.191$, respectively) among the average wind speed based on a 6 hour average. From the correlation analysis, it appeared that $e^{-0.02*d}$, $SL_{(Total)}^{1/4}$, $T_{air(Change)}$, and $W_{(Avg\ 23)}$ could be key factors in the model. In addition, several interaction terms between environmental variables appeared a moderate correlation. For example, the correlation between $SL_{(Total)}^{1/4}$ and $T_{air(Change)}$ was 0.590. $T_{air(Average)}$ and $W_{(Max)}$ was moderate correlated ($R=0.303$).

5.3.3 Variable selection for the equation development

There are three strategies for selecting variables, known as: forward selection method, backward elimination method and best subsets regression method. A forward selection method is focused on deciding whether a single variable should be added to a model. A backward elimination method is focused on deciding whether a single variable should be deleted from a model. A best subsets regression method is an efficient way to identify model that achieve the goal with as few predictors as possible [45]. In this study, a best subsets regression method was used in order to select predictor variables for the model equation.

The method identifies the subset models that produce the highest R^2 values from a full set of the predictor variables that were specified. R^2 is the square of the sample multiple correlation coefficient. This quality naturally varies between 0 and 1. The larger the value of R^2 means the stronger the linear

relationship between the maximum thermal contrast and the predictor variables. The method may also estimate the regression coefficients and predict future responses with smaller variance (i.e. **SSE**) than the full model using all predictors [46]. In this study, Minitab statistical computer program [44] was used as a tool to examine all possible subsets of the predictors, beginning with the model containing one predictor, and then the model containing two predictors, and so on.

All the predictors that were obtained to be significant during the correlation analysis were considered in the best subsets regression procedure, including $e^{-0.02 \cdot d}$, $SL_{(Total)}^{1/4}$, $T_{air(Change)}$, and $W_{(Avg\ 23)}$. Interaction term between $SL_{(Total)}^{1/4}$ and $T_{air(Change)}$ and interaction term between $SL_{(Total)}^{1/4}$ and $T_{air(Change)}$ were also taken into account in best subset formulation for the model as shown in Table 5.3.

As said before, the best model was selected based on two criterions including their goodness of fit (i.e. coefficient of determination, R^2) and their variability (i.e. standard error of estimate, **SSE**). The result of the statistical procedure was presented in Table 5.3. It can be seen that of 6 possible terms in the model, only the 4 variables (highlighted row) demonstrated to be significant in the model equation form. The contribution of interaction terms was remarkably low (0.003) that means the interaction terms did not significantly improve the model's fit. Thus, both of the interaction terms were dropped from the model.

Table 5.3 Best subsets regression method on the maximum thermal contrast for the South side datasets

Total of predictor variables	Criterion		Predictor variables					
	R ²	SEE	e ^{-0.02 x depth}	SL _(Total) ^{1/4}	T _{air (Change)}	W _(Avg 23)	SL _(Total) ^{1/4} x T _{air (Change)}	T _{air (Avg)} x W _(Max)
1	66.5	1.22	X					
1	7.4	2.03		X				
2	77.9	0.99	X	X				
2	77.8	1.00	X				X	
3	86.0	0.79	X			X	X	
3	85.2	0.81	X		X	X		
4	87.2	0.76	X	X	X	X		
4	87.0	0.76	X	X		X	X	
5	87.5	0.75	X	X	X	X	X	
5	87.2	0.76	X	X	X	X		X
6	87.5	0.75	X	X	X	X	X	X

5.3.4 The final equation for the South side

The model equation form was developed based on a multiple linear regression analysis. The general form of the model shows in Equation 5.1 [45].

$$\Delta T_{max} = a + \sum C_i * T_i \quad \text{Eq. 5.1}$$

where ΔT_{max} is the maximum thermal contrast in °C, a is intercept of the model (constant), C_i is a regression coefficient of the i th term, and T_i is i th term.

Figure 5.2 displays Minitab output from the multiple linear regression analysis using all the terms that were obtained in the correlation analysis and variable selection. The value of a and C_i in Eq. 5.1 could be obtained from the column labeled “Coef.” (for coefficient) in the Figure. Therefore, the best model for the maximum thermal contrast (ΔT_{max}) in °C was found to be

$$\Delta T_{\max} = -5.11 + 10.03 e^{-0.02 \times d} + 0.85 \sqrt[4]{SL_{(\text{total})}} + 0.13 T_{\text{air}(\text{Change})} - 0.48 W_{(\text{Avg}23)} \quad \text{Eq. 5.2}$$

where $e=2.7183$, d is the depth of void in mm, $SL_{(\text{Total})}$ is the daily total solar radiation intensity which was calculated by integrating the solar radiation intensity during a day in $W \cdot \text{hr}/\text{m}^2$, $T_{\text{air}(\text{Change})}$ is the daily air temperature change which was obtained by subtracting the daily maximum air temperature and the daily minimum air temperature in K, and $W_{(\text{Avg} 23)}$ is the average wind speed calculated during 12 hours (from 6:00 am to 6:00 pm) in m/s.

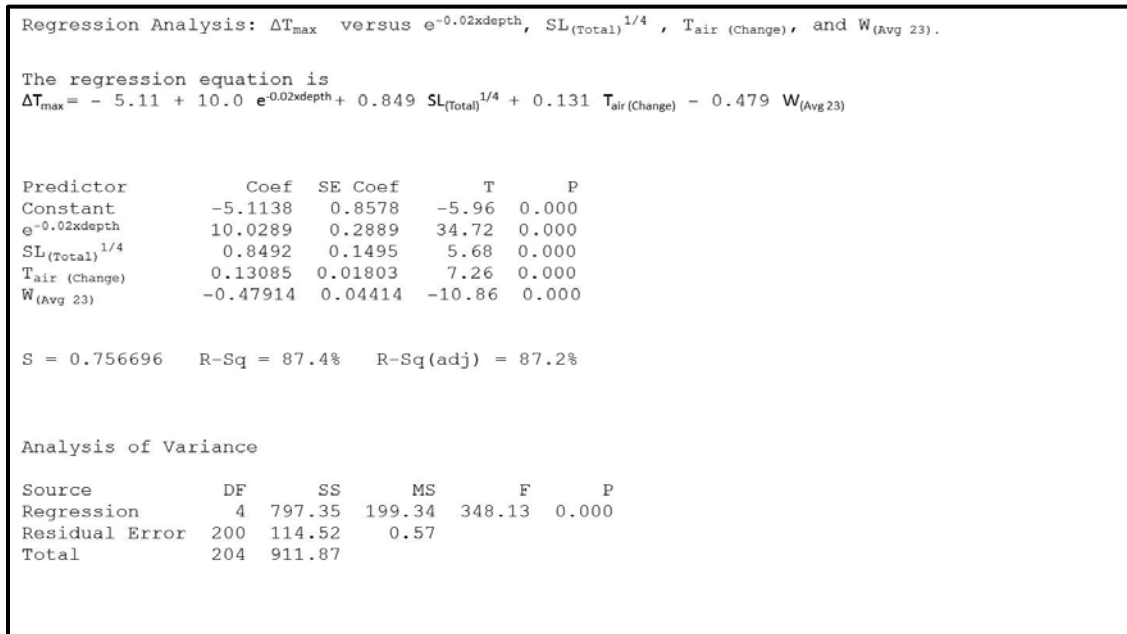


Figure 5.2 Minitab output for multiple regression analysis of ΔT_{\max} versus $e^{-0.02 \times \text{depth}}$, $SL_{(\text{Total})}^{1/4}$, $T_{\text{air}(\text{Max})}$, $T_{\text{air}(\text{Avg})-1}$, $W_{(\text{Avg} 23)}$

In addition, the columns of **T** and **P** in Fig. 5.2 contain the results of a statistical test that evaluates the significance of each regression coefficient. The test results show that the intercept (constant) and all the predictor coefficients were significant (p-level is less than 0.05). The results show also that the model was particularly strong ($R^2_{adj} = 87.2\%$). The standard error of estimate (**SEE**) was 0.76°C.

5.3.5 Residual analysis for the South side

The residuals (actual maximum thermal contrast minus predicted maximum thermal contrast) of the model equation were plotted against the main environmental variables. The results were shown in Figure 5.3A through 5.3C. It can be seen that the residuals seem to be randomly distributed with no obvious trend. The residuals of the model ranged from -2.76°C to 2.33°C, with a standard error of 0.76°C. In addition, Figure 5.3D presents the result of frequency distribution for the residuals. It can be noticed that the distribution of residuals was concentrated in the range -0.75°C to 0.5°C.

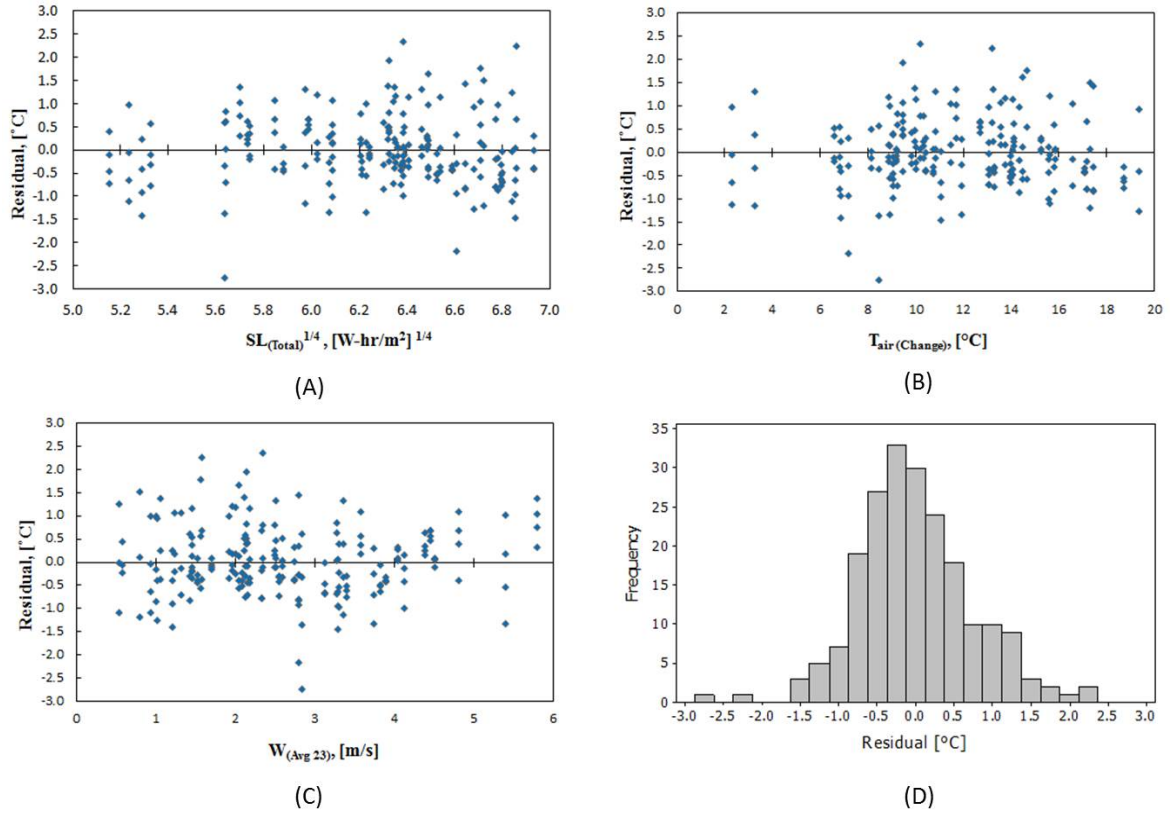


Figure 5.3 Residual of the maximum thermal contrast vs. environmental variables: (A) Solar loading; (B) Ambient temperature change; (C) Wind speed; and (D) Residual histogram for the maximum thermal contrast

5.3.6 Equation verification

5.3.6.1 Comparison of the equation results with the numerical model results

The equation developed from statistical method was compared to those obtained from the finite element method (FEM) model to demonstrate the difference between the models. Figure 5.4 shows the predicted maximum thermal contrast based on Eq.5.2 versus actual maximum thermal contrast obtained from the FEM for the South side dataset. As Fig.5.4 shows, the

maximum thermal contrast determined by the equation (dash line) has reasonable agreement ($R^2 = 0.874$) with the FEM model. The estimated maximum contrasts by the equation may be as much as 0.5°C higher and as much as 0.75°C lower than the FEM model (equality line). Therefore, it can be deduced that the equation predicts the maximum thermal contrast with reasonable accuracy with those obtained from the FEM results.

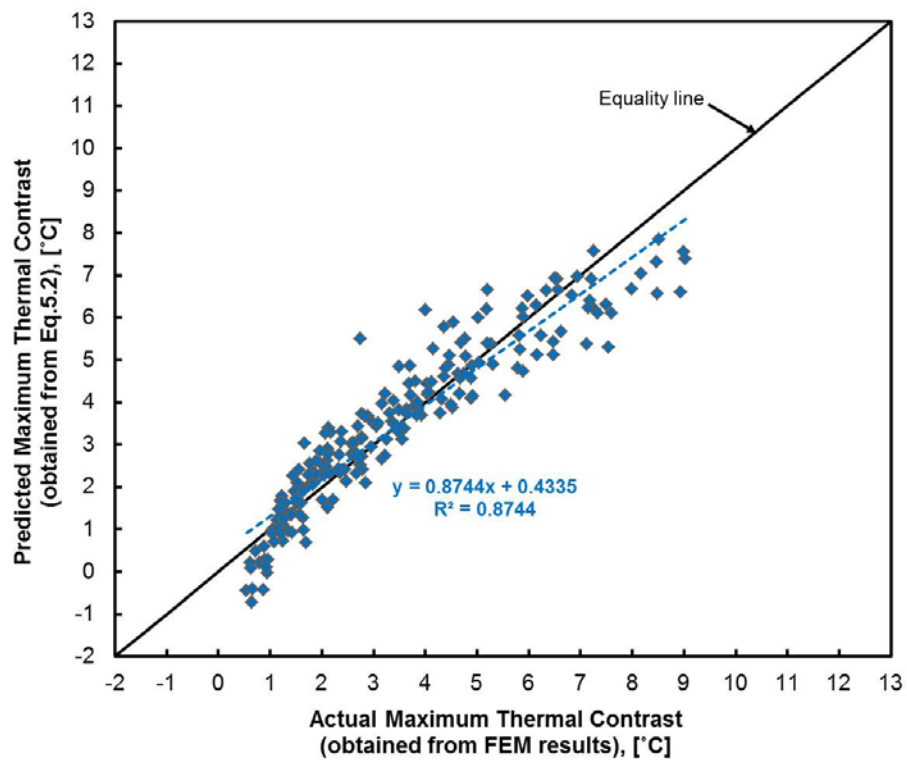


Figure 5.4 Predicted versus actual maximum thermal contrast obtained from the FEM results (based on the South side dataset)

5.3.6.2 Comparison of the equation results with the experimental results

The maximum thermal contrast obtained by the equation developed under the study was compared to the previous experimental testing to assess the reliability of the chosen model. The pair-matching data for the daily maximum thermal contrast were compared and shown in Figure 5.5. As Fig.5.5 shows, the maximum thermal contrast determined by the model equation (dash line) has reasonable agreement ($R^2=0.759$) with the experimental data. The estimated maximum contrasts by the equation may be slightly better when ΔT_{max} measured from the experimental in the range 1.5°C to 7.0°C. For this range, the differences of maximum contrast from both the model and the experimental result were within 1°C. These results indicate that the model chosen was reasonable for the data in the study.

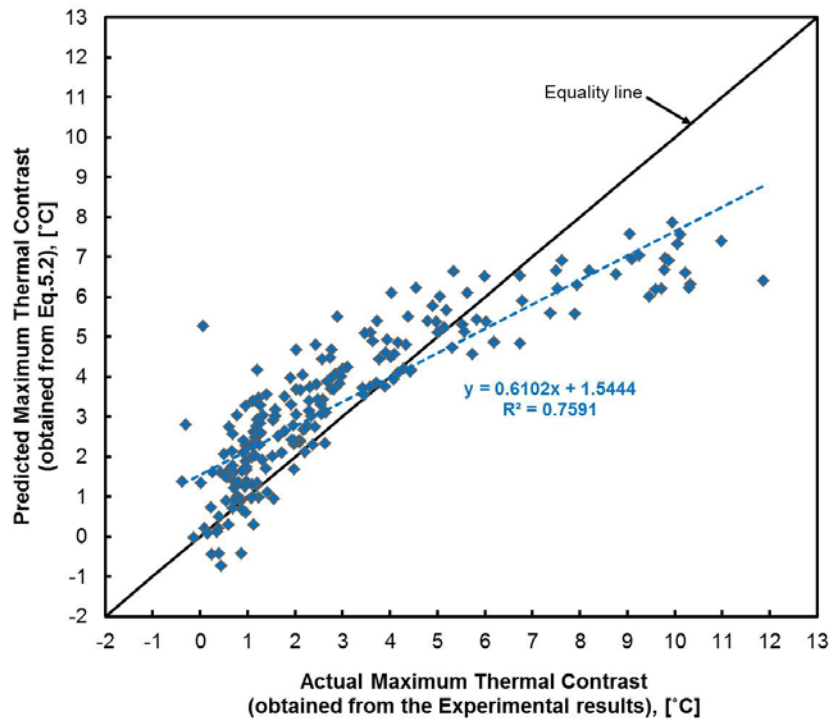
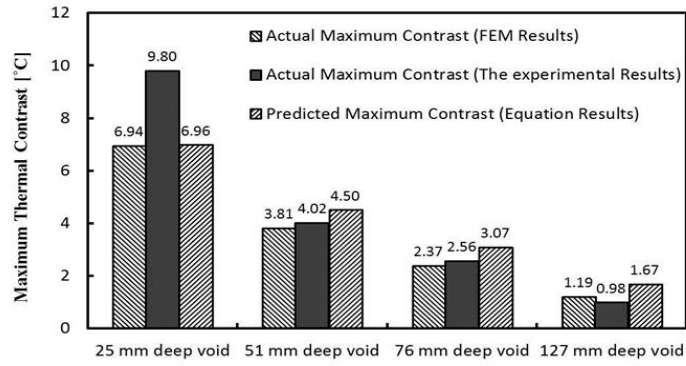


Figure 5.5 Predicted versus actual maximum thermal contrast obtained from the experimental results (based on the South side dataset)

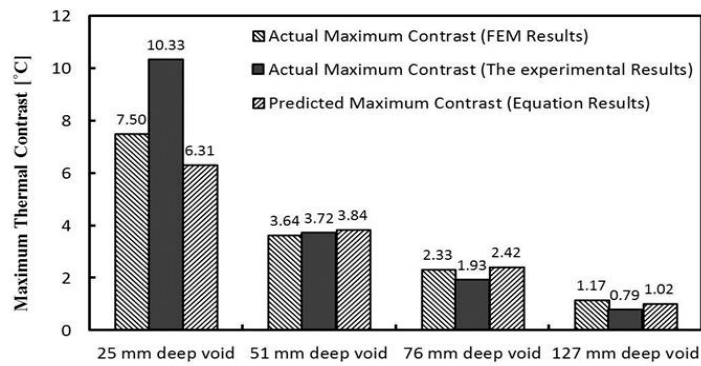
5.3.6.3 Case examples (the South side)

The model equation was tested for values within the range of the South side dataset to evaluate the application of the model compared to those obtained from the FEM and the experimental results. A day from each month was randomly taken from the dataset, and the comparisons among those results were presented in Figure 5.6. The results indicated that the maximum thermal contrast for 25 mm deep void would be difficult to characterize accurately using the equation. However, the equation was sufficiently accurate to estimate the maximum thermal contrast for 51, 76, and 127 mm deep voids.



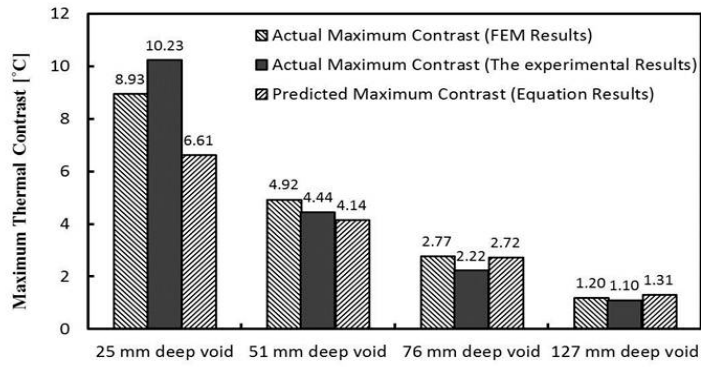
November 5, 2007

(A)



December 30, 2007

(B)



January 12, 2008

(C)

Figure 5.6 The comparison among the maximum thermal contrast of the equation, the FEM model, and the experimental testing

5.4 Equation Development for the Shaded Surface (the North Side)

As with the South side model equation development, a range of statistical analysis were performed on the data in the North side dataset to develop a model for estimating the anticipated level of maximum thermal contrast for subsurface delaminations based on actual environmental conditions surrounding the concrete and the anticipated depth of a delamination.

5.4.1 Dataset for the equation development

The daily North side dataset was thoroughly checked for outliers. The data that were found visually to be excessively large or small values were removed from the dataset. The boxplot graph was used to check the presence of outliers. For example, the boxplots as shown in Figure 5.7A and 5.7B represent the distribution of the daily maximum air temperature and the daily average wind speed over 6 a.m. to 12 p.m. period, respectively. The outliers (symbolized by asterisks) at the upper and lower end part of the box indicate the data that were eliminated for the regression analysis.

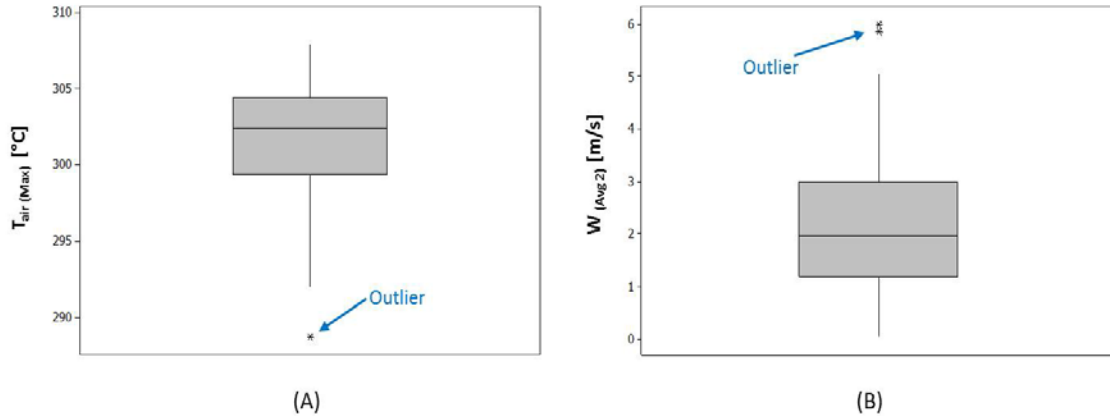


Figure 5.7 Data check for outliers: (A) Daily maximum air temperature, and (B) Daily average wind speed over 6 a.m. to 12 p.m.

Filtering the North side dataset from the outliers resulted in 199 data points for model equation development. These data were listed in **Appendix E** by date (May 2008 to July 2008), daily ambient temperature, daily wind speed, depth of void, and maximum thermal contrast.

Descriptive statistics of the dataset in Appendix E were listed in Table 5.4. The maximum thermal contrast ranged from 0.09°C to 2.87°C. The ranges for daily ambient temperature change and daily average wind speed were 7.22°C to 19.28°C, and 0.38 m/s to 4.76 m/s, respectively.

Table 5.4 Descriptive statistics of data in the North side datasets

Variable*	N	Mean	Std.Dev.	Minimum	Maximum	Range
T_{air} (Max)	199	301.96	3.49	294.04	307.87	13.83
T_{air} (Min)	199	289.85	4.63	277.15	297.93	20.78
T_{air} (Min*)	199	290.03	4.48	277.15	297.93	20.78
T_{air} (Change)	199	12.10	2.81	7.22	19.28	12.06
T_{air} (Change*)	199	11.93	2.98	6.39	19.28	12.89
T_{air} (Avg)	199	295.73	3.65	287.85	302.58	14.73
T_{air} (Avg)-1	199	294.63	3.79	285.18	302.58	17.40
W_(Avg 1)	199	0.99	1.22	0.00	4.00	4.00
W_(Avg 2)	199	2.11	1.21	0.06	5.05	4.99
W_(Avg 3)	199	2.90	1.34	0.94	6.50	5.56
W_(Avg 4)	199	1.40	1.29	0.10	5.04	4.94
W_(Avg 12)	199	1.55	1.16	0.03	4.39	4.35
W_(Avg)	199	1.85	1.12	0.38	4.76	4.37
W_(Max)	199	5.51	2.12	2.55	11.36	8.81
d	199	74.34	36.74	25.00	127.00	102.00
e^{-0.02*depth}	199	0.29	0.18	0.08	0.61	0.53
ΔT_(Max) obtained from FEM	199	0.98	0.67	0.09	2.87	2.78

*Description of each variable is shown in **Appendix E**.

5.4.2 Correlation analysis of all variables

A correlation matrix as shown in Table 5.5 was created based on the dataset. It can be seen that $e^{-0.02*d}$ had a significant correlation with ΔT_{max} (R=0.893). The correlation between ΔT_{max} and $T_{air(Change*)}$ was 0.229, that was slightly stronger correlated than $T_{air(Change)}$ (R=0.216). $W_{(Max)}$ and $W_{(Avg1)}$ were

slightly better correlated ($R=-0.136$ and $R=-0.124$, respectively) among the wind speed categories. From the correlation analysis, it showed that $e^{-0.02*d}$, $T_{air(Change*)}$, $W_{(Max)}$ and $W_{(Avg1)}$ could be key factors in the model.

Table 5.5 Pearson correlation coefficient (R) matrix for the North side datasets

	$\Delta T_{(Max)}$	d	$e^{-0.02*depth}$	$T_{air (Max)}$	$T_{air (Min)}$	$T_{air (Min*)}$	$T_{air (Change)}$	$T_{air (Change*)}$	$T_{air (Avg)}$	$T_{air (Avg)-1}$	$W_{(Avg 1)}$	$W_{(Avg 2)}$	$W_{(Avg 3)}$	$W_{(Avg 4)}$	$W_{(Avg 12)}$	$W_{(Avg)}$	$W_{(Max)}$
$\Delta T_{(Max)}$	1.000	-0.858	0.893	0.017	-0.118	-0.139	0.216	0.229	-0.057	-0.053	-0.124	-0.104	-0.122	-0.124	-0.120	-0.134	-0.136
d	-0.858	1.000	-0.951	0.013	-0.034	-0.042	0.073	0.078	-0.014	-0.055	0.014	0.023	0.025	0.023	0.019	0.024	0.040
$e^{-0.02*depth}$	0.893	-0.951	1.000	-0.017	0.045	0.055	-0.095	-0.102	0.019	0.069	-0.015	-0.026	-0.030	-0.027	-0.021	-0.028	-0.047
$T_{air (Max)}$	0.017	0.013	-0.017	1.000	0.795	0.747	-0.068	0.048	0.931	0.776	-0.183	-0.135	-0.015	-0.120	-0.166	-0.125	-0.088
$T_{air (Min)}$	-0.118	-0.034	0.045	0.795	1.000	0.982	-0.659	-0.546	0.933	0.827	0.116	0.053	0.148	0.089	0.089	0.116	0.069
$T_{air (Min*)}$	-0.139	-0.042	0.055	0.747	0.982	1.000	-0.690	-0.629	0.907	0.838	0.132	0.064	0.144	0.066	0.103	0.115	0.079
$T_{air (Change)}$	0.216	0.073	-0.095	-0.068	-0.659	-0.690	1.000	0.957	-0.380	-0.398	-0.418	-0.254	-0.261	-0.295	-0.352	-0.345	-0.222
$T_{air (Change*)}$	0.229	0.078	-0.102	0.048	-0.546	-0.629	0.957	1.000	-0.273	-0.351	-0.412	-0.254	-0.234	-0.240	-0.349	-0.319	-0.221
$T_{air (Avg)}$	-0.057	-0.014	0.019	0.931	0.933	0.907	-0.380	-0.273	1.000	0.840	-0.011	0.000	0.131	0.022	-0.005	0.043	0.006
$T_{air (Avg)-1}$	-0.053	-0.055	0.069	0.776	0.827	0.838	-0.398	-0.351	0.840	1.000	-0.142	-0.228	-0.053	-0.227	-0.194	-0.181	-0.153
$W_{(Avg 1)}$	-0.124	0.014	-0.015	-0.183	0.116	0.132	-0.418	-0.412	-0.011	-0.142	1.000	0.825	0.593	0.651	0.956	0.859	0.630
$W_{(Avg 2)}$	-0.104	0.023	-0.026	-0.135	0.053	0.064	-0.254	-0.254	0.000	-0.228	0.825	1.000	0.748	0.682	0.955	0.914	0.810
$W_{(Avg 3)}$	-0.122	0.025	-0.030	-0.015	0.148	0.144	-0.261	-0.234	0.131	-0.053	0.593	0.748	1.000	0.793	0.701	0.889	0.861
$W_{(Avg 4)}$	-0.124	0.023	-0.027	-0.120	0.089	0.066	-0.295	-0.240	0.022	-0.227	0.651	0.682	0.793	1.000	0.698	0.885	0.727
$W_{(Avg 12)}$	-0.120	0.019	-0.021	-0.166	0.089	0.103	-0.352	-0.349	-0.005	-0.194	0.956	0.955	0.701	0.698	1.000	0.927	0.753
$W_{(Avg)}$	-0.134	0.024	-0.028	-0.125	0.116	0.115	-0.345	-0.319	0.043	-0.181	0.859	0.914	0.889	0.885	0.927	1.000	0.856
$W_{(Max)}$	-0.136	0.040	-0.047	-0.088	0.069	0.079	-0.222	-0.221	0.006	-0.153	0.630	0.810	0.861	0.727	0.753	0.856	1.000

5.4.3 Variable selection for the equation development

In order to select predictor variables for the shaded side model equation, a best subsets regression method was used. All the predictors that were obtained to be significant during the correlation analysis were considered in the best subsets regression procedure, including $e^{-0.02*d}$, $T_{air(Change*)}$, $W_{(Max)}$ and $W_{(Avg 1)}$. The result of the procedure was presented in Table 5.6. It can be seen that of 4 initial terms in the model, only the 2 terms (highlighted row) shown to be significant in the model equation form. The terms of $e^{-0.02*d}$ and $T_{air(Change*)}$ were

selected for the model equation based on the R^2 values and **SSE** values. The contribution of the wind speed terms was insignificant in the model's fit. Thus, the terms of $W_{(Max)}$ and $W_{(Avg\ 1)}$ were not included in the model.

Table 5.6 Best subsets regression method on the maximum thermal contrast for the North side datasets

Total of predictor variables	Criterion		Predictor variables			
	R^2	SEE	$e^{-0.02 \times \text{depth}}$	$T_{\text{air (Change*)}}$	$W_{(Max)}$	$W_{(Avg\ 1)}$
1	79.8	0.2994	X			
1	5.3	0.6490		X		
2	90.2	0.2094	X	X		
2	80.9	0.2908	X			X
3	90.1	0.2093	X	X		X
3	90.1	0.2094	X	X	X	
4	90.3	0.2075	X	X	X	X

5.4.1 The final equation for the North side

Similar to those developed for the South side model, the model equation form for the North side was developed based on a multiple linear regression analysis. The model took the general form of Eq. 5.1 and their regression coefficients (labeled Coef.) are shown in Figure 5.8.

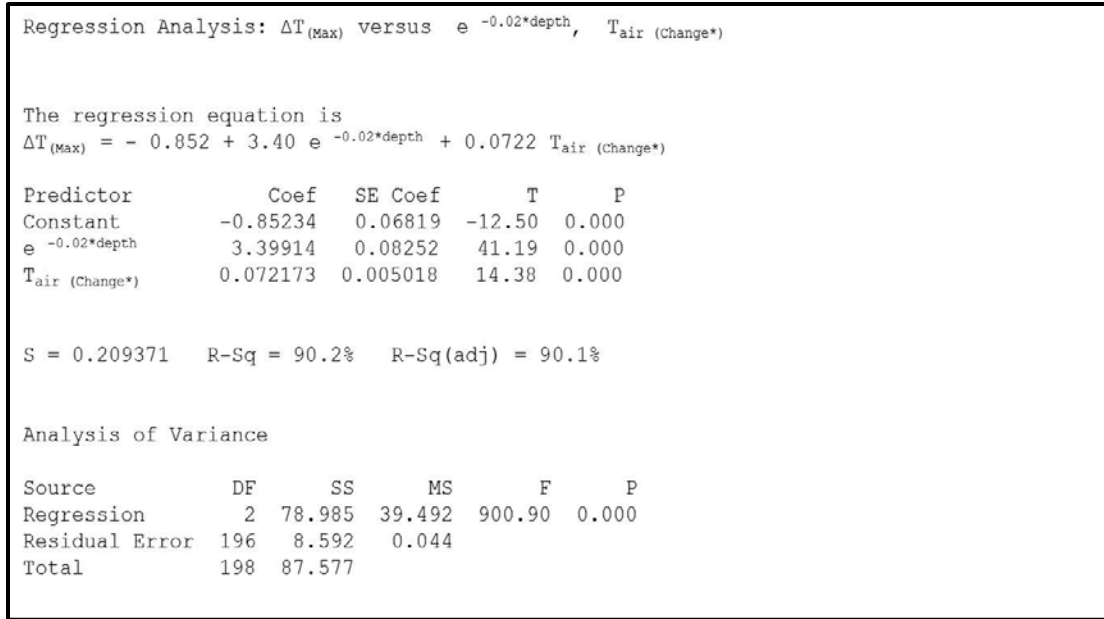


Figure 5.8 Minitab output for multiple regression analysis of ΔT_{\max} versus $e^{-0.02 \times \text{depth}}$, $T_{\text{air}}(\text{Change}^*)$

The best practical model for the maximum thermal contrast based on the Shaded side dataset was found to be

$$\Delta T_{\max} = -0.85 + 3.40 e^{-0.02 \times d} + 0.07 T_{\text{air}}(\text{Change}^*) \quad \text{Eq. 5.3}$$

where $e=2.7183$, d is the depth of void in mm, and $T_{\text{air}}(\text{Change}^*)$ is the daily air temperature change which was obtained by subtracting the daily maximum air temperature and the daily minimum air temperature in K. In this case, the minimum air temperature was taken during night time in the preceding day. In addition, the columns of T and P in Fig. 5.8 contain the results of a statistical test that evaluates the significance of each regression coefficient. The test results indicate that at a significance level of 95 percent, all the intercept and the coefficients were significant (p -level is less than 0.05). The goodness of fit

statistics indicates that the model was very strong ($R^2_{adj} = 90.1\%$). The standard error of estimate (**SEE**) was 0.21 °C.

5.4.2 Residual analysis for the North side

Figure 5.9A shows the residual analysis of the daily maximum thermal contrast versus the daily ambient temperature change. The residual appeared to be randomly distributed with $T_{air(Change^*)}$ and ranged between -0.52°C to 0.65°C. Figure 5.9B presents the residual histogram for the maximum thermal contrast in the Shaded side model. It can be seen that the distribution of residuals is concentrated in the range -0.2°C to 0.2°C.

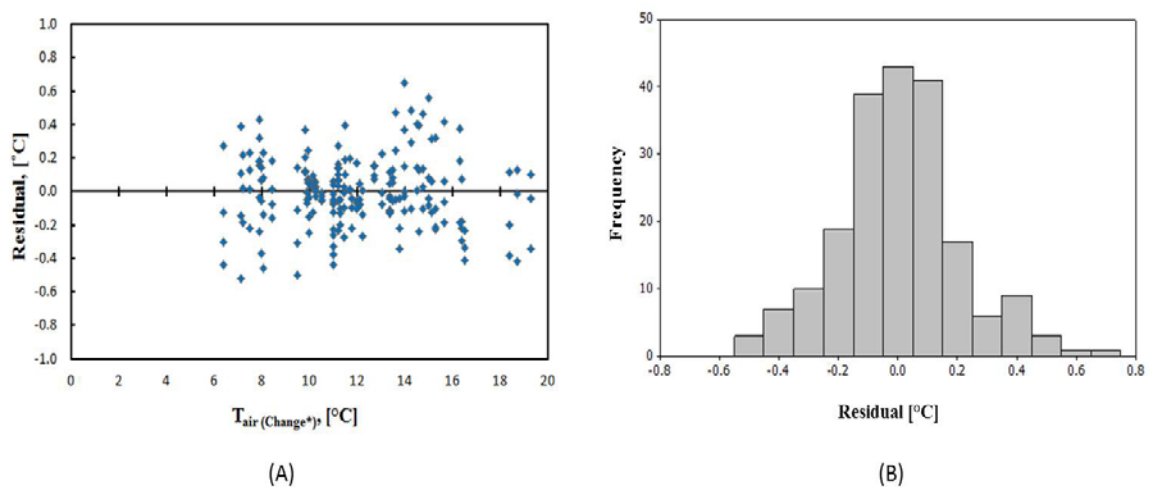


Figure 5.9 (A) Residual of the maximum thermal contrast vs. Ambient temperature change; and (B) Residual histogram for the maximum thermal contrast

5.4.3 Equation verification

5.4.3.1 Comparison of the equation results with the numerical model results

The model equation developed from statistical method was compared to those obtained from the finite element model to demonstrate the difference between the models. Figure 5.10 shows the predicted maximum thermal contrast based on Eq. 5.3 versus actual maximum thermal contrast obtained from the FEM for the Shaded dataset under this study. As Figure 5.10 shows, the maximum thermal contrast determined by the model equation (dash line) has a strong agreement ($R^2 = 0.902$) with the FEM model. The estimated maximum contrasts by the equation may be as much as 0.1°C higher and as much as 0.3°C lower than the FEM model (equality line). Therefore, it can be deduced that the model equation predicts the maximum thermal contrast with reasonable accuracy with those obtained from the finite element results.

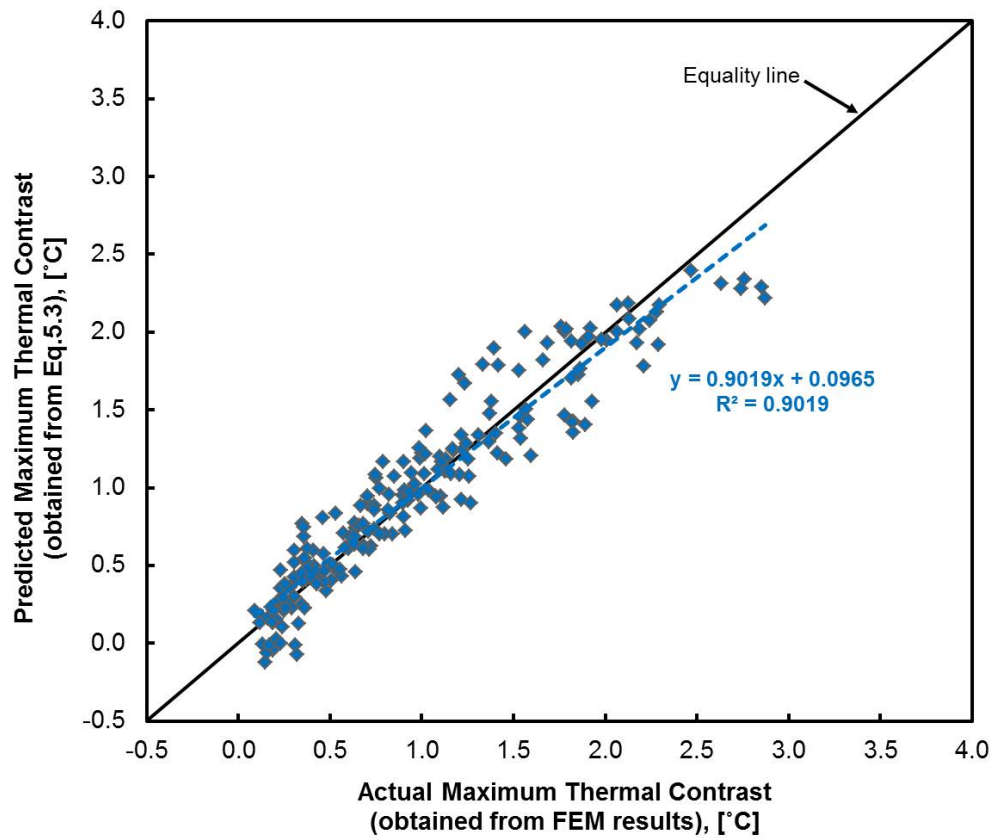


Figure 5.10 Predicted versus actual maximum thermal contrast obtained from the FEM results (based on the North side dataset)

5.4.3.2 Comparison of the equation results with the experimental results

The maximum thermal contrast obtained by the previous experimental testing was compared to those obtained from the model equation developed under this study to assess the reliability of the chosen model. The pair-matching data for the daily maximum thermal contrast were compared and shown in Figure 5.11. As Figure 5.11 shows, the maximum thermal contrast determined by the model equation has reasonable agreement ($R^2 = 0.777$) with the experimental data. The estimated maximum contrasts by the equation were different within

1°C with those obtained in the experimental data. These results indicate that the model chosen was reasonable for the data in the study.

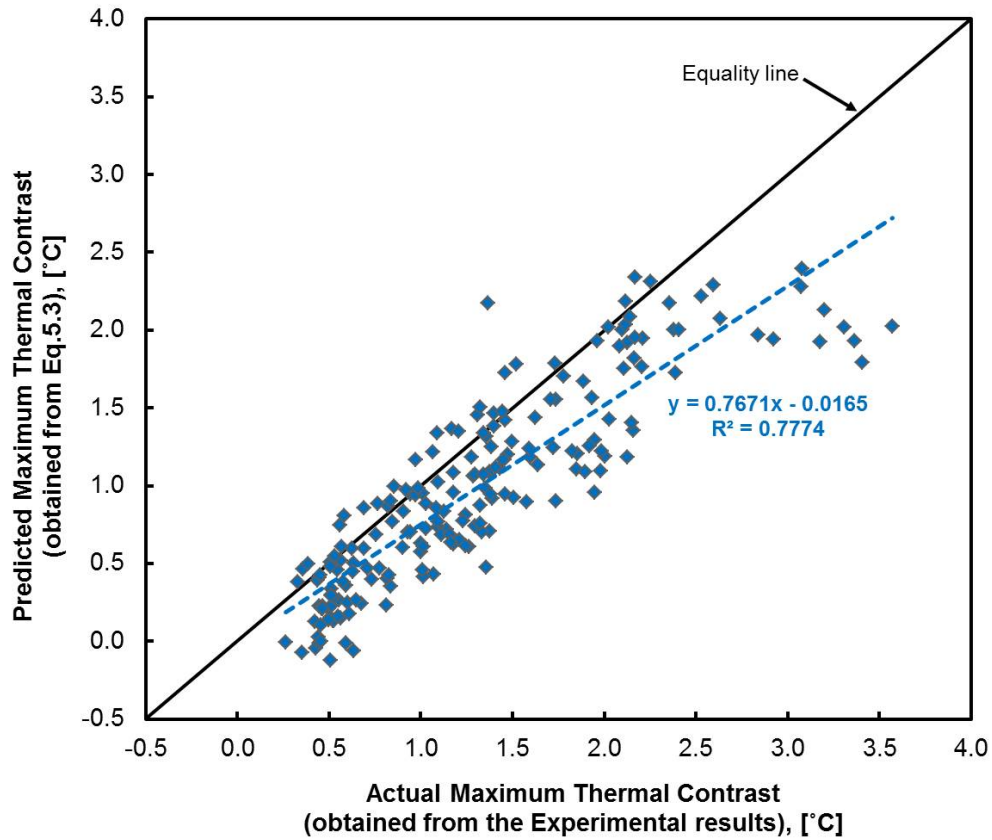


Figure 5.11 Predicted versus actual maximum thermal contrast obtained from the Experimental results (based on the North side dataset)

5.4.3.3 Case examples

The equation was checked for values within the range of the Shade side dataset to evaluate the application of the model equation compared to those obtained from the FEM and the experimental results. A day from each month was randomly taken from dataset, and the comparisons among those results

were presented in Figure 5.12. It can be seen that the model proved to produce reasonable results.

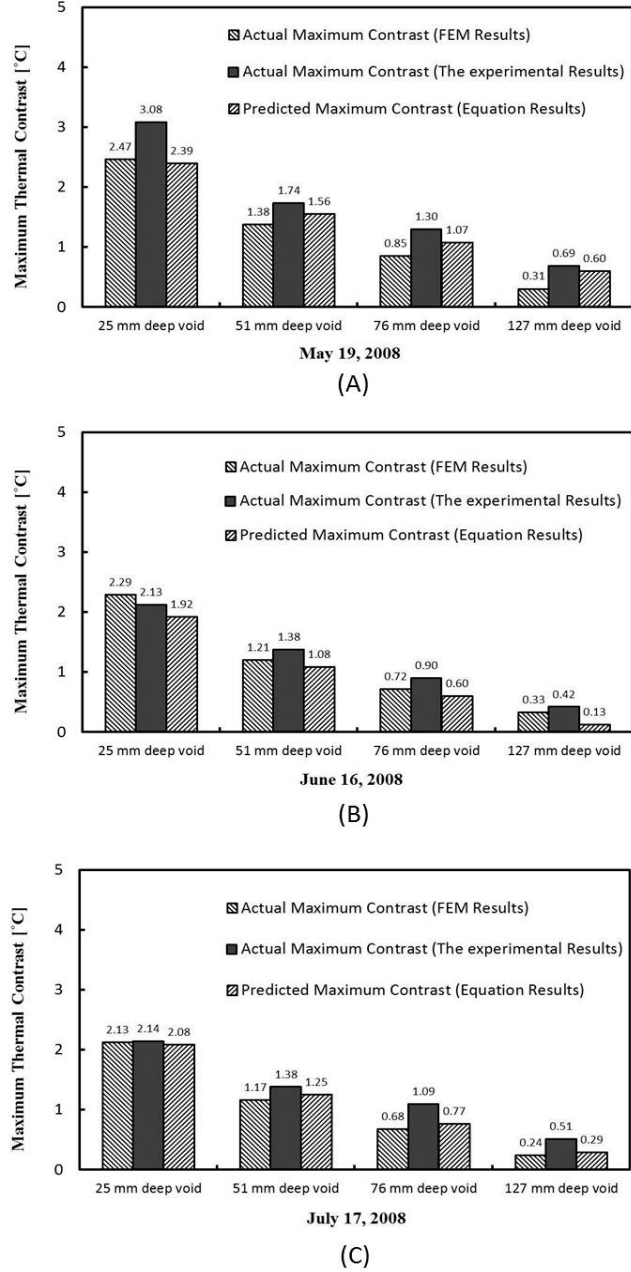


Figure 5.12 The comparison among the maximum thermal contrast of the model equation, the FEM model, and the experimental testing

5.5 Conclusion

This chapter presented the results of statistical analyses for prediction of the maximum thermal contrast at various depths of void in concrete under a given set of environmental conditions. The 10 minutes data of solar loading, ambient temperature and wind speed obtained from the experiment were characterized into a daily dataset. The maximum hourly running average of thermal contrast at 25, 51, 76 and 127 mm deep voids obtained from the finite element method was related with the daily environmental data for both cases of the South side and the North side. The correlation analysis, the best subset regression method, and the multiple regression analysis were used to formulate an equation for quantifying the relationship between environmental variables and thermal contrast in variations of void depths.

The findings from the study of the statistical analyses demonstrated that **Eq.5.2** and **Eq.5.3** were the best recommended models to predict maximum thermal contrasts for the South side and the North side, respectively. For the South side model, it was found that including the terms of $e^{-0.02*d}$, $SL_{(Total)}^{1/4}$, $T_{air(Change)}$, and $W_{(Avg\ 23)}$ significantly improved the accuracy of the prediction. The model equation (**Eq. 5.2**) had an R^2 value of 0.874 and a standard error of estimate of 0.76°C. The equation shows also a good agreement with the experimental results ($R^2=0.759$). For estimation of maximum thermal contrasts on the North side, the model including the terms of $e^{-0.02*d}$ and $T_{air(Change^*)}$ as the predictors showed a high R^2 (0.902) and a low standard error of estimate

(0.21°C). The model equation (**Eq.5.3**) shows also a strong agreement with the experimental results ($R^2=0.777$). In addition, the residual analysis was completed to evaluate the magnitude of variations between the model equation and the FEM model results. For the South side, the distribution of residuals was more concentrated in the range -0.75°C to 0.5°C. For the North side, the distribution of residuals was more concentrated in the range -0.2°C to 0.2°C.

Based on the results of these studies, it was concluded that the proposed model equations predicted the maximum thermal contrasts with reasonable accuracy when compared to the FEM results and the experimental results for both the South and the North conditions. The model equation would be a useful tool to predict the thermal contrast obtainable at various depths of void in concrete from specific daily environmental variables. On the other hand, the model would inform to inspectors about the conditions required in the field for effective thermography technique at a range of void depths.

6. SUMMARY

6.1 Major Results

This section summarizes the major results of the numerical model development and model evaluation, the parametric studies, and the equation development in the research.

6.1.1 Numerical Model Development and Model Evaluation

A 3D, nonlinear, numerical model of transient heat transfer was developed using finite element analysis to study the environmental effects on the thermal response of simulated subsurface voids (i.e. delaminations) in a large concrete block, for the purpose of providing an analytical tool to support thermographic inspection of concrete bridge components. The effects of solar radiation, ambient temperature variation, and wind speed on the thermal images that appear on the South (sunny) and North (shaded) side of a concrete block model with subsurface voids over a 6 month period were assessed. The surface temperature variations were examined in terms of thermal contrast to perform quantitative analysis of the model results. The model performance was

evaluated by comparing the thermal contrast of the model results with those obtained from the experimental testing.

In summary, the following major results were made based on the model evaluation:

- The model provided an overall pattern of temperature contrasts that was similar to the pattern of experimental results, showing the model was successful in capturing the basic physical behavior of the concrete block.
- The thermal contrasts obtained from the model had good linear correlations with the experimental testing.
 - For the South side, the correlation coefficients between model and experimental results were 0.93, 0.92, 0.89, and 0.68 for 25 mm, 51 mm, 76 mm and 127 mm deep void, respectively.
 - For the North side, the correlation coefficients were 0.78, 0.70, 0.70, and 0.49 for 25 mm, 51 mm, 76 mm and 127 mm deep void, respectively.
- Time-series error analysis of thermal contrast differences between the model and the experimental results showed that the model predicted the thermal contrasts with reasonable accuracy, but it was least accurate for the shallowest void (i.e. 25 mm deep void).
 - *MBE*, *MAE* and *RMSE* values were below 1°C for both the South and the North side, except for 25 mm deep void.

- For the South side, the distribution of thermal contrast differences between model and experimental results was concentrated in the range 0°C to 1°C for 51 mm, 76 mm, and 127 mm deep void.
- For the North side, the distribution of thermal contrast differences was within 0.5°C for 51 mm, 76 mm, and 127 mm deep void.

Based on these results, it was concluded that the model developed in this study was sufficiently accurate to provide a useful tool for estimating the thermal contrasts resulting from subsurface voids in the concrete, and provide a tool to support practical thermal inspection.

6.1.2 Parametric Studies

The effect of other field test parameters expected to influence the detectability of the subsurface voids was examined analytically using the validated numerical model. These parameters included: void depth, void thickness, material contained within the void, material properties of the concrete, and presence of an asphalt overlay. The effect of these parameters on the thermal response (i.e. the maximum thermal contrast) was assessed under a specific set of environmental conditions.

In summary, the following major results were made based on these parametric studies:

- Increasing depth of void reduced the thermal contrast, and increasing thickness of void raised the thermal contrast.
 - The maximum thermal contrast decreased exponentially by a constant multiple of 0.98 as the void depth increased
 - The maximum thermal contrast increased nonlinearly (as a logarithm function) with increasing thickness of the void.
 - Changes in maximum thermal contrast were more pronounced for voids located closer to the surface.
- Air-filled void produced a significant thermal contrast compared to water-filled void, ice-filled void, and epoxy adhesive-filled void.
 - The thermal conductivity, k , of the material in void dominated the thermal contrast behavior.
- Variations in the thermal conductivities, volumetric heats, and emissivity of the concrete did not significantly affect thermal contrast.
 - The maximum thermal contrast increased as the thermal conductivity of the concrete increased.
 - The maximum thermal contrast decreased as the volumetric heat of the concrete increased, as same as the effect of the emissivity of the concrete.
- The presence of an asphalt overlay reduced the maximum thermal contrast. The thicker the overlay, the more limited the thermal contrast from a void.

The results of these parametric studies provided valuable information on the expected thermal responses and possible limitations of using thermographic technique to detect subsurface voids in concrete bridges.

A Post-test model was provided that illustrated the application for the model to reveal thermal contrast from thermography measurements. The model was developed using the known weather patterns surrounding the field test and the characteristics of void (depth and thickness) obtained from the coring test. The results showed that the thermal contrasts obtained from the model agreed with those detected by the field thermography measurements. The approach showed promise as a method to support practical thermographic inspection, for the purpose of improving condition assessments of the existing concrete bridges.

6.1.3 Equation Development for Maximum Thermal Contrast of Subsurface Damage in Concrete

A practical equation to predict the thermal contrast at various depths of void in concrete under various environmental variables was developed using statistical analyses. Data of the “response variable” (i.e. the maximum thermal contrasts) obtained from the FEM model and the “predictor variables” (i.e. the environmental conditions) obtained from the experimental testing were used in the equation development for both the South and the North side. Correlation analysis was used to find the potential “predictor variables” to be considered on the equation development. The best subset regression method was used to

determine the most influential “predictor variables” for the equation based on the value of the coefficient of determination (R^2), and the standard error of estimation (**SSE**). Multi-parameter regression analysis was used to formulate the equation for quantifying the relationship between “predictor variables” and “response variable”. The residual analysis was completed to evaluate the magnitude of variations between the maximum thermal contrast of the proposed equation and the FEM model results.

In summary, the following major results were made based on the equation development:

- The best recommended equation to predict maximum thermal contrasts for the South side was shown in **Eq.5.2**.
 - Including the terms of $e^{-0.02*d}$, $SL_{(Total)}^{1/4}$, $T_{air(Change)}$, and $W_{(Avg\ 23)}$ as the predictor variables in the equation significantly improved the accuracy of the maximum thermal contrast prediction.
 - The equation showed a high R^2 (0.874) and a low **SSE** (0.76°C).
 - The distribution of residuals was concentrated in the range -0.75°C to 0.5°C.
- The best recommended equation to predict maximum thermal contrasts for the North side was shown in **Eq.5.3**.
 - Including the terms of $e^{-0.02*d}$ and $T_{air(Change^*)}$ as the predictor variables in the equation significantly improved the accuracy of the maximum thermal contrast prediction.

- The equation showed a high R^2 (0.902) and a low SSE (0.21°C).
- The distribution of residuals was more concentrated in the range - 0.2°C to 0.2°C.

The proposed equations (**Eq.5.2** and **Eq.5.3**) were evaluated by comparing the maximum thermal contrast obtained from the equations with those obtained from the experimental testing. The result showed that:

- For the South side, the thermal contrasts obtained from Eq.5.2 had a strong agreement with the experimental testing ($R^2=0.759$).
- For the North side, the thermal contrasts obtained from Eq.5.3 had a strong agreement with the experimental testing ($R^2=0.777$).

Based on these results, these proposed equations predicted the maximum thermal contrasts with reasonable accuracy when compared to the FEM model and to the experimental testing results for both the South and the North side.

These practical equations could be used as a rapid tool to assess if a particular day's weather would produce the thermal contrast required to be imaged using a common IR thermography camera given the anticipated depth of a delamination and predicted weather conditions. The equations would also inform inspectors about the conditions required in the field for effective thermography technique at a range of void depths.

6.2 Recommendations

Overall, the research results described an effective approach for the improvement of inspection procedures for concrete bridge components using IR thermography. However, the following tasks should be considered in the future to improve the research:

1. Implementation of wind direction and relative humidity effects in the input parameters for the model. The simulation results would be more accurate and the boundary conditions would be closer to reality.
2. Development of nomographs (or charts) as a practical tool for field inspectors. These graphs would be useful for presenting the response variable (i.e. the maximum thermal contrast) as a function of the predictor variables (i.e. solar loading, ambient temperature variation, wind speed, and void depth).

BIBLIOGRAPHY

1. Bertolini, L., Elsener, B., Pedferri, P., and Polder, R., *Corrosion of Steel in Concrete*. 1 ed. 2004: Wiley-VCH. 392.
2. Maser, K.R. and Roddis, W.M.K., *Principles of Thermography and Radar for Bridge Deck Assessment*. Journal of Transportation Engineering, 1990. **116**(5): p. 583-601.
3. Russell, H.G., *NCHRP Synthesis 333: Concrete Bridge Deck Performance*, 2004, Transportation Research Board: Washington, D.C. p. 188.
4. Ghorbanpoor, A. and Benish, N., *Non-Destructive Testing of Wisconsin Highway Bridges*, 2003, Wisconsin Department of Transportation.
5. ACI, *222R-01 : Protection of Metals in Concrete against Corrosion.*, 2001, American Concrete Institute.
6. Roddis, W.M.K., *Concrete Bridge Deck Assessment using Thermography and Radar*, in *Civil Engineering*1987, Massachusetts Institute of Technology.
7. Moore, M.E., Phares, B.M., Graybeal, B.A., Rolander, D.D., and Washer, G.A., *Reliability of Visual Inspection of Highway Bridges*, FHWA, Editor 2001, USDOT: Washington, DC.
8. Yehia, S., Abudayyeh, O., Nabulsi, S., and Abdelqader, I., *Detection of Common Defects in Concrete Bridge Decks using Nondestructive Evaluation Techniques*. Journal of Bridge Engineering, 2007. **12**(2): p. 215-225.
9. Olson, L.D., Tinkey, Y., and Miller, P. *Concrete Bridge Condition Assessment with Impact Echo Scanning*. 2011. Hunan, China: ASCE.

10. Maierhofer, C., *Nondestructive Evaluation of Concrete Infrastructure with Ground Penetrating Radar*. Journal of Materials in Civil Engineering, 2003. **15**(3): p. 287-297.
11. Parrillo, R., Haggan, A., and Roberts, R., *Bridge Deck Condition Assessment using Ground Penetrating Radar*, in *9th European NDT Conference (ECNDT)2006*: Berlin, GR.
12. Washer, G., *Advances in the Use of Thermographic Imaging for the Condition Assessment of Bridges*. Bridge Structures - Assessment, Design & Construction, 2012. **8**(2): p. 81-90.
13. Manning, D.G., *Detecting Defects and Deterioration in Highway Structures*, in *Tech. Report NCHRP Synthesis 118*1985, National Cooperative Highway Research Program (NCHRP), Transportation Research Board, National Research Council, Washington, D.C.
14. Joyce, R., *Rapid Non-destructive Delamination Detection*, in *Technical Report FHWA/RD-84/076*1985, Federal Highway Administration Report.
15. Washer, G., Fenwick, R., and Bolleni, N., *Development of Hand-held Thermographic Inspection Technologies*. MoDOT: Missouri Department of Transportation, Jefferson City, MO, 2009: p. 124.
16. Washer, G., Fenwick, R., and Bolleni, N., *Effects of Solar Loading on Infrared Imaging of Subsurface Features in Concrete*. Journal of Bridge Engineering 2010. **July/August 2010**: p. 384-390.
17. Washer, G., Fenwick, R., Bolleni, N., and Harper, J., *Effects of Environmental Variables on Infrared Imaging of Subsurface Features of Concrete Bridges*. Transportation Research Record: Journal of the Transportation Research Board, 2009. **2108**: p. 107-114.
18. Bolleni, N., *Environmental Effects on Subsurface Defect Detection in Concrete Structures using Infrared Thermography*, in *Civil Engineering*2009, University of Missouri-Columbia: Columbia, MO. p. 120.

19. Fenwick, R., *Environmental Effects on Subsurface Defect Detection Without Solar Load*, in *Civil Engineering* 2010, University of Missouri-Columbia: Columbia, MO. p. 161.
20. Liu, Y., *Modeling the Time-to-Corrosion Cracking of the Cover Concrete in Chloride Contaminated Reinforced Concrete Structures*, 1996, Virginia Polytechnic Institute and State University.
21. *KNBC News : Concrete Shakes Loose from Oklahoma Bridges*. 2009. <http://www.newson6.com/global/story.asp?s=9886259>.
22. *The Boston Channel : Concrete Chunks Fall from Bridge, Crash onto Sidewalk*. 2013. <http://www.wcvb.com/news/local/metro/Concrete-chunks-fall-from-bridge-crash-onto-sidewalk/-/11971628/18328418/-/x7go6rz/-/index.html?absolute=true>.
23. Boyd, A.J., Birgisson, B., Ferraro, C., and Cumming, S., *Nondestructive Testing for Advanced Monitoring and Evaluation of Damage in Concrete Materials*, 2005.
24. ASTM, *D4580-03 : Standard Practice for Measuring Delaminations in Concrete Bridge Decks by Sounding*, 2012, American Society for Testing and Materials.
25. Scott, M., Rezaizadeh, A., Delahaza, A., Santos, C., Moore, M., Graybeal, B., and Washer, G., *A Comparison of Nondestructive Evaluation Methods for Bridge Deck Assessment*. NDT & E International, 2003. **36**(4): p. 245-255.
26. ACI, *228.2R-98 : Nondestructive Test Methods for Evaluation of Concrete in Structures*, 1998, American Concrete Institute.
27. ASTM, *C 1383 : Standard Test Method for Measuring the P-Wave Speed and the Thickness of Concrete Plates using the Impact-Echo Method.*, 2006, American Society for Testing and Materials.
28. Carino, N.J. *The Impact-echo Method: an Overview*. in *Proceedings of the 2001 Structures Congress & Exposition*. 2001.

29. Rhazi, J., *NDT in Civil Engineering: the Case of Concrete Bridge Decks*. CSNDT JOURNAL, 2000. **21**(5): p. 18-25.
30. ASTM, *D6087-08 : Test Method for Evaluating Asphalt-covered Concrete Bridge Decks using Ground Penetrating Radar*, 2008, American Society for Testing and Materials.
31. ACI, *122R-02 : Guide to Thermal Properties of Concrete and Masonry Systems*, 2002, American Concrete Institute.
32. Clemena, G.G. and McKeel Jr, W.T., *The Applicability of Infrared Thermography in the Detection of Delamination in Bridge Decks* 1977, Virginia Highway and Transportation Research Council: Virginia.
33. FLIR, *User's Manual ThermaCAM™ Researcher Professional edition. Version 2.8 SR-3*. 2006.
34. Kaplan, H., *Practical Applications of Infrared Thermal Sensing and Imaging Equipment*. Vol. 75. 2007: Society of Photo Optical.
35. Branco, F.A. and Mendes, P.A., *Thermal Actions for Concrete Bridge Design*. Journal of Structural Engineering, 1993. **119**: p. 2313.
36. Lienhard, J.H., *A Heat Transfer Textbook*. 2011, Mineola, N.Y.: Dover Publications.
37. Manning, D.G. and Holt, F.B., *Detecting Delaminations in Concrete Bridge Decks*. Concrete International, 1980. **2**: p. 34-41.
38. Manning, D.G. and Holt, F.B., *The Development of Deck Assessment by Radar and Thermography*. Transportation Research Record, 1985. **1083**: p. 13-20.
39. ASTM, *D4788-03 : Standard Test Method for Detecting Delaminations in Bridge Decks using Infrared Thermography*, 2007, American Society for Testing and Materials.

40. Kipp, J.S. and Kunz, J.T., *Thermographic Investigation of a Bridge Deck*. Public Works, 1983. **114**(9): p. 70-73.
41. Allport, J.J. and McHugh, S.L., *Quantitative Evaluation of Transient Video Thermography*. Review of Progress in Quantitative Nondestructive Evaluation, 1988. **7A**: p. 253-262.
42. MatWeb *Material Property Data*. 2013. <http://www.matweb.com/>.
43. Nelson, S.E., *Field Testing Hand-Held Thermographic Inspection Technologies Phase II*, in *Civil Engineering 2013*, University of Missouri-Columbia: Columbia, MO.
44. Ryan, B.F., Joiner, B.L., and Cryer, J.D., *Minitab Handbook : updated for Release 14*. 2005, Belmont, California; Mexico: Brooks/Cole.
45. Kleinbaum, D.G., *Applied Regression Analysis and other Multivariable Methods*. 2008, Australia; Belmont, CA: Brooks/Cole.
46. Carver, R.H., *Doing Data Analysis with Minitab 14*. 2004, London: Brooks/Cole, Thomson Learning.

APPENDIX A
Comsol-Multiphysics Files

Summary

This appendix focuses on the description of simulation on environmental conditions effect of a concrete block containing subsurface voids at different depths using [Comsol-Multiphysics](#).

The actual weather data on **November 2007**, including direct solar loading, ambient temperature variation, and wind speed, were used as model inputs in simulation.

Contents

1. Model 1 (mod1)
 - 1.1. Definitions
 - 1.2. Geometry
 - 1.3. Materials
 - 1.4. Heat transfer (ht)
 - 1.5. Mesh
2. Study
 - 2.1. Time dependent
 - 2.2. Solver configurations
3. Result
 - 3.1. Data Sets
 - 3.2. Derived values
 - 3.3. Plot group

1 Model 1 (mod1)

1.1 Definitions

1.1.1 Variables

Variables solar radiation with incident angle

Name	Expression	Description
Q2	int2({t[1/s]})*[W/m^2]	Projection of solar radiation on a vertical facade

Variables Ambient Temperature

Name	Expression	Description
T1	int3({t[1/s]})*[K]	Variation of ambient temperature

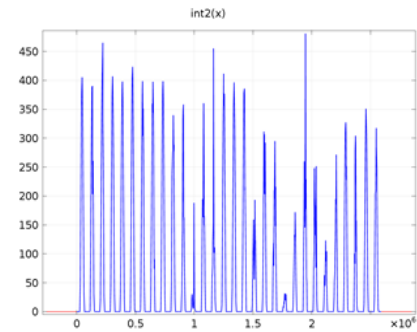
Variables Wind Velocity

Name	Expression	Description
U1	int4({t[1/s]})*[m/s]	Wind velocity

1.1.2 Functions

Solar Radiation with incident angle

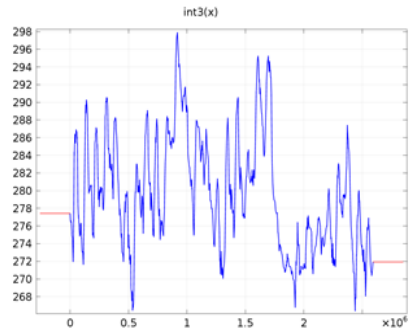
Function name	int2
Function type	Interpolation



Solar Radiation with incident angle

Ambient Temperature

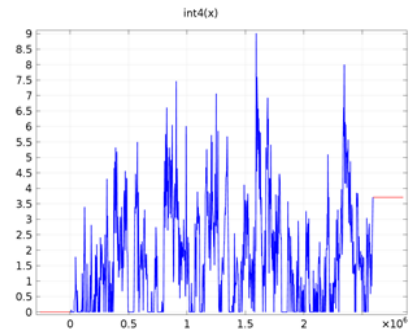
Function name	int3
Function type	Interpolation



Ambient Temperature

Wind velocity

Function name	int4
Function type	Interpolation

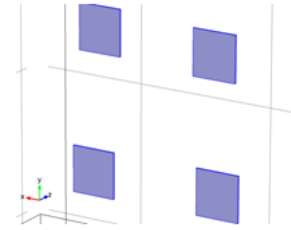


Wind velocity

1.1.3 Selections

Void Defects

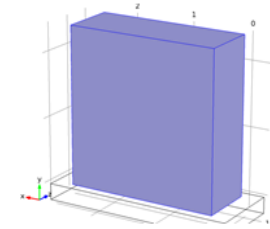
Selection
Domains 3-6



Void Defects

Concrete Block

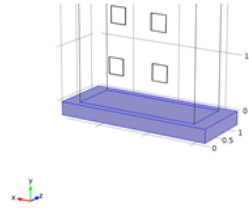
Selection
Domain 2



Concrete Block

Footing Foundation

Selection
Domain 1



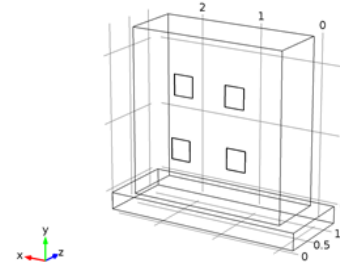
Footing Foundation

1.1.4 Coordinate Systems**Boundary System 1**

Coordinate system type	Boundary system
Identifier	sys1

Settings

Name	Value
Coordinate names	{t1, t2, n}
Create first tangent direction from	Global Cartesian

1.2 Geometry 1

Geometry 1

units

Length unit	m
Angular unit	deg

Geometry statistics

Property	Value
Space dimension	3
Number of domains	6
Number of boundaries	36
Number of edges	72
Number of vertices	48

1.2.1 Concrete block (blk1)**Position**

Name	Value
Position	{0, 0, 0}

Size and shape

Name	Value
Size	{2438[mm], 2438[mm], 914[mm]}

1.2.2 Footing foundation (blk2)

Position

Name	Value
Position	{305[mm], 250[mm], 152.5[mm]}

Size and shape

Name	Value
Size	{3048[mm], 250[mm], 1219[mm]}

1.2.3 25 mm target (A) (blk3)

Position

Name	Value
Position	{614[mm], 1519[mm], 25[mm]}

Size and shape

Name	Value
Size	{305[mm], 305[mm], 13[mm]}

1.2.4 51 mm target (B) (blk4)

Position

Name	Value
Position	{1519[mm], 614[mm], 51[mm]}

Size and shape

Name	Value
Size	{305[mm], 305[mm], 13[mm]}

1.2.5 76 mm target (C) (blk5)

Position

Name	Value
Position	{614[mm], 614[mm], 76[mm]}

Size and shape

Name	Value
Size	{305[mm], 305[mm], 13[mm]}

1.2.6 127 mm target (D) (blk6)

Position

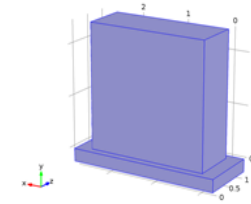
Name	Value
Position	{1519[mm], 1519[mm], 127[mm]}

Size and shape

Name	Value
Size	{305[mm], 305[mm], 13[mm]}

1.3 Materials

1.3.1 Concrete material



Concrete material

Selection

Geometric entity level	Domain
Selection	Domains 1-2

Material parameters

Name	Value	Unit
Density	2300[kg/m ³]	kg/m ³
Thermal conductivity	1.8[W/(m*K)]	W/(m*K)
Heat capacity at constant pressure	1000	J/(kg*K)

Basic Settings

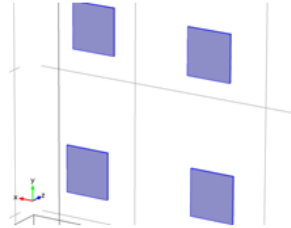
Description	Value
Coefficient of thermal expansion	{{{10e6[1/K], 0, 0}, {0, 10e6[1/K], 0}, {0, 0, 10e6[1/K]}}
Density	2300[kg/m ³]

Description	Value
Thermal conductivity	{{1.8[W/(m*K)], 0, 0}, {0, 1.8[W/(m*K)], 0}, {0, 0, 1.8[W/(m*K)]}}
Heat capacity at constant pressure	1000

Young's modulus and Poisson's ratio Settings

Description	Value
Young's modulus	25e9[Pa]
Poisson's ratio	0.33

1.3.2 Air material



Air material

Selection

Geometric entity level	Domain
Selection	Domains 3–6

Material parameters

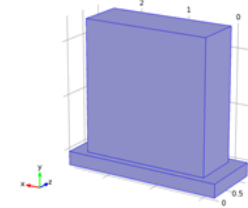
Name	Value	Unit
Ratio of specific heats	1.4	1
Heat capacity at constant pressure	700	J/(kg*K)
Density	1.2	kg/m^3
Thermal conductivity	0.024	W/(m*K)

Basic Settings

Description	Value
Ratio of specific heats	1.4
Heat capacity at constant pressure	700[J/(kg*K)]

Description	Value
Density	1.2[kg/m^3]
Thermal conductivity	{{0.024[W/(m*K)], 0, 0}, {0, 0.024[W/(m*K)], 0}, {0, 0, 0.024[W/(m*K)]}}

1.4 Heat Transfer (ht)



Heat Transfer

Selection

Geometric entity level	Domain
Selection	Domains 1–6

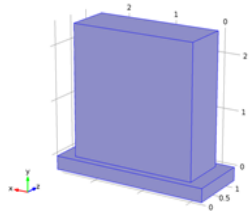
Equations

$$\rho C_p \frac{\partial T}{\partial t} + \rho C_p \mathbf{u} \cdot \nabla T = \nabla \cdot (k \nabla T) + Q$$

Settings

Description	Value
Temperature	Linear
Show equation assuming	std1/time

1.4.1 Heat Transfer in Solids 1



Heat Transfer in Solids 1

Selection

Geometric entity level	Domain
Selection	Domains 1–2

Equations

$$\rho C_p \frac{\partial T}{\partial t} + \rho C_p \mathbf{u} \cdot \nabla T = \nabla \cdot (k \nabla T) + Q$$

Properties from material

Property	Material	Property group
Thermal conductivity	Concrete material	Basic
Density	Concrete material	Basic
Heat capacity at constant pressure	Concrete material	Basic

Variables

Name	Expression	Unit	Description	Selection
ht.kxx	model.input.k11	W/(m*K)	Thermal conductivity, xx component	Domains 1–2
ht.kyx	model.input.k21	W/(m*K)	Thermal conductivity, yx component	Domains 1–2
ht.kzx	model.input.k31	W/(m*K)	Thermal conductivity, zx component	Domains 1–2
ht.kxy	model.input.k12	W/(m*K)	Thermal conductivity, xy component	Domains 1–2
ht.kyy	model.input.k22	W/(m*K)	Thermal conductivity, yy component	Domains 1–2
ht.kzy	model.input.k32	W/(m*K)	Thermal conductivity, zy component	Domains 1–2

Name	Expression	Unit	Description	Selection
ht.kxz	model.input.k13	W/(m*K)	Thermal conductivity, xz component	Domains 1–2
ht.kyz	model.input.k23	W/(m*K)	Thermal conductivity, yz component	Domains 1–2
ht.kzz	model.input.k33	W/(m*K)	Thermal conductivity, zz component	Domains 1–2
ht.rho	model.input.rho	kg/m ³	Density	Domains 1–2
ht.Cp	model.input.Cp	J/(kg*K)	Heat capacity at constant pressure	Domains 1–2
ht.k_effxx	ht.kxx	W/(m*K)	Effective thermal conductivity, xx component	Domains 1–2
ht.k_effyx	ht.kyx	W/(m*K)	Effective thermal conductivity, yx component	Domains 1–2
ht.k_effzx	ht.kzx	W/(m*K)	Effective thermal conductivity, zx component	Domains 1–2
ht.k_effxy	ht.kxy	W/(m*K)	Effective thermal conductivity, xy component	Domains 1–2
ht.k_effyy	ht.kyy	W/(m*K)	Effective thermal conductivity, yy component	Domains 1–2
ht.k_effzy	ht.kzy	W/(m*K)	Effective thermal conductivity, zy component	Domains 1–2
ht.k_effxz	ht.kxz	W/(m*K)	Effective thermal conductivity, xz component	Domains 1–2
ht.k_effyz	ht.kyz	W/(m*K)	Effective thermal conductivity, yz component	Domains 1–2
ht.k_effzz	ht.kzz	W/(m*K)	Effective thermal conductivity, zz component	Domains 1–2
ht.C_eff	ht.rho*ht.Cp	J/(m ³ *K)	Effective volumetric heat capacity	Domains 1–2
ht.alphap	-d(ht.rho, T)/(ht.rho + eps)	1/K	Isobaric compressibility coefficient	Domains 1–2
ht.pA	1[atm]	Pa	Absolute pressure	Domains 1–2
ht.ux	0	m/s	Velocity field, x component	Domains 1–2
ht.uy	0	m/s	Velocity field, y component	Domains 1–2
ht.uz	0	m/s	Velocity field, z component	Domains 1–2

Name	Expression	Unit	Description	Selection
ht.gradTx	Tx	K/m	Temperature gradient, x component	Domains 1–2
ht.gradTy	Ty	K/m	Temperature gradient, y component	Domains 1–2
ht.gradTz	Tz	K/m	Temperature gradient, z component	Domains 1–2
ht.gradTmag	$\sqrt{(\text{ht.gradTx})^2 + (\text{ht.gradTy})^2 + (\text{ht.gradTz})^2}$	K/m	Temperature gradient magnitude	Domains 1–2
ht.kmean	$\frac{(\text{root.mod1.ht.k_eff_p1} + \text{root.mod1.ht.k_eff_p2} + \text{root.mod1.ht.k_eff_p3})}{3}$	W/(m ² K)	Mean effective thermal conductivity	Domains 1–2
ht.dfluxx	$-\text{ht.k_effxx} \cdot \text{Tx} - \text{ht.k_effxy} \cdot \text{Ty} - \text{ht.k_effxz} \cdot \text{Tz}$	W/m ²	Conductive heat flux, x component	Domains 1–2
ht.dfluxy	$-\text{ht.k_effyx} \cdot \text{Tx} - \text{ht.k_effyy} \cdot \text{Ty} - \text{ht.k_effyz} \cdot \text{Tz}$	W/m ²	Conductive heat flux, y component	Domains 1–2
ht.dfluxz	$-\text{ht.k_effzx} \cdot \text{Tx} - \text{ht.k_effzy} \cdot \text{Ty} - \text{ht.k_effzz} \cdot \text{Tz}$	W/m ²	Conductive heat flux, z component	Domains 1–2
ht.dfluxMag	$\sqrt{(\text{ht.dfluxx})^2 + (\text{ht.dfluxy})^2 + (\text{ht.dfluxz})^2}$	W/m ²	Conductive heat flux magnitude	Domains 1–2
ht.Q	0	W/m ³	Heat source	Domains 1–2
ht.qs	0	W/(m ³ *K)	Production/absorption coefficient	Domains 1–2
ht.Qmet	0	W/m ³	Metabolic heat source	Domains 1–2
ht.Qtot	0	W/m ³	Total heat source	Domains 1–2
ht.rhoInt	ht.rho	kg/m ³	Density for integration	Domains 1–2
ht.CpInt	ht.Cp	J/(kg*K)	Specific heat capacity for integration	Domains 1–2
ht.gammat	ht.gamma	1	Ratio of specific heats for integration	Domains 1–2
ht.HRef	$\text{subst}(\text{subst}(\text{ht.CpInt}, \text{ht.pA}, 1[\text{atm}]), \text{T}, 298.15[\text{K}]) \cdot 298.15[\text{K}]$	J/kg	Reference enthalpy	Domains 1–2
ht.DeltaH	$0.05 \cdot (\text{subst}(\text{subst}(\text{ht.CpInt}, \text{ht.pA}, 1[\text{atm}]), \text{T}, 298.15[\text{K}]) + 2 \cdot \text{subst}(\text{subst}(\text{ht.CpInt}, \text{ht.pA}, 1[\text{atm}]), \text{T}, 0.9 \cdot 298.15[\text{K}] + 0.1 \cdot \text{T}) + 2 \cdot \text{subst}(\text{subst}(\text{ht.CpInt}, \text{ht.pA}, 1[\text{atm}]), \text{T}, 0.8 \cdot 298.15[\text{K}] + 0.2 \cdot \text{T}) + 2 \cdot \text{subst}(\text{subst}(\text{ht.CpInt}, \text{ht.pA}, 1[\text{atm}]), \text{T}, 0.7 \cdot 298.15[\text{K}] + 0.3 \cdot \text{T}) + 2 \cdot \text{subst}(\text{subst}(\text{ht.CpInt}, \text{ht.pA}, 1[\text{atm}]), \text{T}, 0.6 \cdot 298.15[\text{K}] + 0.4 \cdot \text{T}) + 2 \cdot \text{subst}(\text{subst}(\text{ht.CpInt}, \text{ht.pA}, 1[\text{atm}]), \text{T}, 0.5 \cdot (298.15[\text{K}] + \text{T})) + 2 \cdot \text{subst}(\text{subst}(\text{ht.CpInt}, \text{ht.pA}, 1[\text{atm}]), \text{T}, 0.4 \cdot 298.15[\text{K}] + 0.6 \cdot \text{T}) + 2 \cdot \text{subst}(\text{subst}(\text{ht.CpInt}, \text{ht.pA}, 1[\text{atm}]), \text{T}, 0.30000000000000004 \cdot 298.15[\text{K}] + 0.7 \cdot \text{T}) + 2 \cdot \text{subst}(\text{subst}(\text{ht.CpInt}, \text{ht.pA}, 1[\text{atm}]), \text{T}, 0.19999999999999996 \cdot 298.15[\text{K}] +$	J/kg	Sensible enthalpy	Domains 1–2

Name	Expression	Unit	Description	Selection
	$0.8 \cdot \text{T} + 2 \cdot \text{subst}(\text{subst}(\text{ht.CpInt}, \text{ht.pA}, 1[\text{atm}]), \text{T}, 0.09999999999999998 \cdot 298.15[\text{K}] + 0.9 \cdot \text{T}) + \text{subst}(\text{ht.CpInt}, \text{ht.pA}, 1[\text{atm}]) \cdot (\text{T} - 298.15[\text{K}])$			
ht.H	ht.HRef + ht.DeltaH	J/kg	Enthalpy	Domains 1–2
ht.H0	ht.H	J/kg	Total enthalpy	Domains 1–2
ht.Ei	ht.H	J/kg	Internal energy	Domains 1–2
ht.Ei0	ht.Ei	J/kg	Total internal energy	Domains 1–2
ht.tfluxx	ht.dfluxx + ht.trifluxx + ht.afluxx	W/m ²	Total heat flux, x component	Domains 1–2
ht.tfluxy	ht.dfluxy + ht.trifluxy + ht.afluxy	W/m ²	Total heat flux, y component	Domains 1–2
ht.tfluxz	ht.dfluxz + ht.trifluxz + ht.afluxz	W/m ²	Total heat flux, z component	Domains 1–2
ht.tfluxMag	$\sqrt{(\text{ht.tfluxx})^2 + (\text{ht.tfluxy})^2 + (\text{ht.tfluxz})^2}$	W/m ²	Total heat flux magnitude	Domains 1–2
ht.tefluxx	ht.dfluxx	W/m ²	Total energy flux, x component	Domains 1–2
ht.tefluxy	ht.dfluxy	W/m ²	Total energy flux, y component	Domains 1–2
ht.tefluxz	ht.dfluxz	W/m ²	Total energy flux, z component	Domains 1–2
ht.tefluxMag	$\sqrt{(\text{ht.tefluxx})^2 + (\text{ht.tefluxy})^2 + (\text{ht.tefluxz})^2}$	W/m ²	Total energy flux magnitude	Domains 1–2
ht.ntriflux	$\text{mean}(\text{ht.trifluxx}) \cdot \text{ht.nx} + \text{mean}(\text{ht.trifluxy}) \cdot \text{ht.ny} + \text{mean}(\text{ht.trifluxz}) \cdot \text{ht.nz}$	W/m ²	Normal translational heat flux	Boundaries 1–36
ht.naflux	$\text{mean}(\text{ht.afluxx}) \cdot \text{ht.nx} + \text{mean}(\text{ht.afluxy}) \cdot \text{ht.ny} + \text{mean}(\text{ht.afluxz}) \cdot \text{ht.nz}$	W/m ²	Normal convective heat flux	Boundaries 1–36
ht.ndflux	$\text{mean}(\text{ht.dfluxx}) \cdot \text{ht.nx} + \text{mean}(\text{ht.dfluxy}) \cdot \text{ht.ny} + \text{mean}(\text{ht.dfluxz}) \cdot \text{ht.nz}$	W/m ²	Normal conductive heat flux	Boundaries 1–36
ht.ntflux	ht.ndflux + ht.ntriflux + ht.naflux	W/m ²	Total normal heat flux	Boundaries 1–36
ht.nteflux	$\text{mean}(\text{ht.tefluxx}) \cdot \text{ht.nx} + \text{mean}(\text{ht.tefluxy}) \cdot \text{ht.ny} + \text{mean}(\text{ht.tefluxz}) \cdot \text{ht.nz}$	W/m ²	Total normal energy flux	Boundaries 1–36
ht.gamma	1	1	Ratio of specific heats	Domains 1–2

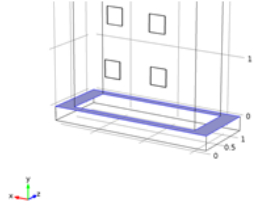
Shape functions

Name	Shape function	Unit	Description	Shape frame	Selection
T	Lagrange (Linear)	K	Temperature	Material	Domains 1–2

Weak expressions

Weak expression	Integration frame	Selection
$-(ht.k_effxx \cdot Tx + ht.k_effxy \cdot Ty + ht.k_effxz \cdot Tz) \cdot test(Tx) - (ht.k_effyx \cdot Tx + ht.k_effyy \cdot Ty + ht.k_effyz \cdot Tz) \cdot test(Ty) - (ht.k_effzx \cdot Tx + ht.k_effzy \cdot Ty + ht.k_effzz \cdot Tz) \cdot test(Tz)$	Material	Domains 1–2

1.4.2 Thermal Insulation 1



Thermal Insulation 1

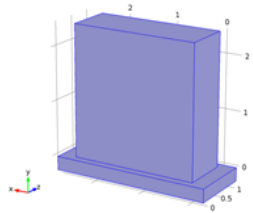
Selection

Geometric entity level	Boundary
Selection	Boundary 5

Equations

$$-\mathbf{n} \cdot (-k \nabla T) = 0$$

1.4.3 Initial Values 1



Initial Values 1

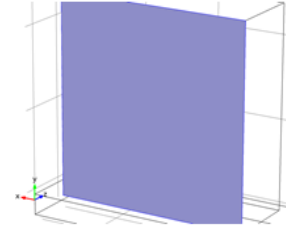
Selection

Geometric entity level	Domain
Selection	Domains 1–6

Settings

Description	Value
Temperature	283.76[K]

1.4.4 Heat Flux 1



Heat Flux 1

Selection

Geometric entity level	Boundary
Selection	Boundary 8

Equations

$$-\mathbf{n} \cdot (-k \nabla T) = q_0$$

Settings

Description	Value
Inward heat flux	Q2

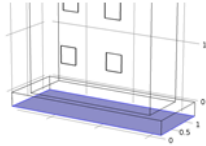
Variables

Name	Expression	Unit	Description	Selection
ht.q0	ht.q0_hf1	W/m^2	Inward heat flux	Boundary 8

Name	Expression	Unit	Description	Selection
ht.q0_hf1	Q2	W/m^2	Inward heat flux	Boundary 8

Weak expressions

Weak expression	Integration frame	Selection
ht.q0_hf1*test(T)	Material	Boundary 8

1.4.5 Heat Flux 2**Heat Flux 2****Selection**

Geometric entity level	Boundary
Selection	Boundary 2

Equations

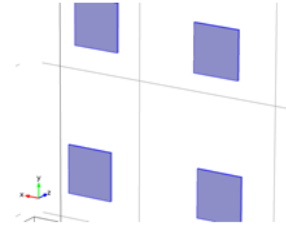
$$-\mathbf{n} \cdot (-k\nabla T) = q_0$$

Variables

Name	Expression	Unit	Description	Selection
ht.q0	ht.q0_hf2	W/m^2	Inward heat flux	Boundary 2
ht.q0_hf2	0	W/m^2	Inward heat flux	Boundary 2

Weak expressions

Weak expression	Integration frame	Selection
ht.q0_hf2*test(T)	Material	Boundary 2

1.4.6 Heat Transfer in Fluids 1**Heat Transfer in Fluids 1****Selection**

Geometric entity level	Domain
Selection	Domains 3-6

Equations

$$\rho C_p \frac{\partial T}{\partial t} + \rho C_p \mathbf{u} \cdot \nabla T = \nabla \cdot (k \nabla T) + Q + Q_{vh} + W_p$$

Properties from material

Property	Material	Property group
Thermal conductivity	Air material	Basic
Density	Air material	Basic
Heat capacity at constant pressure	Air material	Basic

Variables

Name	Expression	Unit	Description	Selection
ht.kxx	model.input.k11	W/(m^2 K)	Thermal conductivity, xx component	Domains 3-6
ht.kyx	model.input.k21	W/(m^2 K)	Thermal conductivity, yx component	Domains 3-6
ht.kzx	model.input.k31	W/(m^2 K)	Thermal conductivity, zx component	Domains 3-6
ht.kxy	model.input.k12	W/(m^2 K)	Thermal conductivity, xy component	Domains 3-6

Name	Expression	Unit	Description	Selection
ht.kyy	model.input.k22	W/(m ² K)	Thermal conductivity, yy component	Domains 3–6
ht.kzy	model.input.k32	W/(m ² K)	Thermal conductivity, zy component	Domains 3–6
ht.kxz	model.input.k13	W/(m ² K)	Thermal conductivity, xz component	Domains 3–6
ht.kyz	model.input.k23	W/(m ² K)	Thermal conductivity, yz component	Domains 3–6
ht.kzz	model.input.k33	W/(m ² K)	Thermal conductivity, zz component	Domains 3–6
ht.rho	model.input.rho	kg/m ³	Density	Domains 3–6
ht.Cp	model.input.Cp	J/(kg*K)	Heat capacity at constant pressure	Domains 3–6
ht.k_eff_xx	ht.kxx	W/(m ² K)	Effective thermal conductivity, xx component	Domains 3–6
ht.k_eff_fyx	ht.kyx	W/(m ² K)	Effective thermal conductivity, yx component	Domains 3–6
ht.k_eff_fzx	ht.kzx	W/(m ² K)	Effective thermal conductivity, zx component	Domains 3–6
ht.k_eff_fxy	ht.kxy	W/(m ² K)	Effective thermal conductivity, xy component	Domains 3–6
ht.k_eff_fyy	ht.kyy	W/(m ² K)	Effective thermal conductivity, yy component	Domains 3–6
ht.k_eff_fzy	ht.kzy	W/(m ² K)	Effective thermal conductivity, zy component	Domains 3–6
ht.k_eff_fxz	ht.kxz	W/(m ² K)	Effective thermal conductivity,	Domains 3–6

Name	Expression	Unit	Description	Selection
			xz component	
ht.k_eff_fyz	ht.kyz	W/(m ² K)	Effective thermal conductivity, yz component	Domains 3–6
ht.k_eff_fzz	ht.kzz	W/(m ² K)	Effective thermal conductivity, zz component	Domains 3–6
ht.C_eff	ht.rho*ht.Cp	J/(m ³ *K)	Effective volumetric heat capacity	Domains 3–6
ht.alpha	-d(ht.rho, T)/(ht.rho + eps)	1/K	Isobaric compressibility coefficient	Domains 3–6
ht.pA	1[atm]	Pa	Absolute pressure	Domains 3–6
ht.ux	model.input.minput_velocity1	m/s	Velocity field, x component	Domains 3–6
ht.uy	model.input.minput_velocity2	m/s	Velocity field, y component	Domains 3–6
ht.uz	model.input.minput_velocity3	m/s	Velocity field, z component	Domains 3–6
ht.gradTx	Tx	K/m	Temperature gradient, x component	Domains 3–6
ht.gradTy	Ty	K/m	Temperature gradient, y component	Domains 3–6
ht.gradTz	Tz	K/m	Temperature gradient, z component	Domains 3–6
ht.gradTmag	sqrt(ht.gradTx^2 + ht.gradTy^2 + ht.gradTz^2)	K/m	Temperature gradient magnitude	Domains 3–6
ht.k_mean	(root.mod1.ht.k_eff_p1 + root.mod1.ht.k_eff_p2 + root.mod1.ht.k_eff_p3)/3	W/(m ² K)	Mean effective thermal conductivity	Domains 3–6
ht.dfluxx	-ht.k_effxx*Tx - ht.k_effxy*Ty - ht.k_effxz*Tz	W/m ²	Conductive heat flux, x component	Domains 3–6
ht.dfluxy	-ht.k_effyx*Tx - ht.k_effyy*Ty - ht.k_effyz*Tz	W/m ²	Conductive heat flux, y component	Domains 3–6
ht.dfluxz	-ht.k_effzx*Tx - ht.k_effzy*Ty - ht.k_effzz*Tz	W/m ²	Conductive	Domains 3–6

Name	Expression	Unit	Description	Selection
xz			heat flux, z component	
ht.dfluxMag	$\sqrt{ht.dfluxx^2 + ht.dfluxy^2 + ht.dfluxz^2}$	W/m ²	Conductive heat flux magnitude	Domains 3-6
ht.Q	0	W/m ³	Heat source	Domains 3-6
ht.qs	0	W/(m ² *K)	Production/absorption coefficient	Domains 3-6
ht.Qmet	0	W/m ³	Metabolic heat source	Domains 3-6
ht.Qtot	0	W/m ³	Total heat source	Domains 3-6
ht.rhoInt	ht.rho	kg/m ³	Density for integration	Domains 3-6
ht.CpInt	ht.Cp	J/(kg*K)	Specific heat capacity for integration	Domains 3-6
ht.gamaint	ht.gamma	1	Ratio of specific heats for integration	Domains 3-6
ht.HRef	$\text{subst}(\text{subst}(\text{ht.CpInt}, \text{ht.pA}, 1[\text{atm}]), T, 298.15[\text{K}]) * 298.15[\text{K}] / \text{subst}(\text{subst}(\text{ht.gamaint}, \text{ht.pA}, 1[\text{atm}]), T, 298.15[\text{K}]) + 1[\text{atm}] / \text{subst}(\text{subst}(\text{ht.rhoInt}, \text{ht.pA}, 1[\text{atm}]), T, 298.15[\text{K}])$	J/kg	Reference enthalpy	Domains 3-6
ht.DeltaH	$0.05 * (\text{subst}(\text{subst}(\text{ht.CpInt}, \text{ht.pA}, 1[\text{atm}]), T, 298.15[\text{K}]) + 2 * \text{subst}(\text{subst}(\text{ht.CpInt}, \text{ht.pA}, 1[\text{atm}]), T, 0.9 * 298.15[\text{K}] + 0.1 * T) + 2 * \text{subst}(\text{subst}(\text{ht.CpInt}, \text{ht.pA}, 1[\text{atm}]), T, 0.8 * 298.15[\text{K}] + 0.2 * T) + 2 * \text{subst}(\text{subst}(\text{ht.CpInt}, \text{ht.pA}, 1[\text{atm}]), T, 0.7 * 298.15[\text{K}] + 0.3 * T) + 2 * \text{subst}(\text{subst}(\text{ht.CpInt}, \text{ht.pA}, 1[\text{atm}]), T, 0.6 * 298.15[\text{K}] + 0.4 * T) + 2 * \text{subst}(\text{subst}(\text{ht.CpInt}, \text{ht.pA}, 1[\text{atm}]), T, 0.5 * (298.15[\text{K}] + T)) + 2 * \text{subst}(\text{subst}(\text{ht.CpInt}, \text{ht.pA}, 1[\text{atm}]), T, 0.4 * 298.15[\text{K}] + 0.6 * T) + 2 * \text{subst}(\text{subst}(\text{ht.CpInt}, \text{ht.pA}, 1[\text{atm}]), T, 0.3000000000000004 * 298.15[\text{K}] + 0.7 * T) + 2 * \text{subst}(\text{subst}(\text{ht.CpInt}, \text{ht.pA}, 1[\text{atm}]), T, 0.1999999999999996 * 298.15[\text{K}] + 0.8 * T) + 2 * \text{subst}(\text{subst}(\text{ht.CpInt}, \text{ht.pA}, 1[\text{atm}]), T, 0.0999999999999998 * 298.15[\text{K}] + 0.9 * T) + \text{subst}(\text{ht.CpInt}, \text{ht.pA}, 1[\text{atm}]) * (T - 298.15[\text{K}]) + (\text{subst}((1 + T^d(\text{ht.rhoInt}, T) / \text{ht.rhoInt}) / \text{ht.rhoInt}, \text{ht.pA}, 1[\text{atm}]) + 2 * \text{subst}((1 + T^d(\text{ht.rhoInt}, T) / \text{ht.rhoInt}) / \text{ht.rhoInt}, \text{ht.pA}, 0.9 * 1[\text{atm}]) +$	J/kg	Sensible enthalpy	Domains 3-6

Name	Expression	Unit	Description	Selection
	$0.1 * \text{ht.pA} + 2 * \text{subst}((1 + T^d(\text{ht.rhoInt}, T) / \text{ht.rhoInt}) / \text{ht.rhoInt}, \text{ht.pA}, 0.8 * 1[\text{atm}]) + 0.2 * \text{ht.pA} + 2 * \text{subst}((1 + T^d(\text{ht.rhoInt}, T) / \text{ht.rhoInt}) / \text{ht.rhoInt}, \text{ht.pA}, 0.7 * 1[\text{atm}]) + 0.3 * \text{ht.pA} + 2 * \text{subst}((1 + T^d(\text{ht.rhoInt}, T) / \text{ht.rhoInt}) / \text{ht.rhoInt}, \text{ht.pA}, 0.6 * 1[\text{atm}]) + 0.4 * \text{ht.pA} + 2 * \text{subst}((1 + T^d(\text{ht.rhoInt}, T) / \text{ht.rhoInt}) / \text{ht.rhoInt}, \text{ht.pA}, 0.5 * 1[\text{atm}]) + \text{ht.pA})) + 2 * \text{subst}((1 + T^d(\text{ht.rhoInt}, T) / \text{ht.rhoInt}) / \text{ht.rhoInt}, \text{ht.pA}, 0.4 * 1[\text{atm}]) + 0.6 * \text{ht.pA} + 2 * \text{subst}((1 + T^d(\text{ht.rhoInt}, T) / \text{ht.rhoInt}) / \text{ht.rhoInt}, \text{ht.pA}, 0.3000000000000004 * 1[\text{atm}]) + 0.7 * \text{ht.pA} + 2 * \text{subst}((1 + T^d(\text{ht.rhoInt}, T) / \text{ht.rhoInt}) / \text{ht.rhoInt}, \text{ht.pA}, 0.1999999999999996 * 1[\text{atm}]) + 0.8 * \text{ht.pA} + 2 * \text{subst}((1 + T^d(\text{ht.rhoInt}, T) / \text{ht.rhoInt}) / \text{ht.rhoInt}, \text{ht.pA}, 0.0999999999999998 * 1[\text{atm}]) + 0.9 * \text{ht.pA} + (1 + T^d(\text{ht.rhoInt}, T) / \text{ht.rhoInt}) / \text{ht.rhoInt} * (\text{ht.pA} - 1[\text{atm}]))$			
ht.H	ht.HRef + ht.DeltaH	J/kg	Enthalpy	Domains 3-6
ht.H0	ht.H + 0.5 * (ht.ux ² + ht.uy ² + ht.uz ²)	J/kg	Total enthalpy	Domains 3-6
ht.Ei	ht.H - ht.pA / ht.rho	J/kg	Internal energy	Domains 3-6
ht.Ei0	ht.Ei + 0.5 * (ht.ux ² + ht.uy ² + ht.uz ²)	J/kg	Total internal energy	Domains 3-6
ht.trifluxxx	0	W/m ²	Translational heat flux, x component	Domains 3-6
ht.trifluxxy	0	W/m ²	Translational heat flux, y component	Domains 3-6
ht.trifluxxz	0	W/m ²	Translational heat flux, z component	Domains 3-6
ht.afluxxx	ht.rho * ht.ux * ht.Ei	W/m ²	Convective heat flux, x component	Domains 3-6
ht.afluxxy	ht.rho * ht.uy * ht.Ei	W/m ²	Convective heat flux, y component	Domains 3-6
ht.afluxxz	ht.rho * ht.uz * ht.Ei	W/m ²	Convective heat flux, z component	Domains 3-6
ht.dfluxx	ht.dfluxx + ht.trifluxx + ht.afluxx	W/m ²	Total heat flux, x component	Domains 3-6

Name	Expression	Unit	Description	Selection
ht.tfluxy	ht.dfluxy + ht.trifluxy + ht.afluxy	W/m ²	Total heat flux, y component	Domains 3–6
ht.tfluxz	ht.dfluxz + ht.trifluxz + ht.afluxz	W/m ²	Total heat flux, z component	Domains 3–6
ht.tfluxMag	$\sqrt{ht.tfluxx^2 + ht.tfluxy^2 + ht.tfluxz^2}$	W/m ²	Total heat flux magnitude	Domains 3–6
ht.tefluxx	ht.dfluxx + ht.rho*ht.ux*ht.H0	W/m ²	Total energy flux, x component	Domains 3–6
ht.tefluxy	ht.dfluxy + ht.rho*ht.uy*ht.H0	W/m ²	Total energy flux, y component	Domains 3–6
ht.tefluxz	ht.dfluxz + ht.rho*ht.uz*ht.H0	W/m ²	Total energy flux, z component	Domains 3–6
ht.tefluxMag	$\sqrt{ht.tefluxx^2 + ht.tefluxy^2 + ht.tefluxz^2}$	W/m ²	Total energy flux magnitude	Domains 3–6
ht.rflux	0	W/m ²	Radiative heat flux	Boundaries 11–34
ht.cflux	0	W/m ²	Convective heat flux	Boundaries 11–34
ht.ntriflux	$\text{mean}(ht.trifluxx)*ht.nx + \text{mean}(ht.trifluxy)*ht.ny + \text{mean}(ht.trifluxz)*ht.nz$	W/m ²	Normal translational heat flux	Boundaries 11–34
ht.naflux	$\text{mean}(ht.afluxx)*ht.nx + \text{mean}(ht.afluxy)*ht.ny + \text{mean}(ht.afluxz)*ht.nz$	W/m ²	Normal convective heat flux	Boundaries 11–34
ht.ndflux	$\text{mean}(ht.dfluxx)*ht.nx + \text{mean}(ht.dfluxy)*ht.ny + \text{mean}(ht.dfluxz)*ht.nz$	W/m ²	Normal conductive heat flux	Boundaries 11–34
ht.ntflux	ht.ndflux + ht.ntriflux + ht.naflux	W/m ²	Total normal heat flux	Boundaries 11–34
ht.nteflux	$\text{mean}(ht.tefluxx)*ht.nx + \text{mean}(ht.tefluxy)*ht.ny + \text{mean}(ht.tefluxz)*ht.nz$	W/m ²	Total normal energy flux	Boundaries 11–34
ht.Qbot	0	W/m ²	Total boundary heat source	Boundaries 11–34
ht.Qlot	0	W/m	Total heat source	Edges 17–64
ht.gam	model.input.gamma	1	Ratio of specific heats	Domains 3–6
ht.res_T	$-\text{ht.k_effxx}*\text{d}(Tx, x) - \text{ht.k_effxy}*\text{d}(Tx, y) - \text{ht.k_effxz}*\text{d}(Tx, z) - \text{ht.k_effyx}*\text{d}(Ty, x) - \text{ht.k_effyy}*\text{d}(Ty, y) - \text{ht.k_effyz}*\text{d}(Ty, z) -$	W/m ³	Equation residual	Domains 3–6

Name	Expression	Unit	Description	Selection
	$\text{ht.k_effxz}*\text{d}(Tz, x) - \text{ht.k_effzy}*\text{d}(Tz, y) - \text{ht.k_effzz}*\text{d}(Tz, z) - (\text{ht.qs} + \text{ht.qs_oop})*T + \text{ht.rho}*ht.Cp*(\text{ht.ux}*Tx + \text{ht.uy}*Ty + \text{ht.uz}*Tz) - \text{ht.Q} - \text{ht.Qoop}$			
ht.cellPe	$0.5*ht.rho*ht.Cp*ht.sqrt(\text{ht.ux}^2 + \text{ht.uy}^2 + \text{ht.uz}^2)/\text{ht.kmean}$	1	Cell Peclet number	Domains 3–6
ht.afluxMag	$\sqrt{(\text{ht.rho}*ht.ux*ht.Ei)^2 + (\text{ht.rho}*ht.uy*ht.Ei)^2 + (\text{ht.rho}*ht.uz*ht.Ei)^2}$	W/m ²	Convective heat flux magnitude	Domains 3–6
ht.fluid1_minput_temperature	model.input.minput_temperature	K	Temperature	Domains 3–6
ht.fluid1_minput_pressure	1[atm]	Pa	Absolute pressure	Domains 3–6
ht.c_s	$\sqrt{(\text{ht.gam}/\text{max}(\text{subst}(\text{d}(\text{ht.rhoInt}, \text{ht.pA}), \text{ht.pA}, \text{ht.fluid1.minput_pressure}), \text{eps})))}$	m/s	Speed of sound	Domains 3–6
ht.Ma	$\sqrt{(\text{model.input.minput_velocity}^2 + \text{model.input.minput_velocity}^2)^2 + \text{model.input.minput_velocity}^3^2}/\sqrt{(\text{ht.gam}/\text{max}(\text{subst}(\text{d}(\text{ht.rhoInt}, \text{ht.pA}), \text{ht.pA}, \text{ht.fluid1.minput_pressure}), \text{eps})))}$	1	Mach number	Domains 3–6

Shape functions

Name	Shape function	Unit	Description	Shape frame	Selection
T	Lagrange (Linear)	K	Temperature	Material	Domains 3–6

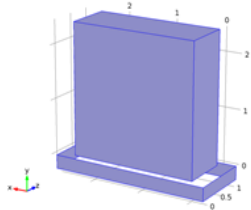
Weak expressions

Weak expression	Integration frame	Selection
$-(\text{ht.k_effxx}*Tx + \text{ht.k_effxy}*Ty + \text{ht.k_effxz}*Tz)*\text{test}(Tx) - (\text{ht.k_effyx}*Tx + \text{ht.k_effyy}*Ty + \text{ht.k_effyz}*Tz)*\text{test}(Ty) - (\text{ht.k_effxz}*Tx + \text{ht.k_effzy}*Ty + \text{ht.k_effzz}*Tz)*\text{test}(Tz)$	Material	Domains 3–6
$-\text{ht.rho}*ht.Cp*(Tx*ht.ux + Ty*ht.uy + Tz*ht.uz)*\text{test}(T)$	Material	Domains 3–6
ht.streamline	Material	Domains 3–6

Name	Expression	Unit	Description	Selection
	$\frac{f1c1hs(1000000000 + ht.Ra_{cc1}, 100000000)^{0.825} + 0.387 \cdot ht.Ra_{cc1}^{1/6}}{(1 + (0.492 \cdot ht.kExtFluid_{cc1} / (ht.muExtFluid_{cc1} \cdot ht.CExtFluid_{cc1}))^{0.5625})^{0.2962962962962963})^2} / 2438 [\text{mm}]$			

Weak expressions

Weak expression	Integration frame	Selection
$ht.h_{cc1} \cdot (ht.Text_{cc1} - T) \cdot \text{test}(T)$	Material	Boundaries 1, 3–4, 6, 8–10, 35–36

1.4.8 Surface-to-Ambient Radiation 1

Surface-to-Ambient Radiation 1

Selection

Geometric entity level	Boundary
Selection	Boundaries 1, 3–4, 6, 8–10, 35–36

Equations

$$-\mathbf{n} \cdot (-k \nabla T) = \epsilon \sigma (T_{\text{amb}}^4 - T^4)$$

Settings

Description	Value
Ambient temperature	T1
Surface emissivity	0.95

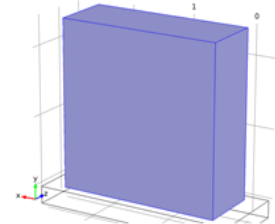
Variables

Name	Expression	Unit	Description	Selection
------	------------	------	-------------	-----------

Name	Expression	Unit	Description	Selection
ht.rflux	$ht.epsilon_{rad} \cdot \sigma \cdot (ht.T_{amb}^4 - ht.T^4)$	W/m ²	Radiative heat flux	Boundaries 1, 3–4, 6, 8–10, 35–36
ht.epsilon_rad	0.95	1	Surface emissivity	Boundaries 1, 3–4, 6, 8–10, 35–36
ht.Tamb	T1	K	Ambient temperature	Boundaries 1, 3–4, 6, 8–10, 35–36
ht.T	model.input.minput_temperature	K	Temperature	Boundaries 1, 3–4, 6, 8–10, 35–36

Weak expressions

Weak expression	Integration frame	Selection
$ht.epsilon_{rad} \cdot \sigma \cdot (ht.T_{amb}^4 - ht.T^4) \cdot \text{test}(ht.T)$	Material	Boundaries 1, 3–4, 6, 8–10, 35–36

1.4.9 Convective Cooling 2

Convective Cooling 2

Selection

Geometric entity level	Boundary
Selection	Boundaries 6, 8–10, 35

Equations

$$-\mathbf{n} \cdot (-k \nabla T) = h \cdot (T_{\text{ext}} - T)$$

$$h = h_{\text{air}}(x_{\text{pl}}) u_{\text{ext}} \rho_A J_{\text{ext}}$$

Settings

Description	Value
External temperature	T1
Velocity, external fluid	U1
Position along the plate	3048[mm]
Heat transfer coefficient	External forced convection
External forced convection	Plate, local transfer coefficient

Variables

Name	Expression	Unit	Description	Selection
ht.ccflux	$-ht.h_cc2*(ht.Text_cc2 - T)$	W/m ²	Convective heat flux	Boundaries 6, 8–10, 35
ht.Text_cc2	T1	K	External temperature	Boundaries 6, 8–10, 35
ht.rhoExtFluid_cc2	$0.006968968005773394*[atm]/(T + ht.Text_cc2)$	kg/m ³	Density, external fluid	Boundaries 6, 8–10, 35
ht.rhoExtFluid_T_cc2	$0.003484484002886697*[atm]/T$	kg/m ³	Density, external fluid	Boundaries 6, 8–10, 35
ht.CExtFluid_cc2	$if(0.5*(T + ht.Text_cc2) < 200, 1006.3173533919999, if(0.5*(T + ht.Text_cc2) > 1600, 1246.7283234080005, 1047.63657 - 0.1862946325*(T + ht.Text_cc2) + 9.46304214E4*(0.5*(T + ht.Text_cc2))^2 - 6.02409443E7*(0.5*(T + ht.Text_cc2))^3 + 1.2858961E10*(0.5*(T + ht.Text_cc2))^4))$	J/(kg*K)	Specific heat capacity, external fluid	Boundaries 6, 8–10, 35
ht.kExtFluid_cc2	$if(0.5*(T + ht.Text_cc2) < 200, 0.017976617530704002, if(0.5*(T + ht.Text_cc2) > 1600, 0.10007092169568399, 0.00227583562 + 5.7740011E5*(T + ht.Text_cc2) - 7.90252856E8*(0.5*(T + ht.Text_cc2))^2 + 4.11702505E11*(0.5*(T + ht.Text_cc2))^3 - 7.43864331E15*(0.5*(T + ht.Text_cc2))^4))$	W/(m ² K)	Thermal conductivity, external fluid	Boundaries 6, 8–10, 35
ht.muExtFluid_cc2	$if(0.5*(T + ht.Text_cc2) < 200, 1.3152794938879997E5, if(0.5*(T + ht.Text_cc2) > 1600, 5.625762160447999E5, 8.38278E7 + 4.17858671E8*(T + ht.Text_cc2) - 7.69429583E11*(0.5*(T + ht.Text_cc2))^2 +$	Pa*s	Dynamic viscosity, external fluid	Boundaries 6, 8–10, 35

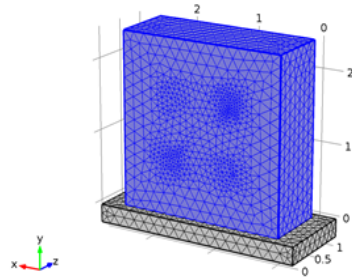
Name	Expression	Unit	Description	Selection
ht.Re_cc2	$4.6437266E14*(0.5*(T + ht.Text_cc2))^3 - 1.06585607E17*(0.5*(T + ht.Text_cc2))^4)$	1	Reynolds number	Boundaries 6, 8–10, 35
ht.Pr_cc2	$ht.muExtFluid_cc2*ht.CExtFluid_cc2/ht.kExtFluid_cc2$	1	Prandtl number	Boundaries 6, 8–10, 35
ht.h_cc2	$nojac(ht.kExtFluid_cc2*ht.Pr_cc2^(1/3)*(0.332*fc1hs(600000 - ht.Re_cc2, 10000)*ht.Re_cc2^0.5 + 0.0296*fc1hs(600000 + ht.Re_cc2, 10000)*ht.Re_cc2^0.8)/max(3048[m], eps^0.5))$	W/(m ² *K)	Heat transfer coefficient	Boundaries 6, 8–10, 35

Weak expressions

Weak expression	Integration frame	Selection
$ht.h_cc2*(ht.Text_cc2 - T)*test(T)$	Material	Boundaries 6, 8–10, 35

1.5 Mesh 1**Mesh statistics**

Property	Value
Minimum element quality	0.05639
Average element quality	0.7139
Tetrahedral elements	62734
Triangular elements	6742
Edge elements	664
Vertex elements	48



Mesh 1

1.5.1 Size (size)

Settings

Name	Value
Maximum element size	0.168
Minimum element size	0.0122
Resolution of curvature	0.4
Resolution of narrow regions	0.7
Maximum element growth rate	1.4
Predefined size	Finer

2 Study 1

2.1 Time Dependent

Times: range(0,600,2591400)

Mesh selection

Geometry	Mesh
Geometry 1 (geom1)	mesh1

Physics selection

Physics	Discretization
Heat Transfer (ht)	physics

2.2 Solver Configurations

2.2.1 Solver 1

Compile Equations: Time Dependent (stf)

Study and step

Name	Value
Use study	Study 1
Use study step	Time Dependent

Dependent Variables 1 (v1)

General

Name	Value
Defined by study step	User defined

mod1.T (mod1_T)

+ General

Name	Value
Field components	mod1.T

Time-Dependent Solver 1 (t1)

General

Name	Value
Defined by study step	User defined
Time	{0, 600, 1200, 1800, 2400, 3000, 3600, 4200, 4800, 5400, 6000, 6600,, 2587800, 2588400, 2589000, 2589600, 2590200, 2590800, 2591400}

Time stepping

Name	Value
Method	Generalized alpha
Steps taken by solver	Intermediate
Amplification for high frequency	0.5
Predictor	Constant

Advanced

Name	Value
Error estimation	Exclude algebraic

Fully Coupled 1 (fc1)

General

Name	Value
Linear solver	iterative 1

Results while solving

Name	Value
Probes	Manual

3 Results**3.1 Data Sets****3.1.1 Solution 1****Selection**

Geometric entity level	Domain
Selection	Geometry geom1

Solution

Name	Value
Solution	Solver 1
Model	Save Point Geometry 1

3.1.2 Cut Point 3D (A) 1" target**Data**

Name	Value
Data set	Solution 1

3.1.3 Cut Point 3D (B) 2" target**Data**

Name	Value
Data set	Solution 1

3.1.4 Cut Point 3D (C) 3" target**Data**

Name	Value
Data set	Solution 1

3.1.5 Cut Point 3D (D) 5" target**Data**

Name	Value
Data set	Solution 1

3.1.6 Cut Point 3D (E) no defect**Data**

Name	Value

Name	Value
Data set	Solution 1

3.2 Derived Values

3.2.1 Point Evaluation Surface no defect

Data

Name	Value
Data set	Cut Point3D (E) no defect

Expression

Name	Value
Expression	T
Unit	degC
Description	Temperature

3.2.2 Point Evaluation A 1" target

Data

Name	Value
Data set	Cut Point3D (A) 1"target

Expression

Name	Value
Expression	T
Unit	degC
Description	Temperature

3.2.3 Point Evaluation B 2" target

Data

Name	Value
Data set	Cut Point3D (B) 2" target

Expression

Name	Value
Expression	T
Unit	degC
Description	Temperature

3.2.4 Point Evaluation C 3" target

Data

Name	Value
Data set	Cut Point3D (C) 3" target

Expression

Name	Value
Expression	T
Unit	degC
Description	Temperature

3.2.5 Point Evaluation D 5" target

Data

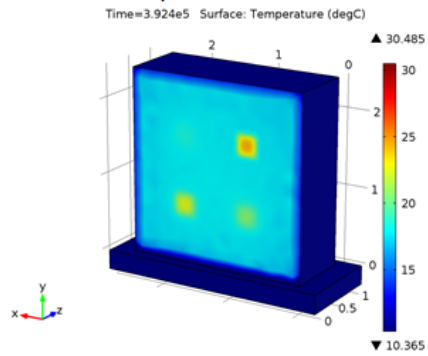
Name	Value
Data set	Cut Point3D (D) 5" target

Expression

Name	Value
Expression	T
Unit	degC
Description	Temperature

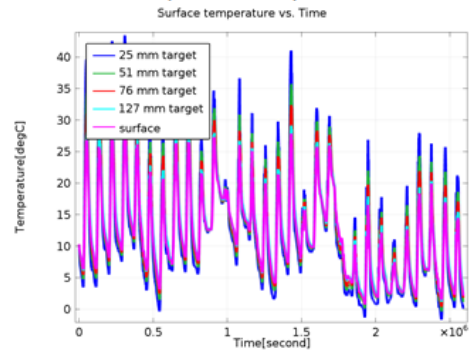
3.3 Plot Groups

3.3.1 3D Plot Group 1



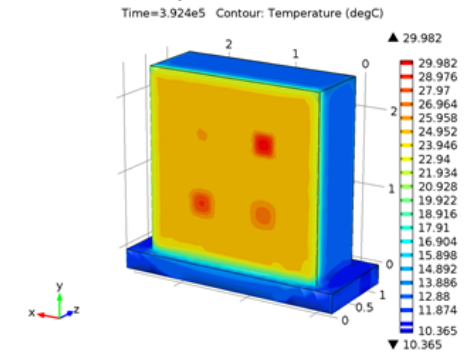
Time=3.924e5 Surface: Temperature (degC)

3.3.2 1D Plot Group 4 Surface Temperature



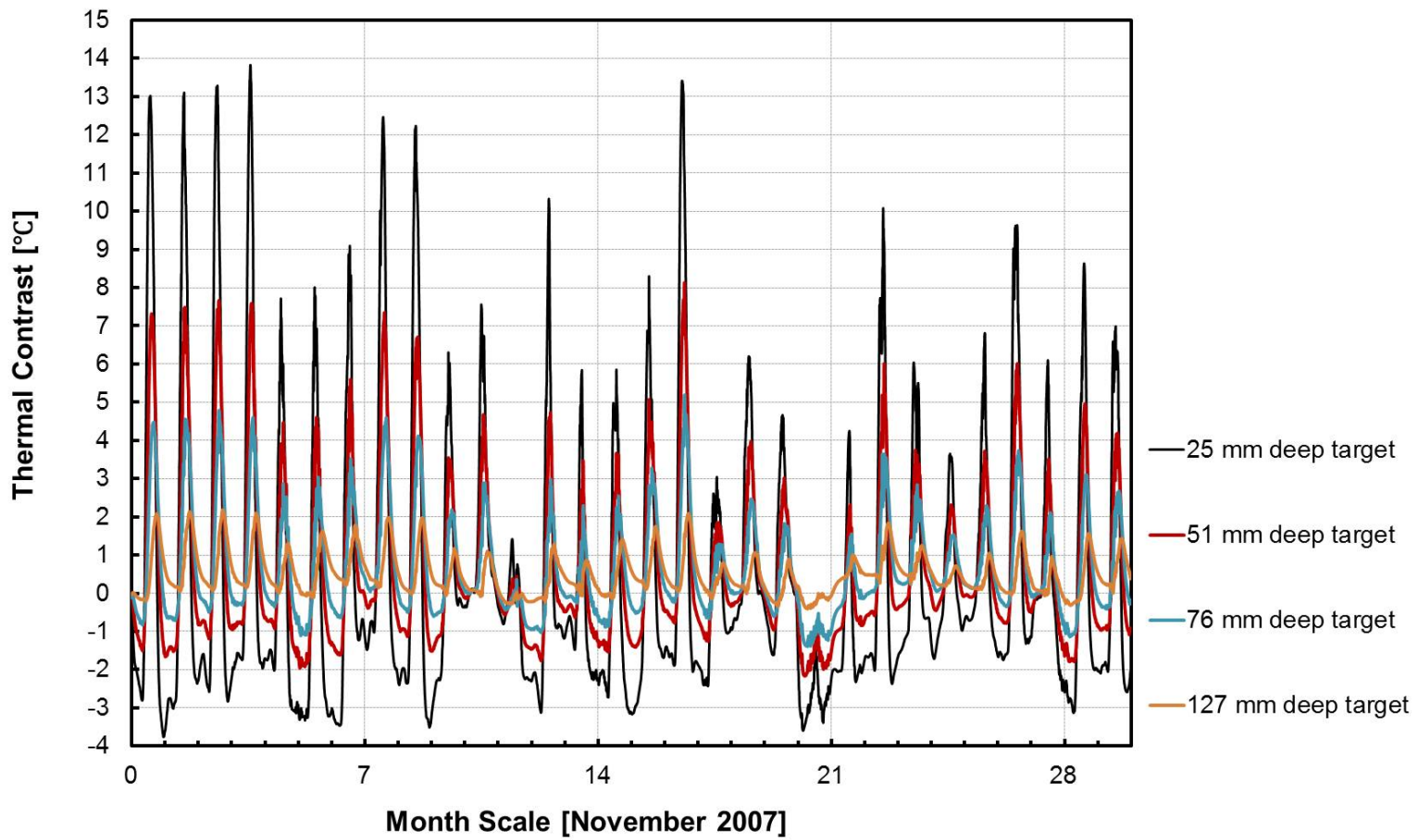
Surface temperature vs. Time

3.3.3 3D Plot Group 12

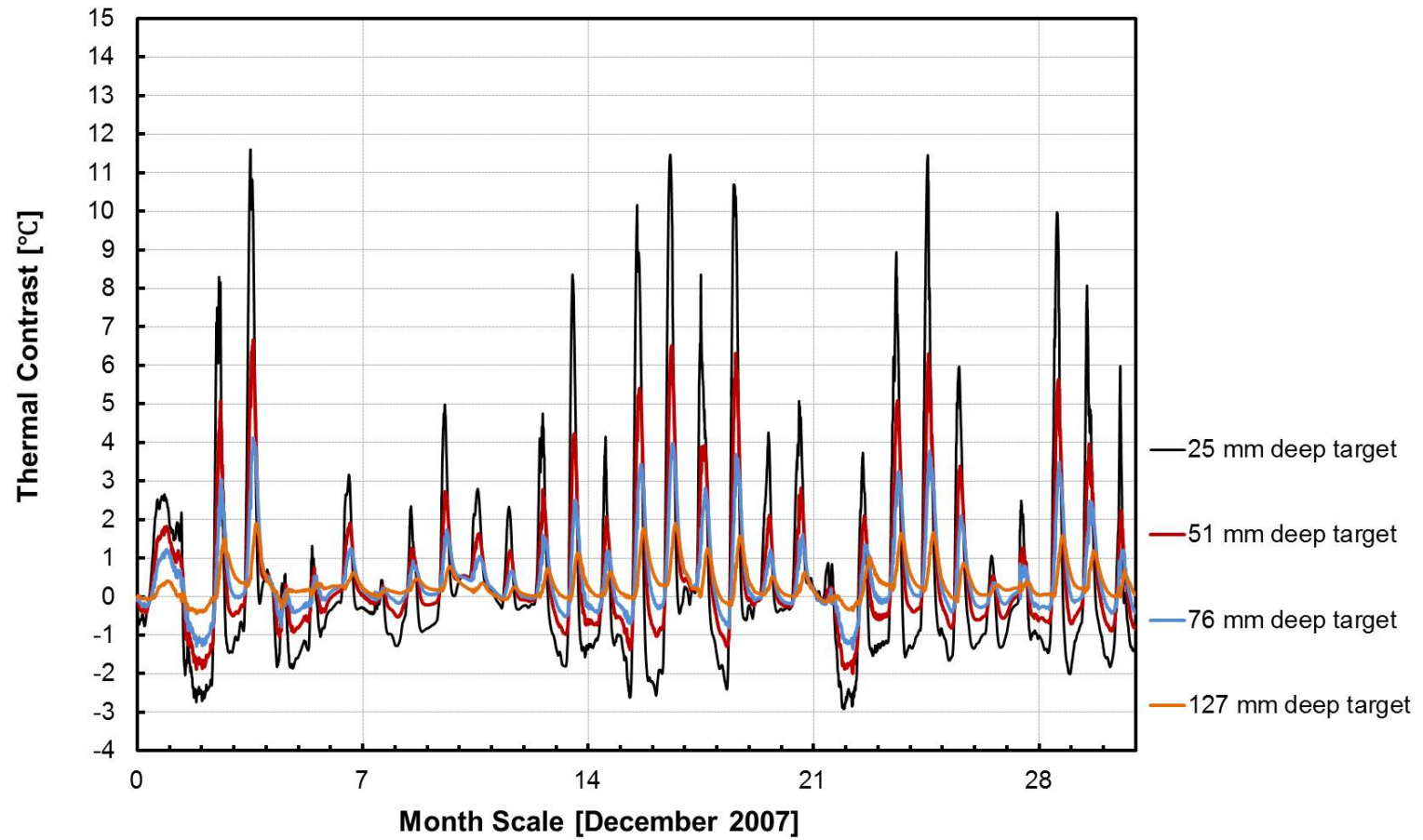


Time=3.924e5 Contour: Temperature (degC)

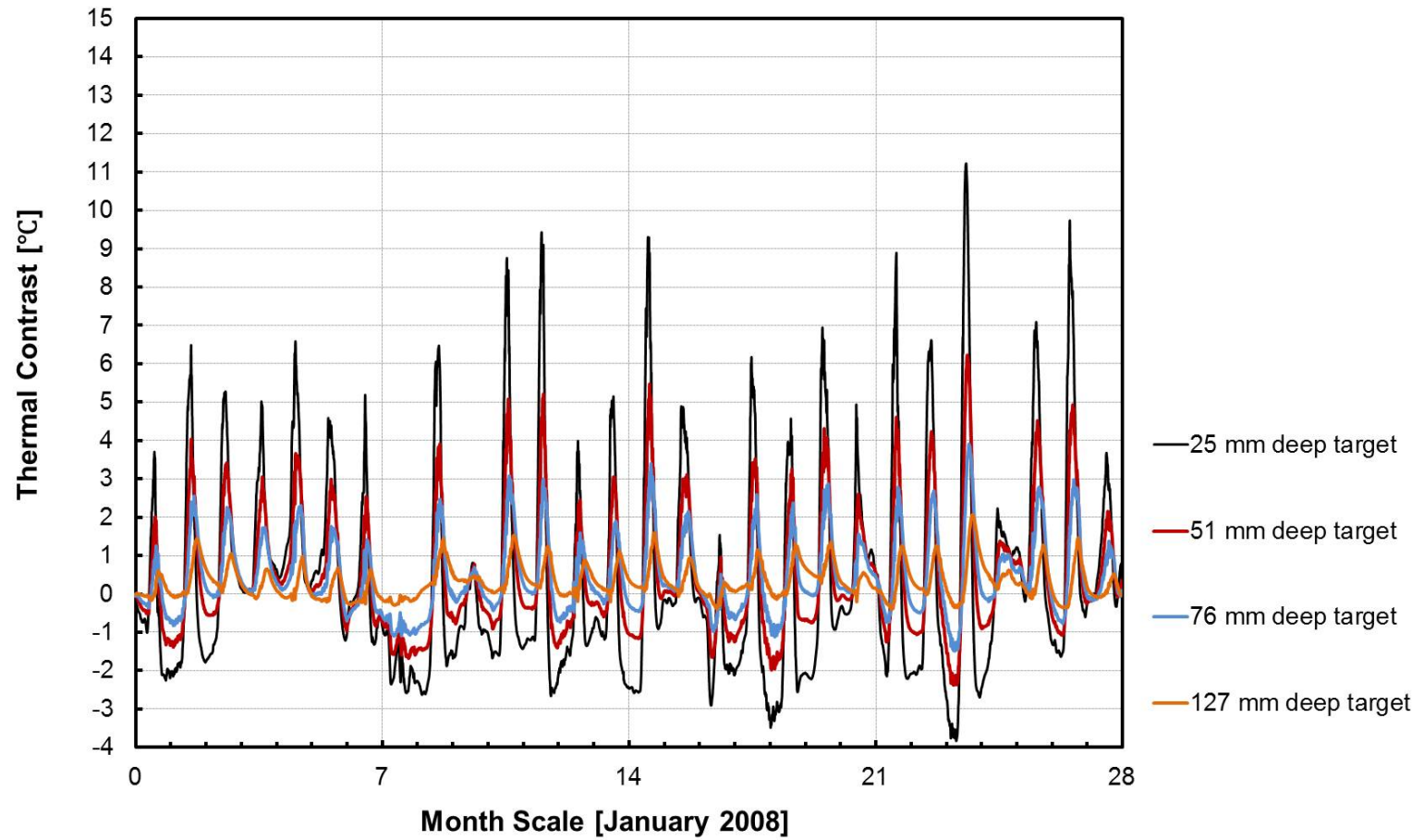
APPENDIX B
Thermal Contrast Results



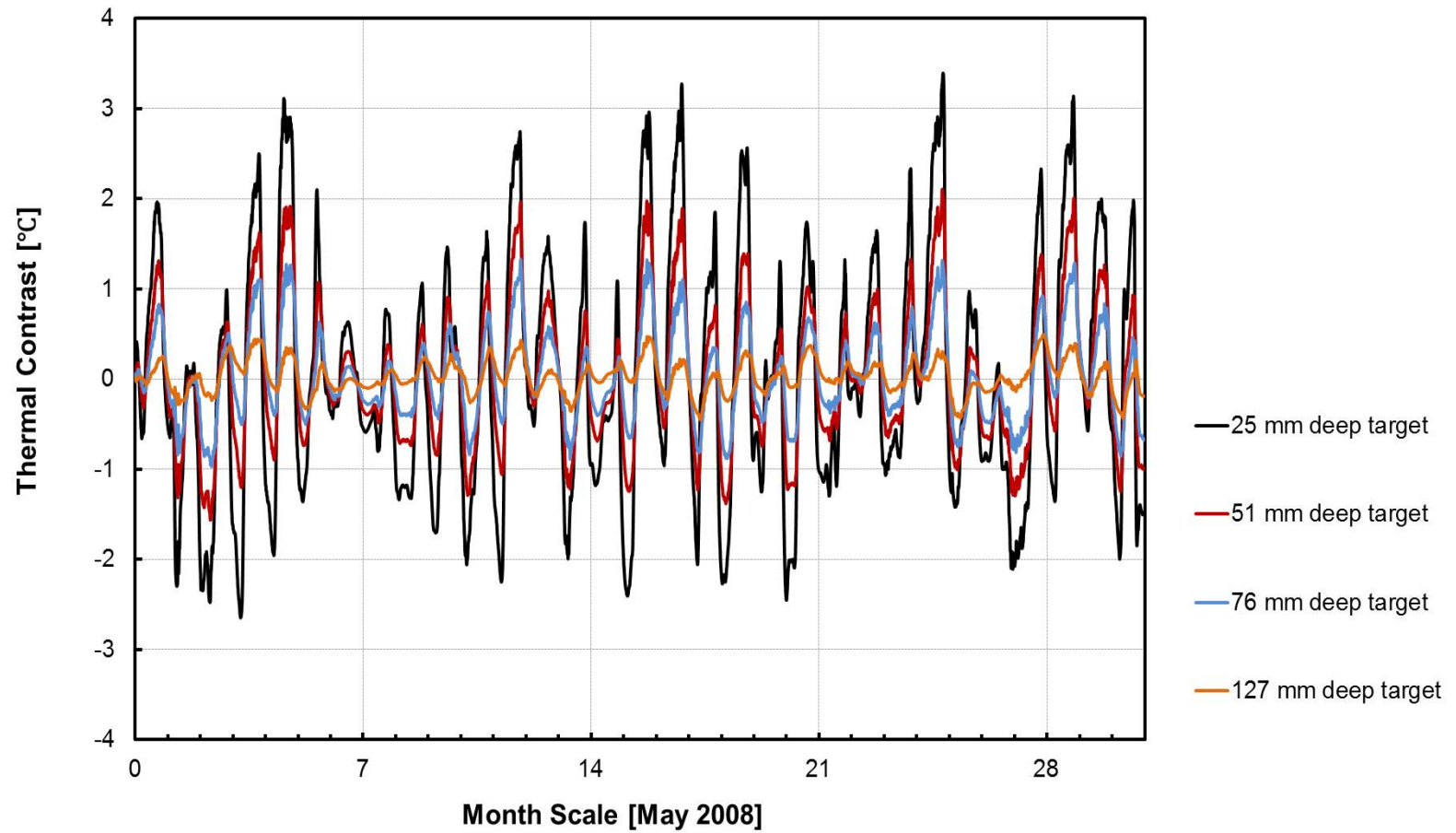
Appendix B. 1 The time varying thermal contrast for November 2007



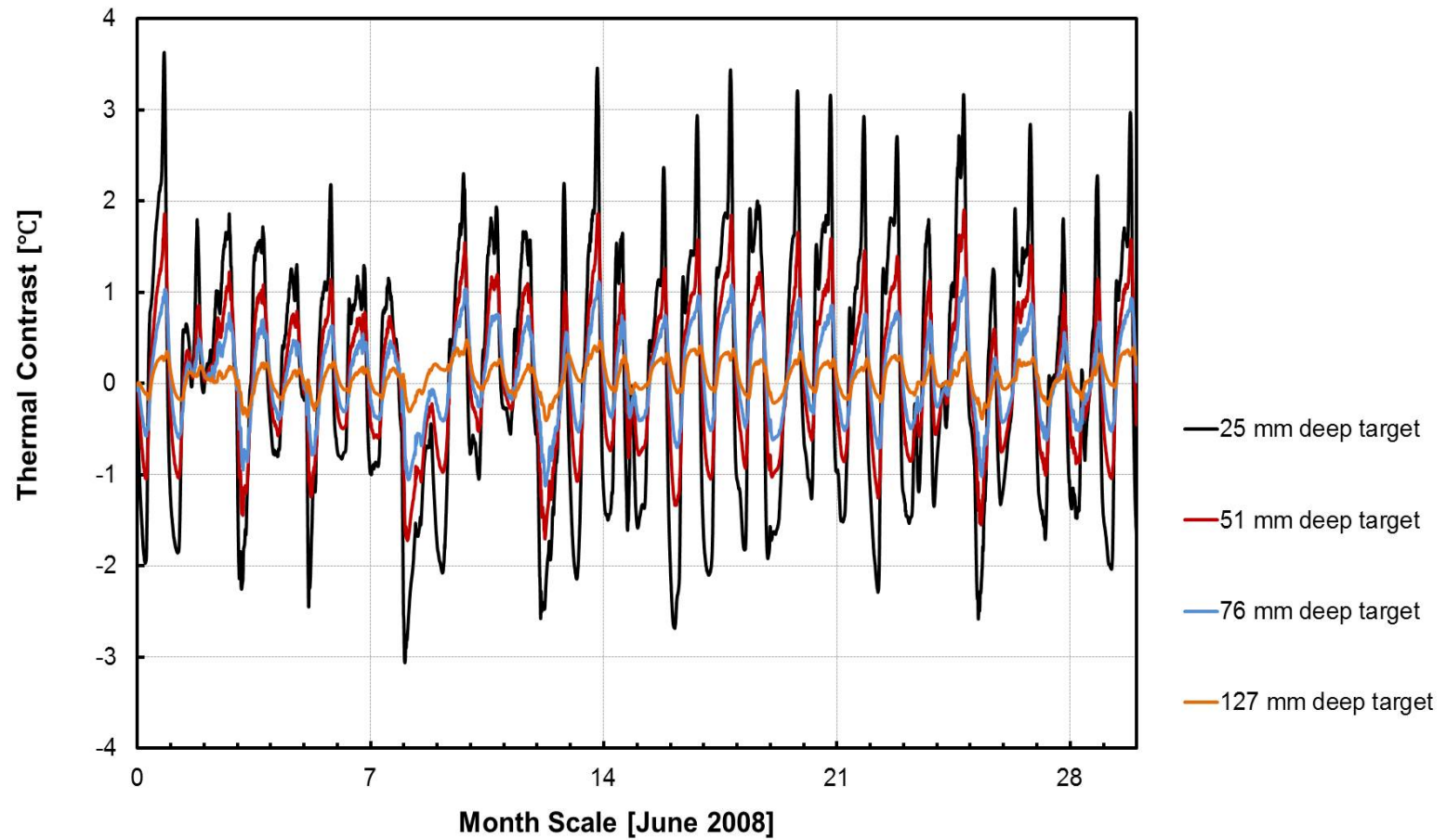
Appendix B. 2 The time varying thermal contrast for December 2007



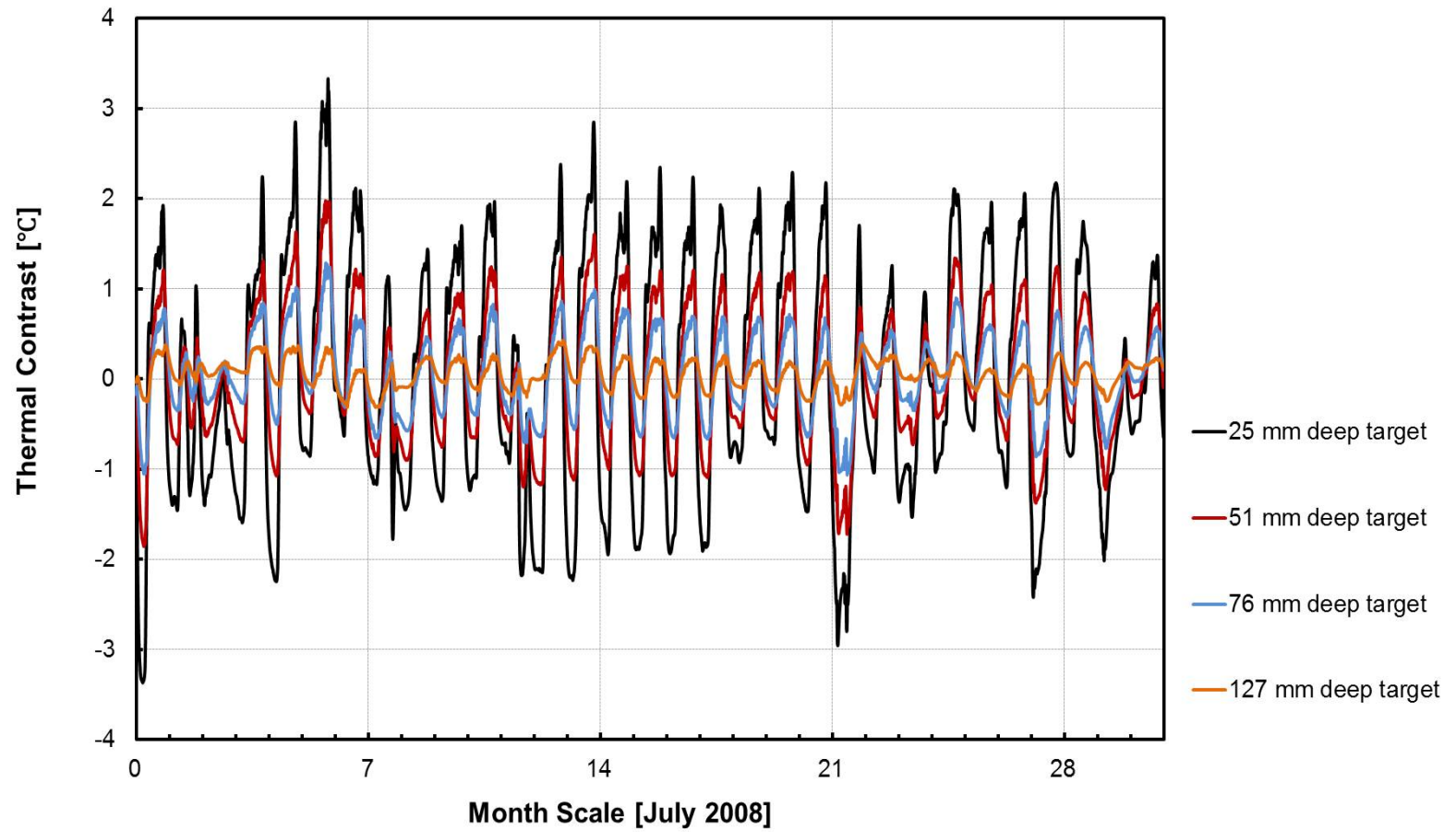
Appendix B. 3 The time varying thermal contrast for January 2008



Appendix B. 4 The time varying thermal contrast for May 2008

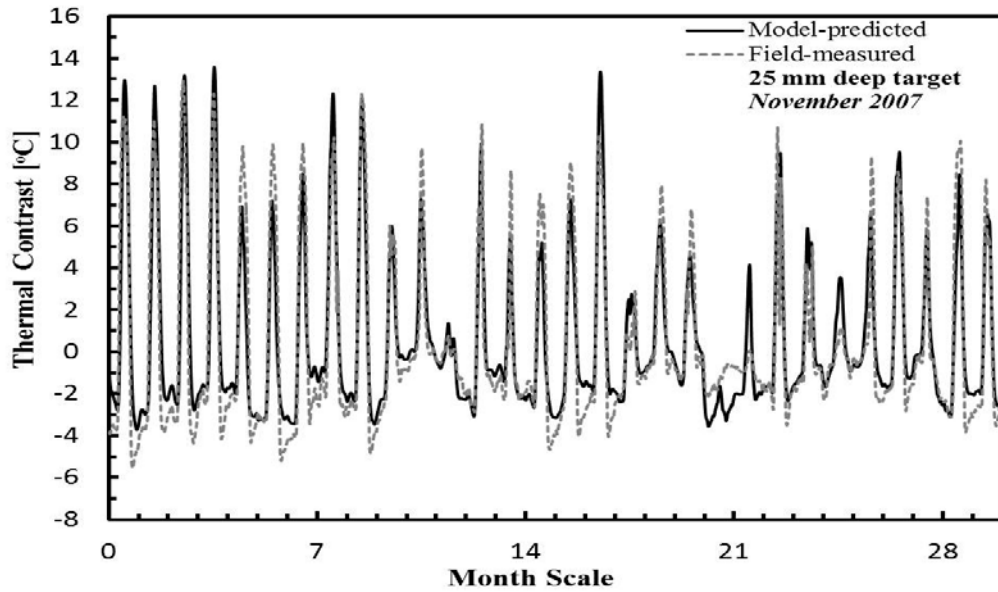


Appendix B. 5 The time varying thermal contrast for June 2008

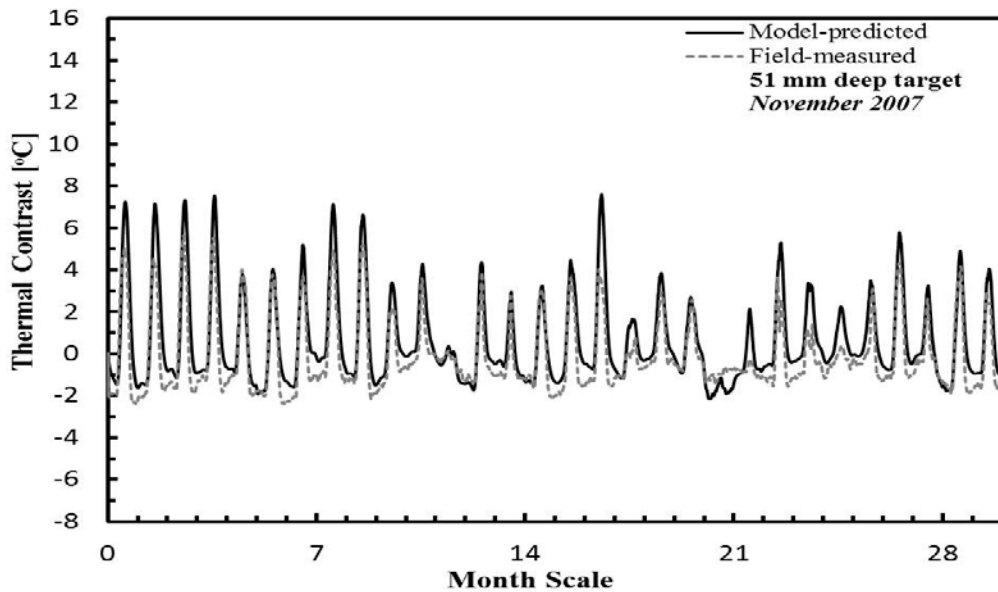


Appendix B. 6 The time varying thermal contrast for July 2008

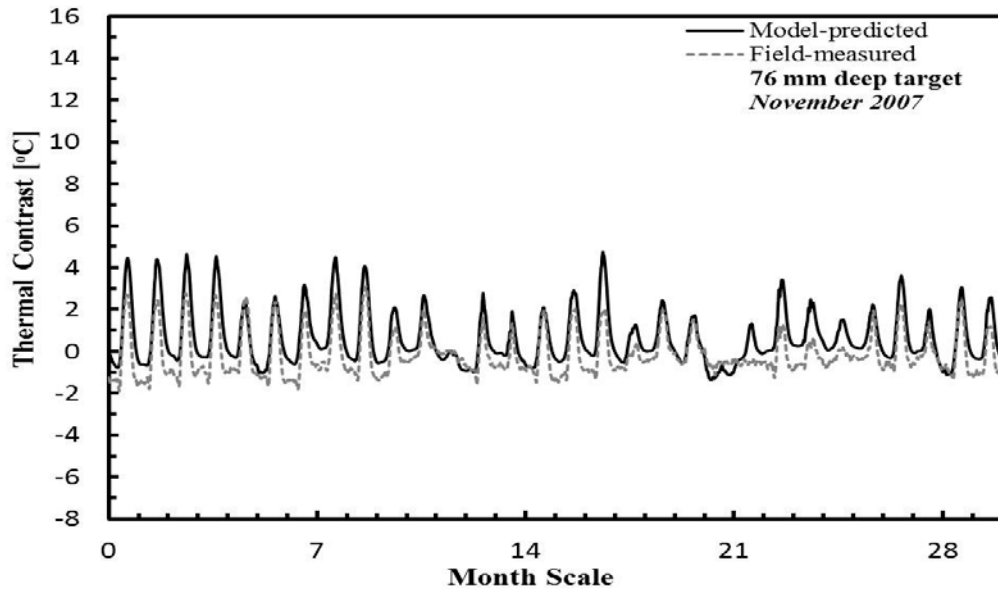
APPENDIX C
Comparison of Model Predicted and Field Measured Of
Thermal Contrast



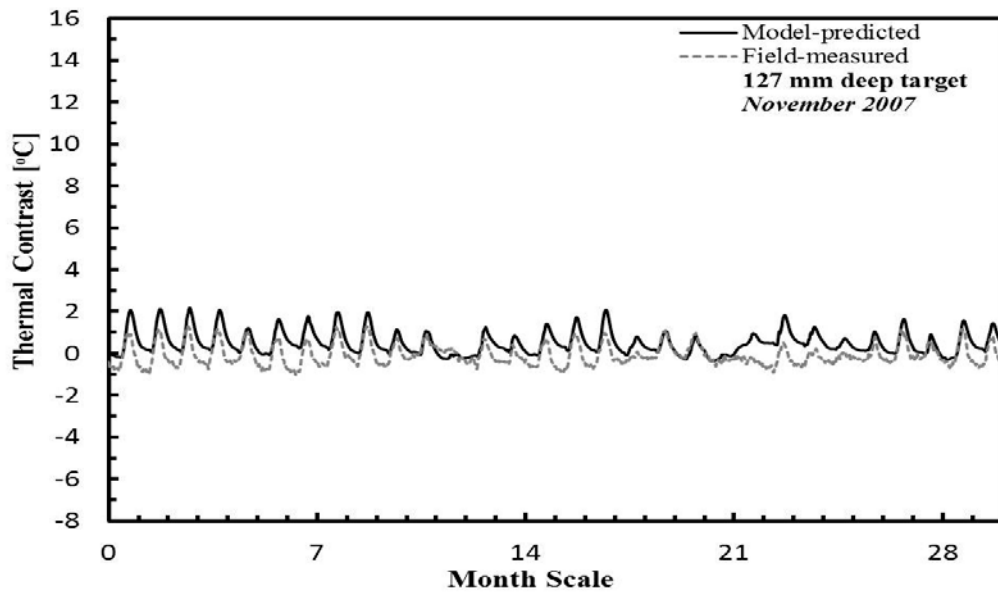
Appendix C. 1 Comparison of model predicted and field-measured of thermal contrast for 25 mm deep target of the Sunny side (Nov 2007)



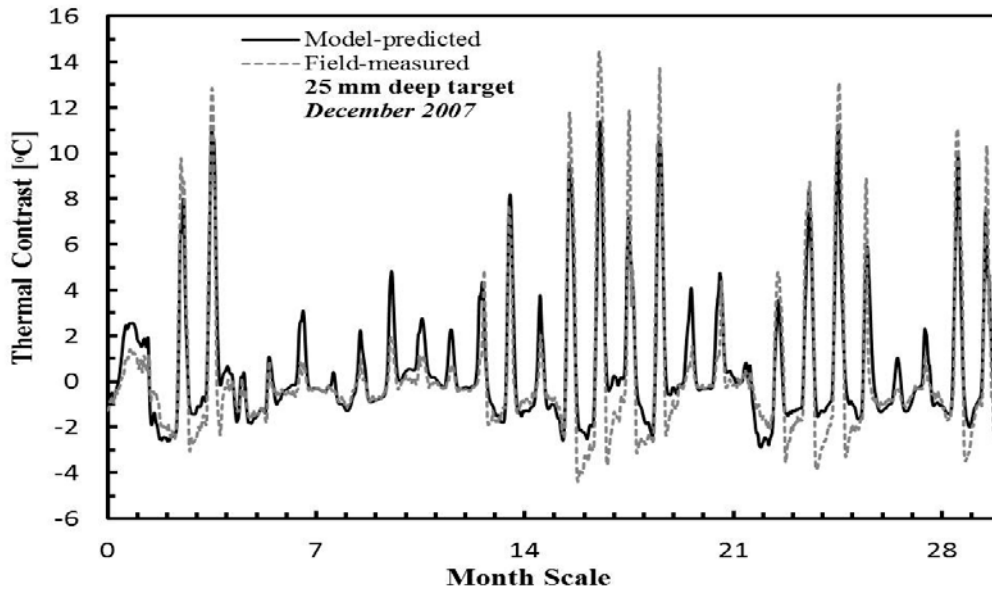
Appendix C. 2 Comparison of model predicted and field-measured of thermal contrast for 51 mm deep target of the Sunny side (Nov 2007)



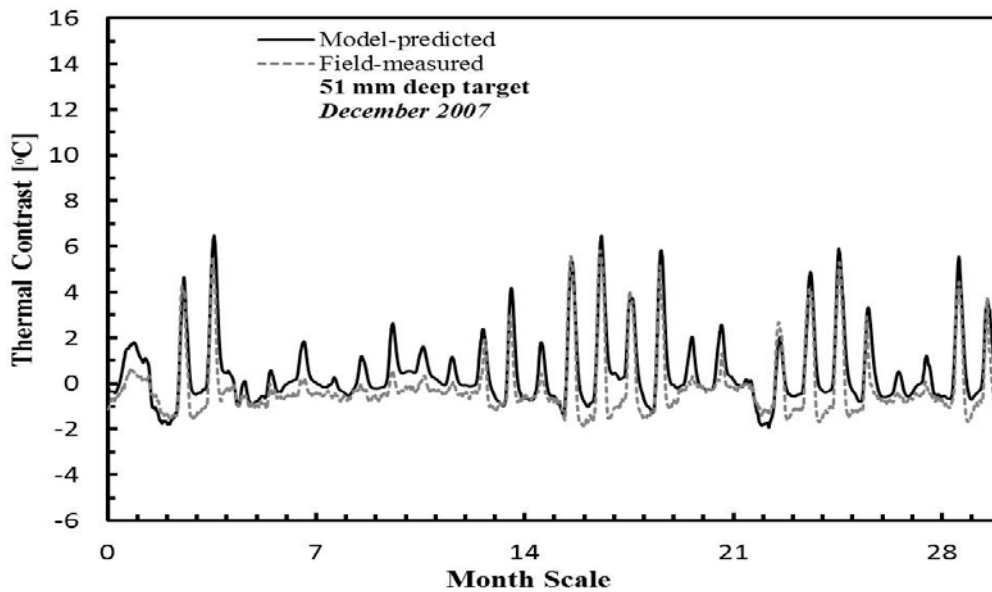
Appendix C. 3 Comparison of model predicted and field-measured of thermal contrast for 76 mm deep target of the Sunny side (Nov 2007)



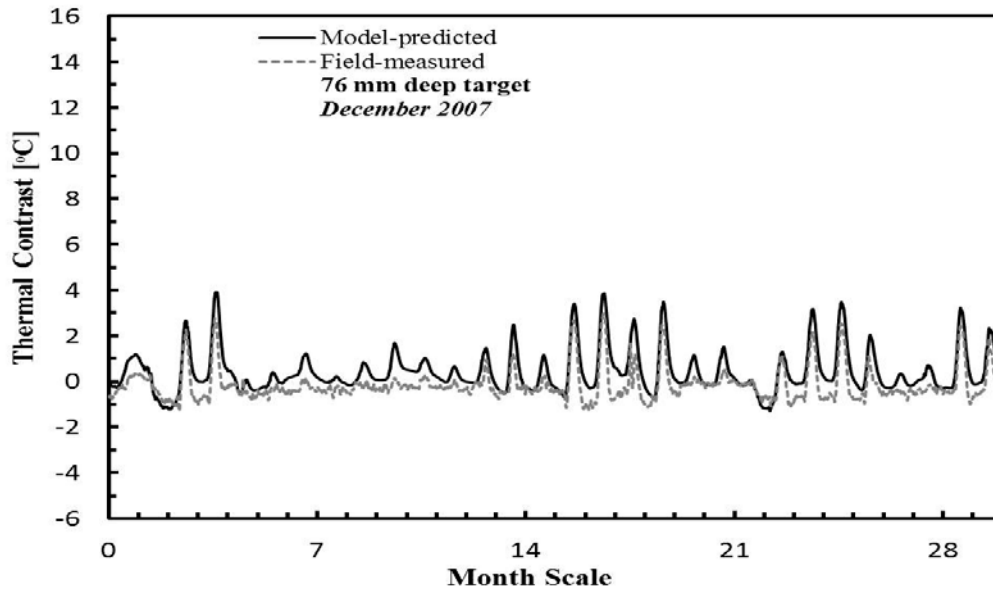
Appendix C. 4 Comparison of model predicted and field-measured of thermal contrast for 127 mm deep target of the Sunny side (Nov 2007)



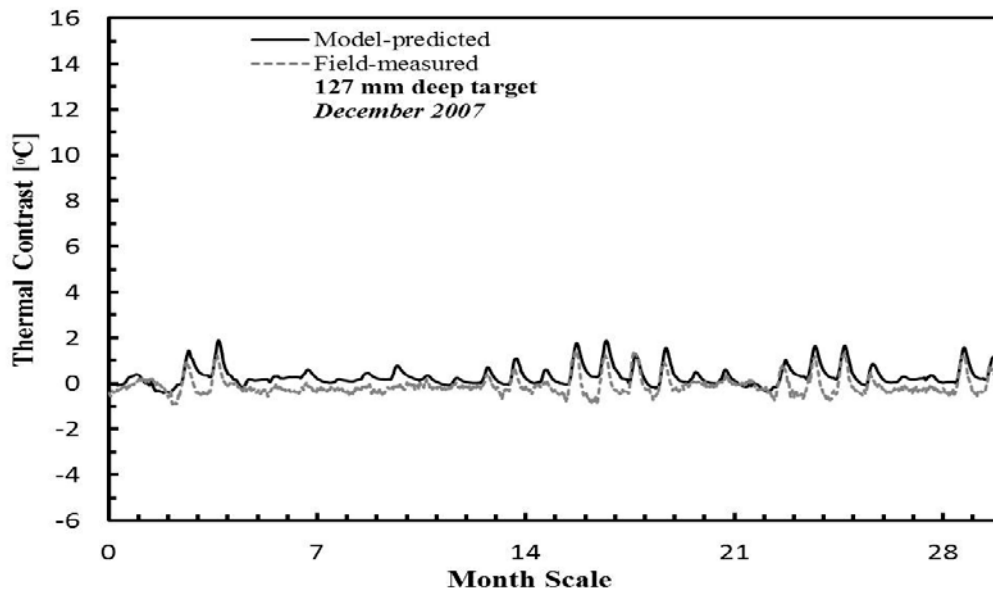
Appendix C. 5 Comparison of model predicted and field-measured of thermal contrast for 25 mm deep target of the Sunny side (Dec 2007)



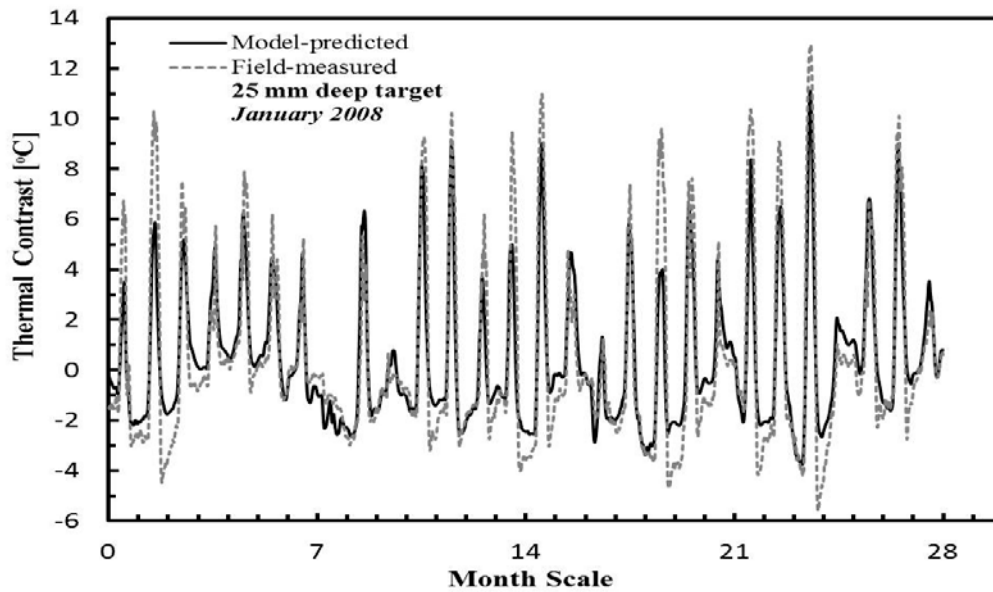
Appendix C. 6 Comparison of model predicted and field-measured of thermal contrast for 51 mm deep target of the Sunny side (Dec 2007)



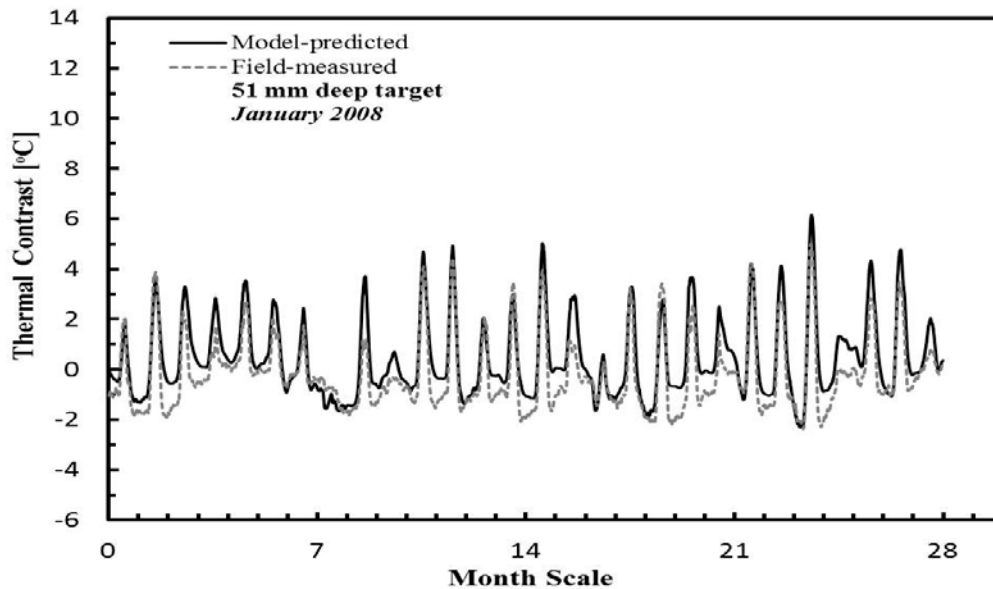
Appendix C. 7 Comparison of model predicted and field-measured of thermal contrast for 76 mm deep target of the Sunny side (Dec 2007)



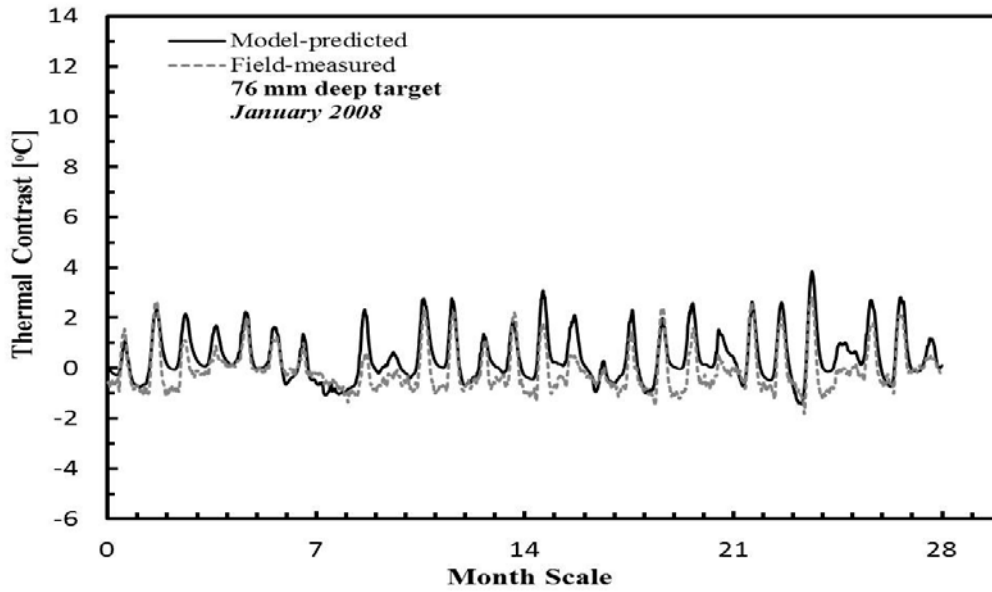
Appendix C. 8 Comparison of model predicted and field-measured of thermal contrast for 127 mm deep target of the Sunny side (Dec 2007)



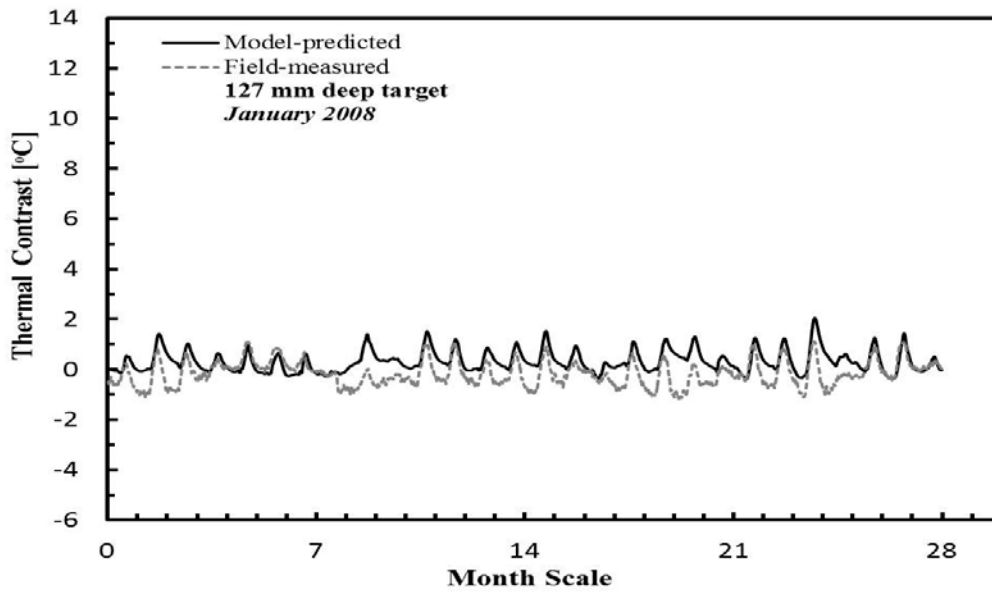
Appendix C. 9 Comparison of model predicted and field-measured of thermal contrast for 25 mm deep target of the Sunny side (Jan 2008)



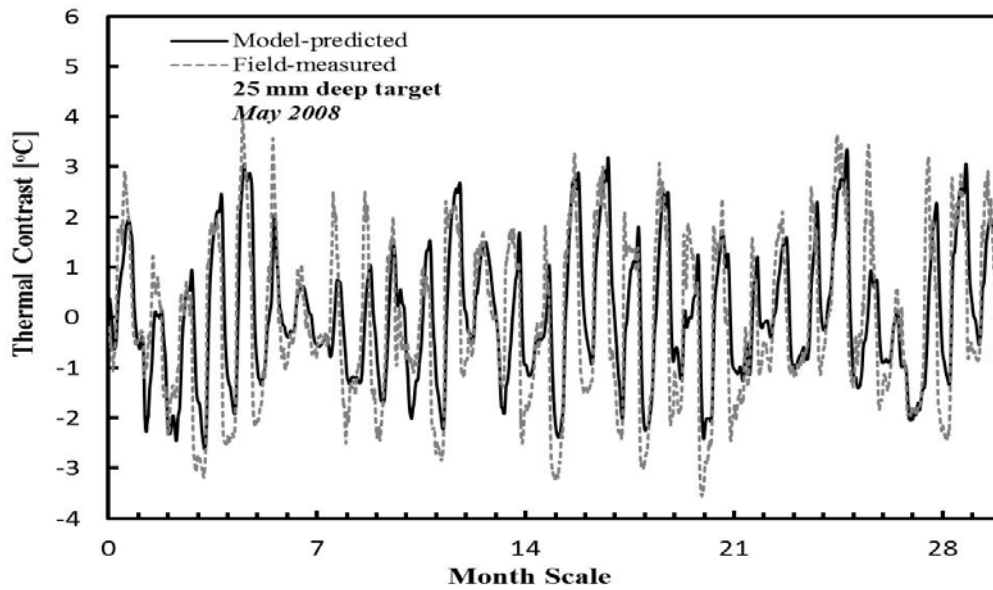
Appendix C. 10 Comparison of model predicted and field-measured of thermal contrast for 51 mm deep target of the Sunny side (Jan 2008)



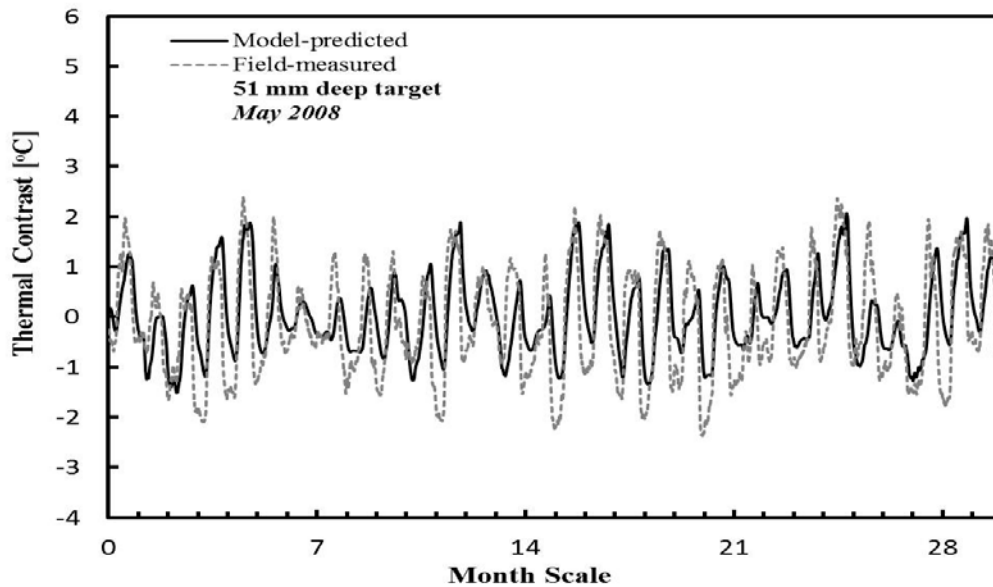
Appendix C. 11 Comparison of model predicted and field-measured of thermal contrast for 76 mm deep target of the Sunny side (Jan 2008)



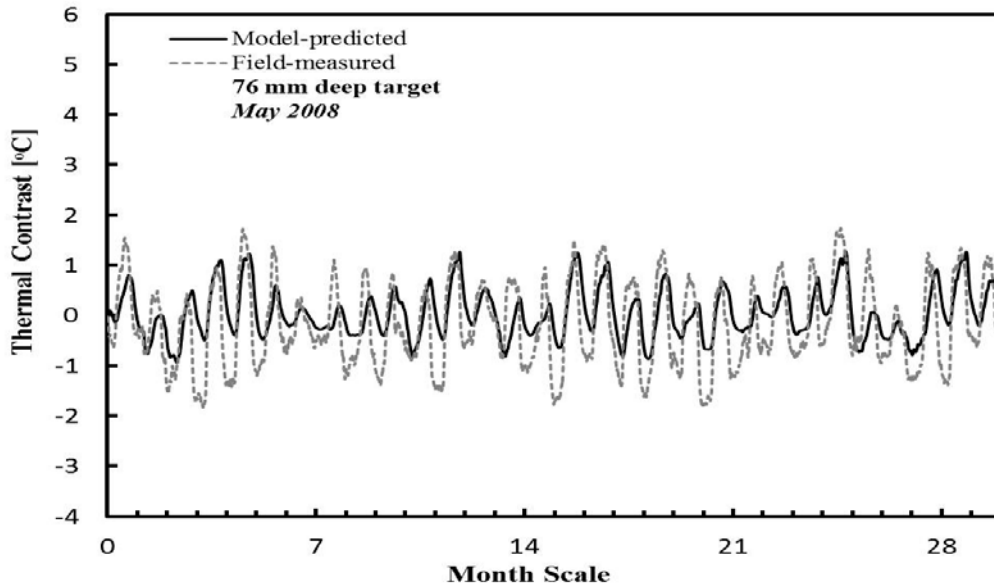
Appendix C. 12 Comparison of model predicted and field-measured of thermal contrast for 127 mm deep target of the Sunny side (Jan 2008)



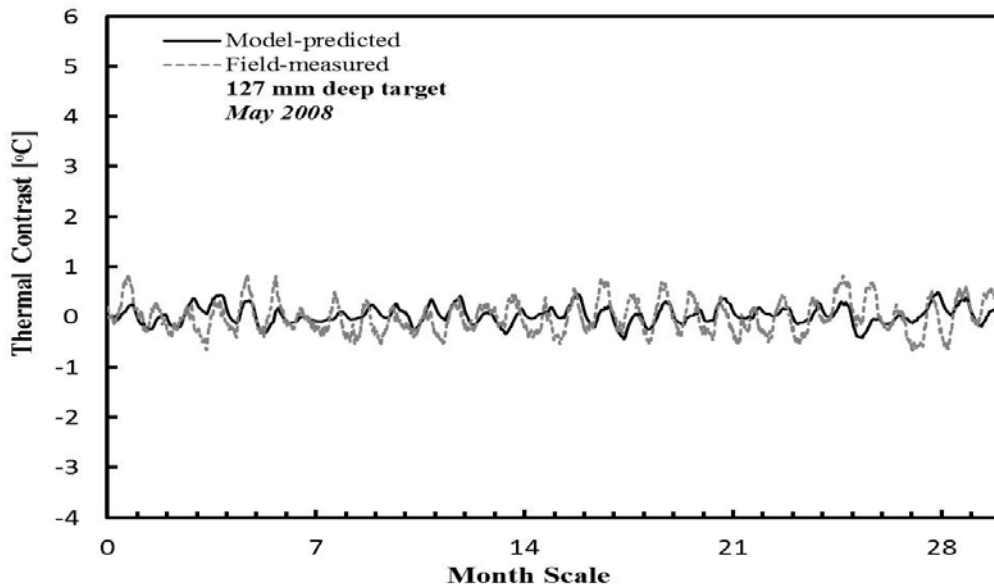
Appendix C. 13 Comparison of model predicted and field-measured of thermal contrast for 25 mm deep target of the Shaded side (May 2008)



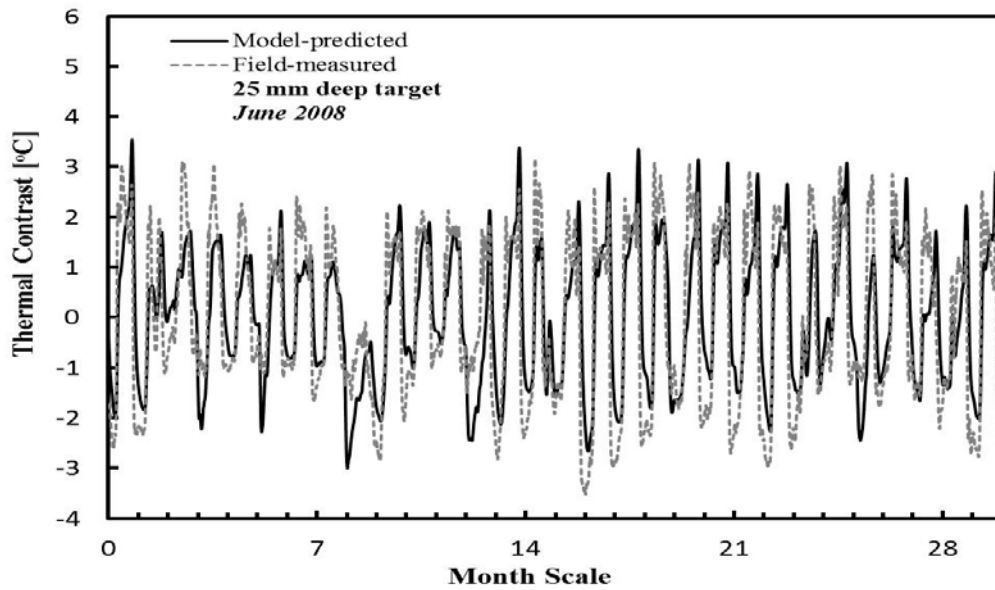
Appendix C. 14 Comparison of model predicted and field-measured of thermal contrast for 51 mm deep target of the Shaded side (May 2008)



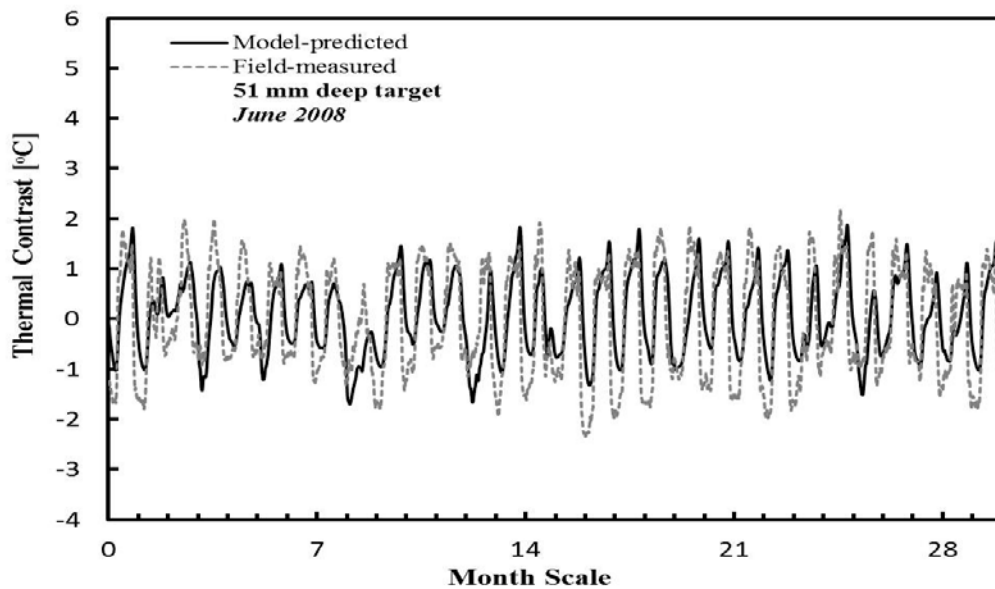
Appendix C. 15 Comparison of model predicted and field-measured of thermal contrast for 76 mm deep target of the Shaded side (May 2008)



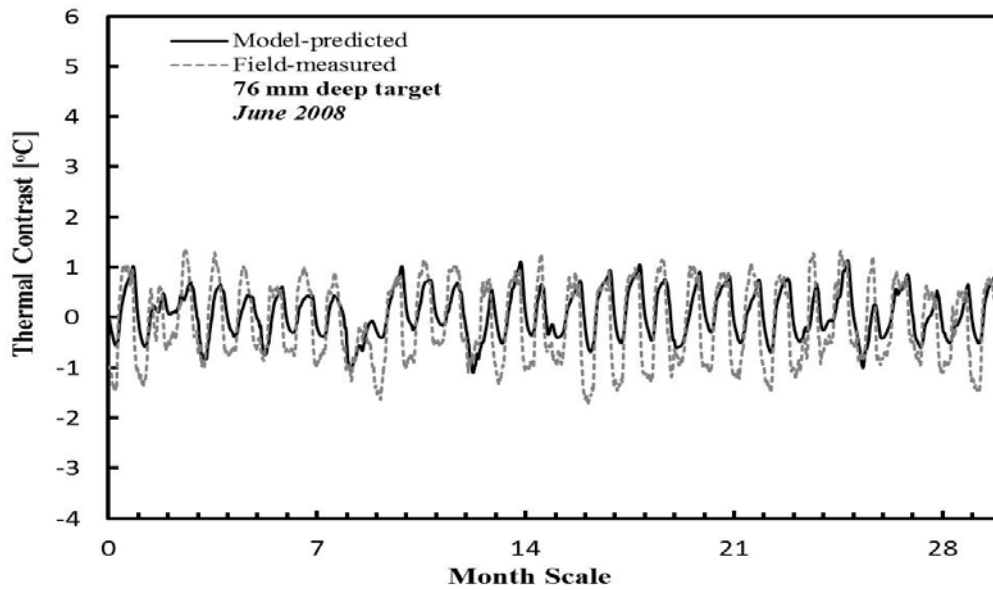
Appendix C. 16 Comparison of model predicted and field-measured of thermal contrast for 127 mm deep target of the Shaded side (May 2008)



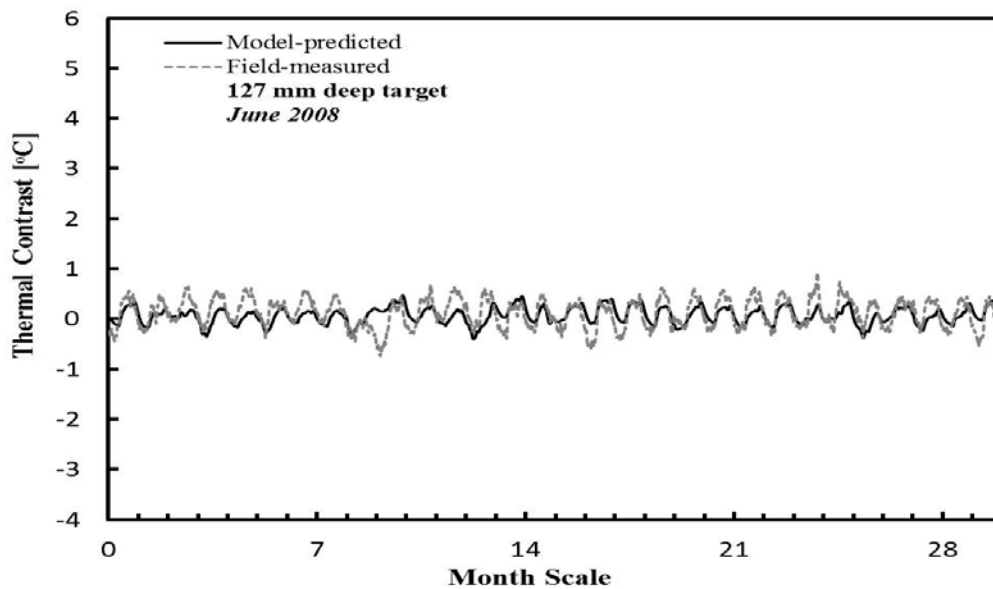
Appendix C. 17 Comparison of model predicted and field-measured of thermal contrast for 25 mm deep target of the Shaded side (June 2008)



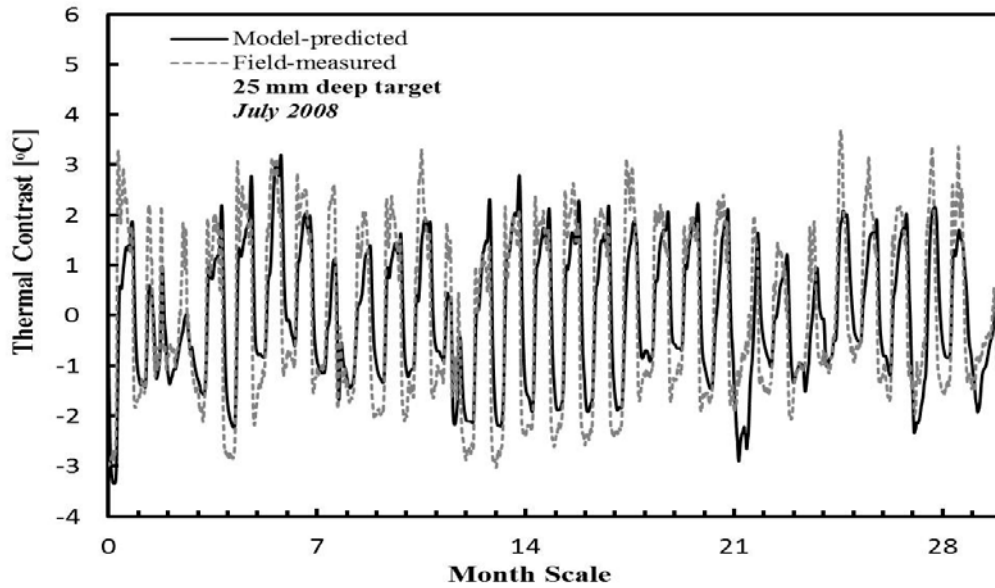
Appendix C. 18 Comparison of model predicted and field-measured of thermal contrast for 51 mm deep target of the Shaded side (June 2008)



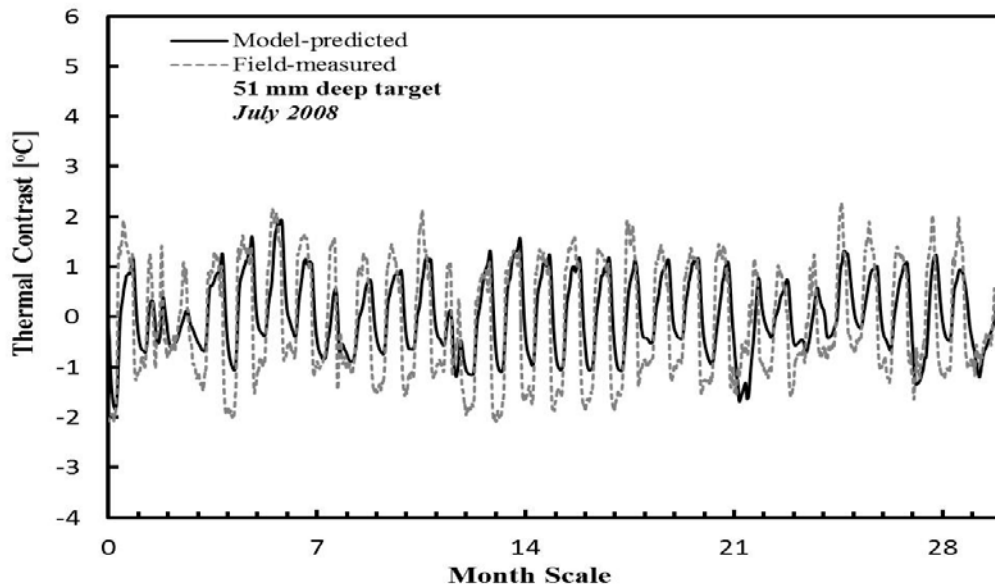
Appendix C. 19 Comparison of model predicted and field-measured of thermal contrast for 76 mm deep target of the Shaded side (June 2008)



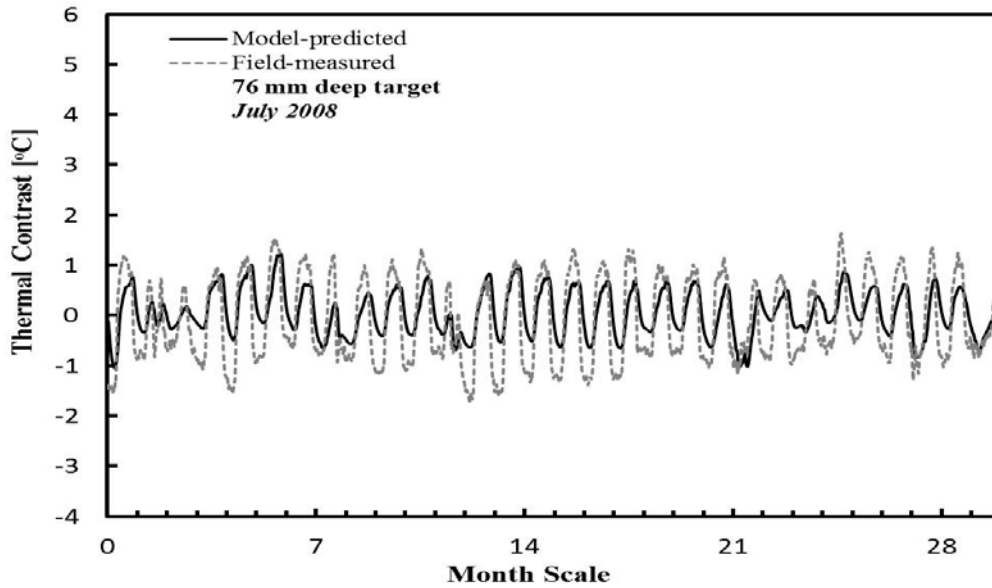
Appendix C. 20 Comparison of model predicted and field-measured of thermal contrast for 127 mm deep target of the Shaded side (June 2008)



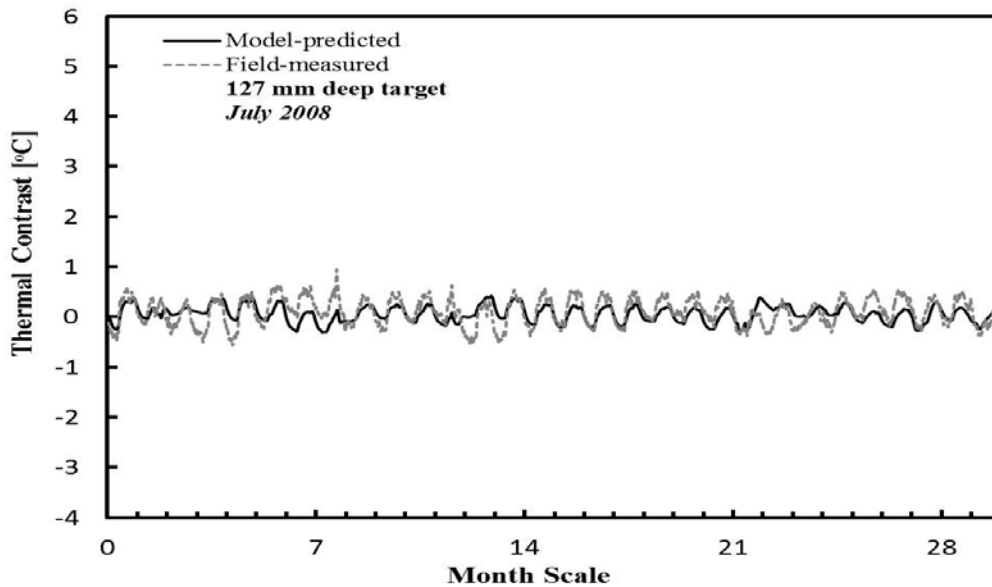
Appendix C. 21 Comparison of model predicted and field-measured of thermal contrast for 25 mm deep target of the Shaded side (July 2008)



Appendix C. 22 Comparison of model predicted and field-measured of thermal contrast for 51 mm deep target of the Shaded side (July 2008)



Appendix C. 23 Comparison of model predicted and field-measured of thermal contrast for 76 mm deep target of the Shaded side (July 2008)



Appendix C. 24 Comparison of model predicted and field-measured of thermal contrast for 127 mm deep target of the Shaded side (July 2008)

APPENDIX D
The Sunny (South) Dataset for Model Equation
Development

Appendix D. 1 Daily environmental variables, depth of voids, and daily maximum thermal contrast for the Sunny side datasets

Variables	Unit	Description of variable
<u>Predictor variables</u>		
$SL_{(Max)}$	[W/m ²]	Daily maximum solar loading
$SL_{(Total)}$	[W-hr/m ²]	Daily total solar loading
$SL_{(Total)}^{1/4}$	[W-hr/m ²] ^(1/4)	Non-linear transformation of the daily total solar loading
$SL_{(Total)-1}$	[W-hr/m ²]	Daily total solar loading of the previous day
$T_{air (Max)}$	[K]	Daily maximum ambient temperature
$T_{air (Min)}$	[K]	Daily minimum ambient temperature
$T_{air (Change)}$	[K]	Daily ambient temperature change = $T_{air (Max)} - T_{air (Min)}$
$T_{air (Avg)}$	[K]	Daily average ambient temperature
$T_{air (Avg)-1}$	[K]	Daily average ambient temperature of the previous day
$W_{(Avg 1)}$	[m/s]	Average wind speed during quarter 1 (12 a.m. to 6 a.m.)
$W_{(Avg 2)}$	[m/s]	Average wind speed during quarter 2 (6 a.m. to 12 p.m.)
$W_{(Avg 3)}$	[m/s]	Average wind speed during quarter 3 (12 p.m. to 6 p.m.)
$W_{(Avg 4)}$	[m/s]	Average wind speed during quarter 4 (6 p.m. to 12 a.m.)
$W_{(Avg 23)}$	[m/s]	Average wind speed during quarter 2 & 3 (6 a.m. to 6 p.m.)
$W_{(Avg)}$	[m/s]	Daily average wind speed
$W_{(Max)}$	[m/s]	Daily maximum wind speed
d	[mm]	Depth of void
$e^{-0.02 \cdot depth}$		Exponential transformation of the depth of void
<u>Response variable</u>		
$\Delta T_{(Max)}$ obtained from FEM simulat	[°C]	Daily maximum thermal contrast

ID	Date	Daily Solar Loading				Daily Ambient Temperature					Daily Wind Speed						Depth of void		$\Delta T_{(Max)}$ obtained from FEM simulation	
		SL _(Max)	SL _(Total)	SL _(Total) ^{1/4}	SL _{(Total)-1}	T _{air (Max)}	T _{air (Min)}	T _{air (Change)}	T _{air (Avg)}	T _{air (Avg)-1}	W _(Avg 1)	W _(Avg 2)	W _(Avg 3)	W _(Avg 4)	W _(Avg 23)	W _(Avg)	W _(Max)	d		e ^{-0.02*depth}
1	November 5, 2007	397.88	2138.04	6.80	2209.72	289.87	276.76	13.11	282.95	283.83	0.34	2.40	3.84	2.24	3.12	2.20	7.02	25	0.6065	6.94
2	November 6, 2007	426.09	2309.05	6.93	2138.04	280.37	269.93	10.44	275.45	282.95	1.98	2.84	2.65	0.02	2.74	1.87	6.17	25	0.6065	7.21
3	November 7, 2007	409.66	2103.72	6.77	2309.05	283.15	265.93	17.22	276.01	275.45	0.00	1.75	2.92	1.49	2.33	1.54	5.50	25	0.6065	8.51
4	November 10, 2007	369.68	1814.67	6.53	2113.48	288.43	274.43	14.00	282.36	280.01	0.11	3.34	4.31	4.53	3.82	3.07	6.62	25	0.6065	5.98
5	November 11, 2007	390.78	1372.20	6.09	1814.67	298.15	284.54	13.61	291.09	282.36	3.74	3.23	3.93	1.49	3.58	3.10	7.47	25	0.6065	7.27
6	November 15, 2007	419.63	2206.30	6.85	1328.61	281.37	270.26	11.11	276.35	282.89	3.31	3.50	3.09	0.10	3.30	2.50	7.06	25	0.6065	5.21
7	November 16, 2007	397.24	2129.73	6.79	2206.30	288.43	269.65	18.78	278.55	276.35	0.92	3.28	3.51	0.29	3.39	2.00	6.71	25	0.6065	7.25
8	November 18, 2007	217.74	1007.52	5.63	2039.69	285.04	276.54	8.50	280.60	282.46	1.66	2.96	2.72	1.28	2.84	2.15	5.54	25	0.6065	2.74
9	November 19, 2007	406.79	1635.28	6.36	1007.52	295.43	279.54	15.89	288.30	280.60	1.24	3.49	5.51	3.90	4.50	3.54	9.30	25	0.6065	6.15
10	November 20, 2007	375.06	1358.78	6.07	1635.28	295.37	283.43	11.94	290.05	288.30	1.13	2.99	4.50	3.40	3.75	3.01	7.69	25	0.6065	4.55
11	November 22, 2007	176.97	750.81	5.23	1358.78	272.87	270.54	2.33	271.53	290.05	0.00	0.00	1.88	1.59	0.94	0.87	4.25	25	0.6065	4.15
12	November 24, 2007	423.53	1087.06	5.74	1598.53	277.37	270.76	6.61	273.98	271.25	0.35	1.11	1.78	0.01	1.45	0.81	3.26	25	0.6065	5.89
13	November 28, 2007	435.08	1077.37	5.73	1773.65	287.43	273.26	14.17	280.33	276.93	5.43	4.96	3.81	3.01	4.39	4.30	8.00	25	0.6065	5.81
14	November 29, 2007	350.92	1827.31	6.54	1077.37	280.37	266.26	14.11	273.69	280.33	1.53	2.49	1.87	1.31	2.18	1.80	5.19	25	0.6065	8.47
15	November 30, 2007	336.67	1518.91	6.24	1827.31	277.26	268.04	9.22	272.73	273.69	0.70	1.45	1.96	1.64	1.71	1.44	4.02	25	0.6065	6.57
16	December 3, 2007	345.04	1743.19	6.46	1518.91	277.15	266.26	10.89	271.14	272.73	1.75	2.24	2.78	0.88	2.51	1.91	4.65	25	0.6065	7.99
17	December 13, 2007	238.87	781.89	5.29	297.02	276.04	269.15	6.89	273.18	272.92	0.00	0.01	2.42	0.16	1.21	0.65	4.96	25	0.6065	4.36
18	December 18, 2007	314.14	1481.58	6.20	1616.37	281.15	270.76	10.39	275.58	269.31	2.13	1.89	3.10	0.44	2.50	1.89	7.78	25	0.6065	7.18
19	December 21, 2007	248.27	703.86	5.15	440.13	285.04	275.93	9.11	280.49	277.57	0.12	0.68	3.62	4.31	2.15	2.18	6.71	25	0.6065	4.77
20	December 24, 2007	314.23	1599.97	6.32	703.86	276.76	267.26	9.50	271.25	280.49	2.15	2.47	1.80	0.22	2.14	1.66	4.78	25	0.6065	8.48
21	December 30, 2007	322.16	1317.52	6.02	1595.75	278.76	269.87	8.89	273.98	271.18	1.02	1.38	2.54	1.05	1.96	1.50	5.10	25	0.6065	7.50
22	December 31, 2007	275.15	804.79	5.33	1317.52	275.26	268.43	6.83	271.60	273.98	0.26	0.59	3.65	4.21	2.12	2.18	6.17	25	0.6065	5.28
23	January 1, 2008	374.07	1502.83	6.23	804.79	269.37	260.43	8.94	265.66	271.60	3.72	5.63	5.15	4.04	5.39	4.63	9.16	25	0.6065	3.50
24	January 2, 2008	325.88	1663.71	6.39	1502.83	267.04	258.87	8.17	261.97	265.66	3.16	2.79	2.40	0.08	2.59	2.11	5.54	25	0.6065	5.88
25	January 3, 2008	329.73	1374.20	6.09	1663.71	275.37	259.76	15.61	268.26	261.97	0.95	3.46	4.78	4.86	4.12	3.51	7.24	25	0.6065	5.20
26	January 4, 2008	278.78	1055.89	5.70	1374.20	282.15	270.43	11.72	276.16	268.26	3.95	5.66	5.92	4.72	5.79	5.06	9.39	25	0.6065	4.88
27	January 5, 2008	400.30	1282.86	5.98	1055.89	290.87	278.15	12.72	284.31	276.16	4.32	4.26	4.65	4.19	4.45	4.35	8.85	25	0.6065	6.23
28	January 6, 2008	281.92	1167.76	5.85	1282.86	294.37	284.87	9.50	289.09	284.31	4.24	4.81	4.80	1.16	4.81	3.75	10.82	25	0.6065	4.46
29	January 9, 2008	367.78	1197.19	5.88	1167.76	279.54	268.76	10.78	274.07	289.09	0.47	0.93	2.13	2.33	1.53	1.46	4.25	25	0.6065	6.34
30	January 11, 2008	328.55	1685.85	6.41	1197.19	278.93	268.87	10.06	273.50	274.07	1.71	0.69	2.21	0.19	1.45	1.20	5.99	25	0.6065	8.17
31	January 12, 2008	328.04	1660.66	6.38	1685.85	281.26	271.04	10.22	274.77	273.50	1.22	1.22	3.47	3.33	2.34	2.31	5.50	25	0.6065	8.93
32	January 13, 2008	483.90	1272.40	5.97	1660.66	273.15	269.87	3.28	271.17	274.77	2.81	3.09	3.63	2.14	3.36	2.92	6.26	25	0.6065	3.70
33	January 14, 2008	355.89	1662.25	6.39	1272.40	273.65	264.54	9.11	270.46	271.17	3.40	3.12	3.47	1.26	3.30	2.81	5.63	25	0.6065	5.02
34	January 15, 2008	339.28	1770.14	6.49	1662.25	275.54	261.04	14.50	269.09	270.46	0.06	1.39	2.70	3.26	2.04	1.85	4.34	25	0.6065	9.03
35	January 16, 2008	210.09	1012.21	5.64	1770.14	281.65	272.37	9.28	276.92	269.09	3.60	3.82	2.73	2.90	3.28	3.26	7.15	25	0.6065	4.69

ID	Date	Daily Solar Loading				Daily Ambient Temperature					Daily Wind Speed						Depth of void		$\Delta T_{(Max)}$ obtained from FEM simulation	
		SL _(Max)	SL _(Total)	SL _(Total) ^{1/4}	SL _(Total) -1	T _{air (Max)}	T _{air (Min)}	T _{air (Change)}	T _{air (Avg)}	T _{air (Avg)} -1	W _(Avg 1)	W _(Avg 2)	W _(Avg 3)	W _(Avg 4)	W _(Avg 23)	W _(Avg)	W _(Max)	d		e ^{-0.02*depth}
36	January 19, 2008	362.00	1906.32	6.61	1012.21	263.87	256.65	7.22	259.57	276.92	2.27	2.41	3.17	0.95	2.79	2.20	5.19	25	0.6065	4.01
37	January 20, 2008	400.43	1652.59	6.38	1906.32	268.37	255.04	13.33	262.55	259.57	0.19	1.87	3.23	3.76	2.55	2.26	5.41	25	0.6065	6.56
38	January 23, 2008	357.93	1884.84	6.59	1652.59	277.87	260.76	17.11	268.25	262.55	1.71	3.05	4.73	3.54	3.89	3.26	7.38	25	0.6065	6.51
39	January 26, 2008	359.26	1767.75	6.48	520.59	283.54	268.26	15.28	275.54	267.14	2.32	3.50	4.59	1.36	4.05	2.94	7.78	25	0.6065	6.83
40	January 27, 2008	393.91	1945.55	6.64	1767.75	286.87	269.37	17.50	278.11	275.54	1.55	2.05	3.55	3.13	2.80	2.57	5.86	25	0.6065	8.99
41	November 2, 2007	459.83	1992.74	6.68	2238.11	290.43	271.04	19.39	280.21	279.04	0.15	1.47	0.56	0.06	1.02	0.56	3.62	51	0.3606	7.16
42	November 3, 2007	472.06	2191.14	6.84	1992.74	288.04	272.37	15.67	280.96	280.21	0.49	0.25	0.83	0.46	0.54	0.51	2.82	51	0.3606	7.33
43	November 4, 2007	409.39	2209.72	6.86	2191.14	290.87	277.65	13.22	283.83	280.96	1.82	1.32	1.82	0.72	1.57	1.42	4.34	51	0.3606	7.54
44	November 5, 2007	397.88	2138.04	6.80	2209.72	289.87	276.76	13.11	282.95	283.83	0.34	2.40	3.84	2.24	3.12	2.20	7.02	51	0.3606	3.81
45	November 6, 2007	426.09	2309.05	6.93	2138.04	280.37	269.93	10.44	275.45	282.95	1.98	2.84	2.65	0.02	2.74	1.87	6.17	51	0.3606	4.03
46	November 7, 2007	409.66	2103.72	6.77	2309.05	283.15	265.93	17.22	276.01	275.45	0.00	1.75	2.92	1.49	2.33	1.54	5.50	51	0.3606	5.20
47	November 8, 2007	399.32	2022.06	6.71	2103.72	289.76	275.04	14.72	282.31	276.01	1.63	2.26	0.88	0.00	1.57	1.19	4.65	51	0.3606	7.13
48	November 9, 2007	398.56	2113.48	6.78	2022.06	288.15	273.76	14.39	280.01	282.31	0.24	0.94	1.06	0.04	1.00	0.57	3.31	51	0.3606	6.63
49	November 10, 2007	369.68	1814.67	6.53	2113.48	288.43	274.43	14.00	282.36	280.01	0.11	3.34	4.31	4.53	3.82	3.07	6.62	51	0.3606	3.39
50	November 11, 2007	390.78	1372.20	6.09	1814.67	298.15	284.54	13.61	291.09	282.36	3.74	3.23	3.93	1.49	3.58	3.10	7.47	51	0.3606	4.29
51	November 13, 2007	360.39	1485.35	6.21	1372.20	288.93	274.93	14.00	283.29	291.09	0.05	0.99	3.18	1.05	2.09	1.32	5.10	51	0.3606	4.37
52	November 15, 2007	419.63	2206.30	6.85	1328.61	281.37	270.26	11.11	276.35	282.89	3.31	3.50	3.09	0.10	3.30	2.50	7.06	51	0.3606	3.23
53	November 16, 2007	397.24	2129.73	6.79	2206.30	288.43	269.65	18.78	278.55	276.35	0.92	3.28	3.51	0.29	3.39	2.00	6.71	51	0.3606	4.47
54	November 17, 2007	400.02	2039.69	6.72	2129.73	291.37	274.04	17.33	282.46	278.55	0.61	0.92	0.67	0.66	0.79	0.71	2.55	51	0.3606	7.60
55	November 18, 2007	217.74	1007.52	5.63	2039.69	285.04	276.54	8.50	280.60	282.46	1.66	2.96	2.72	1.28	2.84	2.15	5.54	51	0.3606	1.66
56	November 19, 2007	406.79	1635.28	6.36	1007.52	295.43	279.54	15.89	288.30	280.60	1.24	3.49	5.51	3.90	4.50	3.54	9.30	51	0.3606	3.86
57	November 20, 2007	375.06	1358.78	6.07	1635.28	295.37	283.43	11.94	290.05	288.30	1.13	2.99	4.50	3.40	3.75	3.01	7.69	51	0.3606	2.70
58	November 22, 2007	176.97	750.81	5.23	1358.78	272.87	270.54	2.33	271.53	290.05	0.00	0.00	1.88	1.59	0.94	0.87	4.25	51	0.3606	2.14
59	November 23, 2007	554.94	1598.53	6.32	750.81	276.43	266.54	9.89	271.25	271.53	0.59	0.36	0.79	0.36	0.57	0.53	3.26	51	0.3606	5.31
60	November 24, 2007	423.53	1087.06	5.74	1598.53	277.37	270.76	6.61	273.98	271.25	0.35	1.11	1.78	0.01	1.45	0.81	3.26	51	0.3606	3.36
61	November 27, 2007	357.17	1773.65	6.49	512.87	283.54	270.43	13.11	276.93	274.33	0.48	1.82	2.02	2.61	1.92	1.73	4.34	51	0.3606	5.78
62	November 28, 2007	435.08	1077.37	5.73	1773.65	287.43	273.26	14.17	280.33	276.93	5.43	4.96	3.81	3.01	4.39	4.30	8.00	51	0.3606	3.25
63	November 29, 2007	350.92	1827.31	6.54	1077.37	280.37	266.26	14.11	273.69	280.33	1.53	2.49	1.87	1.31	2.18	1.80	5.19	51	0.3606	4.90
64	November 30, 2007	336.67	1518.91	6.24	1827.31	277.26	268.04	9.22	272.73	273.69	0.70	1.45	1.96	1.64	1.71	1.44	4.02	51	0.3606	4.05
65	December 3, 2007	345.04	1743.19	6.46	1518.91	277.15	266.26	10.89	271.14	272.73	1.75	2.24	2.78	0.88	2.51	1.91	4.65	51	0.3606	4.67
66	December 4, 2007	355.09	1620.63	6.34	1743.19	283.65	270.37	13.28	277.92	271.14	0.51	0.99	1.14	2.68	1.06	1.33	4.02	51	0.3606	6.48
67	December 13, 2007	238.87	781.89	5.29	297.02	276.04	269.15	6.89	273.18	272.92	0.00	0.01	2.42	0.16	1.21	0.65	4.96	51	0.3606	2.39
68	December 17, 2007	321.98	1616.37	6.34	781.89	276.54	259.93	16.61	269.31	273.18	0.22	0.39	2.25	2.15	1.32	1.25	3.89	51	0.3606	6.47
69	December 18, 2007	314.14	1481.58	6.20	1616.37	281.15	270.76	10.39	275.58	269.31	2.13	1.89	3.10	0.44	2.50	1.89	7.78	51	0.3606	3.81
70	December 19, 2007	389.80	1574.78	6.30	1481.58	281.37	265.54	15.83	274.42	275.58	0.24	0.92	1.93	2.36	1.43	1.37	4.47	51	0.3606	5.83

ID	Date	Daily Solar Loading				Daily Ambient Temperature					Daily Wind Speed							Depth of void		$\Delta T_{(Max)}$ obtained from FEM simulation
		SL _(Max)	SL _(Total)	SL _(Total) ^{1/4}	SL _{(Total)-1}	T _{air (Max)}	T _{air (Min)}	T _{air (Change)}	T _{air (Avg)}	T _{air (Avg)-1}	W _(AVG 1)	W _(AVG 2)	W _(AVG 3)	W _(AVG 4)	W _(AVG 23)	W _(AVG)	W _(Max)	d	e ^{-0.02*depth}	
71	December 21, 2007	248.27	703.86	5.15	440.13	285.04	275.93	9.11	280.49	277.57	0.12	0.68	3.62	4.31	2.15	2.18	6.71	51	0.3606	2.59
72	December 24, 2007	314.23	1599.97	6.32	703.86	276.76	267.26	9.50	271.25	280.49	2.15	2.47	1.80	0.22	2.14	1.66	4.78	51	0.3606	4.90
73	December 25, 2007	315.04	1625.39	6.35	1599.97	283.04	269.26	13.78	275.73	271.25	1.01	1.73	2.27	1.82	2.00	1.71	3.93	51	0.3606	5.89
74	December 29, 2007	314.41	1595.75	6.32	252.04	276.93	266.93	10.00	271.18	271.89	0.48	2.30	1.92	0.06	2.11	1.19	4.47	51	0.3606	5.55
75	December 30, 2007	322.16	1317.52	6.02	1595.75	278.76	269.87	8.89	273.98	271.18	1.02	1.38	2.54	1.05	1.96	1.50	5.10	51	0.3606	3.64
76	December 31, 2007	275.15	804.79	5.33	1317.52	275.26	268.43	6.83	271.60	273.98	0.26	0.59	3.65	4.21	2.12	2.18	6.17	51	0.3606	2.12
77	January 1, 2008	374.07	1502.83	6.23	804.79	269.37	260.43	8.94	265.66	271.60	3.72	5.63	5.15	4.04	5.39	4.63	9.16	51	0.3606	1.81
78	January 2, 2008	325.88	1663.71	6.39	1502.83	267.04	258.87	8.17	261.97	265.66	3.16	2.79	2.40	0.08	2.59	2.11	5.54	51	0.3606	3.63
79	January 3, 2008	329.73	1374.20	6.09	1663.71	275.37	259.76	15.61	268.26	261.97	0.95	3.46	4.78	4.86	4.12	3.51	7.24	51	0.3606	3.31
80	January 4, 2008	278.78	1055.89	5.70	1374.20	282.15	270.43	11.72	276.16	268.26	3.95	5.66	5.92	4.72	5.79	5.06	9.39	51	0.3606	2.84
81	January 5, 2008	400.30	1282.86	5.98	1055.89	290.87	278.15	12.72	284.31	276.16	4.32	4.26	4.65	4.19	4.45	4.35	8.85	51	0.3606	3.55
82	January 6, 2008	281.92	1167.76	5.85	1282.86	294.37	284.87	9.50	289.09	284.31	4.24	4.81	4.80	1.16	4.81	3.75	10.82	51	0.3606	2.78
83	January 9, 2008	367.78	1197.19	5.88	1167.76	279.54	268.76	10.78	274.07	289.09	0.47	0.93	2.13	2.33	1.53	1.46	4.25	51	0.3606	3.72
84	January 11, 2008	328.55	1685.85	6.41	1197.19	278.93	268.87	10.06	273.50	274.07	1.71	0.69	2.21	0.19	1.45	1.20	5.99	51	0.3606	4.68
85	January 12, 2008	328.04	1660.66	6.38	1685.85	281.26	271.04	10.22	274.77	273.50	1.22	1.22	3.47	3.33	2.34	2.31	5.50	51	0.3606	4.92
86	January 13, 2008	483.90	1272.40	5.97	1660.66	273.15	269.87	3.28	271.17	274.77	2.81	3.09	3.63	2.14	3.36	2.92	6.26	51	0.3606	2.06
87	January 14, 2008	355.89	1662.25	6.39	1272.40	273.65	264.54	9.11	270.46	271.17	3.40	3.12	3.47	1.26	3.30	2.81	5.63	51	0.3606	2.97
88	January 15, 2008	339.28	1770.14	6.49	1662.25	275.54	261.04	14.50	269.09	270.46	0.06	1.39	2.70	3.26	2.04	1.85	4.34	51	0.3606	5.03
89	January 16, 2008	210.09	1012.21	5.64	1770.14	281.65	272.37	9.28	276.92	269.09	3.60	3.82	2.73	2.90	3.28	3.26	7.15	51	0.3606	2.95
90	January 19, 2008	362.00	1906.32	6.61	1012.21	263.87	256.65	7.22	259.57	276.92	2.27	2.41	3.17	0.95	2.79	2.20	5.19	51	0.3606	2.78
91	January 20, 2008	400.43	1652.59	6.38	1906.32	268.37	255.04	13.33	262.55	259.57	0.19	1.87	3.23	3.76	2.55	2.26	5.41	51	0.3606	3.69
92	January 23, 2008	357.93	1884.84	6.59	1652.59	277.87	260.76	17.11	268.25	262.55	1.71	3.05	4.73	3.54	3.89	3.26	7.38	51	0.3606	4.13
93	January 24, 2008	381.37	2025.96	6.71	1884.84	266.54	255.04	11.50	260.36	268.25	2.91	1.69	0.78	0.07	1.24	1.36	4.65	51	0.3606	6.16
94	January 26, 2008	359.26	1767.75	6.48	520.59	283.54	268.26	15.28	275.54	267.14	2.32	3.50	4.59	1.36	4.05	2.94	7.78	51	0.3606	4.32
95	January 27, 2008	393.91	1945.55	6.64	1767.75	286.87	269.37	17.50	278.11	275.54	1.55	2.05	3.55	3.13	2.80	2.57	5.86	51	0.3606	4.78
96	November 2, 2007	459.83	1992.74	6.68	2238.11	290.43	271.04	19.39	280.21	279.04	0.15	1.47	0.56	0.06	1.02	0.56	3.62	76	0.2187	4.39
97	November 3, 2007	472.06	2191.14	6.84	1992.74	288.04	272.37	15.67	280.96	280.21	0.49	0.25	0.83	0.46	0.54	0.51	2.82	76	0.2187	4.64
98	November 4, 2007	409.39	2209.72	6.86	2191.14	290.87	277.65	13.22	283.83	280.96	1.82	1.32	1.82	0.72	1.57	1.42	4.34	76	0.2187	4.53
99	November 5, 2007	397.88	2138.04	6.80	2209.72	289.87	276.76	13.11	282.95	283.83	0.34	2.40	3.84	2.24	3.12	2.20	7.02	76	0.2187	2.37
100	November 6, 2007	426.09	2309.05	6.93	2138.04	280.37	269.93	10.44	275.45	282.95	1.98	2.84	2.65	0.02	2.74	1.87	6.17	76	0.2187	2.63
101	November 7, 2007	409.66	2103.72	6.77	2309.05	283.15	265.93	17.22	276.01	275.45	0.00	1.75	2.92	1.49	2.33	1.54	5.50	76	0.2187	3.17
102	November 8, 2007	399.32	2022.06	6.71	2103.72	289.76	275.04	14.72	282.31	276.01	1.63	2.26	0.88	0.00	1.57	1.19	4.65	76	0.2187	4.50
103	November 9, 2007	398.56	2113.48	6.78	2022.06	288.15	273.76	14.39	280.01	282.31	0.24	0.94	1.06	0.04	1.00	0.57	3.31	76	0.2187	4.07
104	November 10, 2007	369.68	1814.67	6.53	2113.48	288.43	274.43	14.00	282.36	280.01	0.11	3.34	4.31	4.53	3.82	3.07	6.62	76	0.2187	2.11
105	November 11, 2007	390.78	1372.20	6.09	1814.67	298.15	284.54	13.61	291.09	282.36	3.74	3.23	3.93	1.49	3.58	3.10	7.47	76	0.2187	2.68

ID	Date	Daily Solar Loading				Daily Ambient Temperature					Daily Wind Speed						Depth of void		$\Delta T_{(Max)}$ obtained from FEM simulation	
		SL _(Max)	SL _(Total)	SL _(Total) ^{1/4}	SL _{(Total)-1}	T _{air (Max)}	T _{air (Min)}	T _{air (Change)}	T _{air (Avg)}	T _{air (Avg)-1}	W _(Avg 1)	W _(Avg 2)	W _(Avg 3)	W _(Avg 4)	W _(Avg 23)	W _(Avg)	W _(Max)	d		e ^{-0.02*depth}
106	November 13, 2007	360.39	1485.35	6.21	1372.20	288.93	274.93	14.00	283.29	291.09	0.05	0.99	3.18	1.05	2.09	1.32	5.10	76	0.2187	2.77
107	November 15, 2007	419.63	2206.30	6.85	1328.61	281.37	270.26	11.11	276.35	282.89	3.31	3.50	3.09	0.10	3.30	2.50	7.06	76	0.2187	2.11
108	November 16, 2007	397.24	2129.73	6.79	2206.30	288.43	269.65	18.78	278.55	276.35	0.92	3.28	3.51	0.29	3.39	2.00	6.71	76	0.2187	2.90
109	November 17, 2007	400.02	2039.69	6.72	2129.73	291.37	274.04	17.33	282.46	278.55	0.61	0.92	0.67	0.66	0.79	0.71	2.55	76	0.2187	4.75
110	November 18, 2007	217.74	1007.52	5.63	2039.69	285.04	276.54	8.50	280.60	282.46	1.66	2.96	2.72	1.28	2.84	2.15	5.54	76	0.2187	1.26
111	November 19, 2007	406.79	1635.28	6.36	1007.52	295.43	279.54	15.89	288.30	280.60	1.24	3.49	5.51	3.90	4.50	3.54	9.30	76	0.2187	2.44
112	November 20, 2007	375.06	1358.78	6.07	1635.28	295.37	283.43	11.94	290.05	288.30	1.13	2.99	4.50	3.40	3.75	3.01	7.69	76	0.2187	1.73
113	November 22, 2007	176.97	750.81	5.23	1358.78	272.87	270.54	2.33	271.53	290.05	0.00	0.00	1.88	1.59	0.94	0.87	4.25	76	0.2187	1.32
114	November 23, 2007	554.94	1598.53	6.32	750.81	276.43	266.54	9.89	271.25	271.53	0.59	0.36	0.79	0.36	0.57	0.53	3.26	76	0.2187	3.40
115	November 24, 2007	423.53	1087.06	5.74	1598.53	277.37	270.76	6.61	273.98	271.25	0.35	1.11	1.78	0.01	1.45	0.81	3.26	76	0.2187	2.48
116	November 27, 2007	357.17	1773.65	6.49	512.87	283.54	270.43	13.11	276.93	274.33	0.48	1.82	2.02	2.61	1.92	1.73	4.34	76	0.2187	3.60
117	November 28, 2007	435.08	1077.37	5.73	1773.65	287.43	273.26	14.17	280.33	276.93	5.43	4.96	3.81	3.01	4.39	4.30	8.00	76	0.2187	2.01
118	November 29, 2007	350.92	1827.31	6.54	1077.37	280.37	266.26	14.11	273.69	280.33	1.53	2.49	1.87	1.31	2.18	1.80	5.19	76	0.2187	3.06
119	November 30, 2007	336.67	1518.91	6.24	1827.31	277.26	268.04	9.22	272.73	273.69	0.70	1.45	1.96	1.64	1.71	1.44	4.02	76	0.2187	2.58
120	December 3, 2007	345.04	1743.19	6.46	1518.91	277.15	266.26	10.89	271.14	272.73	1.75	2.24	2.78	0.88	2.51	1.91	4.65	76	0.2187	2.67
121	December 4, 2007	355.09	1620.63	6.34	1743.19	283.65	270.37	13.28	277.92	271.14	0.51	0.99	1.14	2.68	1.06	1.33	4.02	76	0.2187	3.93
122	December 13, 2007	238.87	781.89	5.29	297.02	276.04	269.15	6.89	273.18	272.92	0.00	0.01	2.42	0.16	1.21	0.65	4.96	76	0.2187	1.47
123	December 17, 2007	321.98	1616.37	6.34	781.89	276.54	259.93	16.61	269.31	273.18	0.22	0.39	2.25	2.15	1.32	1.25	3.89	76	0.2187	3.86
124	December 18, 2007	314.14	1481.58	6.20	1616.37	281.15	270.76	10.39	275.58	269.31	2.13	1.89	3.10	0.44	2.50	1.89	7.78	76	0.2187	2.75
125	December 19, 2007	389.80	1574.78	6.30	1481.58	281.37	265.54	15.83	274.42	275.58	0.24	0.92	1.93	2.36	1.43	1.37	4.47	76	0.2187	3.49
126	December 21, 2007	248.27	703.86	5.15	440.13	285.04	275.93	9.11	280.49	277.57	0.12	0.68	3.62	4.31	2.15	2.18	6.71	76	0.2187	1.52
127	December 24, 2007	314.23	1599.97	6.32	703.86	276.76	267.26	9.50	271.25	280.49	2.15	2.47	1.80	0.22	2.14	1.66	4.78	76	0.2187	3.16
128	December 25, 2007	315.04	1625.39	6.35	1599.97	283.04	269.26	13.78	275.73	271.25	1.01	1.73	2.27	1.82	2.00	1.71	3.93	76	0.2187	3.48
129	December 29, 2007	314.41	1595.75	6.32	252.04	276.93	266.93	10.00	271.18	271.89	0.48	2.30	1.92	0.06	2.11	1.19	4.47	76	0.2187	3.23
130	December 30, 2007	322.16	1317.52	6.02	1595.75	278.76	269.87	8.89	273.98	271.18	1.02	1.38	2.54	1.05	1.96	1.50	5.10	76	0.2187	2.33
131	December 31, 2007	275.15	804.79	5.33	1317.52	275.26	268.43	6.83	271.60	273.98	0.26	0.59	3.65	4.21	2.12	2.18	6.17	76	0.2187	1.17
132	January 1, 2008	374.07	1502.83	6.23	804.79	269.37	260.43	8.94	265.66	271.60	3.72	5.63	5.15	4.04	5.39	4.63	9.16	76	0.2187	1.10
133	January 2, 2008	325.88	1663.71	6.39	1502.83	267.04	258.87	8.17	261.97	265.66	3.16	2.79	2.40	0.08	2.59	2.11	5.54	76	0.2187	2.35
134	January 3, 2008	329.73	1374.20	6.09	1663.71	275.37	259.76	15.61	268.26	261.97	0.95	3.46	4.78	4.86	4.12	3.51	7.24	76	0.2187	2.16
135	January 4, 2008	278.78	1055.89	5.70	1374.20	282.15	270.43	11.72	276.16	268.26	3.95	5.66	5.92	4.72	5.79	5.06	9.39	76	0.2187	1.69
136	January 5, 2008	400.30	1282.86	5.98	1055.89	290.87	278.15	12.72	284.31	276.16	4.32	4.26	4.65	4.19	4.45	4.35	8.85	76	0.2187	2.23
137	January 6, 2008	281.92	1167.76	5.85	1282.86	294.37	284.87	9.50	289.09	284.31	4.24	4.81	4.80	1.16	4.81	3.75	10.82	76	0.2187	1.65
138	January 9, 2008	367.78	1197.19	5.88	1167.76	279.54	268.76	10.78	274.07	289.09	0.47	0.93	2.13	2.33	1.53	1.46	4.25	76	0.2187	2.34
139	January 11, 2008	328.55	1685.85	6.41	1197.19	278.93	268.87	10.06	273.50	274.07	1.71	0.69	2.21	0.19	1.45	1.20	5.99	76	0.2187	2.77
140	January 12, 2008	328.04	1660.66	6.38	1685.85	281.26	271.04	10.22	274.77	273.50	1.22	1.22	3.47	3.33	2.34	2.31	5.50	76	0.2187	2.77

ID	Date	Daily Solar Loading				Daily Ambient Temperature					Daily Wind Speed						Depth of void		$\Delta T_{(Max)}$ obtained from FEM simulation	
		$SL_{(Max)}$	$SL_{(Total)}$	$SL_{(Total)}^{1/4}$	$SL_{(Total)-1}$	$T_{air (Max)}$	$T_{air (Min)}$	$T_{air (Change)}$	$T_{air (Avg)}$	$T_{air (Avg)-1}$	$W_{(Avg 1)}$	$W_{(Avg 2)}$	$W_{(Avg 3)}$	$W_{(Avg 4)}$	$W_{(Avg 23)}$	$W_{(Avg)}$	$W_{(Max)}$	d		$e^{-0.02 \cdot depth}$
141	January 13, 2008	483.90	1272.40	5.97	1660.66	273.15	269.87	3.28	271.17	274.77	2.81	3.09	3.63	2.14	3.36	2.92	6.26	76	0.2187	1.36
142	January 14, 2008	355.89	1662.25	6.39	1272.40	273.65	264.54	9.11	270.46	271.17	3.40	3.12	3.47	1.26	3.30	2.81	5.63	76	0.2187	1.86
143	January 15, 2008	339.28	1770.14	6.49	1662.25	275.54	261.04	14.50	269.09	270.46	0.06	1.39	2.70	3.26	2.04	1.85	4.34	76	0.2187	3.10
144	January 16, 2008	210.09	1012.21	5.64	1770.14	281.65	272.37	9.28	276.92	269.09	3.60	3.82	2.73	2.90	3.28	3.26	7.15	76	0.2187	2.12
145	January 19, 2008	362.00	1906.32	6.61	1012.21	263.87	256.65	7.22	259.57	276.92	2.27	2.41	3.17	0.95	2.79	2.20	5.19	76	0.2187	2.00
146	January 20, 2008	400.43	1652.59	6.38	1906.32	268.37	255.04	13.33	262.55	259.57	0.19	1.87	3.23	3.76	2.55	2.26	5.41	76	0.2187	2.58
147	January 23, 2008	357.93	1884.84	6.59	1652.59	277.87	260.76	17.11	268.25	262.55	1.71	3.05	4.73	3.54	3.89	3.26	7.38	76	0.2187	2.61
148	January 24, 2008	381.37	2025.96	6.71	1884.84	266.54	255.04	11.50	260.36	268.25	2.91	1.69	0.78	0.07	1.24	1.36	4.65	76	0.2187	3.85
149	January 26, 2008	359.26	1767.75	6.48	520.59	283.54	268.26	15.28	275.54	267.14	2.32	3.50	4.59	1.36	4.05	2.94	7.78	76	0.2187	2.72
150	January 27, 2008	393.91	1945.55	6.64	1767.75	286.87	269.37	17.50	278.11	275.54	1.55	2.05	3.55	3.13	2.80	2.57	5.86	76	0.2187	2.83
151	November 2, 2007	459.83	1992.74	6.68	2238.11	290.43	271.04	19.39	280.21	279.04	0.15	1.47	0.56	0.06	1.02	0.56	3.62	127	0.0789	2.12
152	November 3, 2007	472.06	2191.14	6.84	1992.74	288.04	272.37	15.67	280.96	280.21	0.49	0.25	0.83	0.46	0.54	0.51	2.82	127	0.0789	2.17
153	November 4, 2007	409.39	2209.72	6.86	2191.14	290.87	277.65	13.22	283.83	280.96	1.82	1.32	1.82	0.72	1.57	1.42	4.34	127	0.0789	2.08
154	November 5, 2007	397.88	2138.04	6.80	2209.72	289.87	276.76	13.11	282.95	283.83	0.34	2.40	3.84	2.24	3.12	2.20	7.02	127	0.0789	1.19
155	November 6, 2007	426.09	2309.05	6.93	2138.04	280.37	269.93	10.44	275.45	282.95	1.98	2.84	2.65	0.02	2.74	1.87	6.17	127	0.0789	1.61
156	November 7, 2007	409.66	2103.72	6.77	2309.05	283.15	265.93	17.22	276.01	275.45	0.00	1.75	2.92	1.49	2.33	1.54	5.50	127	0.0789	1.77
157	November 8, 2007	399.32	2022.06	6.71	2103.72	289.76	275.04	14.72	282.31	276.01	1.63	2.26	0.88	0.00	1.57	1.19	4.65	127	0.0789	1.97
158	November 9, 2007	398.56	2113.48	6.78	2022.06	288.15	273.76	14.39	280.01	282.31	0.24	0.94	1.06	0.04	1.00	0.57	3.31	127	0.0789	1.97
159	November 10, 2007	369.68	1814.67	6.53	2113.48	288.43	274.43	14.00	282.36	280.01	0.11	3.34	4.31	4.53	3.82	3.07	6.62	127	0.0789	1.13
160	November 11, 2007	390.78	1372.20	6.09	1814.67	298.15	284.54	13.61	291.09	282.36	3.74	3.23	3.93	1.49	3.58	3.10	7.47	127	0.0789	1.06
161	November 13, 2007	360.39	1485.35	6.21	1372.20	288.93	274.93	14.00	283.29	291.09	0.05	0.99	3.18	1.05	2.09	1.32	5.10	127	0.0789	1.23
162	November 15, 2007	419.63	2206.30	6.85	1328.61	281.37	270.26	11.11	276.35	282.89	3.31	3.50	3.09	0.10	3.30	2.50	7.06	127	0.0789	1.40
163	November 16, 2007	397.24	2129.73	6.79	2206.30	288.43	269.65	18.78	278.55	276.35	0.92	3.28	3.51	0.29	3.39	2.00	6.71	127	0.0789	1.73
164	November 17, 2007	400.02	2039.69	6.72	2129.73	291.37	274.04	17.33	282.46	278.55	0.61	0.92	0.67	0.66	0.79	0.71	2.55	127	0.0789	2.08
165	November 18, 2007	217.74	1007.52	5.63	2039.69	285.04	276.54	8.50	280.60	282.46	1.66	2.96	2.72	1.28	2.84	2.15	5.54	127	0.0789	0.79
166	November 19, 2007	406.79	1635.28	6.36	1007.52	295.43	279.54	15.89	288.30	280.60	1.24	3.49	5.51	3.90	4.50	3.54	9.30	127	0.0789	1.06
167	November 20, 2007	375.06	1358.78	6.07	1635.28	295.37	283.43	11.94	290.05	288.30	1.13	2.99	4.50	3.40	3.75	3.01	7.69	127	0.0789	0.88
168	November 22, 2007	176.97	750.81	5.23	1358.78	272.87	270.54	2.33	271.53	290.05	0.00	0.00	1.88	1.59	0.94	0.87	4.25	127	0.0789	0.95
169	November 23, 2007	554.94	1598.53	6.32	750.81	276.43	266.54	9.89	271.25	271.53	0.59	0.36	0.79	0.36	0.57	0.53	3.26	127	0.0789	1.83
170	November 24, 2007	423.53	1087.06	5.74	1598.53	277.37	270.76	6.61	273.98	271.25	0.35	1.11	1.78	0.01	1.45	0.81	3.26	127	0.0789	1.24
171	November 27, 2007	357.17	1773.65	6.49	512.87	283.54	270.43	13.11	276.93	274.33	0.48	1.82	2.02	2.61	1.92	1.73	4.34	127	0.0789	1.61
172	November 28, 2007	435.08	1077.37	5.73	1773.65	287.43	273.26	14.17	280.33	276.93	5.43	4.96	3.81	3.01	4.39	4.30	8.00	127	0.0789	0.90
173	November 29, 2007	350.92	1827.31	6.54	1077.37	280.37	266.26	14.11	273.69	280.33	1.53	2.49	1.87	1.31	2.18	1.80	5.19	127	0.0789	1.56
174	November 30, 2007	336.67	1518.91	6.24	1827.31	277.26	268.04	9.22	272.73	273.69	0.70	1.45	1.96	1.64	1.71	1.44	4.02	127	0.0789	1.43
175	December 3, 2007	345.04	1743.19	6.46	1518.91	277.15	266.26	10.89	271.14	272.73	1.75	2.24	2.78	0.88	2.51	1.91	4.65	127	0.0789	1.45

ID	Date	Daily Solar Loading				Daily Ambient Temperature					Daily Wind Speed						Depth of void		$\Delta T_{(Max)}$ obtained from FEM simulation	
		SL _(Max)	SL _(Total)	SL _(Total) ^{1/4}	SL _(Total) -1	T _{air (Max)}	T _{air (Min)}	T _{air (Change)}	T _{air (Avg)}	T _{air (Avg)} -1	W _(Avg 1)	W _(Avg 2)	W _(Avg 3)	W _(Avg 4)	W _(Avg 23)	W _(Avg)	W _(Max)	d		e ^{-0.02*depth}
176	December 4, 2007	355.09	1620.63	6.34	1743.19	283.65	270.37	13.28	277.92	271.14	0.51	0.99	1.14	2.68	1.06	1.33	4.02	127	0.0789	1.90
177	December 13, 2007	238.87	781.89	5.29	297.02	276.04	269.15	6.89	273.18	272.92	0.00	0.01	2.42	0.16	1.21	0.65	4.96	127	0.0789	0.72
178	December 17, 2007	321.98	1616.37	6.34	781.89	276.54	259.93	16.61	269.31	273.18	0.22	0.39	2.25	2.15	1.32	1.25	3.89	127	0.0789	1.89
179	December 18, 2007	314.14	1481.58	6.20	1616.37	281.15	270.76	10.39	275.58	269.31	2.13	1.89	3.10	0.44	2.50	1.89	7.78	127	0.0789	1.24
180	December 19, 2007	389.80	1574.78	6.30	1481.58	281.37	265.54	15.83	274.42	275.58	0.24	0.92	1.93	2.36	1.43	1.37	4.47	127	0.0789	1.56
181	December 21, 2007	248.27	703.86	5.15	440.13	285.04	275.93	9.11	280.49	277.57	0.12	0.68	3.62	4.31	2.15	2.18	6.71	127	0.0789	0.62
182	December 24, 2007	314.23	1599.97	6.32	703.86	276.76	267.26	9.50	271.25	280.49	2.15	2.47	1.80	0.22	2.14	1.66	4.78	127	0.0789	1.63
183	December 25, 2007	315.04	1625.39	6.35	1599.97	283.04	269.26	13.78	275.73	271.25	1.01	1.73	2.27	1.82	2.00	1.71	3.93	127	0.0789	1.65
184	December 29, 2007	314.41	1595.75	6.32	252.04	276.93	266.93	10.00	271.18	271.89	0.48	2.30	1.92	0.06	2.11	1.19	4.47	127	0.0789	1.58
185	December 30, 2007	322.16	1317.52	6.02	1595.75	278.76	269.87	8.89	273.98	271.18	1.02	1.38	2.54	1.05	1.96	1.50	5.10	127	0.0789	1.17
186	December 31, 2007	275.15	804.79	5.33	1317.52	275.26	268.43	6.83	271.60	273.98	0.26	0.59	3.65	4.21	2.12	2.18	6.17	127	0.0789	0.63
187	January 1, 2008	374.07	1502.83	6.23	804.79	269.37	260.43	8.94	265.66	271.60	3.72	5.63	5.15	4.04	5.39	4.63	9.16	127	0.0789	0.55
188	January 2, 2008	325.88	1663.71	6.39	1502.83	267.04	258.87	8.17	261.97	265.66	3.16	2.79	2.40	0.08	2.59	2.11	5.54	127	0.0789	1.43
189	January 3, 2008	329.73	1374.20	6.09	1663.71	275.37	259.76	15.61	268.26	261.97	0.95	3.46	4.78	4.86	4.12	3.51	7.24	127	0.0789	1.04
190	January 4, 2008	278.78	1055.89	5.70	1374.20	282.15	270.43	11.72	276.16	268.26	3.95	5.66	5.92	4.72	5.79	5.06	9.39	127	0.0789	0.64
191	January 5, 2008	400.30	1282.86	5.98	1055.89	290.87	278.15	12.72	284.31	276.16	4.32	4.26	4.65	4.19	4.45	4.35	8.85	127	0.0789	0.96
192	January 6, 2008	281.92	1167.76	5.85	1282.86	294.37	284.87	9.50	289.09	284.31	4.24	4.81	4.80	1.16	4.81	3.75	10.82	127	0.0789	0.66
193	January 9, 2008	367.78	1197.19	5.88	1167.76	279.54	268.76	10.78	274.07	289.09	0.47	0.93	2.13	2.33	1.53	1.46	4.25	127	0.0789	1.41
194	January 11, 2008	328.55	1685.85	6.41	1197.19	278.93	268.87	10.06	273.50	274.07	1.71	0.69	2.21	0.19	1.45	1.20	5.99	127	0.0789	1.52
195	January 12, 2008	328.04	1660.66	6.38	1685.85	281.26	271.04	10.22	274.77	273.50	1.22	1.22	3.47	3.33	2.34	2.31	5.50	127	0.0789	1.20
196	January 13, 2008	483.90	1272.40	5.97	1660.66	273.15	269.87	3.28	271.17	274.77	2.81	3.09	3.63	2.14	3.36	2.92	6.26	127	0.0789	0.87
197	January 14, 2008	355.89	1662.25	6.39	1272.40	273.65	264.54	9.11	270.46	271.17	3.40	3.12	3.47	1.26	3.30	2.81	5.63	127	0.0789	1.09
198	January 15, 2008	339.28	1770.14	6.49	1662.25	275.54	261.04	14.50	269.09	270.46	0.06	1.39	2.70	3.26	2.04	1.85	4.34	127	0.0789	1.53
199	January 16, 2008	210.09	1012.21	5.64	1770.14	281.65	272.37	9.28	276.92	269.09	3.60	3.82	2.73	2.90	3.28	3.26	7.15	127	0.0789	0.93
200	January 19, 2008	362.00	1906.32	6.61	1012.21	263.87	256.65	7.22	259.57	276.92	2.27	2.41	3.17	0.95	2.79	2.20	5.19	127	0.0789	1.21
201	January 20, 2008	400.43	1652.59	6.38	1906.32	268.37	255.04	13.33	262.55	259.57	0.19	1.87	3.23	3.76	2.55	2.26	5.41	127	0.0789	1.30
202	January 23, 2008	357.93	1884.84	6.59	1652.59	277.87	260.76	17.11	268.25	262.55	1.71	3.05	4.73	3.54	3.89	3.26	7.38	127	0.0789	1.24
203	January 24, 2008	381.37	2025.96	6.71	1884.84	266.54	255.04	11.50	260.36	268.25	2.91	1.69	0.78	0.07	1.24	1.36	4.65	127	0.0789	2.06
204	January 26, 2008	359.26	1767.75	6.48	520.59	283.54	268.26	15.28	275.54	267.14	2.32	3.50	4.59	1.36	4.05	2.94	7.78	127	0.0789	1.26
205	January 27, 2008	393.91	1945.55	6.64	1767.75	286.87	269.37	17.50	278.11	275.54	1.55	2.05	3.55	3.13	2.80	2.57	5.86	127	0.0789	1.44

APPENDIX E
The Shaded (North) Dataset for Model Equation
Development

Appendix E.1 Daily environmental variables, depth of voids, and daily maximum thermal contrast for the Shaded side datasets

Variables	Unit	Description of variable
<u>Predictor variables</u>		
$T_{air (Max)}$	[K]	Daily maximum ambient temperature
$T_{air (Min)}$	[K]	Daily minimum ambient temperature
$T_{air (Min^*)}$	[K]	Daily minimum ambient temperature calculated over the 12 hours preceding the sunrise time at the day
$T_{air (Change)}$	[K]	Daily ambient temperature change = $T_{air (Max)} - T_{air (Min)}$
$T_{air (Change^*)}$	[K]	$T_{air (Max)} - T_{air (Min^*)}$
$T_{air (Avg)}$	[K]	Daily average ambient temperature
$T_{air (Avg)-1}$	[K]	Daily average ambient temperature of the previous day
$W_{(Avg 1)}$	[m/s]	Average wind speed during quarter 1 (12 a.m. to 6 a.m.)
$W_{(Avg 2)}$	[m/s]	Average wind speed during quarter 2 (6 a.m. to 12 p.m.)
$W_{(Avg 3)}$	[m/s]	Average wind speed during quarter 3 (12 p.m. to 6 p.m.)
$W_{(Avg 4)}$	[m/s]	Average wind speed during quarter 4 (6 p.m. to 12 a.m.)
$W_{(Avg 12)}$	[m/s]	Average wind speed during quarter 1 & 2 (12 a.m. to 12 p.m.)
$W_{(Avg)}$	[m/s]	Daily average wind speed
$W_{(Max)}$	[m/s]	Daily maximum wind speed
d	[mm]	Depth of void
$e^{-0.02 \cdot depth}$		Exponential transformation of the depth of void
<u>Response variable</u>		
$\Delta T_{(Max)}$ obtained from FEM simulation	[°C]	Daily maximum thermal contrast

ID	Date	Daily Ambient Temperature						Daily Wind Speed						Depth of void		$\Delta T_{(Max)}$ obtained		
		$T_{air (Max)}$	$T_{air (Min)}$	$T_{air (Min^*)}$	$T_{air (Change)}$	$T_{air (Change^*)}$	$T_{air (Avg)}$	$T_{air (Avg)-1}$	$W_{(Avg 1)}$	$W_{(Avg 2)}$	$W_{(Avg 3)}$	$W_{(Avg 4)}$	$W_{(Avg 12)}$	$W_{(Avg)}$	$W_{(Max)}$	d	$e^{-0.02 \cdot depth}$	from FEM simulation
1	May 6, 2008	296.54	285.26	285.26	11.28	11.28	289.86	289.42	0.25	1.76	5.80	4.26	1.01	3.02	10.24	25	0.6065	1.92
2	May 13, 2008	294.76	286.76	286.76	8.00	8.00	291.20	286.96	3.57	4.48	4.05	3.83	4.02	3.98	7.06	25	0.6065	1.42
3	May 18, 2008	295.87	284.15	284.87	11.72	11.00	290.95	293.55	0.91	1.93	3.21	0.52	1.42	1.64	5.99	25	0.6065	1.78
4	May 19, 2008	299.54	283.15	283.15	16.39	16.39	291.55	290.95	0.53	2.92	2.07	0.96	1.73	1.62	6.26	25	0.6065	2.47
5	May 20, 2008	294.04	282.26	287.65	11.78	6.39	289.87	291.55	1.39	2.66	3.01	0.65	2.03	1.93	5.77	25	0.6065	1.23
6	May 23, 2008	295.15	287.65	287.65	7.50	7.50	290.67	287.86	3.45	4.04	3.35	3.89	3.75	3.68	7.24	25	0.6065	1.53
7	May 28, 2008	296.37	283.65	283.65	12.72	12.72	288.40	290.56	2.11	2.46	1.85	0.64	2.28	1.76	4.02	25	0.6065	2.28
8	May 30, 2008	302.93	292.76	292.76	10.17	10.17	297.56	293.78	3.36	5.05	5.09	2.46	4.21	3.99	10.46	25	0.6065	1.82
9	June 10, 2008	300.37	286.87	286.87	13.50	13.50	294.09	292.22	0.28	2.21	3.16	2.87	1.24	2.13	4.87	25	0.6065	2.13
10	June 11, 2008	302.87	291.43	291.43	11.44	11.44	297.70	294.09	4.00	4.77	5.41	4.85	4.39	4.76	8.94	25	0.6065	1.76
11	June 16, 2008	299.87	287.93	290.04	11.94	9.83	293.96	294.81	0.23	0.50	1.60	0.41	0.36	0.68	2.86	25	0.6065	2.29
12	June 17, 2008	300.26	285.26	285.26	15.00	15.00	292.71	293.96	0.00	0.69	1.45	0.15	0.34	0.57	2.82	25	0.6065	2.85
13	June 23, 2008	302.65	287.37	287.37	15.28	15.28	295.51	295.89	0.02	0.53	0.99	0.17	0.27	0.43	2.55	25	0.6065	2.63
14	June 28, 2008	300.87	292.43	292.43	8.44	8.44	296.08	298.41	2.32	1.89	4.20	2.25	2.10	2.67	6.30	25	0.6065	1.66
15	June 29, 2008	299.43	290.15	291.54	9.28	7.89	294.23	296.08	3.62	3.72	3.34	0.97	3.67	2.91	7.69	25	0.6065	2.21
16	June 30, 2008	301.26	287.26	287.26	14.00	14.00	294.13	294.23	0.44	0.96	1.83	0.22	0.70	0.86	3.62	25	0.6065	2.87
17	July 4, 2008	299.37	288.15	288.15	11.22	11.22	293.19	293.08	0.08	1.52	1.60	0.27	0.80	0.86	4.25	25	0.6065	2.19
18	July 5, 2008	300.65	285.87	285.87	14.78	14.78	293.83	293.19	0.00	0.85	2.21	1.12	0.43	1.05	4.11	25	0.6065	2.74
19	July 7, 2008	306.93	296.43	296.43	10.50	10.50	301.61	298.81	2.47	3.00	3.64	2.51	2.74	2.91	5.86	25	0.6065	1.91
20	July 9, 2008	303.65	294.15	294.15	9.50	9.50	297.77	298.53	0.05	0.82	1.48	0.24	0.44	0.65	2.86	25	0.6065	1.39
21	July 10, 2008	304.43	293.43	293.43	11.00	11.00	298.75	297.77	0.24	2.21	3.27	1.29	1.23	1.76	5.19	25	0.6065	1.56
22	July 11, 2008	306.37	295.15	295.15	11.22	11.22	300.50	298.75	0.54	2.13	3.64	1.99	1.34	2.08	5.77	25	0.6065	1.79
23	July 13, 2008	302.43	289.04	289.04	13.39	13.39	295.04	296.63	0.54	2.11	2.86	0.40	1.32	1.48	5.23	25	0.6065	2.29
24	July 14, 2008	304.54	288.87	288.87	15.67	15.67	296.91	295.04	0.00	1.96	2.43	0.39	0.98	1.20	4.78	25	0.6065	2.76
25	July 15, 2008	304.04	290.65	290.65	13.39	13.39	297.67	296.91	0.00	1.77	4.12	0.66	0.89	1.64	6.26	25	0.6065	2.06
26	July 16, 2008	304.26	292.26	292.26	12.00	12.00	298.32	297.67	0.33	2.00	2.82	0.69	1.16	1.46	5.95	25	0.6065	2.25
27	July 17, 2008	304.37	292.26	292.26	12.11	12.11	298.37	298.32	0.00	1.95	3.17	0.50	0.98	1.41	5.19	25	0.6065	2.13
28	July 19, 2008	305.65	295.76	295.43	9.89	10.22	300.54	298.45	0.03	1.36	2.79	1.50	0.70	1.42	4.38	25	0.6065	2.01
29	July 20, 2008	307.87	297.93	297.93	9.94	9.94	302.58	300.54	1.30	3.00	3.06	0.69	2.15	2.01	5.63	25	0.6065	2.17
30	July 21, 2008	307.76	296.76	296.76	11.00	11.00	301.84	302.58	0.55	0.83	2.50	0.90	0.69	1.19	4.11	25	0.6065	2.07
31	July 23, 2008	301.04	293.76	293.93	7.28	7.11	296.76	295.35	0.36	2.40	2.82	0.67	1.38	1.56	4.96	25	0.6065	1.20
32	July 26, 2008	305.65	295.76	295.76	9.89	9.89	299.41	297.59	0.03	0.41	1.03	0.14	0.22	0.40	2.64	25	0.6065	1.87
33	July 27, 2008	304.65	294.37	294.37	10.28	10.28	299.70	299.41	0.30	1.33	2.26	1.25	0.82	1.28	4.69	25	0.6065	1.98
34	July 29, 2008	305.43	295.43	295.43	10.00	10.00	299.48	297.11	0.55	1.20	0.94	1.43	0.88	1.03	3.62	25	0.6065	1.68
35	July 31, 2008	301.93	293.87	293.87	8.06	8.06	296.52	294.55	0.00	0.06	1.20	0.54	0.03	0.45	3.71	25	0.6065	1.33

ID	Date	Daily Ambient Temperature							Daily Wind Speed							Depth of void		$\Delta T_{(Max)}$ obtained from FEM simulation
		$T_{air (Max)}$	$T_{air (Min)}$	$T_{air (Min^*)}$	$T_{air (Change)}$	$T_{air (Change^*)}$	$T_{air (Avg)}$	$T_{air (Avg)-1}$	$W_{(Avg 1)}$	$W_{(Avg 2)}$	$W_{(Avg 3)}$	$W_{(Avg 4)}$	$W_{(Avg 12)}$	$W_{(Avg)}$	$W_{(Max)}$	d	$e^{-0.02 \cdot depth}$	
36	May 5, 2008	297.65	278.93	278.93	18.72	18.72	289.42	285.18	0.22	1.75	2.93	0.53	0.99	1.36	5.41	51	0.3606	1.86
37	May 6, 2008	296.54	285.26	285.26	11.28	11.28	289.86	289.42	0.25	1.76	5.80	4.26	1.01	3.02	10.24	51	0.3606	0.99
38	May 13, 2008	294.76	286.76	286.76	8.00	8.00	291.20	286.96	3.57	4.48	4.05	3.83	4.02	3.98	7.06	51	0.3606	0.89
39	May 16, 2008	296.43	277.15	277.15	19.28	19.28	287.85	285.36	0.18	2.25	3.53	2.27	1.21	2.06	5.32	51	0.3606	1.86
40	May 17, 2008	300.87	286.26	286.26	14.61	14.61	293.55	287.85	2.78	3.21	2.88	1.81	3.00	2.67	5.01	51	0.3606	1.82
41	May 18, 2008	295.87	284.15	284.87	11.72	11.00	290.95	293.55	0.91	1.93	3.21	0.52	1.42	1.64	5.99	51	0.3606	0.79
42	May 19, 2008	299.54	283.15	283.15	16.39	16.39	291.55	290.95	0.53	2.92	2.07	0.96	1.73	1.62	6.26	51	0.3606	1.38
43	May 20, 2008	294.04	282.26	287.65	11.78	6.39	289.87	291.55	1.39	2.66	3.01	0.65	2.03	1.93	5.77	51	0.3606	0.53
44	May 21, 2008	296.04	282.54	282.26	13.50	13.78	289.03	289.87	0.81	1.04	1.40	0.13	0.93	0.85	4.11	51	0.3606	1.02
45	May 23, 2008	295.15	287.65	287.65	7.50	7.50	290.67	287.86	3.45	4.04	3.35	3.89	3.75	3.68	7.24	51	0.3606	0.93
46	May 28, 2008	296.37	283.65	283.65	12.72	12.72	288.40	290.56	2.11	2.46	1.85	0.64	2.28	1.76	4.02	51	0.3606	1.37
47	May 29, 2008	300.87	284.54	284.54	16.33	16.33	293.78	288.40	0.18	2.71	4.02	3.08	1.44	2.50	6.30	51	0.3606	1.93
48	May 30, 2008	302.93	292.76	292.76	10.17	10.17	297.56	293.78	3.36	5.05	5.09	2.46	4.21	3.99	10.46	51	0.3606	1.13
49	June 1, 2008	306.15	287.76	287.76	18.39	18.39	295.46	295.23	0.16	0.86	1.07	0.10	0.51	0.55	2.86	51	0.3606	1.82
50	June 4, 2008	303.54	291.76	291.76	11.78	11.78	297.62	299.40	3.46	3.36	4.70	3.33	3.41	3.71	8.67	51	0.3606	1.00
51	June 5, 2008	303.37	296.15	296.15	7.22	7.22	299.72	297.62	2.94	3.57	6.02	5.04	3.25	4.39	8.54	51	0.3606	0.71
52	June 7, 2008	304.43	296.54	296.54	7.89	7.89	300.08	298.34	2.19	4.53	6.50	2.78	3.36	4.00	9.70	51	0.3606	0.71
53	June 10, 2008	300.37	286.87	286.87	13.50	13.50	294.09	292.22	0.28	2.21	3.16	2.87	1.24	2.13	4.87	51	0.3606	1.40
54	June 11, 2008	302.87	291.43	291.43	11.44	11.44	297.70	294.09	4.00	4.77	5.41	4.85	4.39	4.76	8.94	51	0.3606	1.10
55	June 14, 2008	302.93	288.43	288.43	14.50	14.50	295.17	294.04	0.16	1.61	2.53	0.56	0.88	1.22	5.50	51	0.3606	1.82
56	June 15, 2008	303.76	290.26	291.54	13.50	12.22	294.81	295.17	0.77	3.27	3.14	2.02	2.02	2.30	11.35	51	0.3606	0.99
57	June 16, 2008	299.87	287.93	290.04	11.94	9.83	293.96	294.81	0.23	0.50	1.60	0.41	0.36	0.68	2.86	51	0.3606	1.21
58	June 17, 2008	300.26	285.26	285.26	15.00	15.00	292.71	293.96	0.00	0.69	1.45	0.15	0.34	0.57	2.82	51	0.3606	1.54
59	June 18, 2008	301.76	286.65	286.65	15.11	15.11	294.35	292.71	0.00	1.79	1.05	0.19	0.90	0.76	3.58	51	0.3606	1.78
60	June 20, 2008	300.87	289.37	289.37	11.50	11.50	294.24	294.96	0.29	0.15	0.99	0.10	0.22	0.38	3.31	51	0.3606	1.60
61	June 21, 2008	302.93	289.87	289.87	13.06	13.06	296.37	294.24	0.14	1.58	1.59	0.19	0.86	0.87	4.02	51	0.3606	1.54
62	June 22, 2008	302.37	290.65	290.65	11.72	11.72	295.89	296.37	0.07	1.14	1.25	0.39	0.61	0.72	3.04	51	0.3606	1.41
63	June 23, 2008	302.65	287.37	287.37	15.28	15.28	295.51	295.89	0.02	0.53	0.99	0.17	0.27	0.43	2.55	51	0.3606	1.37
64	June 25, 2008	305.37	292.93	291.76	12.44	13.61	298.82	294.24	1.68	2.55	4.17	1.94	2.12	2.59	6.39	51	0.3606	1.82
65	June 27, 2008	303.65	292.93	292.43	10.72	11.22	298.41	294.83	1.82	2.95	4.12	1.64	2.38	2.63	6.62	51	0.3606	1.46
66	June 28, 2008	300.87	292.43	292.43	8.44	8.44	296.08	298.41	2.32	1.89	4.20	2.25	2.10	2.67	6.30	51	0.3606	0.91
67	June 29, 2008	299.43	290.15	291.54	9.28	7.89	294.23	296.08	3.62	3.72	3.34	0.97	3.67	2.91	7.69	51	0.3606	1.10
68	June 30, 2008	301.26	287.26	287.26	14.00	14.00	294.13	294.23	0.44	0.96	1.83	0.22	0.70	0.86	3.62	51	0.3606	1.53
69	July 1, 2008	303.15	286.65	286.65	16.50	16.50	295.73	294.13	0.00	1.08	2.91	1.65	0.54	1.41	4.78	51	0.3606	1.15
70	July 4, 2008	299.37	288.15	288.15	11.22	11.22	293.19	293.08	0.08	1.52	1.60	0.27	0.80	0.86	4.25	51	0.3606	1.25

ID	Date	Daily Ambient Temperature							Daily Wind Speed							Depth of void		$\Delta T_{(Max)}$ obtained from FEM simulation
		$T_{air (Max)}$	$T_{air (Min)}$	$T_{air (Min^*)}$	$T_{air (Change)}$	$T_{air (Change^*)}$	$T_{air (Avg)}$	$T_{air (Avg)-1}$	$W_{(Avg 1)}$	$W_{(Avg 2)}$	$W_{(Avg 3)}$	$W_{(Avg 4)}$	$W_{(Avg 12)}$	$W_{(Avg)}$	$W_{(Max)}$	d	$e^{-0.02 \cdot depth}$	
71	July 5, 2008	300.65	285.87	285.87	14.78	14.78	293.83	293.19	0.00	0.85	2.21	1.12	0.43	1.05	4.11	51	0.3606	1.58
72	July 6, 2008	306.15	292.04	291.87	14.11	14.28	298.81	293.83	1.01	2.24	3.52	1.05	1.63	1.96	5.86	51	0.3606	1.89
73	July 7, 2008	306.93	296.43	296.43	10.50	10.50	301.61	298.81	2.47	3.00	3.64	2.51	2.74	2.91	5.86	51	0.3606	1.12
74	July 9, 2008	303.65	294.15	294.15	9.50	9.50	297.77	298.53	0.05	0.82	1.48	0.24	0.44	0.65	2.86	51	0.3606	0.75
75	July 10, 2008	304.43	293.43	293.43	11.00	11.00	298.75	297.77	0.24	2.21	3.27	1.29	1.23	1.76	5.19	51	0.3606	0.90
76	July 11, 2008	306.37	295.15	295.15	11.22	11.22	300.50	298.75	0.54	2.13	3.64	1.99	1.34	2.08	5.77	51	0.3606	1.13
77	July 13, 2008	302.43	289.04	289.04	13.39	13.39	295.04	296.63	0.54	2.11	2.86	0.40	1.32	1.48	5.23	51	0.3606	1.31
78	July 14, 2008	304.54	288.87	288.87	15.67	15.67	296.91	295.04	0.00	1.96	2.43	0.39	0.98	1.20	4.78	51	0.3606	1.57
79	July 15, 2008	304.04	290.65	290.65	13.39	13.39	297.67	296.91	0.00	1.77	4.12	0.66	0.89	1.64	6.26	51	0.3606	1.21
80	July 16, 2008	304.26	292.26	292.26	12.00	12.00	298.32	297.67	0.33	2.00	2.82	0.69	1.16	1.46	5.95	51	0.3606	1.17
81	July 17, 2008	304.37	292.26	292.26	12.11	12.11	298.37	298.32	0.00	1.95	3.17	0.50	0.98	1.41	5.19	51	0.3606	1.17
82	July 19, 2008	305.65	295.76	295.43	9.89	10.22	300.54	298.45	0.03	1.36	2.79	1.50	0.70	1.42	4.38	51	0.3606	1.14
83	July 20, 2008	307.87	297.93	297.93	9.94	9.94	302.58	300.54	1.30	3.00	3.06	0.69	2.15	2.01	5.63	51	0.3606	1.16
84	July 21, 2008	307.76	296.76	296.76	11.00	11.00	301.84	302.58	0.55	0.83	2.50	0.90	0.69	1.19	4.11	51	0.3606	1.11
85	July 23, 2008	301.04	293.76	293.93	7.28	7.11	296.76	295.35	0.36	2.40	2.82	0.67	1.38	1.56	4.96	51	0.3606	0.74
86	July 26, 2008	305.65	295.76	295.76	9.89	9.89	299.41	297.59	0.03	0.41	1.03	0.14	0.22	0.40	2.64	51	0.3606	1.02
87	July 27, 2008	304.65	294.37	294.37	10.28	10.28	299.70	299.41	0.30	1.33	2.26	1.25	0.82	1.28	4.69	51	0.3606	1.09
88	July 29, 2008	305.43	295.43	295.43	10.00	10.00	299.48	297.11	0.55	1.20	0.94	1.43	0.88	1.03	3.62	51	0.3606	0.95
89	July 31, 2008	301.93	293.87	293.87	8.06	8.06	296.52	294.55	0.00	0.06	1.20	0.54	0.03	0.45	3.71	51	0.3606	0.82
90	May 5, 2008	297.65	278.93	278.93	18.72	18.72	289.42	285.18	0.22	1.75	2.93	0.53	0.99	1.36	5.41	76	0.2187	1.23
91	May 6, 2008	296.54	285.26	285.26	11.28	11.28	289.86	289.42	0.25	1.76	5.80	4.26	1.01	3.02	10.24	76	0.2187	0.57
92	May 13, 2008	294.76	286.76	286.76	8.00	8.00	291.20	286.96	3.57	4.48	4.05	3.83	4.02	3.98	7.06	76	0.2187	0.54
93	May 16, 2008	296.43	277.15	277.15	19.28	19.28	287.85	285.36	0.18	2.25	3.53	2.27	1.21	2.06	5.32	76	0.2187	1.24
94	May 17, 2008	300.87	286.26	286.26	14.61	14.61	293.55	287.85	2.78	3.21	2.88	1.81	3.00	2.67	5.01	76	0.2187	1.07
95	May 18, 2008	295.87	284.15	284.87	11.72	11.00	290.95	293.55	0.91	1.93	3.21	0.52	1.42	1.64	5.99	76	0.2187	0.36
96	May 19, 2008	299.54	283.15	283.15	16.39	16.39	291.55	290.95	0.53	2.92	2.07	0.96	1.73	1.62	6.26	76	0.2187	0.85
97	May 20, 2008	294.04	282.26	287.65	11.78	6.39	289.87	291.55	1.39	2.66	3.01	0.65	2.03	1.93	5.77	76	0.2187	0.23
98	May 21, 2008	296.04	282.54	282.26	13.50	13.78	289.03	289.87	0.81	1.04	1.40	0.13	0.93	0.85	4.11	76	0.2187	0.67
99	May 23, 2008	295.15	287.65	287.65	7.50	7.50	290.67	287.86	3.45	4.04	3.35	3.89	3.75	3.68	7.24	76	0.2187	0.56
100	May 25, 2008	303.76	289.93	289.76	13.83	14.00	296.87	289.37	2.93	4.15	4.42	3.22	3.54	3.68	11.22	76	0.2187	1.27
101	May 28, 2008	296.37	283.65	283.65	12.72	12.72	288.40	290.56	2.11	2.46	1.85	0.64	2.28	1.76	4.02	76	0.2187	0.90
102	May 29, 2008	300.87	284.54	284.54	16.33	16.33	293.78	288.40	0.18	2.71	4.02	3.08	1.44	2.50	6.30	76	0.2187	1.26
103	May 30, 2008	302.93	292.76	292.76	10.17	10.17	297.56	293.78	3.36	5.05	5.09	2.46	4.21	3.99	10.46	76	0.2187	0.72
104	June 1, 2008	306.15	287.76	287.76	18.39	18.39	295.46	295.23	0.16	0.86	1.07	0.10	0.51	0.55	2.86	76	0.2187	1.02
105	June 4, 2008	303.54	291.76	291.76	11.78	11.78	297.62	299.40	3.46	3.36	4.70	3.33	3.41	3.71	8.67	76	0.2187	0.64

ID	Date	Daily Ambient Temperature						Daily Wind Speed							Depth of void		$\Delta T_{(Max)}$ obtained from FEM simulation	
		$T_{air (Max)}$	$T_{air (Min)}$	$T_{air (Min^*)}$	$T_{air (Change)}$	$T_{air (Change^*)}$	$T_{air (Avg)}$	$T_{air (Avg)-1}$	$W_{(Avg 1)}$	$W_{(Avg 2)}$	$W_{(Avg 3)}$	$W_{(Avg 4)}$	$W_{(Avg 12)}$	$W_{(Avg)}$	$W_{(Max)}$	d		$e^{-0.02 \cdot \text{depth}}$
106	June 5, 2008	303.37	296.15	296.15	7.22	7.22	299.72	297.62	2.94	3.57	6.02	5.04	3.25	4.39	8.54	76	0.2187	0.43
107	June 7, 2008	304.43	296.54	296.54	7.89	7.89	300.08	298.34	2.19	4.53	6.50	2.78	3.36	4.00	9.70	76	0.2187	0.42
108	June 10, 2008	300.37	286.87	286.87	13.50	13.50	294.09	292.22	0.28	2.21	3.16	2.87	1.24	2.13	4.87	76	0.2187	0.99
109	June 11, 2008	302.87	291.43	291.43	11.44	11.44	297.70	294.09	4.00	4.77	5.41	4.85	4.39	4.76	8.94	76	0.2187	0.71
110	June 14, 2008	302.93	288.43	288.43	14.50	14.50	295.17	294.04	0.16	1.61	2.53	0.56	0.88	1.22	5.50	76	0.2187	1.08
111	June 15, 2008	303.76	290.26	291.54	13.50	12.22	294.81	295.17	0.77	3.27	3.14	2.02	2.02	2.30	11.35	76	0.2187	0.63
112	June 16, 2008	299.87	287.93	290.04	11.94	9.83	293.96	294.81	0.23	0.50	1.60	0.41	0.36	0.68	2.86	76	0.2187	0.72
113	June 17, 2008	300.26	285.26	285.26	15.00	15.00	292.71	293.96	0.00	0.69	1.45	0.15	0.34	0.57	2.82	76	0.2187	0.93
114	June 18, 2008	301.76	286.65	286.65	15.11	15.11	294.35	292.71	0.00	1.79	1.05	0.19	0.90	0.76	3.58	76	0.2187	1.04
115	June 20, 2008	300.87	289.37	289.37	11.50	11.50	294.24	294.96	0.29	0.15	0.99	0.10	0.22	0.38	3.31	76	0.2187	0.91
116	June 21, 2008	302.93	289.87	289.87	13.06	13.06	296.37	294.24	0.14	1.58	1.59	0.19	0.86	0.87	4.02	76	0.2187	0.83
117	June 22, 2008	302.37	290.65	290.65	11.72	11.72	295.89	296.37	0.07	1.14	1.25	0.39	0.61	0.72	3.04	76	0.2187	0.74
118	June 23, 2008	302.65	287.37	287.37	15.28	15.28	295.51	295.89	0.02	0.53	0.99	0.17	0.27	0.43	2.55	76	0.2187	0.77
119	June 25, 2008	305.37	292.93	291.76	12.44	13.61	298.82	294.24	1.68	2.55	4.17	1.94	2.12	2.59	6.39	76	0.2187	1.12
120	June 27, 2008	303.65	292.93	292.43	10.72	11.22	298.41	294.83	1.82	2.95	4.12	1.64	2.38	2.63	6.62	76	0.2187	0.84
121	June 28, 2008	300.87	292.43	292.43	8.44	8.44	296.08	298.41	2.32	1.89	4.20	2.25	2.10	2.67	6.30	76	0.2187	0.52
122	June 29, 2008	299.43	290.15	291.54	9.28	7.89	294.23	296.08	3.62	3.72	3.34	0.97	3.67	2.91	7.69	76	0.2187	0.64
123	June 30, 2008	301.26	287.26	287.26	14.00	14.00	294.13	294.23	0.44	0.96	1.83	0.22	0.70	0.86	3.62	76	0.2187	0.90
124	July 1, 2008	303.15	286.65	286.65	16.50	16.50	295.73	294.13	0.00	1.08	2.91	1.65	0.54	1.41	4.78	76	0.2187	0.75
125	July 4, 2008	299.37	288.15	288.15	11.22	11.22	293.19	293.08	0.08	1.52	1.60	0.27	0.80	0.86	4.25	76	0.2187	0.80
126	July 5, 2008	300.65	285.87	285.87	14.78	14.78	293.83	293.19	0.00	0.85	2.21	1.12	0.43	1.05	4.11	76	0.2187	0.98
127	July 6, 2008	306.15	292.04	291.87	14.11	14.28	298.81	293.83	1.01	2.24	3.52	1.05	1.63	1.96	5.86	76	0.2187	1.22
128	July 7, 2008	306.93	296.43	296.43	10.50	10.50	301.61	298.81	2.47	3.00	3.64	2.51	2.74	2.91	5.86	76	0.2187	0.62
129	July 9, 2008	303.65	294.15	294.15	9.50	9.50	297.77	298.53	0.05	0.82	1.48	0.24	0.44	0.65	2.86	76	0.2187	0.46
130	July 10, 2008	304.43	293.43	293.43	11.00	11.00	298.75	297.77	0.24	2.21	3.27	1.29	1.23	1.76	5.19	76	0.2187	0.61
131	July 11, 2008	306.37	295.15	295.15	11.22	11.22	300.50	298.75	0.54	2.13	3.64	1.99	1.34	2.08	5.77	76	0.2187	0.77
132	July 13, 2008	302.43	289.04	289.04	13.39	13.39	295.04	296.63	0.54	2.11	2.86	0.40	1.32	1.48	5.23	76	0.2187	0.82
133	July 14, 2008	304.54	288.87	288.87	15.67	15.67	296.91	295.04	0.00	1.96	2.43	0.39	0.98	1.20	4.78	76	0.2187	0.96
134	July 15, 2008	304.04	290.65	290.65	13.39	13.39	297.67	296.91	0.00	1.77	4.12	0.66	0.89	1.64	6.26	76	0.2187	0.74
135	July 16, 2008	304.26	292.26	292.26	12.00	12.00	298.32	297.67	0.33	2.00	2.82	0.69	1.16	1.46	5.95	76	0.2187	0.66
136	July 17, 2008	304.37	292.26	292.26	12.11	12.11	298.37	298.32	0.00	1.95	3.17	0.50	0.98	1.41	5.19	76	0.2187	0.68
137	July 19, 2008	305.65	295.76	295.43	9.89	10.22	300.54	298.45	0.03	1.36	2.79	1.50	0.70	1.42	4.38	76	0.2187	0.68
138	July 20, 2008	307.87	297.93	297.93	9.94	9.94	302.58	300.54	1.30	3.00	3.06	0.69	2.15	2.01	5.63	76	0.2187	0.68
139	July 21, 2008	307.76	296.76	296.76	11.00	11.00	301.84	302.58	0.55	0.83	2.50	0.90	0.69	1.19	4.11	76	0.2187	0.64
140	July 23, 2008	301.04	293.76	293.93	7.28	7.11	296.76	295.35	0.36	2.40	2.82	0.67	1.38	1.56	4.96	76	0.2187	0.51

ID	Date	Daily Ambient Temperature							Daily Wind Speed							Depth of void		$\Delta T_{(Max)}$ obtained from FEM simulation
		$T_{air (Max)}$	$T_{air (Min)}$	$T_{air (Min^*)}$	$T_{air (Change)}$	$T_{air (Change^*)}$	$T_{air (Avg)}$	$T_{air (Avg)-1}$	$W_{(Avg 1)}$	$W_{(Avg 2)}$	$W_{(Avg 3)}$	$W_{(Avg 4)}$	$W_{(Avg 12)}$	$W_{(Avg)}$	$W_{(Max)}$	d	$e^{-0.02 \cdot depth}$	
141	July 26, 2008	305.65	295.76	295.76	9.89	9.89	299.41	297.59	0.03	0.41	1.03	0.14	0.22	0.40	2.64	76	0.2187	0.60
142	July 27, 2008	304.65	294.37	294.37	10.28	10.28	299.70	299.41	0.30	1.33	2.26	1.25	0.82	1.28	4.69	76	0.2187	0.64
143	July 29, 2008	305.43	295.43	295.43	10.00	10.00	299.48	297.11	0.55	1.20	0.94	1.43	0.88	1.03	3.62	76	0.2187	0.58
144	July 31, 2008	301.93	293.87	293.87	8.06	8.06	296.52	294.55	0.00	0.06	1.20	0.54	0.03	0.45	3.71	76	0.2187	0.55
145	May 5, 2008	297.65	278.93	278.93	18.72	18.72	289.42	285.18	0.22	1.75	2.93	0.53	0.99	1.36	5.41	127	0.0789	0.35
146	May 6, 2008	296.54	285.26	285.26	11.28	11.28	289.86	289.42	0.25	1.76	5.80	4.26	1.01	3.02	10.24	127	0.0789	0.18
147	May 13, 2008	294.76	286.76	286.76	8.00	8.00	291.20	286.96	3.57	4.48	4.05	3.83	4.02	3.98	7.06	127	0.0789	0.13
148	May 16, 2008	296.43	277.15	277.15	19.28	19.28	287.85	285.36	0.18	2.25	3.53	2.27	1.21	2.06	5.32	127	0.0789	0.46
149	May 17, 2008	300.87	286.26	286.26	14.61	14.61	293.55	287.85	2.78	3.21	2.88	1.81	3.00	2.67	5.01	127	0.0789	0.23
150	May 18, 2008	295.87	284.15	284.87	11.72	11.00	290.95	293.55	0.91	1.93	3.21	0.52	1.42	1.64	5.99	127	0.0789	0.09
151	May 19, 2008	299.54	283.15	283.15	16.39	16.39	291.55	290.95	0.53	2.92	2.07	0.96	1.73	1.62	6.26	127	0.0789	0.31
152	May 20, 2008	294.04	282.26	287.65	11.78	6.39	289.87	291.55	1.39	2.66	3.01	0.65	2.03	1.93	5.77	127	0.0789	0.15
153	May 21, 2008	296.04	282.54	282.26	13.50	13.78	289.03	289.87	0.81	1.04	1.40	0.13	0.93	0.85	4.11	127	0.0789	0.37
154	May 23, 2008	295.15	287.65	287.65	7.50	7.50	290.67	287.86	3.45	4.04	3.35	3.89	3.75	3.68	7.24	127	0.0789	0.19
155	May 25, 2008	303.76	289.93	289.76	13.83	14.00	296.87	289.37	2.93	4.15	4.42	3.22	3.54	3.68	11.22	127	0.0789	0.31
156	May 28, 2008	296.37	283.65	283.65	12.72	12.72	288.40	290.56	2.11	2.46	1.85	0.64	2.28	1.76	4.02	127	0.0789	0.48
157	May 29, 2008	300.87	284.54	284.54	16.33	16.33	293.78	288.40	0.18	2.71	4.02	3.08	1.44	2.50	6.30	127	0.0789	0.41
158	May 30, 2008	302.93	292.76	292.76	10.17	10.17	297.56	293.78	3.36	5.05	5.09	2.46	4.21	3.99	10.46	127	0.0789	0.20
159	June 1, 2008	306.15	287.76	287.76	18.39	18.39	295.46	295.23	0.16	0.86	1.07	0.10	0.51	0.55	2.86	127	0.0789	0.36
160	June 4, 2008	303.54	291.76	291.76	11.78	11.78	297.62	299.40	3.46	3.36	4.70	3.33	3.41	3.71	8.67	127	0.0789	0.23
161	June 5, 2008	303.37	296.15	296.15	7.22	7.22	299.72	297.62	2.94	3.57	6.02	5.04	3.25	4.39	8.54	127	0.0789	0.15
162	June 7, 2008	304.43	296.54	296.54	7.89	7.89	300.08	298.34	2.19	4.53	6.50	2.78	3.36	4.00	9.70	127	0.0789	0.17
163	June 10, 2008	300.37	286.87	286.87	13.50	13.50	294.09	292.22	0.28	2.21	3.16	2.87	1.24	2.13	4.87	127	0.0789	0.47
164	June 11, 2008	302.87	291.43	291.43	11.44	11.44	297.70	294.09	4.00	4.77	5.41	4.85	4.39	4.76	8.94	127	0.0789	0.26
165	June 14, 2008	302.93	288.43	288.43	14.50	14.50	295.17	294.04	0.16	1.61	2.53	0.56	0.88	1.22	5.50	127	0.0789	0.47
166	June 15, 2008	303.76	290.26	291.54	13.50	12.22	294.81	295.17	0.77	3.27	3.14	2.02	2.02	2.30	11.35	127	0.0789	0.31
167	June 16, 2008	299.87	287.93	290.04	11.94	9.83	293.96	294.81	0.23	0.50	1.60	0.41	0.36	0.68	2.86	127	0.0789	0.33
168	June 17, 2008	300.26	285.26	285.26	15.00	15.00	292.71	293.96	0.00	0.69	1.45	0.15	0.34	0.57	2.82	127	0.0789	0.42
169	June 18, 2008	301.76	286.65	286.65	15.11	15.11	294.35	292.71	0.00	1.79	1.05	0.19	0.90	0.76	3.58	127	0.0789	0.38
170	June 20, 2008	300.87	289.37	289.37	11.50	11.50	294.24	294.96	0.29	0.15	0.99	0.10	0.22	0.38	3.31	127	0.0789	0.35
171	June 21, 2008	302.93	289.87	289.87	13.06	13.06	296.37	294.24	0.14	1.58	1.59	0.19	0.86	0.87	4.02	127	0.0789	0.28
172	June 22, 2008	302.37	290.65	290.65	11.72	11.72	295.89	296.37	0.07	1.14	1.25	0.39	0.61	0.72	3.04	127	0.0789	0.27
173	June 23, 2008	302.65	287.37	287.37	15.28	15.28	295.51	295.89	0.02	0.53	0.99	0.17	0.27	0.43	2.55	127	0.0789	0.31
174	June 25, 2008	305.37	292.93	291.76	12.44	13.61	298.82	294.24	1.68	2.55	4.17	1.94	2.12	2.59	6.39	127	0.0789	0.35
175	June 27, 2008	303.65	292.93	292.43	10.72	11.22	298.41	294.83	1.82	2.95	4.12	1.64	2.38	2.63	6.62	127	0.0789	0.29

ID	Date	Daily Ambient Temperature							Daily Wind Speed							Depth of void		$\Delta T_{(Max)}$ obtained from FEM simulation
		T _{air} (Max)	T _{air} (Min)	T _{air} (Min*)	T _{air} (Change)	T _{air} (Change*)	T _{air} (Avg)	T _{air} (Avg)-1	W _(Avg 1)	W _(Avg 2)	W _(Avg 3)	W _(Avg 4)	W _(Avg 12)	W _(Avg)	W _(Max)	d	e ^{-0.02*depth}	
176	June 28, 2008	300.87	292.43	292.43	8.44	8.44	296.08	298.41	2.32	1.89	4.20	2.25	2.10	2.67	6.30	127	0.0789	0.21
177	June 29, 2008	299.43	290.15	291.54	9.28	7.89	294.23	296.08	3.62	3.72	3.34	0.97	3.67	2.91	7.69	127	0.0789	0.31
178	June 30, 2008	301.26	287.26	287.26	14.00	14.00	294.13	294.23	0.44	0.96	1.83	0.22	0.70	0.86	3.62	127	0.0789	0.40
179	July 1, 2008	303.15	286.65	286.65	16.50	16.50	295.73	294.13	0.00	1.08	2.91	1.65	0.54	1.41	4.78	127	0.0789	0.38
180	July 4, 2008	299.37	288.15	288.15	11.22	11.22	293.19	293.08	0.08	1.52	1.60	0.27	0.80	0.86	4.25	127	0.0789	0.36
181	July 5, 2008	300.65	285.87	285.87	14.78	14.78	293.83	293.19	0.00	0.85	2.21	1.12	0.43	1.05	4.11	127	0.0789	0.38
182	July 6, 2008	306.15	292.04	291.87	14.11	14.28	298.81	293.83	1.01	2.24	3.52	1.05	1.63	1.96	5.86	127	0.0789	0.35
183	July 7, 2008	306.93	296.43	296.43	10.50	10.50	301.61	298.81	2.47	3.00	3.64	2.51	2.74	2.91	5.86	127	0.0789	0.12
184	July 9, 2008	303.65	294.15	294.15	9.50	9.50	297.77	298.53	0.05	0.82	1.48	0.24	0.44	0.65	2.86	127	0.0789	0.24
185	July 10, 2008	304.43	293.43	293.43	11.00	11.00	298.75	297.77	0.24	2.21	3.27	1.29	1.23	1.76	5.19	127	0.0789	0.25
186	July 11, 2008	306.37	295.15	295.15	11.22	11.22	300.50	298.75	0.54	2.13	3.64	1.99	1.34	2.08	5.77	127	0.0789	0.26
187	July 13, 2008	302.43	289.04	289.04	13.39	13.39	295.04	296.63	0.54	2.11	2.86	0.40	1.32	1.48	5.23	127	0.0789	0.43
188	July 14, 2008	304.54	288.87	288.87	15.67	15.67	296.91	295.04	0.00	1.96	2.43	0.39	0.98	1.20	4.78	127	0.0789	0.36
189	July 15, 2008	304.04	290.65	290.65	13.39	13.39	297.67	296.91	0.00	1.77	4.12	0.66	0.89	1.64	6.26	127	0.0789	0.25
190	July 16, 2008	304.26	292.26	292.26	12.00	12.00	298.32	297.67	0.33	2.00	2.82	0.69	1.16	1.46	5.95	127	0.0789	0.22
191	July 17, 2008	304.37	292.26	292.26	12.11	12.11	298.37	298.32	0.00	1.95	3.17	0.50	0.98	1.41	5.19	127	0.0789	0.24
192	July 19, 2008	305.65	295.76	295.43	9.89	10.22	300.54	298.45	0.03	1.36	2.79	1.50	0.70	1.42	4.38	127	0.0789	0.21
193	July 20, 2008	307.87	297.93	297.93	9.94	9.94	302.58	300.54	1.30	3.00	3.06	0.69	2.15	2.01	5.63	127	0.0789	0.19
194	July 21, 2008	307.76	296.76	296.76	11.00	11.00	301.84	302.58	0.55	0.83	2.50	0.90	0.69	1.19	4.11	127	0.0789	0.19
195	July 23, 2008	301.04	293.76	293.93	7.28	7.11	296.76	295.35	0.36	2.40	2.82	0.67	1.38	1.56	4.96	127	0.0789	0.32
196	July 26, 2008	305.65	295.76	295.76	9.89	9.89	299.41	297.59	0.03	0.41	1.03	0.14	0.22	0.40	2.64	127	0.0789	0.12
197	July 27, 2008	304.65	294.37	294.37	10.28	10.28	299.70	299.41	0.30	1.33	2.26	1.25	0.82	1.28	4.69	127	0.0789	0.16
198	July 29, 2008	305.43	295.43	295.43	10.00	10.00	299.48	297.11	0.55	1.20	0.94	1.43	0.88	1.03	3.62	127	0.0789	0.19
199	July 31, 2008	301.93	293.87	293.87	8.06	8.06	296.52	294.55	0.00	0.06	1.20	0.54	0.03	0.45	3.71	127	0.0789	0.23

VITA

Rilya Rumbayan was born in Manado, Indonesia. She received the B.S. in Civil Engineering from University of Sam Ratulangi, in Manado, Indonesia in 2002. Then, she pursued the master degree with the Asian Development Bank-Japan Scholarship Program (ADB-JSP) in University of Tokyo, Japan and earned the M.Eng. in 2006. After graduation, she joined Polytechnic of Manado as a faculty member. She entered the University of Missouri, Columbia, Missouri in August, 2008 with Fulbright scholarship for a PhD. program in Civil Engineering.